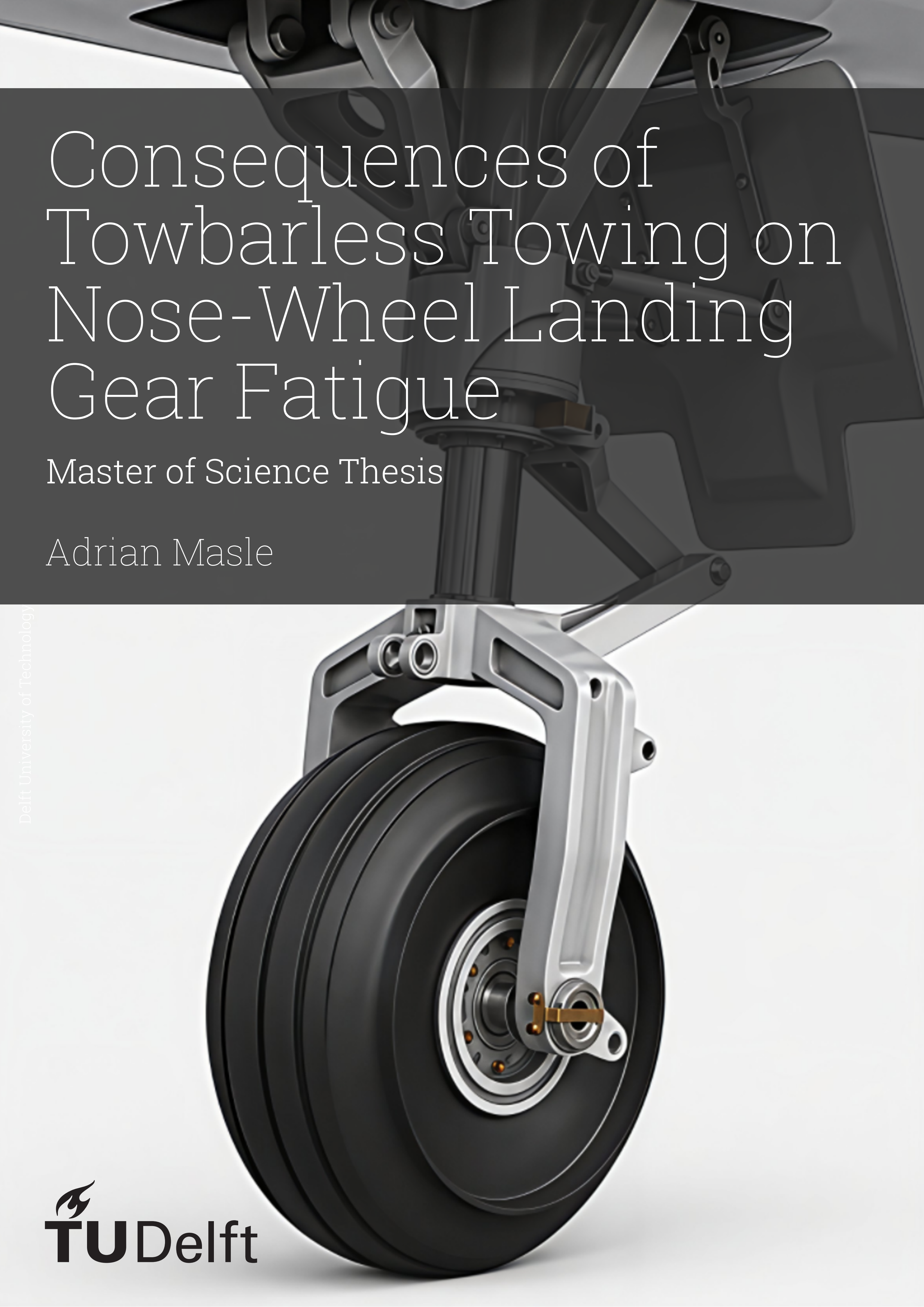

Consequences of Towbarless Towing on Nose-Wheel Landing Gear Fatigue

Master of Science Thesis

Adrian Masle

Delft University of Technology

Consequences of Towbarless Towing on Nose-Wheel Landing Gear Fatigue

Master of Science Thesis

by

Adrian Masle

To obtain the degree of Master of Science at Delft University of Technology,
to be defended publicly on June 3rd, 2026 at 09:30

Student number:	5032148
Project duration:	August 25th, 2025 - May 15th, 2026
Chair:	Prof.dr.ir. R.C. Alderliesten, TU Delft
Supervisors:	Dr.ir. J.A. Pascoe, TU Delft L. Tofoni, AOG4Jets
External member:	Dr.ir. S. Giovani Pereira Castro, TU Delft
Faculty:	Faculty of Aerospace Engineering, Delft

Cover: Pilatus PC-24 NWLG illustration generated using ChatGPT
Style: TU Delft Report Style, with modifications by Daan Zwaneveld

Preface

This thesis marks the conclusion of my MSc programme in Aerospace Engineering at Delft University of Technology. Looking back, this project has been a particularly enjoyable, challenging, and above all, highly educational final stage of my studies. What I valued most in this thesis was its strong practical focus, as gaining real-world experience was one of my main reasons for choosing this project.

Although this thesis was submitted under my name, it is by no means the result of individual effort alone. I am sincerely grateful to John-Alan Pascoe for his day-to-day supervision, his readiness to answer every question, and his consistent support through weekly meetings, constructive feedback, and critical guidance throughout the project. His involvement has been of great value at every stage of this work.

I would also like to express my gratitude to Lorenzo Tofoni for making this research possible in practice. By facilitating access to equipment, operational insights, and valuable opportunities in the general aviation sector, he enabled me to observe aircraft towing in its real-world context, speak with experienced professionals, and develop a much deeper understanding of the subject than would otherwise have been possible.

In addition, I would like to thank Dave Ruijtenbeek for his support in the laboratory and for helping make the fatigue testing possible, and Alexander in ’t Veld for his help during the test activities at Rotterdam The Hague Airport.

On a personal note, I am deeply thankful to my family and friends for their constant encouragement and support, particularly during the more demanding moments of this project. In this thesis, I would like to provide the reader with a clear and accessible account of the research conducted.

Adrian Masle
Delft, May 2026

Abstract

Towbarless towing is increasingly used in general aviation ground handling, yet its consequences for nose-wheel landing gear fatigue remain insufficiently understood. This thesis investigated whether, and to what extent, towbarless towing leads to different fatigue behaviour than conventional towbar towing for the selected aft-folding tricycle nose-wheel landing gear reference configuration considered within the 4,000–9,000 kg maximum take-off mass class. The study was fundamentally comparative and focused on relative fatigue severity rather than defining a universally transferable absolute in-service life.

A sequential in-field, structural, and laboratory fatigue methodology was adopted. First, representative towbar manoeuvres were obtained through in-field measurements using a calibrated instrumented towbar and supporting kinematic data. Because direct like-for-like measurement of towbarless loads was limited in practice, a translation framework was used to reconstruct corresponding towbarless manoeuvre histories. These histories were assembled into towing spectra and applied in a staged global–local finite-element analysis to identify the governing structural response and define equivalent laboratory fatigue spectra. Finally, laboratory fatigue tests were performed on spectra derived from the finite-element hotspot response to assess the resulting relative life differences.

The results showed that the primary difference between towbar and towbarless towing did not lie in steady towing, but in a limited set of transient-sensitive manoeuvres, particularly braking and selected acceleration cases. Structurally, towbarless towing redistributed the force-introduction path from tow-lug-dominated loading towards axle-dominated loading. However, it did not create a new globally governing fatigue hotspot. Instead, the drag-brace region remained governing, while fatigue-driven severity increased. Although the laboratory results could not be directly related to the fatigue behaviour of the actual drag-brace structure, they did provide an indication of the difference in fatigue severity between towbarless and towbar towing. In the base-spectrum laboratory comparison, the measured towbar→towbarless specimen life decreased from 54.2 ± 6.0k to 27.3 ± 3.1k laboratory cycles. When converted using the spectrum-specific cycle content of the repeated 100-operation mission block, this corresponded to a reduction from 303 ± 34 to 41 ± 5 equivalent mission blocks. Overload-insertion tests further indicated sequence effects consistent with retardation. The overload-insertion results suggested that, under mixed towing operations, the net fatigue penalty of towbarless towing might be less severe than a direct comparison between pure towbar and pure towbarless spectra would imply. However, this effect remained secondary and did not overturn the primary ranking observed in the present test programme.

Overall, within the investigated general-aviation nose-wheel landing gear context, the results indicate that towbarless towing is more fatigue-severe than conventional towbar towing. This conclusion is supported at the manoeuvre, structural, and laboratory levels, and is most clearly expressed as a relative ranking rather than as a directly transferable absolute in-service life reduction. Within the adopted methodology, towbarless towing did not introduce a fundamentally new governing fatigue mechanism or hotspot, but intensified the existing towing-related fatigue problem by amplifying critical transients and by shifting load transfer from the tow-lug path towards the axle/fork path. At the same time, the quantitative life reduction should be interpreted within the limits of the adopted methodology, since the study remained configuration-specific and relied on reconstructed towbarless histories, finite-element-based hotspot translation, and simplified laboratory proxy testing. The thesis, therefore, provides a structurally grounded comparative basis for assessing the effects of towing methods on fatigue severity, while further work is still required on mixed operational spectra, configuration dependence, and service representativeness.

Contents

List of Figures

List of Tables

Nomenclature

Symbols

Symbol	Description	Unit
A	Area	m^2
A_{db}	Net cross-sectional area of the dog-bone gauge section	m^2
a	Crack length	m
a_0	Initial crack length	m
a_f	Final crack length	m
$a_{\text{tug}}(t) = [a_x, a_y, a_z]$	Tug linear accelerations	$\text{m}\,\text{s}^{-2}$
B_k	Normalised bin interval	–
C	Paris-law coefficient	–
C	Intercept parameter of the MMPDS-style fitted S–N relation	–
C_{cal}	Calibration intercept	N
$C_{L\,\text{max}}$	Maximum lift coefficient	–
da/dN	Fatigue crack growth rate	m/cycle
D	Damage indicator / accumulated damage, depending on context	–
D^*	Normalised summary damage indicator used for hotspot ranking	–
D_{blk}	Palmgren–Miner damage per repeated laboratory block	–
dt	Sampling interval	s
E	Young's modulus	Pa
$F_{\text{bar}}(t)$	Towbar axial load time history	N
F_{eq}	Gravity-corrected equivalent force	N
$F_m(t)$	Towing-force time history for manoeuvre m	N
$F_{\text{pk},m}$	Peak absolute tow force for manoeuvre m	N
F_{req}	Resultant towing force used for turning-force decomposition	N
$F_{\text{rr,tot}}$	Total rolling-resistance force	N
$F_{\text{rr},N}$	Nose-wheel rolling-resistance force	N
$F_{\text{rr},N,\text{PC24}}$	PC-24-scaled nose-wheel rolling-resistance force	N
F_{spec}	Applied axial force in the fatigue specimen	N
$F_{\text{TB}}(t)$	Towbar axial load time history	N
$F_{\text{TBL}}(t)$	Towbarless axial load time history	N
F_{UTM}	Force reported by test machine during calibration	N
F_x	Longitudinal (axial) force component at NWLG	N
F_y	Lateral force component at NWLG	N
F_z	Vertical force component at NWLG	N
F_j^*	Specimen force level chosen to reproduce hotspot stress for case j	N
f_s	Sampling frequency	Hz
GF	Strain-gauge factor	–
h_{CG}	CG height above ground	m
$h_{i,k}$	Histogram count in bin k for mission spectrum i	–
$H^{(100)}$	Aggregated 100-mission block total	–
$H_k^{(100)}$	Bin-k count in the aggregated 100-mission block	–
k	Irregularity factor of load history	–
k_i	Stress offset applied to cycle i during R-conditioning	Pa
k_m	Manoeuvre-specific linear force-to-stress scaling coefficient	$\text{MPa}\,\text{kN}^{-1}$
k_W	Weight-scaling factor used to map PC-12 loads to the PC-24 model	–
K	Stress-intensity factor	$\text{MPa}\sqrt{\text{m}}$
K_I	Mode-I stress-intensity factor	$\text{MPa}\sqrt{\text{m}}$
K_{Ic}	Fracture toughness	$\text{MPa}\sqrt{\text{m}}$
K_{cal}	Calibration slope	N

Continued on next page

Symbol	Description	Unit
K_t	Stress concentration factor	–
$K_{t,\text{eff}}$	Effective notch severity inferred from specimen behaviour	–
$K_{t,\text{geom}}$	Geometric stress concentration factor of the specimen geometry	–
$K_{t,\text{grip}}$	Grip-induced effective stress concentration factor	–
L_W	Wing lift	N
L_{HT}	Horizontal-tail lift	N
M	Slope parameter of the MMPDS-style fitted S–N relation	–
M_0	Aircraft reference mass moment (W&B)	kg m
M_f	Fuel mass moment (W&B)	kg m
M_{rep}	Representative mass moment (W&B)	kg m
M_W	Wing pitch moment	N m
M_x	Moment about aircraft-fixed x-axis	N m
M_y	Moment about aircraft-fixed y-axis	N m
M_z	Moment about aircraft-fixed z-axis	N m
m	Paris-law exponent	–
m	Aircraft mass	kg
m_{BOW}	Basic operating weight mass	kg
m_f	Fuel mass	kg
m_0	Reference mass	kg
m_{rep}	Representative mass	kg
N	Number of cycles in life integrations	–
$N_i^{(100)}$	Number of missions of type i in a 100-mission horizon	–
$N_{\text{blk,pred}}$	Predicted number of repeated blocks to failure	blocks
N_f	Cycles to failure	cycles
$N_{f,i}$	Cycles to failure for level i	cycles
$\bar{N}_{\text{missions,exp}}$	Mean measured missions to failure	missions
n_i	Number of cycles at discrete level i in a block	cycles
$n_{\text{RF},X,pq}$	Rainflow cycle count in mean–range bin (p, q) for spectrum X	–
N_p	Number of peaks	–
N_c	Number of level crossings	–
N_{NW}	Nose-wheel / NWLG normal load	N
p	Roll rate	rad s^{-1}
q	Pitch rate	rad s^{-1}
r	Yaw rate	rad s^{-1}
$p_{\text{GPS,tug}}(t) = [\phi, \lambda, h]$	Tug position (latitude, longitude, height)	deg, deg, m
P	Exponent in the MMPDS-style equivalent-stress definition	–
R	Stress ratio $\sigma_{\text{min}}/\sigma_{\text{max}}$	–
R_j	Stress ratio of counted cycle j	–
R_N	nose-wheel landing gear vertical reaction	N
R_M	Main-gear vertical reaction	N
R_{Nx}	Longitudinal ground-friction force at nose-wheel landing gear	N
R_{Mx}	Longitudinal ground-friction force at main gear	N
r	Local radius at gauge location/section	m
r_k	Ratiometric bridge output of calibration channel k	–
S	Nominal far-field stress	Pa
$S_{e,-1}$	Fully-reversed endurance strength ($R \approx -1$)	Pa
S_{eq}	Equivalent stress parameter in the MMPDS-style relation	Pa
$S_{\text{eq},i}$	Equivalent stress parameter for level i in the MMPDS-style relation	Pa
S_{max}	Maximum stress used in the MMPDS-style relation	Pa
S_{op}	Crack opening stress	Pa
S_f	Endurance limit in tension / bending	Pa
τ_f	Endurance limit in torsion	Pa
S_u	Ultimate tensile strength	Pa
T	Torque	N m
$U(R)$	Crack-closure function (effective range factor)	–
U	Goodman utilisation parameter used for endurance filtering	–

Continued on next page

Symbol	Description	Unit
$V_{\text{diff},k}$	Differential bridge voltage of calibration channel k	V
V_{ex}	Bridge excitation voltage	V
$v_{\text{tug}}(t)$	Tug ground speed	$\text{m}\,\text{s}^{-1}$
V_{air}	Airspeed	$\text{m}\,\text{s}^{-1}$
W	Aircraft weight	N
W_{ax}	Axial weight component	N
w	Interpolation weight MMPDS curves	–
x_{CG}	Longitudinal CG station / location	m
x_N	CG-to-nose-gear moment arm	m
x_M	CG-to-main-gear moment arm	m
α_i	Share (weight) of mission spectrum i in usage mix	–
β	Geometry factor in K	–
$\gamma_{z\theta}$	Shear strain used for torsion channel	–
ΔK	Stress-intensity factor range	$\text{MPa}\sqrt{\text{m}}$
ΔK_{eff}	Effective stress-intensity range	$\text{MPa}\sqrt{\text{m}}$
$\Delta\sigma$	Stress range	Pa
$\Delta\sigma_j$	Stress range of counted cycle j	Pa
$\Delta\sigma_{\text{bin}}$	Stress discretisation	Pa
δ_{tight}	Representative tight-turn steering angle	deg
δ_{wide}	Representative wide-turn steering angle	deg
ε	Strain (generic); also small fraction parameter in Sec. 2.5.4	–
ε_{avg}	Average axial strain from rosette	–
θ	Circumferential gauge angle	deg
λ_N	Nose-load fraction of the aircraft weight	–
μ	Ground friction coefficient	–
μ_{RR}	Rolling-resistance coefficient	–
ν	Poisson's ratio	–
ρ	Air density	$\text{kg}\,\text{m}^{-3}$
$\rho_{\text{TBL/TB}}$	Experimental life ratio of TBL to TB	–
$\rho_{\text{RET,TB}}$	Experimental overload-effect life ratio for TB	–
$\rho_{\text{RET,TBL}}$	Experimental overload-effect life ratio for TBL	–
σ_a	Stress amplitude	Pa
$\sigma_{a,\text{eq},R=0.1}$	Equivalent stress amplitude expressed at $R = 0.1$	Pa
$\sigma_{a,\text{lim}}(R)$	Allowable stress amplitude at stress ratio R	Pa
$\sigma_{\text{blk}}(t)$	Stress history of the assembled repeating laboratory block	Pa
σ_m	Mean stress	Pa
$\sigma_m(t)$	Reconstructed hotspot stress history for manoeuvre m	Pa
$\sigma_{m,\text{lim}}(R)$	Allowable mean stress at stress ratio R	Pa
σ_{max}	Maximum stress in a cycle	Pa
σ_{min}	Minimum stress in a cycle	Pa
$\sigma_{\text{max,lim}}$	Limiting maximum stress at the chosen constant-life point	Pa
$\sigma_{\text{min,lim}}$	Limiting minimum stress at the chosen constant-life point	Pa
$\sigma_{\text{max,cap}}$	Maximum stress cap for non-retardation cycles	Pa
$\sigma_{\text{max,ovl}}$	Maximum stress assigned to the overload cycle	Pa
$\sigma_{\text{max}}^{\text{nonRET}}$	Maximum stress in non-retardation cycles	Pa
$\sigma_{\text{max}}^{\text{RET}}$	Maximum stress in retardation cycles	Pa
$\sigma_{\text{pk},m}$	Hotspot stress at peak tow force for manoeuvre m	Pa
σ_{ref}	Reference stress used for normalisation / discretisation	Pa
σ_{spec}	Nominal axial stress in the specimen gauge section	Pa
σ_{vM}	von Mises equivalent stress	Pa
σ_y	Yield strength	Pa
σ_0	Baseline hotspot stress at zero tow load	Pa
$\bar{\sigma}_{1,\text{local}}$	Volume-averaged local maximum principal stress at the hotspot	Pa
σ_1	First principal stress	Pa
σ_2	Second principal stress	Pa
σ_3	Third principal stress	Pa

Continued on next page

Symbol	Description	Unit
$\sigma_a^{(0)}$	Fully-reversed equivalent stress amplitude (mean-stress corrected)	Pa
$\varphi(t)$	Normalised stress history	–
$\varphi_{r,p}$	Normalised range bin midpoint	–
$\varphi_{m,q}$	Normalised mean bin midpoint	–
$\chi_{\text{GPS}}(t)$	Course over ground	deg
$\psi._{\text{tug}}(t)$	Tug yaw rate	rad s^{-1}

Abbreviations

Abbreviation	Definition
AC	Advisory Circular
ADC	Analogue-to-Digital Converter
AOG	Aircraft on Ground
AMC	Acceptable Means of Compliance
AMM	Aircraft Maintenance Manual
APC	Amplitude Phase Control
ASTM	American Society for Testing and Materials
BOW	Basic Operating Weight
CA	Constant Amplitude
CG	Centre of Gravity
CS-23	Certification Specifications 23
DAQ	Data Acquisition
DOF	Degree of Freedom
EASA	European Union Aviation Safety Agency
FAA	Federal Aviation Administration
FBD	Free-Body Diagram
FEM	Finite-Element Model
GA	General Aviation
GNSS	Global Navigation Satellite System
GPS	Global Positioning System
HAT	Hardware Attached on Top
I2C	Inter-Integrated Circuit
ICAS	International Congress of the Aeronautical Sciences
IMU	Inertial Measurement Unit
ISO	International Organisation for Standardisation
LAX	Los Angeles International Airport
LOV	Limit of Validity
MMPDS	Metallic Materials Properties Development and Standardisation
MPC	Multi-Point Constraint
MTOM	Maximum Take-Off Mass
MTOW	Maximum Take-Off Weight
NDT	Non-Destructive Testing
NWLG	Nose-Wheel Landing Gear
OEW	Operating Empty Weight
POD	Probability of Detection
PPS	Pulse Per Second
RET	Retardation
RP	Reference Point
SAE	Society of Automotive Engineers
SPI	Serial Peripheral Interface
TB	Towbar
TBT	Towbar Towing
TBL	Towbarless
TBLT	Towbarless Towing
TLTV	Towbarless Towing Vehicle

Continued on next page

Abbreviation	Definition
UART	Universal Asynchronous Receiver-Transmitter
UTM	Universal Testing Machine
VA	Variable Amplitude
W&B	Weight and Balance
WFD	Widespread Fatigue Damage
WP	Work Package

1

Introduction

During ground operations, an aircraft's nose-wheel landing gear is subjected to repeated loading from activities such as taxiing, braking, turning, and towing. Although these loads generally occur at lower speeds than flight and landing loads, their repeated application over the aircraft's service life means they can remain relevant from a fatigue perspective. Within this broader set of ground-induced loads, towing is of particular interest because it forms a recurring part of aircraft repositioning, hangar movement, and maintenance support.

Traditionally, towing loads are introduced into the aircraft through a towbar connected to dedicated tow fittings, resulting in a relatively well-defined load path into the nose-wheel landing gear. In current practice, however, towbarless towing vehicles are becoming more common. Unlike conventional towbar towing, towbarless systems engage the nose wheels directly, transferring towing loads to the landing gear via a different interface and load path. As a result, the structural response of the landing gear may differ from that associated with conventional towbar towing, including differences in local force distribution, bending and torsional response, and the location at which fatigue-critical stresses develop. [1, 2, 3]

This development gave rise to the central problem addressed in this thesis. Although towbarless towing is becoming increasingly common in aircraft ground handling, its structural implications for nose-wheel landing gear fatigue remain insufficiently understood. Because towbarless towing introduces loads into the landing gear through a different interface and load path than conventional towbar towing, and may also modify the handling characteristics and kinematics of representative ground manoeuvres, it may change the local stress distribution and, consequently, the rate and location of fatigue damage development. [4, 5]

At present, limited information is available on whether these differences are negligible, beneficial, or adverse relative to conventional towbar towing. It is likewise unclear to what extent such effects are configuration-dependent, that is, specific to particular nose-wheel landing gear designs, or whether broader tendencies can be identified across representative general-aviation configurations. [5, 6]

The motivation for this thesis originated from the research collaboration with AOG4Jets [7]. In practice, AOG4Jets had reported field indications that certain nose-wheel landing gear components in general-aviation aircraft appeared to exhibit earlier-than-expected service degradation. One possible explanation, and the working hypothesis underlying this research, was that the increasing use of towbarless towing contributed to this observed degradation through its different load introduction and manoeuvre characteristics. Since open literature on the fatigue implications of towbarless towing remains limited, there was a relevant need for a more structured investigation of the underlying structural effects. [3, 5]

A better understanding of the structural consequences of towbarless towing is relevant both scientifically and practically. Scientifically, it contributes to the broader question of how changes in operational loading should be translated into structural response and fatigue implications. In practice, it can support improved awareness of potential towing-related degradation and a more technically grounded evaluation of whether towbarless towing may affect the safe operation of general-aviation aircraft. [2, 8, 9]

Against this background, the objective of this thesis was to investigate whether, and to what extent, towbarless towing led to different fatigue behaviour in general-aviation nose-wheel landing gear than conventional towbar towing. This research examined how the two towing methods differed in load introduction during representative ground manoeuvres, how these differences affected the resulting structural response of the landing gear, and whether they translated into differences in fatigue-critical locations and relative fatigue severity.

The objective was, therefore, fundamentally comparative in nature. Rather than seeking to establish a universal absolute fatigue life for all nose-wheel landing gear systems, the thesis aimed to determine, on a relative basis, whether towbarless towing led to lower, comparable, or higher fatigue severity than towbar towing for the representative configurations and loading spectra considered. In this way, the thesis addressed the broader research question of whether towbarless towing introduced structurally meaningful fatigue effects, whether these effects should be understood primarily as configuration-specific or as part of a more general trend, and whether the topic warranted further investigation.

To address this objective, the scope of the thesis was limited to towing-induced fatigue effects in nose-wheel landing gear during ground operations, with emphasis on representative steerable tricycle nose-wheel landing gear configurations within general-aviation turboprops and light- to midsize jets. In the representative design catalogue considered, this corresponded to aircraft with maximum take-off masses of approximately 4,000-9,000 kg. More broadly, recent work has likewise treated landing-gear fatigue as a safe-life, high-cycle fatigue problem in which local geometric stress concentrations govern crack initiation, and has therefore combined material testing, component testing, FE validation, and local-stress-based life prediction within an integrated experimental–numerical framework [10]. Multiple representative nose-wheel landing gear and drag-brace arrangements were considered to assess whether the effect of towbarless towing was design-dependent. One representative steerable, straight-oleo configuration with a double fork and single nose wheel was then selected for detailed finite-element and laboratory correlation work. The thesis did not aim to provide a complete reassessment of all landing gear load cases, nor to establish a universal framework applicable to all aircraft types. Instead, it focused on whether towbarless towing led to structurally meaningful differences in load introduction, local stress response, fatigue-critical locations, and relative fatigue severity compared with conventional towbar towing.

Methodologically, the thesis followed a sequential field-to-structure-to-fatigue approach. First, the operational context was established through a literature review that identified the relevant towing mechanisms, likely load-path differences, suspected degradation mechanisms, and the principal knowledge gaps this work aimed to address. Next, an in-field towing campaign was conducted to obtain representative towbar manoeuvres and supporting kinematic data, supported by towbar calibration and a minimally intrusive measurement strategy. Because direct like-for-like measurement of towbarless loads was not practically available for the full test programme, a translation framework was used to reconstruct representative towbarless loading histories from the measured towbar data. These manoeuvre-level histories were subsequently assembled into loading spectra representative of the towing concepts under study.

The resulting towing spectra formed the input to a finite-element analysis of the nose-wheel landing gear. Within this framework, a global model was first used to apply the towing loads and screen for governing critical regions, after which a local model was used to resolve the hotspot response with greater fidelity. This modelling stage compared the structural consequences of towbar and towbarless loading at the component level and assessed whether the towing method changed the ranking or location of fatigue-critical regions. In addition, the local hotspot stresses were converted into an equivalent laboratory-specimen loading definition, enabling the structural response predicted by the finite-element analysis to be assessed experimentally.

Finally, laboratory fatigue testing was performed on spectra derived from the finite-element hotspot response. To this end, representative manoeuvre histories were converted into executable test spectra, simplified where necessary for laboratory implementation, and adapted to the constraints of the fatigue test machine. The laboratory campaign was then used to compare the relative fatigue behaviour of the different towing spectra, including their severity ordering and resulting life ratios. The combined approach, therefore, linked observed towing practice to reconstructed loading spectra, structural hotspot response, and experimental fatigue behaviour, allowing the effect of towbarless towing to be assessed on a relative and structurally grounded basis.

This thesis is organised as follows. Chapter 2 presents the literature review, covering towing methods, load-path differences, fatigue background, representative nose-wheel landing gear configurations, and the current regulatory and operational context. Chapter 3 summarises expert technical field observations that provided additional practical context regarding possible degradation signatures associated with towing operations. Chapter 4 defines the research questions, hypotheses, and overall methodological approach of the thesis.

Chapter 5 describes Work Package 1 (WP1), in which in-field towing measurements were performed and processed into representative towbar and towbarless manoeuvre spectra. Chapter 6 presents WP2, which used finite-element analysis to evaluate the structural response of the nose-wheel landing gear and to identify the governing fatigue-critical locations under the considered towing loads. Chapter 7 describes WP3, in which the translated loading spectra were implemented in laboratory fatigue tests to assess relative fatigue severity and fatigue-life behaviour.

Chapter 8 consolidates the results of the three work packages and answers the research questions. Chapter 9 evaluates the verification and validation of the adopted methodology. Finally, Chapters 10 and 11 present the main conclusions of the thesis, discuss the principal limitations, and provide recommendations for further research.

2

Literature Study

This literature review examines towing-induced loading, structural response, and fatigue of general-aviation nose-wheel landing gear. It first introduces the nose-wheel landing gear's main components in Section 2.1. Next, the towing methods and their associated load-path differences are discussed in Section 2.2, after which Section 2.3 examines how these loads are transmitted through the main nose-wheel landing gear components and where fatigue-critical responses may arise. Section 2.4 then outlines the loading-spectrum and damage-metric concepts required for fatigue assessment, while Section 2.5 discusses the extent to which these responses depend on nose-wheel landing gear configuration and detailed design. The fatigue and life-assessment background is subsequently summarised in Section 2.6, followed by relevant laboratory testing and finite-element modelling approaches in Section 2.7. Finally, Section 2.8 reviews the principal operational and certification constraints, and Section 2.9 identifies the remaining gaps in the literature that motivate the present research.

2.1. Main Components of the Nose-Wheel Landing Gear

The nose-wheel landing gear fulfils several functions during ground operation, including supporting the forward part of the aircraft, enabling steering and manoeuvring, and transmitting ground loads into the airframe. Although detailed configurations vary among aircraft, most steerable tricycle-type NWLG (nose-wheel landing gear) systems share a common set of structural and kinematic elements. Figure 2.1 provides an annotated overview of the principal NWLG components referenced throughout this thesis, and Table 2.1 summarises their towing- and taxi-related roles before the most important parts are discussed in more detail.

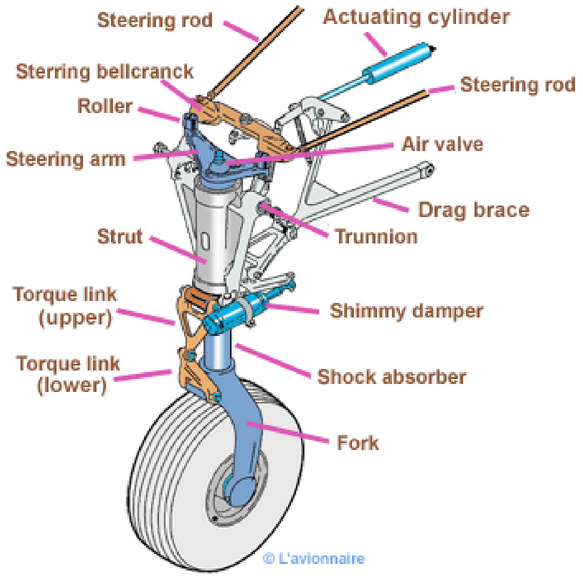

Figure 2.1: Representative NWLG layout showing the main components [11]

Coordinate system and notation. Unless stated otherwise, forces and moments at the NWLG are expressed in an aircraft-fixed Cartesian frame with x forward, y to the right (starboard), and z downward. The associated moments M_x, M_y, and M_z follow the right-hand rule.

Table 2.1: NWLG parts and function under towing/taxi loads

Parts	Role (towing/taxi)
Shock strut (oleo)	Absorbs vertical energy; routes global bending to trunnion/drag brace.
Fork & axle	Carry F_z and transmit M_z/M_y; axle fillets/crown are stress concentrators.
Torque links	Constrain fork–strut rotation; react steering torque and torsional scrub.
Steering collar	Transmit steering moments (steerable); react clamp-induced torsion (TBL).
Drag brace/trunnion	Transmits longitudinal forces into fuselage; hinge lugs see cyclic towing/taxi loads.
Shimmy damper	Suppresses oscillations; mounts/brackets take high-cycle loads.

The component overview shows that the NWLG is not a single load-carrying element, but a structural system in which vertical, longitudinal, lateral, and steering-related loads are distributed across multiple interconnected parts. Understanding the function of these components is therefore necessary before considering how towing and taxi operations affect the local structural response of the gear.

2.2. Towing Methods and Load-Path Differences in General Aviation

Conventional towing uses a towbar that attaches to dedicated tow fittings on the nose-wheel landing gear and typically includes a shear pin designed to fail before excessive force reaches the gear [4]. This fuse-pin mechanism, therefore, acts as a mechanical weak link between tug and aircraft. In contrast, towbarless towing vehicles clamp and cradle the nose-wheel(s) directly, eliminating the towbar and shifting the point of load introduction from the towing lugs to the wheel-level interface [12]. As a result, the applied towing loads no longer pass through a sacrificial pin connection, but instead enter the landing gear through the tyre–rim–fork path.

This difference changes both the load path and the protection philosophy. In towbar towing, longitudinal loads are introduced primarily through the tow lugs, steering collar, and torque-link assembly into the shock strut, with only limited torsion unless the towbar is misaligned. In towbarless towing, the wheel-level interface can introduce not only longitudinal force but also additional torsional and lateral effects through clamp geometry, tyre scrub, and tug kinematics. Certification guidance reflects this distinction, as towbar systems rely on a mechanical fuse, whereas towbarless vehicles must rely on tug-side load limiting and controlled operation to remain within the aircraft manufacturer's towing load envelope. [1, 2, 8]

Empirical data illustrate the severity of towing-induced loads. In instrumented tests on a commuter turboprop (Saab 340), it was found that nose-wheel landing gear loads during towing and tight steering represented some of the largest ground-induced loads measured on the aircraft. By comparison, zig-zag taxi manoeuvres without towing produced lower lateral loads than symmetric brake steering or towing events. This experiment provides a valuable baseline for assessing the relative severity of towbar towing. [13]

Towbarless towing introduces additional transient load phenomena. FAA-sponsored test campaigns demonstrated that sudden tractor braking can excite large horizontal forces at the nose-wheel landing gear. The peak loads were found to be highly sensitive to the brake input profile (step versus ramp) and to tractor–aircraft dynamic interaction. Importantly, these peaks did not scale linearly with aircraft mass, underscoring the need for careful control logic and load-limiting in tug design [4]. Peer-reviewed system models further confirm that wheel-clamp geometry and dynamic constraints materially affect gear responses. For example, higher towing speeds amplify oscillatory loads, while optimised clamp geometries reduce induced vibration. [14, 15]

Recent academic work has extended analysis to long-distance tow-taxi operations. A finite-element and modal test study on a transport-class nose-wheel landing gear showed how longitudinal towing loads couple with torsional and lateral bending at the fork, axle, and steering collar. The simulation was validated against experimental modal data, lending credibility to its prediction of stress concentrations in the lower strut cylinder under towing conditions [3]. Complementing this, a broader review of towing and taxi technologies concluded that long-distance towbarless taxiing demands high-fidelity control, with real-time load feedback at the clamp interface being essential to prevent overload. [5]

In summary, prior studies demonstrate that towbarless towing alters the load path and introduces additional torsional and bending effects absent in conventional towing. While certification standards and recent modelling efforts address aspects of these phenomena, the implications for fatigue behaviour, particularly in general-aviation nose-wheel landing gear, remain insufficiently quantified. This research gap motivates the present study.

2.2.1. Quantitative Comparison to Other NWLG Load Cases

A large-scale FAA study on the Lockheed L-1011 (maximum take-off mass (MTOM) $\sim$212,300 kg) provides valuable quantitative benchmarks for towing spectra [16]. Field measurements at Los Angeles International Airport (LAX) showed that the steady towbar force required to keep the aircraft rolling at 8-15 km/h was modest, typically only 9–22 kN ($\sim$0.004–0.01 W). Dynamic load spikes during start/stop or tug gear shifts were more significant, reaching 44–67 kN tension in normal use ($\sim$0.02–0.03 W). An especially hurried tow produced $\sim$125 kN, and controlled Palmdale tests generated deliberate spikes up to 133–160 kN ($\sim$0.06–0.08 W). The corresponding load spectrum was therefore dominated by frequent low-amplitude cycles ($<$44 kN) with progressively fewer events in the 67–89 kN range, and rare extremes $>$133 kN. Winter towing at Montreal (Dorval) confirmed that snow and ice did not amplify loads: peak forces remained comparable to dry-pavement values, since tug traction, rather than tyre-runway friction, limited forces. These results support the notion that GA spectra should likewise be constructed from frequent rolling cycles, with discrete high-load transients (steering stops, tug jerks) explicitly included, even if rare.

Several key studies have quantified the loads applied to the nose-wheel landing gear during towing through both field measurements and simulations. A notable full-scale test comes from Boeing's evaluation of towbarless tug braking dynamics. In one scenario with a fully loaded widebody ($\approx$186,000 kg) being maintenance-towed at $\sim$32 km/h, an emergency stop of the towbarless towing vehicle (TLTV) led to a large transient increase in nose-wheel landing gear load, peaking at about 207 kN of horizontal force at the nose-wheel landing gear. This peak occurred as the tractor-aircraft system oscillated after brake application, and Boeing compared it against the nose-wheel landing gear's design allowables. The data showed that if the aircraft's own brakes had been applied suddenly in that configuration, the nose-wheel landing gear load would far exceed Boeing's allowable limits, potentially causing structural damage or collapse. This real-world testing led Boeing to prohibit flight crews from using aircraft brakes during towbarless towing, particularly for certain aircraft/tug combinations classified as "critical". Instead, Boeing recommends that towbarless tugs themselves incorporate a structural fuse or automatic disconnect to prevent overload, since, unlike a towbar, they do not inherently fail before the gear structure is overstressed. [4]

Another source of empirical data is instrumented taxi/towing trials. An early study instrumented a commuter aircraft's landing gear to record loads during ground operations (including pushback, taxi over bumps, and braking). Results indicated that nose-wheel landing gear longitudinal loads during towing can be severe, especially during abrupt starts/stops or when the nose wheels traverse uneven surfaces. In those tests, when the main wheels hit an obstacle, a significant jolt was transmitted to the nose-wheel landing gear, producing large stress ranges that were captured via rainflow cycle counting in the fatigue analysis [17]. Yang *et al.* expanded on such scenarios by creating a multi-body dynamics model of a towbarless towing system and running simulations at various speeds. They found that towing at high speeds (≈50–54 km/h) on a fully loaded 727 over a 2 km taxi led to markedly higher nose-wheel landing gear forces than low-speed tows. The maximum vertical load on the nose-wheel landing gear occurred at the highest tow speed with max gross weight, and finite-element analysis results confirmed the locations of peak stress as discussed earlier. Importantly, these simulation studies were validated by comparing natural frequencies and static deflections with real tests, lending credibility to the predicted stress hotspots. [17]

Eurocontrol's CONOPS defines dispatch towing as an on-ground operating concept in which an aircraft is towed from the gate/stand toward the departure runway, with the towing vehicle providing the motion and steering rather than the flight crew. Compared to conventional pushback or maintenance repositioning, dispatch towing is intended as a routine taxi-out alternative and therefore may occur repeatedly across flight cycles. The CONOPS notes that tow operations are constrained by aircraft speed and weight, and that some aircraft require strengthened nose-wheel constructions to enable towing to the runway entry. It further states that the maximum amount of towbarless towing for flight (dispatch towing) is typically limited to approximately 25% of total flight cycles because it may reduce nose-wheel landing gear service life (citing Boeing SL-7x7–09-002-H); in addition, practical constraints such as returning the towing vehicle to the terminal area contribute to limited operational uptake. [18]

Overall, the literature establishes that towbarless towing changes both the point of load introduction and the protection philosophy of the nose-wheel landing gear, replacing a lug-based interface with mechanical fuse protection by a wheel-level interface governed by tug-side load limiting and control. What remains insufficiently resolved, however, is how these qualitative differences translate into quantitative load histories for general-aviation aircraft under comparable manoeuvres. This unresolved step directly motivates the present research need for matched towbar and towbarless measurements and for a fatigue-oriented comparison that extends beyond qualitative load-path descriptions.

2.3. Impact of Towing Loads on Nose-Wheel Landing Gear Components

Towing inputs are introduced and transmitted through the nose-wheel landing gear in different ways under towbar and towbarless operation. These load paths highlight the mechanisms driving torsion, side load, and overturning at the fork/steering assembly, and motivate the FBDs and component fatigue mapping that follow.

2.3.1. Free Body Diagrams and Load Decomposition

The following free-body diagrams idealise the external force and moment components introduced at the wheel/fork interface and at the tow interface:

$$\{F_x,\, F_y,\, F_z\} \quad \text{and} \quad \{M_x,\, M_y,\, M_z\}.$$

Towbar towing

In towbar towing, force entry occurs through the tow lugs close to the axle line, so the dominant effect is longitudinal push/pull F_x with limited M_z (torsion) unless the towbar is yaw-misaligned. Figure 2.2 shows the corresponding free-body diagram.

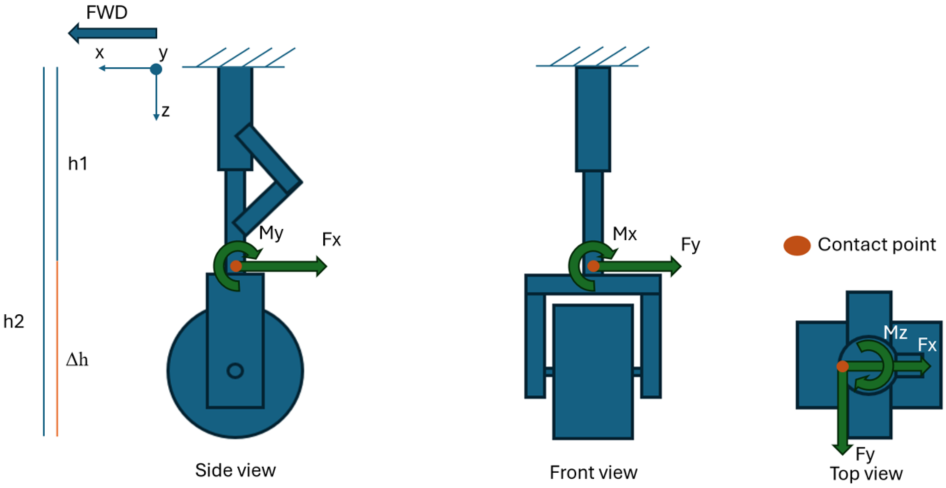

Figure 2.2: FBD of NWLG under towbar towing. Primary force components and induced moments are shown at the tow lug

Notes on towbar towing representation:

- Only external forces and moments transmitted via the towbar are shown; tyre patch reaction forces (R_x, R_y, R_z) are omitted for clarity.
- Longitudinal force F_x is dominant during acceleration/braking; fore–aft bending moment M_y arises when the towbar height differs from where the strut is connected to the fuselage:

$$M_y = F_x \cdot h_1$$

- Lateral force F_y generates a side bending moment M_x, linked to the vertical distance h_1 between lug and axle:

$$M_x = F_y \cdot h_1$$

- Torsional moment M_z results from misalignment or eccentricity e in the towbar connection:

$$M_z = F_x \cdot e$$

- The shear pin in conventional towbars provides a sacrificial weak link, designed to fail before F_x (or combined load) exceeds the certified nose-wheel landing gear limit.

Towbarless towing

In towbarless towing, force entry occurs through clamp pads at the nose-wheel, so the longitudinal push/pull F_x acts at the tyre–clamp interface. Small vertical or lateral offsets in the clamp line of action introduce overturning M_y and yaw torsion M_z, while lateral F_y develops in misalignment and tight-radius turns. Compared with towbar towing, this path couples torsion and side load directly into the fork/steering collar; peak loads are sensitive to tug braking and acceleration profiles and turn geometry, and overload protection relies on the tug's load-limiting system rather than a shear pin [4]. Figure 2.3 shows the corresponding free-body diagram.

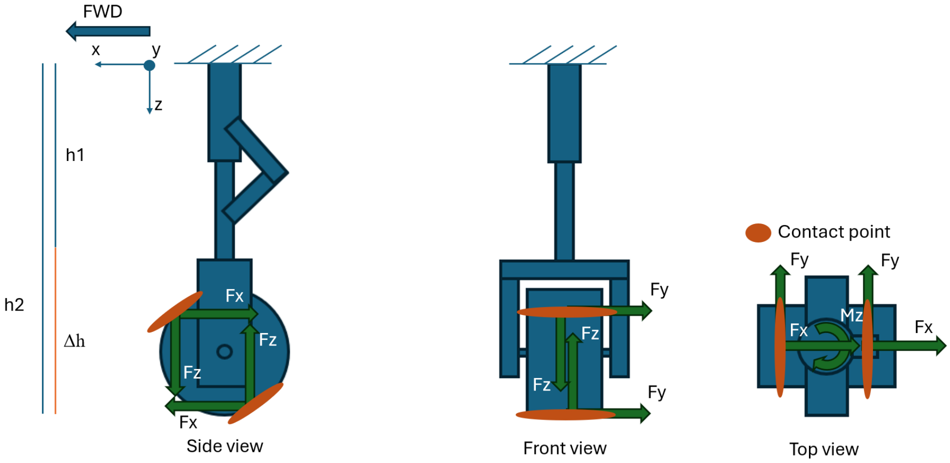

Figure 2.3: FBD of NWLG under towbarless towing. Clamp forces are transmitted directly at the wheel axle level

Notes on towbarless towing representation:

- Only external forces and moments transmitted via the clamp pads are shown; tyre patch reaction forces (R_x, R_y, R_z) are omitted for clarity.
- Longitudinal force F_x is dominant during acceleration/braking; fore–aft bending moment M_y arises when the clamp height differs from the section of interest by h_2:

$$M_y = F_x \cdot h_2$$

- Lateral force F_y generates a side bending moment M_x, linked to the same vertical distance h_2 between the clamp line of action and the section:

$$M_x = F_y \cdot h_2$$

- Torsional moment M_z results from yaw misalignment or effective eccentricity e in the clamp load path:

$$M_z = F_x \cdot e$$

- In contrast to a conventional towbar, there is no shear pin; overload protection relies on the tug's load-limiting system and control logic.

The free-body diagrams in Figures 2.2 and 2.3 compare the load introduction paths of towbar and towbarless towing. Towbar systems channel forces through the tow lugs, whereas towbarless vehicles clamp the wheels directly, adding torsion and side loads via the fork and axle. The resulting shift in load paths could also change which structural regions are most fatigue-critical. [19]

Torsional loading about the strut (M_z) is of particular concern for TBL operations. In towbarless towing, M_z arises from clamp traction and braking, as well as from lateral scrub in turns, producing sustained torsion that must be reacted by the fork, torque links, steering collar, drag brace, and trunnion. At the same time, the bending moment about the y-axis (M_y) also becomes more significant, since the towbarless force is introduced at the wheel/axle and therefore acts through a substantially larger effective moment arm than in towbar towing, as discussed previously and illustrated in the comparative force-introduction figures. FAA- and OEM-backed evaluations show that step-braking of the tug can create horizontal force spikes and associated torsion that exceed allowable limits unless the vehicle incorporates load-limiting and smooth control laws. These combined torsional and bending effects are far less pronounced for towbar towing.

2.3.2. Main Affected Components

Based on these load-path differences, the literature identifies a limited number of NWLG components in which towing-induced torsion, bending, and side-load effects are most strongly concentrated.

Torque links and steering collar. Torque links constrain relative rotation between fork and strut; under TBL, sustained torsion M_z and lateral F_y induce alternating shear at link lugs and pins, amplifying stress at hole fillets and keyways. FEM studies and component analyses consistently identify torque-link lugs and steering-collar keys as fatigue-sensitive under combined torsion–bending–shear. [3, 20]

Fork crown, axle fillets, and wheel–fork interface. Clamp traction and eccentricity introduce M_z and M_y, producing peak bending/torsion at the fork crown and at axle fillets. Validated FEM for tow-taxi scenarios localises maximum stress in the lower outer cylinder/fork region under high towing loads, even when global margins remain acceptable. For GA forks with modest section thickness, these locations become important points. [3, 19]

Pivot bushings, trunnion, and drag-brace attachments. Side load F_y and torsion M_z must be reacted at bearings and trunnion attachments; repeated small-amplitude cycles (turns, clamp scrub) superposed with rare transients (step braking, stop approaches) create damage at bushing interfaces and at brace lugs. Historic ground-test data showed that towing/steering produced some of the largest measured lateral loads, supporting the inclusion of such events in GA spectra. [13, 21]

Overall, the literature indicates that towbar and towbarless towing introduce materially different load paths into the NWLG. Whereas towbar towing is dominated mainly by axial F_x through the tow lugs, with limited torsion unless misalignment occurs, towbarless towing introduces sustained M_z together with additional M_y and F_y, which can shift fatigue sensitivity toward regions such as the fork crown, axle fillets, and torque-link lugs. Although existing studies therefore identify several plausible fatigue-sensitive locations, they do not yet provide a validated conclusion on which region governs for representative GA nose-wheel landing gears under like-for-like towbar and towbarless operation. This unresolved point motivates the structural mapping adopted in this thesis, in which measured manoeuvre loads are translated into local structural responses so that the governing hotspot is identified from the response itself rather than assumed beforehand.

2.4. Loading Spectra and Damage Metrics

Fatigue assessment at the NWLG requires representative load histories at critical locations rather than a single static case. Taxiing, turning, braking, towing, and traversal of surface irregularities generate variable-amplitude multi-axial stresses. Constructing realistic loading spectra enables equivalent damage comparison between towing methods using standard cycle-counting and damage rules [6, 13]. A complete GA NWLG spectrum should combine:

- **Taxi-out / taxi-in:** Frequent, low–medium amplitude cycles in vertical and lateral load (F_z, F_y) with longitudinal drag (F_x) due to rolling resistance and low-speed braking.
- **Braking events:** Transient increases in F_x with mean-stress shift in F_z, and torsion M_z from tyre scrub; amplitude and rate shape (step vs. ramp) matter. [4]
- **Turns:** Lateral F_y and torsion M_z; near stop-angle steering increases side load and may create stop-impact transients.
- **Towing events:** Infrequent but higher-amplitude, method-dependent signatures:
    - Towbar: axial push/pull cycles aligned with fork; low torsion unless misalignment occurs.
    - Towbarless: coupled torsion M_z + side load F_y + bending (overturning M_y) through wheel clamp and fork.
- **Take-off:** Unloading of F_z with small F_x; short transient/ramp

- **Landing:** Large F_z transient; F_x (spin-up drag/torque) and torsion M_z at the axle; typically one high-amplitude transient per flight.
- **Rare overloads:** Hard landing, steering-stop impacts; abrupt tug accelerations/braking; curb/ramp lips. [4]
- **Surface condition modifiers:** Dry/wet/snow influence friction, tyre scrub, and torsional response.

A complete flight spectrum is shown in Figure 2.4a. This figure makes clear that ground operations constitute only a limited part of the overall aircraft operational spectrum, and that towing is itself only one subset within that ground-operation envelope. For the present study, however, this on-ground portion is the relevant part of the spectrum, since the research focuses specifically on towing-induced loading and its fatigue consequences for the nose-wheel landing gear. For that reason, Figure 2.4b shows the ground-operation segment in more detail. Although it does not yet define the exact towing manoeuvres or their analytical treatment, it does show that this part of the spectrum cannot be reduced to only a gate-to-runway and runway-to-gate transition. Rather, it consists of multiple distinct phases and manoeuvring conditions whose combined effect determines the loading history relevant for fatigue. Capturing these effects in representative load spectra is therefore essential for reliable fatigue assessment and for quantifying the incremental impact of towbarless towing.

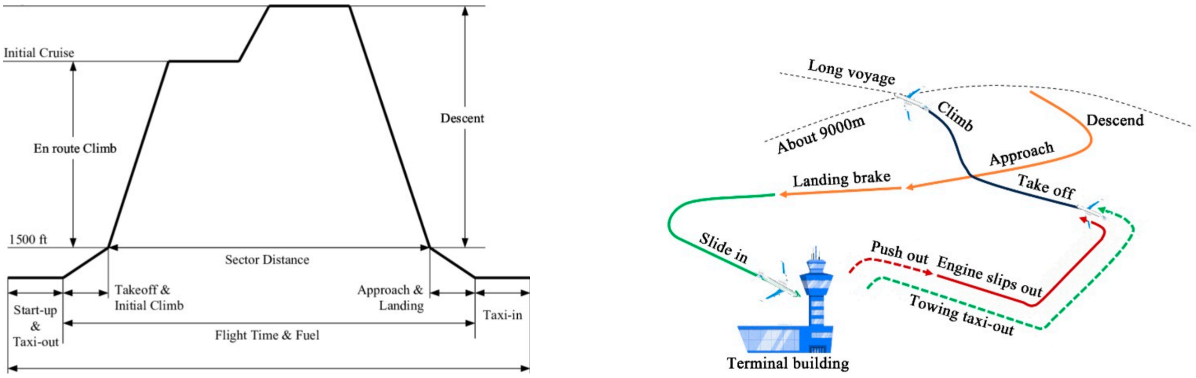

(a) Full flight cycle [22]

(b) Flight cycle ground manoeuvres [23]

Figure 2.4: Flight profile overview

Taken together, these figures highlight that a single deterministic load history cannot represent a GA mission. Instead, variability in usage, the contribution of rare but severe towing transients, and the scarcity of field measurements necessitate a probabilistic and multi-axial treatment of the flight cycle. As emphasised in prior empirical and modelling studies [3, 5], the mission spectrum thus provides not only a chronological account of operations but also a fundamental building block for fatigue assessment, ensuring that cumulative damage captures both typical and exceptional ground-loading conditions. The construction of the towing load spectra is further discussed in Chapters 5, 6 and 7.

Relative severity of ground-handling vs. landing loads

Flight-test strain-gauge measurements on a SAAB SF-340 provide a like-for-like comparison of towing, taxiing, and landing loads. Loads are reported via ground-reaction factors, $e_x = F_x/F_{z,\text{stat}}$ and $e_y = F_y/F_{z,\text{stat}}$, where $F_{z,\text{stat}}$ is the static vertical load on the gear. During zig-zag taxiing at normal speed, the nose-wheel landing gear lateral factor reaches $e_y \approx 2.5$, whereas the four measured landings remain below $e_y \approx 1.0$. Towing produces the largest longitudinal excursions on the nose-wheel landing gear, with $e_x \approx 4$–5 (depending on tow approach angle) and pronounced F_x spikes at discrete events. Using the sign convention that drag is negative, measured peaks of $e_x \simeq -0.66$ at the nose-wheel and $e_x \simeq -0.63$ at the left main landing gear are of similar ratio magnitude; however, because $F_{z,\text{stat}}$ is much smaller on the NWLG than on the main landing gear, the same ratio translates to a much smaller absolute F_x when expressed as a fraction of aircraft weight. Taken together, these data indicate that, relative to landing and taxiing loads, handling manoeuvres can dominate the NWLG's stress ranges and are therefore critical for fatigue assessment in this study. [13]

2.4.1. Force and Moment Characteristic Comparison

Building on the fundamental load-path differences outlined in Section 2.2, the specific forces and moments transmitted into the NWLG differ markedly between towbar and towbarless towing.

Towbar towing

In towbar operations, loads enter the nose-wheel landing gear through tow lugs located near the fork/axle. The dominant component is the longitudinal push–pull force F_x. A secondary change in normal load ΔF_z can arise from towbar height offset, and torsion M_z is generally small unless the towbar is yaw-misaligned. These inputs transmit along a short, largely axial path from the tow lugs → strut, such that strut torsion remains limited. Consequently, manufacturers typically restrict steering angles and discourage powered turns against the stops [6, 13]. Figure 2.5 illustrates a representative GA towbar arrangement, highlighting the lug–axle interface through which the longitudinal force is introduced.

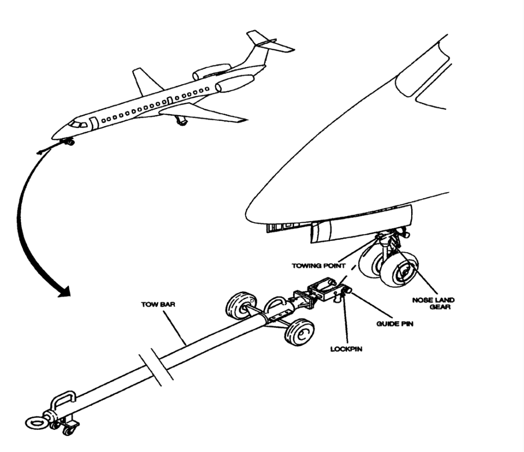

Figure 2.5: Towbar towing configuration for GA aircraft [24]

Towbarless towing

In towbarless operations, clamp pads grasp the nose-wheel(s) so that loads enter through the tyre–clamp interface at the contact patch. The primary components are the longitudinal push–pull force F_x and a change in normal load ΔF_z. Parasitic torsion M_z arises from traction/braking and tyre scrub, while side load F_y develops under misalignment or tight turns. These inputs propagate along the path wheel → fork → torque links/steering collar → trunnion, engaging more torsional and lateral stiffness than in towbar towing [3, 5]. Dynamic testing and analyses further indicate that step-braking by the tug can drive nose-wheel landing gear horizontal loads beyond design allowables unless tightly controlled; aircraft brakes must therefore not be applied during TBL operations [4]. Figure 2.6 illustrates a representative TBL arrangement, with clamp pads transferring longitudinal, torsional, and side loads through the wheel into the fork and subsequently the strut.

Figure 2.6: Towbarless towing configuration for GA aircraft [25]

Table 2.2 summarises the characteristic force and moment transmission for typical towing manoeuvres, contrasting towbar and towbarless operation. The comparison emphasises the additional torsional and bending components unique to TBL, particularly under braking and in tight turns.

Table 2.2: Towing manoeuvres and associated load characterisation (TB vs. TBL)

Towing manoeuvre	Towbar	Towbarless
Straight-line acceleration (push/pull)	Dominant F_x at lugs; small ΔF_z from bar height; $M_z \approx 0$ if aligned; M_y small.	Dominant F_x at tyre–clamp interface; small ΔF_z from clamp height; $M_z \approx 0$ if aligned; M_y from clamp height offset.
Constant-speed straight	Low, steady F_x; $F_y \approx 0$; ΔF_z minimal; $M_z \approx 0$.	Low, steady F_x; $F_y \approx 0$; ΔF_z minimal; $M_z \approx 0$.
Braking (progressive)	Increase in drag F_x; modest ΔF_z from tug attitude; $M_z \approx 0$ if aligned.	Increase in F_x; ΔF_z from decel/geometry; M_z small if aligned, grows with scrub; M_y from clamp height offset.
Braking (abrupt / step)	Short F_x impulse limited by fuse/shear pin; M_z remains small unless yaw-misaligned.	Peak F_x at contact patch; M_z spike if wheels scrub; M_y can be significant without load limiting. [2, 4]
Turning (wide radius)	Sustained F_y via steering; ΔF_z from roll; M_z small if free-castering and aligned.	Sustained F_y plus continuous M_z from tyre scrub; ΔF_z from roll; M_y if clamp height offset/camber. [3, 5]
Turning (tight / near-stop)	High F_y; risk of stop impact; M_z increases mainly with yaw misalignment; local crown stresses.	High F_y and M_z from scrub at low speed; M_y grows with clamp offset; elevated bearing/torque-link demand.
Surface irregularities/slope transitions	ΔF_z fluctuations; small ripples in F_x; $M_z \approx 0$.	ΔF_z fluctuations plus added M_z from intermittent scrub; M_y from clamp height over ramps.
Emergency stop / decouple	Fuse/shear pin caps peak F_x; M_z limited if aligned.	Without decouple/load limiting, F_x and M_z peaks may exceed towing allowables; automatic relief recommended. [2]

For fatigue assessment, towing events should therefore be represented with method-appropriate amplitudes, mean-stress effects, and multi-axial characteristics. Towbarless loads are generally more multi-axial than towbar loads because they combine torsion, side load, and bending more directly. This supports the use of critical-plane or equivalent-stress approaches when comparing cumulative damage between the two towing concepts.

2.4.2. Towing Manoeuvres and Load Spectrum Implications

A consistent theme in the literature is that aircraft landing gear fatigue must be evaluated under variable-amplitude loading representative of real operations. Ground handling loads, including towing straight, turning, braking, taxiing over uneven pavement, and pushback events, occur with varying magnitudes and frequencies, all of which contribute to cumulative fatigue damage. Certification authorities now explicitly require that towbarless towing loads be included in the design's fatigue spectrum. EASA's guidance (AMC 25.509) specifies that manufacturers evaluate how towbarless operational loads contribute to the overall nose-wheel landing gear and airframe fatigue life [26]. This includes determining whether the gear's certified life limits need to be adjusted once towing loads are accounted for. The fatigue spectra for evaluation should encompass the range of service conditions encountered in towbarless operations (pushback, high-speed maintenance tows, tight turns, emergency stops, etc.) and, ideally, be based on measured data or well-founded simulations rather than guesses [26]. In practice, manufacturers and researchers build these spectra by collecting load time-histories and then condensing them into repeating sequences or distributions of load cycles.

Because landing gear loads are often multi-axial, it is common to reduce the problem to an equivalent uniaxial stress spectrum for fatigue life calculations. One approach is the critical plane method, which finds the orientation in the material that experiences the maximum damage per cycle, effectively converting multi-directional stresses into an equivalent stress range [27]. Regardless of the method, engineers apply mean-stress correction models to account for the fact that many ground loads have a non-zero mean (the static weight of the gear plus dynamic loads). Recent landing gear fatigue studies explicitly follow this approach: for example, Jiang *et al.* applied Miner's rule to evaluate fatigue life at critical nodes of a main gear, based on a synthesised spectrum combining multiple Ground-Air-Ground cycles [28]. The inclusion of towing loads in these spectra is crucial, even if tow events are infrequent relative to normal taxi and landing cycles, they may introduce high stress ranges that appreciably consume fatigue life if not accounted for.

In general-aviation, nose-wheel landing gear durability is governed by variable-amplitude ground loads. While landing impacts dominate vertical energy absorption on the mains, GA NWLGs accumulate substantial cycles from taxiing, braking, turning, and towing. Compared with transport-category aircraft, GA routinely operates on tighter ramps with more frequent repositioning, creating load spectra rich in lateral forces (F_y), longitudinal forces (F_x), and torsion about the strut (M_z). [5]

It is important to construct representative ground-operation spectra that can be applied directly in FEM-based hotspot analysis and laboratory testing. For first-order scaling of common manoeuvre loads, the following relations are used: rolling resistance proportional to normal load [29], longitudinal load transfer under braking [30], and lateral inertial loading in steady turning. [31]

$$\text{Rolling/drag:} \quad F_x \approx C_{\text{RR}}\, F_z \tag{2.1}$$

where,

- F_x longitudinal ground force (rolling-resistance drag) [N]
- F_z vertical wheel normal load [N]
- C_{RR} rolling-resistance coefficient [-]

$$\text{Braking transfer:} \quad \Delta F_z \approx \frac{m\, a_x\, h_{\text{CG}}}{L} \tag{2.2}$$

where,

- ΔF_z change in vertical load due to longitudinal load transfer [N]
- m aircraft mass [kg]
- a_x longitudinal acceleration/deceleration [$\mathrm{m\,s^{-2}}$]
- h_{CG} centre-of-gravity height above the ground [m]
- L wheelbase [m]

$$\text{Turning lateral:} \quad F_{y,N} \approx \frac{mv^2}{R}\,\frac{x_M}{L} \tag{2.3}$$

where,

- $F_{y,N}$ nose-wheel landing gear lateral reaction force [N]
- v ground speed [$\mathrm{m\,s^{-1}}$]
- R turn radius [m]
- x_M longitudinal distance from CG to main-gear contact line [m]
- L wheelbase [m]

The main implication is that towbar versus towbarless comparisons should be made at the spectral level rather than based on isolated peak values. Even if average towing loads are similar, differences in manoeuvre execution (speed, turn radius, braking transients) shift the cycle distribution in F_x and $F_{y,N}$, and thereby the hotspot stress ranges that drive cumulative damage. A like-for-like comparison, therefore, requires manoeuvre definitions that control these drivers and a spectrum construction route that preserves their frequency and severity when converting time histories into fatigue-relevant cycle counts.

Viewed together, the reviewed studies show that a meaningful fatigue comparison between towing methods must be made at the spectrum level rather than through isolated peak loads. At the same time, the open literature offers limited guidance on how to construct GA-representative towing spectra that preserve rare but fatigue-relevant transients without becoming impractical for analysis or testing. This motivates the present study's emphasis on manoeuvre-resolved histories, explicit cycle counting, and damage metrics that retain both frequency and severity differences between towbar and towbarless operation.

2.5. Variability of Nose-Wheel Landing Gear Design and Design-Dependent Effects

The response of a GA nose-wheel landing gear to towing loads is also dependent on its architectural configuration and the design of its key components. While all tricycle gears share common elements, such as fork, strut, and drag brace, the presence or absence of steering linkages, torque links, or free-castering pivots alters how longitudinal, lateral, and torsional forces are transmitted and distributed. These design-dependent effects govern where fatigue-critical hotspots arise and how sensitive they are to the additional torsion and bending introduced by towbarless towing. The following subsections map the principal design variations, their associated load paths, and the implications for fatigue-critical regions.

2.5.1. Landing Gear Arrangement Options

Whether GA nose-wheel landing gear configurations respond differently to towbar and towbarless inputs determines whether a unified towing spectrum is defensible or whether configuration-specific modelling is required. This subsection identifies the conditions under which each approach is appropriate.

While multiple arrangements exist: tricycle, taildragger, monowheel, tandem, the present thesis focused on tricycle gear, which dominates GA turboprops, light, midsize, and heavy jets, due to inherent ground stability and compatibility with powered towing [6, 32]. After defining the tricycle layout as the relevant scope, the remaining design variation lies within the tricycle nose-wheel landing gear configuration itself. Figure 2.7a shows the basic dimensions that are relevant for the landing gear tricycle layout, while Figure 2.7b is relevant for the turning radius and ground handling by keeping the centre of gravity within the stability triangle formed by the nose and main gear, thereby preventing tip-over during turning and braking.

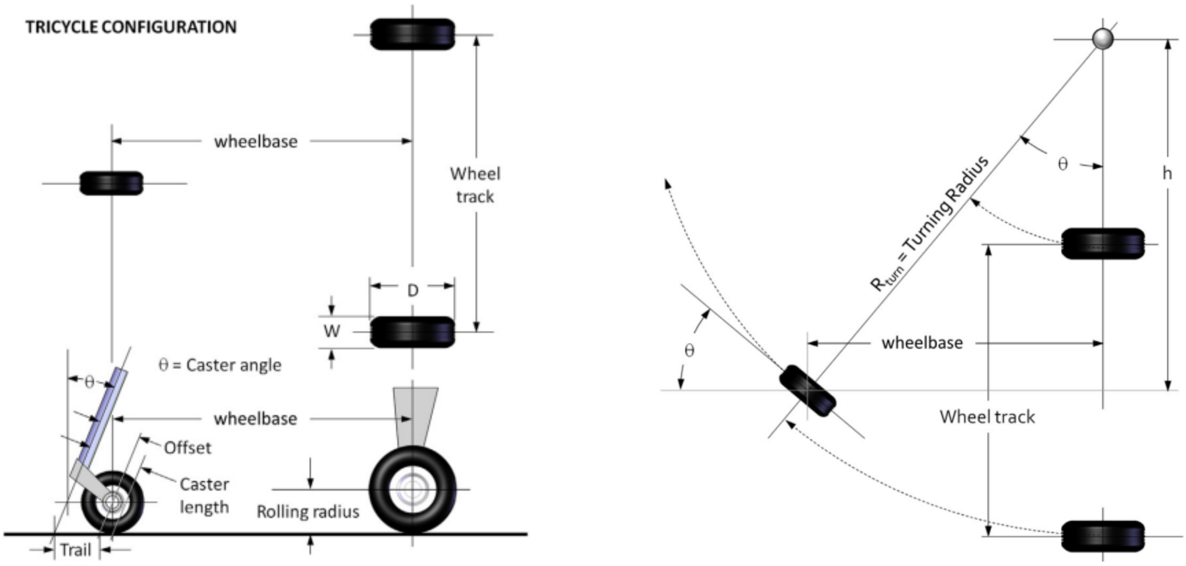

(a) Side view **(b)** Top view

Figure 2.7: Representative GA landing gear geometry [6]

Furthermore, Figures 2.8a and 2.8b illustrate two fundamental aspects of GA nose-wheel landing gear geometry and design. The first shows the principal steering and caster angles, as well as the geometric offsets that govern how nose-wheel loads are transmitted into the strut. These parameters strongly influence handling stability, shimmy tendency, and load path sensitivity during towing. For most general-aviation aircraft, including light and midsize business jets, the prevalent nose-wheel layout is configuration A or B [6]. Figure 2.8b shows a typical oleo-pneumatic shock strut, the standard energy-absorbing element used in almost all aircraft nose and main gears. An oleo-pneumatic strut is a telescoping piston–cylinder in which vertical loads force oil through a metering orifice to dissipate energy while compressing a nitrogen charge that provides the spring force, thereby absorbing impact and controlling rebound as loads are transmitted to the airframe. Therefore, its configuration determines how loads are reacted and dissipated during taxiing, towing, and landing.

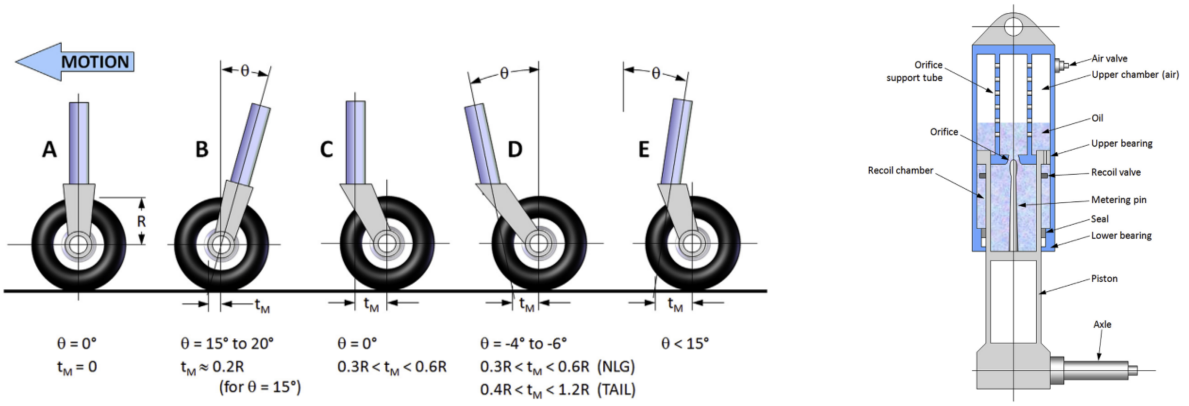

(a) Geometric angles of a nose-wheel (D is not used for NWLG)

(b) Oleo-pneumatic shock strut cylinder

Figure 2.8: Nose-wheel and shock strut [6]

The tricycle configuration is mainly used in modern GA aircraft. The NWLG provides steering and supports a fraction of the static weight, which increases under braking/towing. Two architectures prevail:

a) **Steerable NWLG:** mechanically linked to the rudder pedals, with a shimmy damper typically fitted. The linkage may be rigid or spring-coupled, affecting torsional compliance and peak load transfer.
b) **Free-castering NWLG:** self-aligning, without a rigid pedal linkage. Directional control is achieved through differential braking, so the caster pivot and damper dominate torsion and side-load reactions.

The GA design and sizing practices summarised by Gudmundsson [6] (layout, reaction sharing, dynamic concerns) remain applicable when towing loads are included. What changes under TBL is the balance between axial vs. torsional/side-load pathways.

2.5.2. Representative Design Catalogue

The preceding sections reviewed the principal design choices and showed that a tricycle-gear layout predominates in GA turboprops and light- to midsize jets. For the towbar versus towbarless comparison, the nose-wheel landing gear configuration selected for detailed study was a steerable, straight oleo with a double-fork, single-wheel configuration. This option tree is shown in Figure 2.9. This configuration was considered the most common arrangement in service, as all examples in Table 2.3 used this exact layout.

There are exceptions with a single-sided fork, such as the Beechcraft King Air B200 (MTOM 5,670 kg [33]). This architectural difference does not affect the central research question. Because the study compares towing-induced global load spectra and cycle counts at the nose-wheel landing gear, the fork choice only redistributes local stresses. It therefore does not materially affect the fatigue drivers or conclusions. Accordingly, the analysis remained restricted to steerable tricycle nose-wheel landing gear configurations, which are predominant among general-aviation turboprops and jets.

Table 2.3: Examples for scope definition by GA aircraft MTOM

Aircraft	**MTOM [kg]**	**Reference**
Cessna Citation Mustang (C510)	3 921	[34]
HondaJet Elite S (HA-420)	4 944	[35]
Pilatus PC-24	8 300	[36]
Cessna Citation Excel / XLS+	9 072	[37]

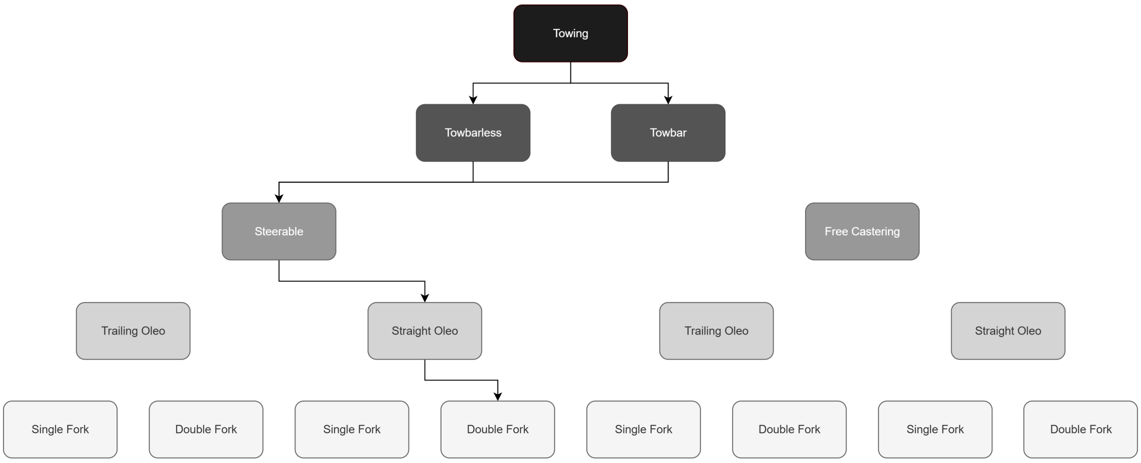

Figure 2.9: Schematic breakdown of GA nose-wheel landing gear architectures

2.5.3. NWLG Drag-Brace Configurations

Within the general-aviation nose-wheel landing gear architecture considered in this research, the overall configuration remains broadly similar, while one of the most relevant structural differences for the present fatigue assessment lies in the drag-brace arrangement. Figure 2.10, therefore, introduces three representative drag-brace configurations within this otherwise typical GA nose-wheel landing gear architecture, corresponding directly to the photographic examples:

- Configuration A: an aft-folding drag brace with centre overlocking mechanism (Figure 2.10a),
- Configuration B: a forward-folding V-shaped brace (Figure 2.10b),
- Configuration C: a brace with an actuator lock strut for the drag brace (Figure 2.10c).

The photographs and drawing in Figure 2.10 span a realistic range of brace angles, pin offsets, and load paths observed in GA-type NWLGs, while retaining the same basic function (over-centre drag brace with down-lock). In the next stage, one of these configurations was taken forward as the basis for the detailed local submodel and subsequent specimen mapping.

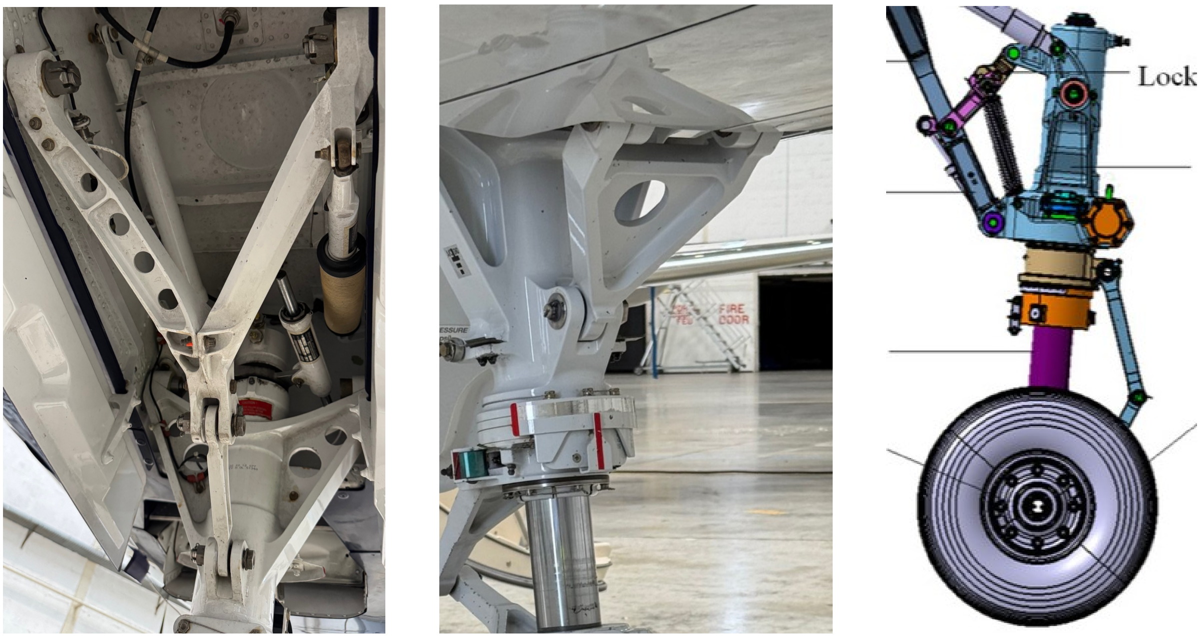

(a) Configuration A: compact, straight drag brace with over-centre locking mechanism

(b) Configuration B: forward-leaning V-shaped brace

(c) Configuration C: Brace with actuator lock strut for drag brace [38]

Figure 2.10: Representative NWLG drag-brace configurations considered for local FEM modelling. All three realise an over-centre drag brace with down-lock function, but differ in brace angle, pin offset and attachment layout

For retractable nose-wheel landing gears, the retraction direction (forward or aft into the bay) determines the orientation of the drag brace. Combined with the towing direction (pushing versus pulling the aircraft), this establishes whether the brace is predominantly loaded in tension or compression during ground handling.

In an aft-folding nose-wheel landing gear, the wheel and strut move aft into the fuselage bay. The drag brace typically runs aft from the strut to a keel or bulkhead fitting. In the down-locked configuration, landing and taxi loads mainly place this brace in tension. When a tug pulls the aircraft forward, the longitudinal reaction tends to draw the strut forward relative to its aft fuselage attachments, increasing the distance between the brace pins and loading the brace predominantly in tension. When the aircraft is pushed backwards, this distance reduces, and the brace is loaded more in compression along its axis.

In a forward-folding nose-wheel landing gear, the geometry is mirrored: the brace runs forward from the strut towards a firewall or nose-bay frame. Landing and taxi loads tend to compress the brace. In this layout, pulling the aircraft forward shortens the distance between the strut and the forward fuselage attachments so that the drag brace is mainly in compression, whereas pushing the aircraft backwards increases this distance and produces a higher tensile load in the brace.

The previous subsection (2.5.1) discussed that there is considerable variability in nose-wheel landing gear layout, as the strut may be raked, and the axle may be offset relative to the strut. In the present context, this is important because these geometric choices directly influence the static axial load in the drag brace. A forward-offset nose-wheel on an aft-running brace, for example, introduces a tensile bias in the brace under the aircraft's weight alone, whereas a forward-running brace with the wheel set forward of the strut tends to see a compressive bias. As a result, the mean stress level and effective stress range in the brace during towing are not only method-dependent (TB versus TBL), but also configuration-dependent through the detailed NWLG geometry.

Both forward- and aft-retracting nose-wheel landing gear configurations are used in general aviation, with the choice primarily dictated by available bay volume and the desired emergency extension scenario. Forward-folding configurations are commonly adopted for nose-wheel landing gears when gravity-assisted extension is desired in the event of hydraulic failure, thereby improving reliability during gear deployment [39]. On the ground, aircraft are typically pushed only short distances, for instance, during pushback from a stand or hangar, while also being pulled over longer distances for repositioning, maintenance towing, or remote parking operations [40]. The cumulative effect of these longer forward towing movements results in significantly more load cycles in the associated loading direction. As a result, the towing direction that occurs most frequently with appreciable force, typically forward pulling, is critical from a fatigue perspective, as it dominates the cyclic range in axial drag-brace loading.

A typical example of an aft-folding nose-wheel landing gear with a forward-offset nose-wheel is the Beechcraft King Air 300, shown in Figure 2.11. In this configuration, the nose-wheel is located ahead of the strut, so that the aircraft's static weight already places the drag brace in tension before towing loads are applied. When such an aircraft is predominantly towed in the forward (pull) direction, the combination of weight-induced and towing-induced tension leads to frequent, relatively high tensile cycles in the drag brace. This makes aft-folding layouts with forward-offset nose wheels particularly relevant and conservative for the fatigue assessment in the present work.

Figure 2.11: Beechcraft King Air 300 nose-wheel landing gear with forward-offset nose wheels and aft-folding drag brace [41]

2.5.4. Load-Reaction Derivation

The reaction-sharing relations from Gudmundsson [6] are reproduced here to emphasise how towing/braking conditions scale the nose-wheel landing gear reaction R_N, and thus the torsion/bending cycles applied in FEM:

$$R_N = \frac{T \cdot y_T + (W + L_{HT} - L_W) \cdot (x_M - \mu \cdot h_{CG}) + L_W \cdot x_W - L_{HT} \cdot l_{HT} - M_W}{x_N + x_M - 2\mu \cdot h_{CG}} \tag{2.4}$$

Main gear reaction, R_M:

$$R_M = W + L_{HT} - L_W - R_N \tag{2.5}$$

where,

- R_N nose-wheel landing gear vertical reaction force [N]
- R_M main-gear vertical reaction force [N]
- W aircraft weight [N]
- T thrust force along the thrust axis [N]
- L_W wing lift [N]
- L_{HT} horizontal tail lift [N]
- M_W aerodynamic pitching moment about the centre of gravity [N m]
- μ effective longitudinal ground-force coefficient [-]
- h_{CG} centre-of-gravity height above the ground [m]
- x_N longitudinal distance from the centre of gravity to the nose-wheel contact line [m]
- x_M longitudinal distance from the centre of gravity to the main-wheel contact line [m]
- y_T vertical offset between the thrust line and the centre of gravity [m]
- x_W longitudinal moment arm of the wing lift with respect to the centre of gravity [m]
- l_{HT} longitudinal moment arm of the horizontal-tail lift with respect to the centre of gravity [m]

During ground towing with engines off and low airspeed, the thrust, lift, and aerodynamic moment terms are small compared with the weight and ground-reaction terms. The reaction expression can therefore be reduced to the terms governed primarily by weight, friction, and towing inputs.

Towing with engines off implies $T = 0$. Because $S_{HT}/S < 1$ and $\bar{c}/\ell$ is relatively small, tail-lift and wing-moment bounds are typically less restrictive; it therefore suffices to bound the main-wing lift to render aerodynamic effects negligible. For a tolerance ε (here 5%), require $L_W/W \leq \varepsilon$ with neutral/locked controls and flaps up:

$$L_W = q\,S\,C_L, \tag{2.6}$$

becomes:

$$\frac{L_W}{W} = \frac{q}{W/S}\,C_L, \tag{2.7}$$

together with:

$$q = \tfrac{1}{2}\rho V_{\text{air}}^2, \tag{2.8}$$

results in:

$$V_{\text{air}} \leq \sqrt{\frac{2\,\varepsilon\,(W/S)}{\rho\,C_{L\,\text{max}}}}. \tag{2.9}$$

where,

- L_W wing lift [N]
- q dynamic pressure [Pa]
- S wing reference area [m^2]
- C_L lift coefficient [-]
- $C_{L\,\text{max}}$ maximum lift coefficient [-]
- V_{air} airspeed relative to the air [m s^{-1}]
- ρ air density [kg m^{-3}]
- W/S wing loading [N m^{-2}]
- ε tolerance fraction used to bound aerodynamic contribution [-]

Numerically, taking $W/S \approx 960\,\text{N/m}^2$ [42] and $C_{L_{max}} \approx 1.3$ [42], with $\rho = 1.225\,\text{kg/m}^3$ and $\varepsilon = 0.05$,

$$V_{air} \;\leq\; \sqrt{\frac{2\,(0.05) \times 960\,\text{N/m}^2}{1.225\,\text{kg/m}^3 \times 1.3}} \;\approx\; 7.8\,\text{m/s} \tag{2.10}$$

Thus, under engines-off operation with neutral/locked controls, maintaining V_{air} below this threshold ensures L_W, and by margin also L_{HT} and M_W, remain below $\varepsilon = 5\%$ of the governing load scales.

The airflow over the wing generates lift that unloads the gear in the vertical (z) direction. The associated drag is governed by the lift-to-drag ratio; with typical light-GA $L/D \approx 10$–12 (e.g., C172 $L/D_{\text{max}} \approx 10.9$ [43], the added drag fraction is $\frac{D}{W} = \frac{0.05}{10.9} \approx 0.5\%$, i.e., an increase in F_x well below 1%, thus considered negligible for this research. With these assumptions, Equation 2.4 reduces to:

$$R_N = \frac{W \cdot (x_M - \mu \cdot h_{CG})}{x_N + x_M - 2\mu \cdot h_{CG}} \tag{2.11}$$

2.5.5. Rolling Resistance Measurement in Towing Operations

An important parameter influencing towing loads is the wheel rolling resistance. The rolling resistance coefficient (C_{RR}) quantifies the drag force resisting wheel motion as a fraction of the normal load. In aircraft towing scenarios, C_{RR} is typically determined by controlled towing tests: the aircraft is towed at constant low speed on a level surface, and the steady-state tow force (F_X) required to overcome rolling friction is measured (for example, via a towbar load cell or an instrumented wheel) [44]. This horizontal force is then divided by the vertical wheel load (F_Z) to yield $C_{\text{RR}} = F_X/F_Z$. Pytka *et al.* applied this method using their instrumented nose-wheel on grass, finding that on a soft, uneven turf runway, the effective C_{RR} was around 0.27 (much higher than the 0.02–0.05 typical for paved surfaces). The large rolling resistance on grass was attributed to soil deformation and tyre sinkage, which increase with moisture and surface softness.

On hard pavements, measuring C_{RR} via towing is straightforward. In smooth rolling tests on concrete or asphalt, the required tow force is usually a small fraction of the aircraft's weight. This coefficient can be slightly higher at breakaway (static friction) and is influenced by tyre pressure, speed, and runway texture. In practice, many ground operations guidelines assume a conservative rolling resistance coefficient to size towing vehicles and estimate tow forces. [44]

Accurate measurement of rolling resistance is critical because it directly affects towing load predictions and nose-wheel landing gear design loads. A higher-than-expected C_{RR} can significantly increase the longitudinal force transmitted into the nose-wheel landing gear during extended towing or taxi-out, contributing to stress and potential fatigue damage. Thus, research efforts continue to refine rolling resistance testing, including on atypical surfaces (grass, gravel, snow), to ensure that nose-wheel landing gears are adequately designed for the range of ground conditions an aircraft may encounter.

The preceding review makes clear that the response of the nose-wheel landing gear to towing cannot be separated from the detailed gear configuration, since steering concept, brace geometry, wheel offset, and local attachment design all influence load transfer and hotspot severity. Consequently, general conclusions from isolated aircraft types cannot be transferred directly to the wider GA fleet without first defining a representative architectural scope. This design dependence motivates the reference-configuration approach adopted in this thesis, while also highlighting the remaining gap in the literature regarding how far towbarless-induced fatigue sensitivity is configuration-dependent within common GA nose-wheel landing gear layouts.

2.6. Fatigue and Life Assessment of Metallic Structures

Fatigue is a primary life-limiting mechanism for metallic landing-gear structures under variable ground loads. This section summarises the fatigue concepts and certification philosophies needed for the remainder of the thesis. This considers safe-life versus damage-tolerant design, inspection and probability-of-detection considerations, and the crack-initiation and crack-growth framework used to define life limits and inspection intervals.

2.6.1. Background on Fatigue

Aviation provides canonical case studies of fatigue-driven risk. Aloha Airlines Flight 243 (1988) suffered explosive decompression after multi-site cracking and disbonding in fuselage lap joints, with a large crown skin section lost in flight [45]. Southwest Airlines experienced multiple fatigue-related events: Flight 2294 (2009), rapid decompression from fuselage crown skin cracking; Flight 812 (2011), over a one-meter upper-fuselage rupture linked to manufacturing-induced fatigue; and Flight 1380 (2018), an uncontained engine event initiated by a fatigued fan blade, leading to rapid depressurisation [46]. These incidents accelerated the sector's shift toward explicit damage-tolerance and ageing-aircraft controls.

Regulatory response centres on preventing widespread fatigue damage (WFD). The FAA's WFD rule mandates a Limit of Validity (LOV) for the engineering data that underpins each transport aeroplane's structural maintenance program and, where necessary, structural modifications or inspection programs to preclude WFD before the LOV [47]. For engineering practice, this institutionalises spectrum-based life prediction, crack-growth integration to detectable sizes, and inspection planning consistent with the demonstrated probability of detection.

Fatigue also has material economic consequences. Findings during inspection or in service can trigger unplanned maintenance and aircraft-on-ground (AOG) events, leading to cascading network disruption. Compliance with WFD/LOV and associated inspection or modification programs also adds direct maintenance burden and downtime that operators budget into life-cycle cost and retirement decisions. [47]

Safe-life design enforces retirement before any detectable fatigue damage, using representative spectra (taxi, shimmy, towing, hard-landing) with scatter factors and, for test correlation, equivalent-damage spectra. Therefore, it is typically applied to single-load-path NWLG items such as fork/axle, inner/outer cylinders, and steering collar [48]. Fail-safe (damage-tolerant) design permits the presence of cracks but requires demonstrated residual strength for the inspection interval and a proven probability-of-detection basis. On the NWLG, this is suited to features with alternate paths or redundancy (e.g., split torque-links, dual lugs/pins), where crack-growth analyses set intervals so a flaw cannot grow from minimum detectable to critical size before the next scheduled inspection. [49, 50]

Damage-tolerant design assumes small defects exist from manufacturing or service. It shows that, under representative spectra, a flaw at least as large as the inspection method's demonstrated detectability ($a_{90/95}$) will not grow to the critical size a_c before the next scheduled inspection. At the same time, residual strength in the presence of that flaw remains above the required load case [48, 49]. For NWLG applications, this approach is particularly relevant at axle fillets, the fork crown, torque-link lugs, and drag-brace joints. At these locations, damage tolerance is established by selecting a non-destructive inspection (NDI) method with a quantified probability of detection (POD) curve, setting inspection intervals through crack-growth integration from $a_{90/95}$ to a_c over representative taxi, steering, shimmy, towing, and hard-landing spectra, and verifying residual strength under the governing side-load and steering-torque conditions [51]. Single-load-path members that cannot provide an alternate path should still carry safe-life limits even within an overall damage-tolerant program [48, 49]. The safe-life and damage-tolerant approaches above define how fatigue is managed in design and in service. Their practical application, however, depends on the underlying physical process by which cyclic loading initiates and propagates cracks in metallic structures. For that reason, the basic fatigue mechanism is outlined below.

Fatigue Mechanisms and Crack-Growth Behaviour

Metal fatigue is the progressive, localised structural damage that develops when a material is subjected to cyclic loading. Under repeated load cycles, cracks may initiate at microstructural inhomogeneities or geometric discontinuities and subsequently propagate under the action of the stress-intensity factor range ΔK. In the mid-growth regime, Paris' relation, $\mathrm{d}a/\mathrm{d}N = C(\Delta K)^m$ describes the rate, bounded below by a near-threshold ΔK_{th} and above by fast fracture as $K \to K_{\mathrm{IC}}$, as shown in Figure 2.12. As metals are homogeneous and isotropic materials with 'local' damage accumulation, this requires consideration of mean stress, sequence effects (overloads/underloads), environment (e.g., corrosion), spectrum loading shift, S–N behaviour, and crack-growth rates. These considerations must be reflected in design, substantiation, and life-cycle management. [52]

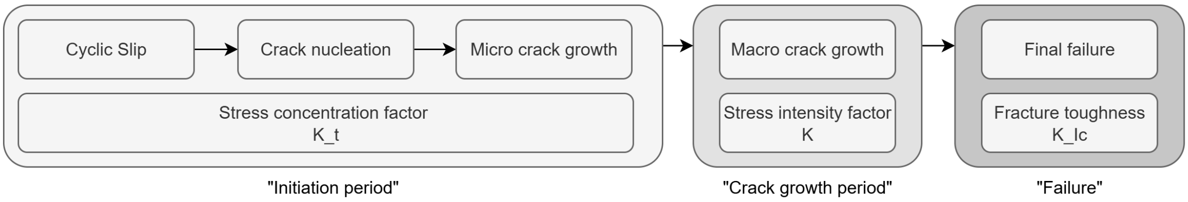

Figure 2.12: Crack growth life-cycle

The fatigue literature provides a mature framework for interpreting cyclic structural loading through safe-life and damage-tolerant philosophies, crack-growth concepts, and inspection planning. However, these principles do not, by themselves, resolve how towing-specific ground spectra, and especially differences between towbar and towbarless operation, affect the fatigue severity of GA nose-wheel landing gear in practice. This motivates the present work to use the established fatigue framework not for full certification substantiation, but for a relative and application-focused assessment of towing-induced stress histories and their life implications.

2.7. Laboratory Testing and Finite-Element Modelling

Laboratory rigs and finite-element models are commonly used together to study landing-gear response under ground loads. Controlled tests apply prescribed vertical, drag, and side loads to an instrumented gear to calibrate measurements and validate models, which are then used to extrapolate stresses to untested manoeuvres and uninstrumented regions. The discussion also summarises spectrum construction for testing and the implications of steep spectra, including truncation and crack-growth retardation.

2.7.1. Laboratory Ground-Load Calibration and Model Correlation

Because towing and taxi loads occur on the ground, they can be reproduced in controlled laboratory settings using static or dynamic test rigs. A standard approach is ground-load calibration on an instrumented gear mounted in a representative fixture, where combined towing, braking, and turning loads are applied in a controlled manner. Tang *et al.* describe a six-degree-of-freedom loading platform developed for landing-gear calibration [53]. The gear is supported under realistic boundary conditions, and hydraulic actuators apply known loads at the wheel contact point in the vertical (F_z), drag (F_x), and side (F_y) directions, together with the associated moments. This enables combined cases such as braking while towing or turning while towing, reproducing the multi-axial stress state that occurs during ground handling. The applied loads are measured using a multi-axis transducer and correlated with the strain-gauge response, yielding calibration factors that map measured strains to load components and providing evidence that the gear sustains the applied load combinations without structural distress.

In addition to static calibration, dynamic test rigs are used to examine NWLG response under repeated or oscillatory tow loads. Skorupka conducted full-scale dynamic testing on a general-aviation nose-wheel landing gear (from the Piper PA-31P) to assess its performance and fatigue life under operational ground loads [54]. In these tests, the NWLG assembly was subjected to numerous loading events representative of taxi and towing conditions, including drop/impact tests and longitudinal drag loads. Strain gauges on the nose-wheel landing gear's fork and barrel recorded stress concentrations during each load cycle, allowing identification of any critical locations prone to fatigue cracking. The results confirmed that the nose-wheel landing gear met required safety margins, with deflections and stresses under tow loads within acceptable limits and no signs of low-cycle fatigue failure. Such endurance testing, often run for tens of thousands of cycles, provides confidence that the gear can withstand the cumulative damage from repeated towing, taxiing, and steering over its service life. However, high-cycle fatigue was not fully assessed in that research.

Laboratory test campaigns often go hand in hand with FEM analysis in a feedback loop. Physical tests (static calibrations, dynamic fatigue tests, and modal surveys) provide data to tune and validate the finite-element models of the landing gear. Conversely, the models help interpret test results and can extrapolate to load cases that are difficult or risky to test directly (for example, extreme towing angles or emergency towing brakes). This combined experimental-numerical approach has been applied not only to civil transports but also to military and commuter aircraft gears. For instance, calibration of strain-gauge-instrumented landing gears using multi-axis loading rigs was pioneered by the Chinese Flight Test Establishment to improve the accuracy of in-flight load measurements on the gears of fighter and trainer aircraft. [53]

2.7.2. Fatigue Spectra Simplification

Designing against fatigue for an NWLG under multi-axial loading requires a thorough understanding of variable-amplitude loading effects on both crack initiation and crack growth. In such critical components, cyclic tension, compression, and bending occur in combination, making fatigue behaviour more complex than in simple uniaxial cases. This section explains how realistic load spectra are created, simplified, and used for fatigue-life assessment. It covers the derivation of service load spectra from field data, spectrum construction and truncation for testing, multi-axial stress reduction, cumulative damage rules, and load-sequence interactions in crack growth.

Figures 2.13–2.14 illustrate how raw service data are transformed into design spectra. Figure 2.13 shows a representative variable-amplitude load history with small cycles, burst segments at high frequency, rest/dwell periods, and intervals at near-constant load.

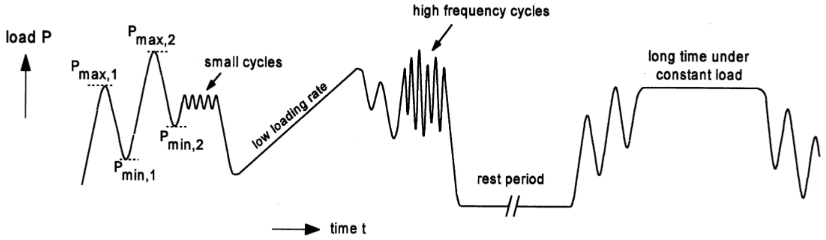

Figure 2.13: Variable amplitude load spectrum [52]

Figure 2.14 then demonstrates standard counting and aggregation: a level-based record of the time series, exceedance curves for maxima and minima, and a cycle-density matrix. Together, these steps convert measured histories into cycle counts by amplitude and mean load, which are used to build test spectra, apply cumulative damage rules, and predict life under multi-axial loading.

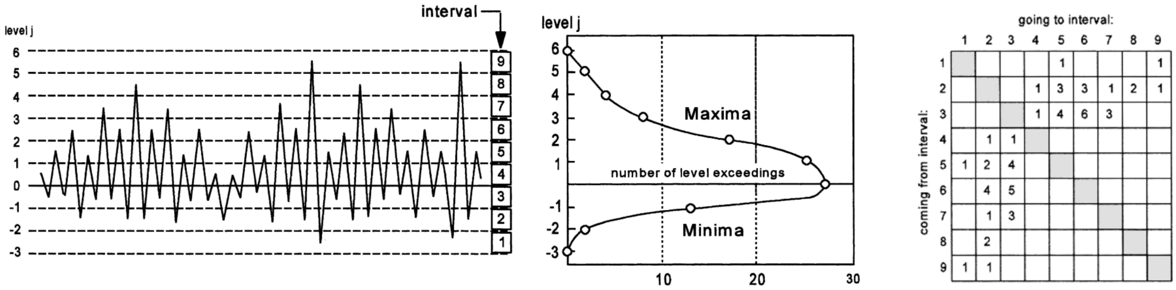

	1	2	3	4	5	6	7	8	9
1					1				1
2				1	3	3	1	2	1
3				1	4	6	3		
4		1	1						
5	1	2	4						
6		4	5						
7		1	3						
8		2							
9	1	1							

Figure 2.14: Load-history counting examples [52]

The irregularity factor k provides a compact measure of how irregular a load-time history is. It is defined by

$$k = \frac{N_p}{N_c} \tag{2.12}$$

where,

- N_p number of peak values in the record [-]
- N_c number of crossings of the chosen reference level [-]

For constant-amplitude histories and for regularly modulated histories in which each half cycle crosses the reference level, $k = 1$. Values $k > 1$ indicate increasing irregularity: peaks occur without proportionate level crossings, implying variable peak-to-peak ranges and the need for range-based counting rather than a single amplitude parameter. [52]

Figure 2.15 shows the typical decomposition of a measured load record into (a) the raw time history, (b) a low-frequency, deterministic component capturing discrete manoeuvres (turns, braking, towing transients), and (c) a high-frequency, random component due to surface roughness and vibrations. This separation enables rainflow counting of the manoeuvre component while the high-frequency residual is filtered as a low-amplitude background before recombination for spectrum definition and damage assessment.

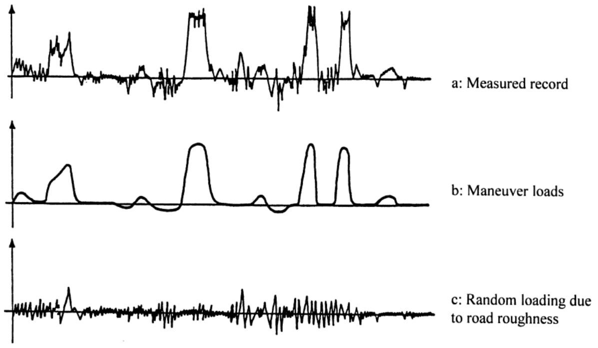

Figure 2.15: Load record separated into deterministic (manoeuvres) and random (road roughness) loads [52]

2.7.3. Background on Retardation

The load spectrum associated with the NWLG towing operation was classified as steep. According to Schijve [52], a steep spectrum is characterised by a relatively small number of high-load events and a very large proportion of low-load cycles. This was precisely the situation observed in the measured towbar-related loads: peak loads approaching the maximum capacity occurred only rarely, whereas small loads, representing manoeuvring and ground-handling disturbances, dominated the spectrum. Such a steep spectrum implied that although occasional overloads existed, they were infrequent compared to the extensive number of low-amplitude cycles. This distribution was significant for fatigue assessment because rare high loads could influence crack closure and retardation effects, while the large population of low loads could continue to propagate any initiated cracks. The classification of the NWLG towbar condition as a steep spectrum, therefore, provided the appropriate framework for constructing the test load history and for interpreting subsequent fatigue test results.

Extremely infrequent peaks can render laboratory replay impractically long and, more importantly, can distort single-specimen outcomes. Schijve notes that in steep spectra, rare overloads may retard subsequent crack growth. Consequently, naïvely removing these peaks can shorten measured life, even though linear damage summation would predict a longer life because the direct damage contribution of the removed peaks is eliminated. For qualification purposes, truncation should therefore be applied conservatively and justified in terms of fleet representativeness. Because not all units see the rarest peaks, test evidence should not rely on their occasional life-extending influence. In flatter spectra, the life reduction from truncation is typically smaller, but still non-negligible.

Modern fatigue crack growth analysis often relies on the concept of plasticity-induced crack closure to explain sequence effects. When a crack experiences a high peak load, it leaves behind an enlarged plastic zone that, upon unloading, causes the crack flanks to contact (close) earlier in the load cycle. This effectively raises the crack's opening stress S_{op} for subsequent cycles, meaning a portion of each following load cycle is used for reopening the crack, thus reducing the effective stress intensity range ΔK_{eff} driving the crack. The result is a retardation of crack growth after an overload, as seen in Figure 2.16.

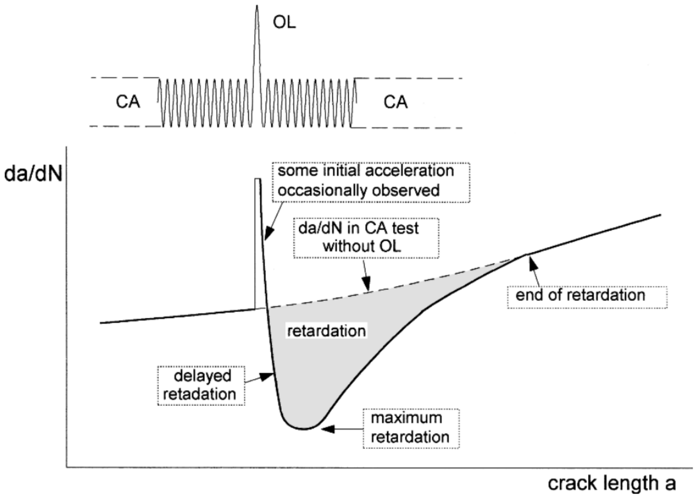

Figure 2.16: Visualisation of retardation [52]

At the opposite end, omitting cycles well below the fatigue limit can significantly reduce test duration with minimal loss of information. However, Schijve emphasises that such cycles are not strictly ”non-damaging” in variable-amplitude histories. Once a crack exists, large populations of sub-threshold cycles in steep spectra can contribute to propagation. Accordingly, omission thresholds must be analytically justified and, where practical, experimentally verified on representative sub-components. For flat spectra, the cumulative effect of low-level cycles is smaller, and higher omission thresholds are generally defensible. [52]

Taken together, the reviewed laboratory and numerical studies demonstrate that controlled testing and finite-element modelling form a credible route for interpreting complex landing-gear load cases. What is still missing in the GA towing context is an integrated chain that starts from representative towing histories, transfers those histories into local structural stress estimates, and finally evaluates their fatigue consequences in a controlled test environment. This missing link directly motivates the staged field-to-model-to-test methodology developed in the present thesis.

2.8. Safety and Operational Considerations

Towing limitations and cautions prescribed in GA Aircraft Maintenance Manuals and Pilot Operating Handbooks define an important part of the operational context for this study. The discussion below evaluates whether that guidance differs between towbar and towbarless methods.

2.8.1. Role of Manuals and Safety Guidance

Pilot Operating Handbooks (POHs) and Aircraft Maintenance Manuals (AMMs) define the approved towing procedures, steering-angle limits, and operational cautions for each aircraft type. These documents therefore govern day-to-day ground handling and, in practice, define the operational envelope within which towing loads are introduced into the nose-wheel landing gear. Exceeding these published limits, for example, by reaching the steering stops under power or by applying abrupt tug inputs, can introduce elevated local loads in components such as the torque links, steering collar, stop bolts, drag brace, and fork crown.

The PC-24 Ground Servicing Guide shows that towbarless towing is not treated as an unrestricted ground-handling activity, but rather as an operation subject to explicit limitations regarding ground conditions, tug suitability, and compliance with the towing-vehicle manufacturer's instructions [55]. From the perspective of the present research, the significance of such manuals is therefore not only procedural but also structural: they define the loading conditions that should normally bound towing operations, indicate which manoeuvres and exceedances are considered potentially damaging, and thereby help frame the fatigue-relevant operational envelope of the nose-wheel landing gear.

In addition to EASA's AMC 25.509, the FAA and other authorities participated in harmonisation efforts in the early 2000s to update regulations. The FAA's *Loads and Dynamics Harmonisation Working Group* recommended that towing loads, including towbarless towing loads, be formally addressed in certification requirements. For the Boeing 777 certification, the FAA subsequently issued a special condition requiring that towbarless towing loads be treated as limit loads and included in the fatigue spectrum for the nose-wheel landing gear and supporting structure [1]. Aircraft Maintenance Manuals likewise specify allowable towing angles, towing forces, and approved towing equipment as part of continued airworthiness. [26]

Industry standards supplement these regulatory requirements, but they are written primarily as general directives for transport-category operations rather than for general-aviation practice. SAE ARP5283B defines towbarless tow-vehicle test requirements and is intended for pushback and maintenance towing; it is not intended for dispatch towing as defined in §2.3 [2]. Dispatch towing typically induces more fatigue-relevant cycles on the nose-wheel landing gear and supporting structure because the aircraft carries passengers, cargo, and fuel, and the manoeuvre involves more starts, stops, and turns. ARP5284 addresses the steering interface and stability when using towbarless vehicles [56]. Internationally, ISO 20683 (Parts 1–2) similarly provides design and performance criteria for towbarless towing vehicles and is not specific to GA operations. [8]

Aircraft manufacturers also issue operational guidance. Boeing service letters and Airbus ground-handling notes commonly require a flight-deck observer during towing and call for logging of abnormal load events followed by nose-wheel landing gear inspection in accordance with the maintenance manual [4]. In practice, two parallel frameworks coexist: aircraft-OEM rules and guidance intended to protect airworthiness and maintenance integrity, and SAE/ISO standards that target the design and testing of towbar and towbarless vehicles. This separation leaves an operational gap at the interface, especially in general aviation, where towing is performed with a wider variety of equipment and procedures. Consequently, existing documents do not fully address how repeated ground-towing exposure contributes to cumulative fatigue damage, which motivates the measurement-based approach adopted in this study.

2.8.2. Event Taxonomy and Exceedances

Towbarless towing also draws attention to certain rare but critical load cases that can drive fatigue damage or even immediate failure if not controlled. One such case is the steering-stop impact, in which a tug turns the NWLG to its mechanical limit. If a towbarless driver inadvertently rotates the nose wheels beyond the allowed angle, the wheels or torque links will slam into the steering stops. This over-rotation can impart a shock load into the nose-wheel landing gear structure. While towing procedures call for avoiding such scenarios, accidents have occurred in both general aviation and air transport when towing limits were exceeded. The NTSB documented a case where a light aircraft's nose-wheel landing gear collapsed on landing after a prior towing incident had forced it past its steering limits, damaging the centring mechanism [57]. In larger aircraft, installing a nose-wheel landing gear lock pin and disconnecting the steering hydraulics are standard practices to allow free caster or prevent pressure build-up during towing. These measures reduce the risk of hard contact with stops by ensuring the nose-wheel landing gear can pivot without fighting the hydraulic system. Nevertheless, as noted, maintenance manuals explicitly warn that power towing must remain within the nose-wheel turn limits or else structural damage could occur [58]. Such damage, even if it does not cause immediate failure, can create stress concentrations or small cracks that degrade the fatigue life of the affected parts.

It is worth noting that military aviation has also explored towbarless towing for large aircraft, and many findings carry over to civilian use. Military tugs for heavy transports similarly must prevent nose-wheel landing gear overload. Field experience across both commercial and military fleets generally affirms that when towbarless procedures are followed, and equipment is within specification, the nose-wheel landing gear can handle the loads without undue fatigue damage [8]. Many airlines have operated with approved towbarless pushback for years on aircraft from narrow-body 737s up through A380s, under the condition that the TLTV's maximum drawbar pull and acceleration/braking limits are set not to exceed the aircraft's certified towing loads. [8, 26]

2.8.3. CS-23 Requirements on Nose-Wheel Landing Gear Towing Loads

For small general-aviation aircraft (certified under EASA CS-23 or FAA Part 23), the rules require the nose-wheel landing gear and towing attachments to withstand specified towing forces. According to CS 23.509 ("Towing loads"), the tow fittings and supporting structure must sustain limit loads applied parallel to the ground. Specifically, the nose-wheel landing gear must be designed for a towing force equal to about 30% of the maximum aircraft weight, applied forward or aft along the direction of travel [9]. When the nose-wheel is turned at an angle (for example, 45°), a reduced load of about 15% of the aircraft's weight is applied in the plane of the wheel. These requirements are summarised in Table 2.4.

Table 2.4: CS 23.509 — Towing loads for nose-wheel landing gear tow fittings and structure

Reg.	**Load case**	**Direction / condition**	**Limit load**	**Notes**
CS 23.509	Tow force (straight)	Parallel to ground, along direction of travel; applied forward or aft	$0.30\,W_{\text{max}}$	Limit load (no permanent set).
CS 23.509	Tow force (turned wheel)	Wheel turned (e.g. 45°); load in the plane of the wheel	$0.15\,W_{\text{max}}$	Reduced with steering angle.

W_{max}: maximum certificated aircraft weight.

In addition to towing-specific loads, CS 23.499 ("Supplementary conditions for nose wheels") specifies other ground load cases relevant to safety. The nose-wheel landing gear must withstand a vertical load of 2.25 times the static wheel load, combined with a drag load of 0.8 times that value to simulate sudden braking or obstacle impact. It must also tolerate a side load of 0.7 times the static load, together with the same vertical factor, representing hard turning or scrubbing. For powered steering systems, the design must allow for up to 1.33 times the maximum steering torque, combined with 1.33 times the static vertical load. These supplementary conditions are summarised in Table 2.5. [9]

Table 2.5: CS 23.499 — Supplementary ground load conditions for nose wheels

Reg.	**Load case**	**Direction / condition**	**Vertical factor**	**Concurrent factor**
CS 23.499	Vertical + drag (braking / obstacle)	Vertical reaction with simultaneous longitudinal drag	$2.25\,W_{\text{NW,stat}}$	$0.8 \times W_{\text{NW,stat}}$ drag
CS 23.499	Vertical + side (turn / scrub)	Vertical reaction with simultaneous lateral side load	$2.25\,W_{\text{NW,stat}}$	$0.7 \times W_{\text{NW,stat}}$ side
CS 23.499	Powered steering torque	Maximum steering torque with vertical reaction	$1.33\,W_{\text{NW,stat}}$	$1.33\,T_{\text{max}}$ (steer torque)

$W_{\text{NW,stat}}$: static vertical load on the nose-wheel; T_{max}: maximum steering torque. All values are *limit loads*.

The towing and supplementary nose-wheel load cases in CS-23.509 and CS-23.499 are defined as limit loads. Under the general CS-23 strength requirements, these limit loads are multiplied by a factor of 1.5 to obtain ultimate loads, which the structure must sustain without failure. The values in Tables 2.4 and 2.5 therefore define the upper boundary of the certified static strength envelope for the nose-wheel landing gear and its towing attachments. In this context, emergency braking during towing is particularly relevant, since either aircraft-brake application or a sudden tug stop can generate short-duration dynamic loads that rapidly approach or exceed this structural envelope.

Although these rules do not explicitly address fatigue, they provide a useful reference for the present research in two ways. First, they offer a basis for normalising measured and FEM-predicted towing loads, for example by expressing peak towbar or towbarless forces as a fraction of the applicable CS-23 limit. Second, they indicate that transient events, such as hard braking or large steering angles during towbarless manoeuvres, become structurally significant as they approach the certified envelope, thereby increasing the risk of local yielding or damage. The CS-23 provisions used here, therefore, act primarily as a structural ceiling against which the measured and reconstructed towing spectra can be interpreted.

Overall, the operational and certification literature largely stops at allowable loads, safe operation, and one-time structural survival. It does not quantify how routine GA towing practice translates into accumulated fatigue damage over repeated service cycles, particularly for towbarless operation. This distinction motivates the present study to move beyond compliance limits and to examine the fatigue consequences of realistic manoeuvre execution within the certified operating envelope.

2.9. Identified Knowledge Gaps and Motivation

The reviewed literature provides a basis for towing-induced load paths, applicable standards, and general fatigue-assessment methods. However, it does not yet resolve the specific questions required for a comparative general-aviation towbar-versus-towbarless assessment. The main gaps identified in this literature study are:

- **Lack of matched, GA-representative TB–TBL manoeuvre-level load histories.** Most published towing datasets concern transport-category aircraft, isolated commuter-aircraft studies, or single towing concepts only. Open literature provides very limited manoeuvre-resolved datasets for general-aviation aircraft in which towbar and towbarless operation are compared under matched conditions such as speed, turn radius, braking input, and surface state.
- **Unresolved translation from towing manoeuvres to representative fatigue spectra.** Although cycle counting, spectrum representation, and truncation methods are well established, the literature offers limited guidance on how to convert towing manoeuvres into GA-representative fatigue spectra that preserve fatigue-relevant transients, sequence effects, and operational frequency without becoming impractical for analysis or testing.
- **No validated conclusion on the governing fatigue-critical location under comparative TB–TBL loading.** Existing FEM studies and component-level analyses identify several plausible towing-sensitive regions, including the fork crown, axle fillets, torque-link lugs, steering collar interfaces, and drag-brace attachments. However, for representative GA nose-wheel landing gear, the literature has not yet established which location governs under like-for-like towbar and towbarless operation, nor whether the towing method causes a meaningful redistribution of hotspots.
- **Unclear configuration dependence within common GA nose-wheel landing gear architectures.** The reviewed studies indicate that steering concept, drag-brace arrangement, wheel offset, and retraction geometry all influence load transfer and local stress development. Nevertheless, the literature does not clearly resolve how far the fatigue sensitivity to towbarless towing depends on these architectural differences within the range of common GA nose-wheel landing gear layouts.
- **Missing validated chain from operational loading to structural response to fatigue consequence.** Prior work addresses individual parts of the problem, such as towing loads, component stresses, or laboratory/model correlation, but the literature has not yet provided a validated GA-focused approach that links representative towing histories to local structural response and, in turn, to comparative fatigue consequences.
- **Operational and certification guidance defines allowable loads, but not cumulative fatigue consequence.** Manuals, CS-23 provisions, and SAE/ISO guidance define towing limits, exceedance cases, and vehicle-performance requirements, but they do not quantify how repeated towbarless exposure contributes to cumulative fatigue damage over service life.

Collectively, these gaps indicate that the current literature still lacks a comparative, GA-specific framework that links representative towing manoeuvres to quantitative load histories, load histories to governing structural response, and structural response to relative fatigue consequence. These identified gaps form the basis for the research questions defined in Chapter 4, which focus on establishing representative GA towing manoeuvres, comparing towbar and towbarless load signatures, identifying the governing structural response, and assessing the resulting relative fatigue severity of the nose-wheel landing gear.

3

Expert Technical Field Observations

Technical field observations from an industry expert with more than 20 years of experience in general-aviation base maintenance and ground handling were synthesised in this chapter, including observations from aircraft repositioning operations using both towbarless equipment and conventional towbars.

These experience-based hypotheses provide operational context for the possible effects of towbarless towing on nose-wheel landing gear loads and degradation. The source text was received after completion of the work packages in this thesis and therefore did not influence the research plan, modelling choices, measurement campaign, or test design. The information is treated as experience-based evidence rather than a controlled dataset. It is used to support qualitative triangulation of mechanisms and directional trends, not to validate numerical magnitudes such as load factors, stress levels, or fatigue life. The unedited source text is provided in Appendix D.1.

Section 3.1 summarises the observed load-path mechanisms and operational severity modifiers, Section 3.2 groups the reported degradation signatures by component, and Section 3.3 consolidates the main operational implications and recommendations.

3.1. Technical Field Observations

Across aircraft that may have been exposed to frequent towbarless (shovel-type) towing, the expert reported progressive component wear and reliability degradation. The effects are described as cumulative and cycle-dependent, and are commonly identified during aircraft-on-ground events rather than being associated with a single isolated overload.

Hypothesised Load-Path Drivers

Relative to conventional towbar towing with shear-limiting protection, towbarless towing is hypothesised to impose different load paths into the nose-wheel landing gear through load application at the tyre contact patch. Key characteristics include:

- increased effective lever arm and increased fork and shock-strut bending moments
- increased lateral and torsional load cycling during constrained manoeuvres
- absence of a mechanical load limiter
- increased sensitivity to dynamic impulses from surface irregularities and transitions
- increased loading on slopes and during braking on uneven terrain

These drivers are linked to cumulative, lifecycle-related degradation rather than immediate structural criticality.

Operational Severity Modifiers

Aircraft mass and fuel load Aircraft gross weight is a primary modifier of towing severity, directly affecting nose-wheel landing gear static load, fork bending moment, shock-strut side loading, bushing contact stress, and tyre deflection and scrubbing forces. Towing at high fuel load increases the static reaction on the nose-wheel landing gear and increases manoeuvre inertia during braking and turning. As a result, longitudinal and lateral towing actions are associated with proportionally higher bending moments and interface contact stresses, which are expected to increase cumulative stress exposure in the nose-wheel landing gear. From an operational perspective, towing at the minimum practical fuel load is therefore preferred when feasible.

Ground surface condition and slope Ground surface conditions and slope introduce additional load components and transient load spikes. Towbarless towing over uneven apron surfaces, expansion joints, steep transitions, hangar ramps, and inclined areas is associated with rapid shifts in vertical load distribution and increased tyre constraint, which in turn increase lateral forces and promote additional torsional transfer through the torque links. Under such conditions, the shock strut is subjected to combined compression and bending, with load spikes occurring at surface transitions. On sloped surfaces, increased braking demand raises longitudinal loading, while the gravitational component increases the nose-wheel landing gear reaction force; during turning, this combination increases tyre scrubbing forces. These combined load patterns are described as amplifying fork-bending moments, increasing internal strut-seal stress, accelerating bushing wear, and promoting the initiation of fretting and corrosion. Towbarless systems are characterised as less forgiving on uneven or inclined surfaces because the load is applied at the tyre contact patch without shear-limiting protection.

3.2. Reported Degradation Signatures

The reported degradation signatures can be grouped by assembly, which helped to identify where the observed in-service effects are concentrated within the nose-wheel landing gear.

Shock strut internal hydraulic leakage and reduced damping Reported indicators include:

- increased internal bypass and reduced damping effectiveness
- visible external leakage
- inconsistent static extension despite correct oleo and nitrogen servicing

Suspected shock strut piston seal wear Accelerated wear of the isolation piston seal separating nitrogen and hydraulic oil is suspected. Proposed contributing mechanisms include:

- elevated lateral loads during constrained towing
- micro-misalignment under side-load
- increased friction at internal sliding interfaces
- circulation of fine wear particles

Structural interfaces and joints Progressive freeplay is reported in:

- torque link bushings
- steering actuator attachments
- drag brace pivots
- trunnion bearings
- shimmy damper mounts

Typical characteristics include bushing ovalisation, bolt-hole elongation, fretting at connecting surfaces, and increased steering compliance. Increasing freeplay may amplify vibration transmission and redistribute loads within the nose-wheel landing gear assembly.

Nose-wheel landing gear door interconnection hardware For aircraft with mechanically interconnected nose-wheel landing gear doors and actuation linkages, reported wear includes bolt fretting, bushing wear, increased bearing clearance, hinge elongation, and progressive door misalignment. These effects are associated with vibration and lateral load transfer into hardware not intended to absorb torsional inputs.

Tyre and wheel effects Tight static turns with high lateral scrubbing may risk internal tyre damage that is not externally visible, including internal carcass or cord damage and localised stiffness variation. A correct balance is insufficient to confirm internal tyre integrity.

Corrosion and surface degradation Increased corrosion is reported at door hinge bolts, torque link hardware, steering actuator bolts, and drag brace interfaces. A proposed mechanism is fretting-driven removal of protective coatings, followed by oxidation promoted by moisture and de-icing residue, with repeated vibration accelerating the breakdown of the coatings.

3.3. Operational Implications

The practitioner observations were consolidated into actionable operational recommendations and into implications for nose-wheel landing gear loading and degradation.

Operational Recommendations

Following towbarless towing, particularly after tight pivot turns, rough transitions, and significant braking inputs, recommended checks include:

- checking nose tyre pressure
- inspecting tread shoulders and sidewalls
- monitoring for abnormal taxi vibration

When feasible, towing at the minimum practical fuel load is recommended to reduce cumulative nose-wheel landing gear loading.

Main Observations and Implications

The observations summarised in this chapter consistently point to a towbarless load introduction at the tyre contact patch that increases effective lever arm effects and promotes combined bending and torsional loading of the nose-wheel landing gear, without shear-limiting protection and with heightened sensitivity to transient impulses. Severity is described as increasing with aircraft mass, and with demanding ground conditions such as uneven surfaces, transitions, slopes, and manoeuvres involving braking and constrained turning. The reported in-service signatures are consistent with cumulative, cycle-dependent degradation, notably reduced shock-strut damping due to internal bypass, progressive freeplay and fretting in structural interfaces, wear in mechanically interconnected door hardware, potential internal tyre degradation, and fretting-driven corrosion at dynamic joints. These findings were used for qualitative triangulation of mechanisms and directional trends, and to motivate follow-on investigation where specific degradation modes fall outside the present measurement scope.

The observations are not treated as independent validation of the measured or predicted magnitudes, but as operational context against which the direction and plausibility of the identified mechanisms can be compared.

4

Research Questions and Methodological Framework

This chapter defines the research questions, comparison logic, and methodological structure used to assess how towbarless towing affected the loading and fatigue behaviour of general-aviation turboprop and light- to midsize-jet (MTOM $\approx 4{,}000$–$9{,}000$ kg) nose-wheel landing gear relative to conventional towbar towing. It follows directly from the knowledge gaps identified in Chapter 2, where the literature review showed that a GA-specific route from representative towing manoeuvres to comparative load histories, governing structural response, and relative fatigue consequences remained lacking. The chapter, therefore, sets out the research questions, the work-package structure, the end-to-end workflow, and the working hypotheses that guided the thesis.

Section 4.1 formulates the main research question and supporting subquestions. Section 4.2 summarises the work packages (WP1–WP3) and defines the TB–TBL comparison metrics. Section 4.3 then provides the end-to-end workflow and the associated iteration logic. Finally, Section 4.4 states the working hypotheses and maps each hypothesis explicitly to the research questions to ensure testability.

4.1. Research Questions

To answer the main research question, the project was structured into thematic blocks. The central research question of this thesis is:

MRQ: What are the consequences of towbarless towing on the loading and fatigue behaviour of general-aviation turboprop and light- to midsize-jet nose-wheel landing gear compared to conventional towbar towing?

Mechanisms and load path differences

The first group of subquestions addressed the mechanics by which towing inputs were transferred to the NWLG. It established the load-path changes introduced by TBL relative to TB and identified the mechanisms that later drove the fatigue assessment. The answers provided the physical basis for the component analysis that followed. Specifically, these subquestions asked:

- SRQ1: What are the primary ground-operation load cases on the nose-wheel landing gear, and how do they populate the measured ground-loading/fatigue spectrum? *(cycle counts, amplitudes, mean stresses, and frequency content*)
- SRQ2: How do towbar and towbarless towing differ in the forces and moments applied to the nose-wheel landing gear, and how do these differences alter the sequence, magnitude, and frequency content of the resulting usage spectra?

Impact of towing loads on nose-wheel landing gear components

The next subquestion group continued the load-path view by narrowing down where loads became damaging stresses. The goal was to connect global inputs to local responses and to focus subsequent modelling and instrumentation on the most sensitive degrees of freedom and parts of the gear. Accordingly, this subquestion asked:

- SRQ3: Which critical nose-wheel landing gear components *(strut, torque links, fork, pivot bushings, drag brace)* are most susceptible to fatigue damage from repeated towing and manoeuvring loads?

Towing manoeuvres and fatigue spectrum implications

The next subquestion group turned to operational comparators. It aimed to assess how realistic sequences of events for TB and TBL towing could be fairly evaluated. The answers defined the variable-amplitude inputs used for analysis and testing. These subquestions asked:

- SRQ4: How should representative ground operation spectra *(taxi, towing, turning, braking)* be constructed for GA aircraft to perform fatigue analysis?
- SRQ5: Which specific towing manoeuvres or conditions lead to the largest differences in peak stress ratio, rainflow damage ratio D_{TBL}/D_{TB}, and change in hotspot ranking between towbar and towbarless methods?

Safety and operational considerations

The final subquestion group connected the technical findings to airworthiness practice. The aim was to understand current guidance, identify any shifts in fatigue hotspots introduced by TBL, and outline where procedures might require refinement. This sequence closed the loop from physics to practice. These subquestions asked:

- SRQ6: Could switching the towing method *(from towbar to towbarless)* introduce new failure modes or shift the primary fatigue hotspots in the nose-wheel landing gear, thereby requiring updated maintenance or operational guidance?
- SRQ7: To what extent does towbarless towing alter the fatigue life of nose-wheel landing gear components compared to towbar towing?

4.2. Research Approach and Work Packages

The aim was to quantify how towbarless towing altered loading and fatigue risk in GA nose-wheel landing gear relative to towbar towing, and to translate field-observed inputs into structural stresses and fatigue spectra. The strategy combined field measurements to capture realistic inputs, a finite-element model to map stresses throughout the nose-wheel landing gear, and laboratory tests to assess the relative fatigue response of hotspot-derived spectra under controlled specimen-level conditions. The three strands provided complementary evidence and consistency checks across the measurement, structural response, and fatigue test levels. The work packages are defined as follows:

- WP1 – Field Measurements: Minimal but high-value instrumentation to capture representative load histories and kinematics from the NWLG and towing vehicle.
- WP2 – FEM Modelling and Structural Mapping: Use WP1-derived towing load histories to map global load introduction to local stress response and identify governing hotspots.
- WP3 – Laboratory Fatigue Testing: Implement hotspot-derived spectra on laboratory specimens to compare relative fatigue severity between TB- and TBL-derived loading.

To compare towbar and towbarless towing analytically, the analysis requires metrics that capture both magnitude and distribution of fatigue demand across manoeuvres and components. The following four metrics quantify cumulative damage, transient severity, shifts in critical locations, and fatigue life, thereby linking field measurements, finite-element stresses, and laboratory lives into a single, testable framework.

- Damage ratio at location j: $\mathcal{D}_j = \dfrac{D_{\text{TBL},j}}{D_{\text{TB},j}}$ (Miner sum with stated mean-stress correction).
- Peak-stress ratio at location j: $\sigma_{TBL/TB} = \frac{\sigma^{\text{max}}_{\text{TBL},j}}{\sigma^{\text{max}}_{\text{TB},j}}$ for matched manoeuvre classes.
- Hotspot rank shift Δr: $\Delta r_j = r_{\text{TBL}}(j) - r_{\text{TB}}(j)$, change in the ordered list of top-k fatigue-critical locations between TB and TBL towing.
- The spectrum life ratio is reported as $\rho_{\text{life}} = \bar{N}_{\text{TBL}}/\bar{N}_{\text{TB}}$ for matched missions.

Table 4.1 shows how the work packages are related to the sub-research questions.

Table 4.1: Traceability from research questions to evidence sources

RQ	Discussed Subject	Primary Evidence (WP)
SRQ1	Towing spectrum structure	WP1 (measured histories) + WP2 (stress mapping)
SRQ2	TB vs. TBL input differences	WP1 (towbar/tug loads, kinematics)
SRQ3	Susceptible components/locations	WP2 (FE stress/hotspots)
SRQ4	Representative mission construction	WP1 (segmentation) + WP3 (damage/life stability)
SRQ5	Manoeuvres driving the difference	WP1 + WP2 (per-manoeuvre metrics)
SRQ6	Hotspot shift / failure-mode implications	WP2 (rank shift)
SRQ7	Net fatigue-life effect	WP2 (damage) + WP3 (spectrum lives)

4.3. Project Workflow

The end-to-end workflow of this thesis is summarised in Figure 4.1. It organises the work into three concurrent lanes: WP1, WP2, and WP3. Solid arrows show mandatory data flow, return arrows denote planned iteration if a gate is not met.

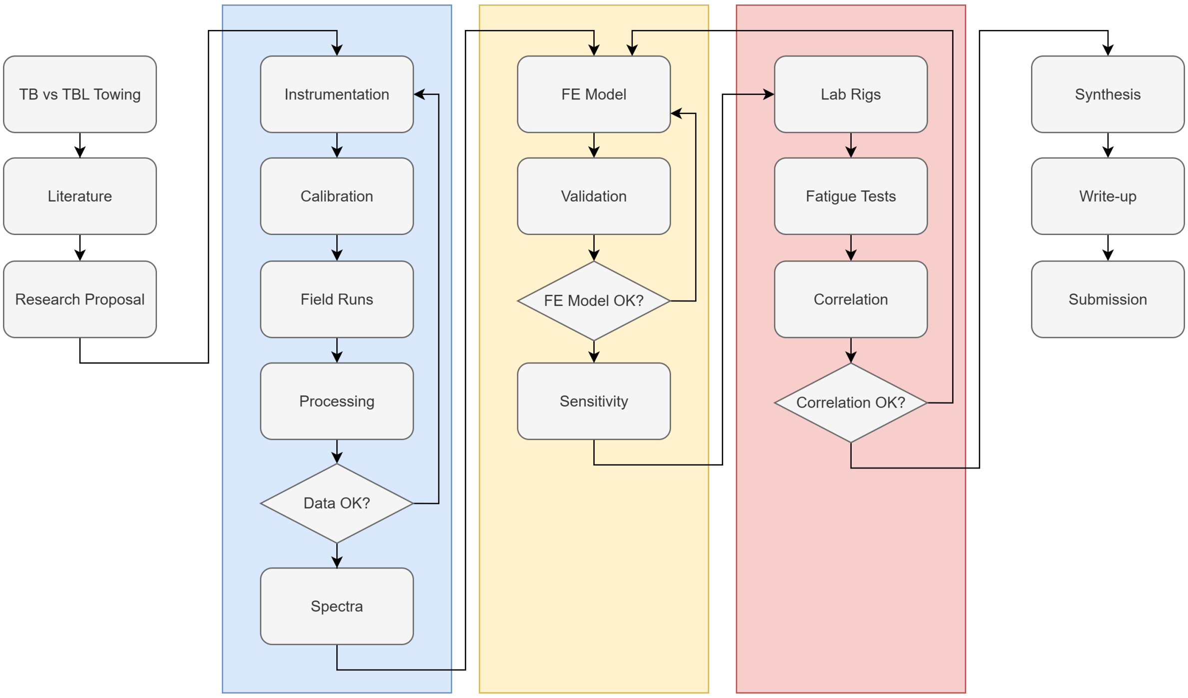

Figure 4.1: Research workflow across WP1 (blue) → WP2 (yellow) → WP3 (red)

The project prioritised WP1 in the opening phase to secure high-quality inputs. At the same time, WP2 progressed in parallel using baseline geometry and assumed properties so that correlation/validation could be completed shortly after WP1. In the same period, WP3 was prepared: the test-rig setup was finalised, fixtures and control scripts were readied, and steel specimens were procured. Once WP1 passed the data-quality gate and WP2 met the model-consistency checks, representative TB/TBL spectra were synthesised and converted to actuator commands. WP3 was then executed by loading these spectra on the fatigue rig to obtain spectrum lives and damage ratios.

4.4. Hypotheses

The working hypotheses that guided the collection and analysis of evidence are stated below. Each hypothesis was formulated to map directly to the research subquestions in Section 4.1 and to remain testable using the adopted comparison metrics.

Prior published towing-load measurements indicate that ground-operation loading is typically characterised by low-amplitude steady rolling combined with occasional transient events (start/stop, braking, tight steering) that can dominate peak forces and fatigue damage. The present work tested whether the same structure held for GA NWLG towing and how it differed between TB and TBL concepts.

(H1) **Spectrum structure (SRQ1).** The measured ground-operation loading spectrum is steep: most cycles occur at low amplitude (steady rolling/gentle manoeuvres), while a small number of transient events (start/stop, brake inputs, tight turns) dominate peak loads and a disproportionate share of fatigue damage.

(H2) **TB vs. TBL input loads (SRQ2).** Towbar towing is dominated by axial tow force transmitted through the tow fittings, with steering effects superposed. Towbarless towing introduces a comparatively larger contribution of combined loading (side load and/or torsion/bending at the fork/axle/brace system), especially during braking and tight-turn transients. Consequently, the distributions of peaks and cycle means/ranges differ between TB and TBL for matched manoeuvre classes.

(H3) **Most susceptible components (SRQ3).** For the investigated GA nose-wheel landing gear architecture, the fatigue-critical response under towing is governed by a limited subset of components (drag-brace joints, fork crown/axle fillets, torque-link lugs). These locations were expected to rank highest by the spectrum damage indicator once the WP2 model was loaded with the WP1-derived manoeuvre histories.

(H4) **Representativeness of constructed missions (SRQ4).** A mission assembled from a finite set of canonical manoeuvres (straight tow, acceleration, braking, wide/tight turns) is sufficient to represent towing for fatigue assessment. It preserves the damage-relevant transients and produces stable rainflow statistics and damage rankings when compared across TB and TBL.

(H5) **Manoeuvrability as the driver of the TB–TBL difference (SRQ5).** The observed TB–TBL differences in $\sigma_{TBL/TB}$, $\mathcal{D}_j$, and Δr are most pronounced during manoeuvres where handling characteristics depend strongly on the towing method. In these cases, the towing concept affects how smoothly the trajectory can be controlled and how readily transient load peaks arise, as reflected directly in the peak- and damage-based metrics.

(H6) **Hotspot shift and operational safety implications (SRQ6).** Switching from TB to TBL can shift the dominant fatigue hotspots ($\Delta r \neq 0$) by changing the load path (tow fittings $\rightarrow$ axle/fork). Under normal operation with qualified equipment and adherence to limitations, peak loads remain within the certified static envelope for both towing methods.

(H7) **Net fatigue-life effect (SRQ7).** For the governing hotspots identified in WP2 under the adopted lifetime mission mix, towbarless towing produces a measurable change in fatigue severity relative to towbar towing, thus $\mathcal{D}_j \neq 1$ and corresponding spectrum life ratios $\rho_{\text{life}} \neq 1$.

In the general-aviation context, these hypotheses suggest that instrumenting the nose-wheel landing gear would most effectively capture the critical loads. However, due to testing constraints, measurements were limited to strain gauges on the towbar and kinematic data. These data were used to construct representative mission spectra for both towbar and towbarless operations. The current state of research and practice supports the following general hypothesis:

Towbarless towing is expected to increase the fatigue severity of general-aviation turboprop and light- to midsize-jet nose-wheel landing gear relative to conventional towbar towing by introducing additional load pathways and higher-severity transients that could alter hotspot ranking, increase cumulative damage, and reduce fatigue life. However, provided qualified equipment is used and operational limitations are respected, the associated risk is expected to remain manageable.

5

WP1 – In-Field Towing

The WP1 in-field towing campaign provided the empirical basis for the loading and fatigue assessments developed in the later work packages. The objective was to obtain a measured towbar baseline together with comparative towbar–towbarless manoeuvre data for representative general-aviation towing operations, and to convert these into usable nose-wheel landing gear load histories and manoeuvre spectra.

Section 5.1 first describes the overall WP1 methodology, after which Section 5.2 presents the instrumentation and data-acquisition setup used during the field campaign. Section 5.3 then establishes the towbar calibration procedure and the selected force-estimation channel. Section 5.4 summarises the two executed field campaigns, their practical constraints, and their respective roles in the dataset. Section 5.5 subsequently discusses the exploratory towbar versus towbarless comparison carried out at Rotterdam The Hague Airport, while Section 5.6 develops the translation from measured towbar data to reconstructed towbarless tow forces. Finally, Section 5.7 assembles the manoeuvre-level load spectra used as input for the later FEM and fatigue analyses.

5.1. WP1 – Methodology

WP1 was designed to produce manoeuvre-resolved TB and TBL load histories using a traceable, non-intrusive measurement strategy. Direct TB force was measured with a calibrated instrumented towbar, while tug and aircraft kinematics were recorded for both towing concepts. The TBL longitudinal force was then reconstructed from measured kinematics and effective rolling resistance.

Method overview

The workflow followed three steps:

1. **Establish traceability by calibration.** The instrumented towbar was calibrated in the laboratory by mapping measured towbar strain to axial towing force, yielding a direct TB force measurement referenced to a traceable load cell.
2. **Acquire synchronised time histories.** Tug and aircraft-side kinematics were recorded for all runs. During TB runs, towbar strain was logged simultaneously to provide a direct axial-force history.
3. **Reconstruct analysis-ready loads and spectra.** A quasi-static longitudinal model (including slope correction and an effective rolling-resistance coefficient) converted kinematics to tow force for TBL, and all manoeuvres were condensed into spectra suitable for downstream FEM loading and fatigue evaluation.

Field manoeuvre measurements and annotation

To populate a representative towing manoeuvre spectrum, the field campaign was structured around a controlled set of manoeuvres covering steady towing, acceleration and braking transients, and turns of different radii. Each run was annotated using a canonical `EventCode`, enabling consistent segmentation and manoeuvre-wise comparison between the TB and TBL datasets.

Table 5.1: Canonical event codes used for annotation

#	Manoeuvre	`EventCode`
1	Straight pull at constant speed	`SP_STEADY_PULL`
2	Straight push at constant speed	`SP_STEADY_PUSH`
3	Smooth pull acceleration	`ACC_PULL_SMOOTH`
4	Smooth pull braking	`BRK_PULL_SMOOTH`
5	Smooth push acceleration	`ACC_PUSH_SMOOTH`
6	Smooth push braking	`BRK_PUSH_SMOOTH`
7	Tight radius pull turns	`TURN_PULL_TIGHT`
8	Tight radius push turns	`TURN_PUSH_TIGHT`
9	Wide-radius pull turns	`TURN_PULL_WIDE`
10	Wide-radius push turns	`TURN_PUSH_WIDE`
11	Controlled pull rapid tug brake	`BRK_PULL_RAPID`
12	Controlled push rapid tug brake	`BRK_PUSH_RAPID`

Recorded outputs

For each manoeuvre, the following time histories were recorded or subsequently derived within a consistent coordinate convention (gear-fixed axes: x forward, y starboard, z down). Together, these signals formed the inputs for later load reconstruction and cycle counting:

$F_{\text{bar}}(t)$	Towbar axial load from strain gauges.
$\widehat{F}_{\text{TBL}}(t)$	Estimated towbarless longitudinal load from kinematics and calibrated resistance.
$a_{\text{tug}}(t)$	Tug linear accelerations: $[a_x(t),\, a_y(t),\, a_z(t)]$.
$\dot{\psi}_{\text{tug}}(t)$	Tug yaw rate.
$v_{\text{tug}}(t)$	Tug ground speed.
$p_{\text{GPS,tug}}(t)$	GNSS position of the tug: $[\phi(t),\, \lambda(t),\, h(t)]$.
$\chi_{\text{GPS}}(t)$	Course over ground (used with $v_{\text{tug}}(t)$ to reconstruct path/turn rate).

Consequently, WP1 delivered a curated and manoeuvre-resolved dataset that could be condensed into spectra and reused directly for FEM loading and laboratory test definition. Prior to the airfield campaign, a short preliminary run was also used to verify the kinematics chain of the test setup, including logging, time alignment, event segmentation, and plotting. The corresponding demonstration output and the associated pre-towing test-area visualisation are provided in Appendix A.1.

Test overview

The WP1 methodology was translated into a practical test concept that defined the measurement approach, the non-intrusive instrumentation choices, and the reference conventions used for later load reconstruction and replay.

Measurement concept The test plan was built around a "kinematics + towbar force" strategy. Tug and aircraft kinematics were logged for all manoeuvres, while the towbar itself was instrumented with strain gauges to measure axial towing force directly during TB runs. In principle, the most direct approach would be to instrument the NWLG itself and back-calculate tow loads from calibrated structural members [59]. Although this approach minimises interface uncertainty and would capture both TB and TBL cases with a single installation, it was not feasible here because the required surface preparation, adhesive bonding, wiring, and protective coatings constitute a maintenance action on certified components. In addition to authorisation and traceability requirements, aircraft operators are generally reluctant to accept temporary gauge installations due to the risk of downtime and rework.

Consequently, a non-intrusive alternative was adopted by instrumenting the towbar to create a large, portable load cell, while tug and aircraft kinematics (IMU/GNSS) were recorded for both TB and TBL runs. For TBL, the longitudinal towing force was reconstructed from the measured kinematics using an equivalent longitudinal equilibrium model that incorporated rolling resistance. The measured or reconstructed tow forces were then transferred to the nose-wheel landing gear interfaces through the FEM-based structural mapping chain developed in WP2. This method preserved airworthiness while enabling the assembly of representative manoeuvre spectra for downstream fatigue assessment.

Towbar configuration The towbar used during the field campaign was a portable telescopic towbar intended for use at remote or unequipped airfields. This towbar was selected because it could be easily transported between test locations, as well as instrumented and calibrated before the in-field campaign. During TB runs, axial towing force was measured directly by strain gauges bonded to the towbar tube, while the associated data-acquisition hardware was mounted on the towbar assembly. Figure 5.1 provides an overview of the resulting strain-gauged towbar setup as implemented during the campaign.

The numbered callouts identified the key components used to acquire the towbar force and kinematics:

1. Towbar including orange carrying handles.
2. Strain gauges under protective rubber.
3. Instrument mounting plate.
4. Electronics enclosure.
5. Sensors and wiring (connectors and main datalogging unit).
6. Test aircraft (Pilatus PC-12).

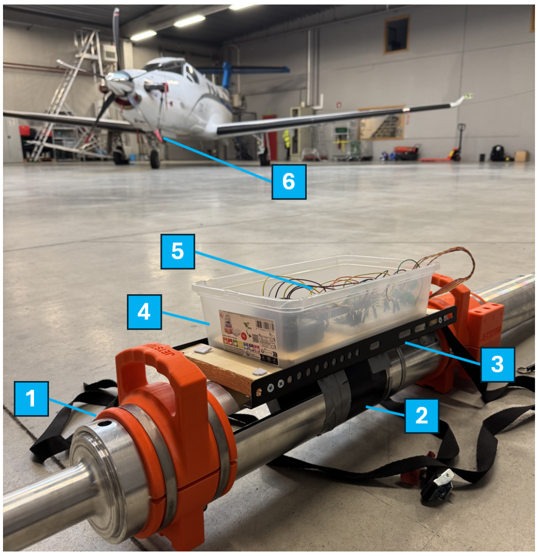

Figure 5.1: Towbar setup including instruments

Reference axes and sign conventions All processing and load application used aircraft body axes: x forward, y starboard, z down. For consistency, $+F_x$ corresponded to the tug driving the aircraft forward, and $+\dot{\psi}$ denoted a right turn (clockwise from above).

5.2. Instrumentation

The setup combined a force-calibrated towbar with kinematic measurements on the tug and aircraft. The aircraft module used an iPhone 15 Pro (built-in IMU/GNSS). The towbar employed two half-bridges of foil strain gauges, an IMU and a GNSS. An overview of the instruments used is given in Table 5.2.

Table 5.2: Instrumentation summary used for in-field testing

Node / Location	Sensor / Platform	Channels	Nominal rate
Towbar axial force	Two half-bridges, $4\times$ 120 Ω foil strain gauges ($\theta = 0^\circ, 90^\circ, 180^\circ, 270^\circ$) on straight tube section; read by ADS1263 (ratiometric)	bridge V_{exc}, shunt events	16.2 Hz (ADC)
Tug kinematics	IMU (LSM6DS3TR-C), rigid mount near NWLG interface; axes aligned tug fwd/right/down	a_x, a_y, a_z [m/s^2], p, q, r [rad/s]	100 Hz (IMU)
Tug GNSS	Adafruit Ultimate GPS HAT	Lat/Lon location, speed, heading, UTC	10 Hz
Aircraft kinematics	iPhone 15 Pro (built-in IMU/GNSS), rigidly mounted and oriented to aircraft axes	a_x, a_y, a_z, p, q, r; Lat/Lon location, speed	100 Hz (IMU), 10 Hz (GNSS)
Data acquisition	Raspberry Pi 5	Synchronised log of all channels	as configured

Diametric pairs $0^\circ - 180^\circ$ and $90^\circ - 270^\circ$ occupy opposite bridge arms around the circumference of the towbar to reject first-order bending. Calibration was performed in the laboratory, as discussed in Section 5.3.

Towbar setup

During the test, a particular towbar was used, designed by AOG4Jets [60]. The Jetstow Celt is a portable, telescopic, lightweight towbar for use at remote or unequipped airfields. The design emphasises onboard stowage, quick self-locking deployment, and a high strength-to-weight ratio. By using this towbar, it was possible to transport it between facilities across Europe, as well as calibrate it in the laboratory. Figure 5.2 shows the extended version of the towbar in use. When contracted, it is only ≈ 0.65 m long.

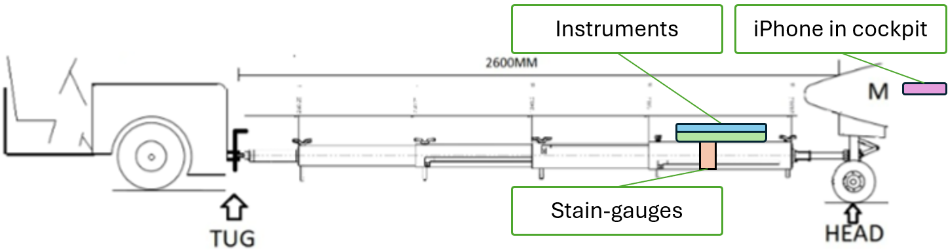

Figure 5.2: AOG4Jets towbar configured as in Figure 5.5; the laptop is omitted, as it only needs to be positioned nearby during operation [AOG4Jets [60] & own work]

Towbarless setup

In the TBL configuration, the strain-gauged towbar was no longer present. Loads were transmitted through the tug's nose-wheel landing gear clamp, and only tug-mounted kinematics and aircraft-side iPhone measurements were used. Figure 5.3 shows the resulting setup, with the instrumentation enclosure (Raspberry Pi, ADC, IMU/GNSS HATs) mounted on the towbarless tug, while the iPhone 15 Pro was installed in a fixed cockpit cradle on the aircraft side.

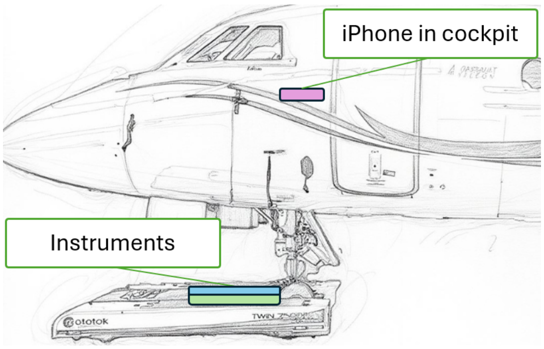

Figure 5.3: Towbarless towing setup; the laptop is omitted, as it only needs to be positioned nearby during operation[1] [sketch by Canva AI]

The instrumented configurations used during testing closely resembled the drawings above. The photos in Figure 5.4 show the physical arrangement of the towbar and towbarless systems as implemented during the measurement campaign.

(a) Towbar configuration

(b) Towbarless configuration

Figure 5.4: In-field towing configuration photos

---

[1] Source: `https://www.aeroexpo.online/prod/mototok-international-gmbh/product-168827-82462.html`

5.2.1. Field Tests Instrumentation

The field campaign relied on the instruments listed below, together with the corresponding roles, core specifications, and sampling strategies. A full overview of the setup is given in Figure 5.5.

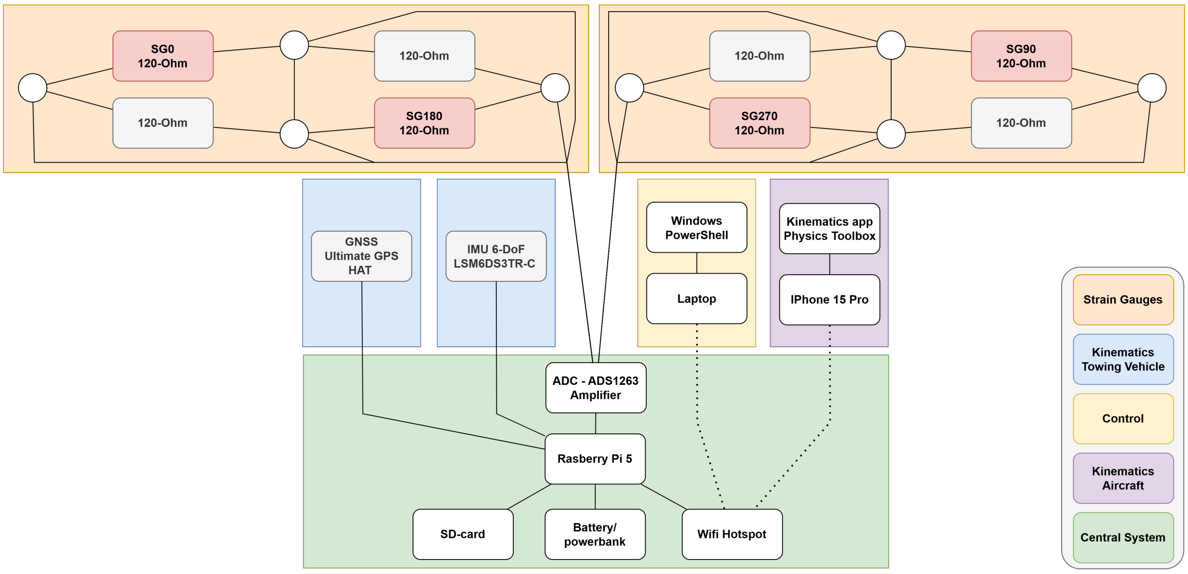

Figure 5.5: In-field test setup layout

The architecture in Figure 5.5 defines the measurement chain used during the field campaign. This section retains the basic function and role of each instrumentation component required to understand the load-reconstruction methodology, while implementation-level details such as Raspberry Pi pin assignments and bridge-to-ADC channel mappings are provided in Appendix A.2.

Raspberry Pi The Raspberry Pi 5 served as the central data acquisition and logging unit for the field setup. It coordinated the towbar force readout through the ADC and the tug-side kinematic measurements from the IMU and GNSS modules, and stored the synchronised measurement streams during the towing tests.

Strain bridges (towbar-mounted) Axial towing load was inferred from strain in a straight, uniform towbar tube section using four foil gauges read through the ADS1263 24-bit ADC in a ratiometric configuration. The gauges, shown in Figure 5.6, were mounted at circumferential angles $0°$, $90°$, $180°$, and $270°$, and wired as two diagonal half-bridges: the diametral pair $90°$–$270°$ formed half-bridge A, and the pair $0°$–$180°$ formed half-bridge B. Each half-bridge used the two active gauges in opposite arms of the Wheatstone network, as sketched in Figure 5.7. This configuration improved sensitivity to axial loading while reducing sensitivity to first-order bending.

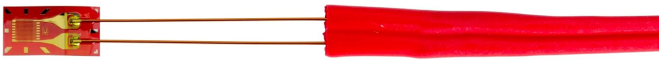

Figure 5.6: Kyowa strain gauges (120 Ω)[1]

With both active gauges in a pair experiencing the same axial strain under tow, the half-bridge output has a form of verification, improving sensitivity. When the tube experiences bending about the diameter that separates a given pair, the two gauges undergo equal and opposite strains, and the corresponding half-bridge largely cancels that bending component. Temperature variations affect both gauges in a pair similarly; ratiometric readout reduces supply-drift effects, but diagonal half-bridges remain more temperature-sensitive than fully self-compensated full bridges. Pre- and post-test zero readings, along with a temperature log, are therefore used to monitor and correct for slow drift. Reading the two half-bridges independently also enables decomposition of the tube loading:

$$s_A \equiv \text{half-bridge A (pair } 90°/270°\text{)}, \qquad s_B \equiv \text{half-bridge B (pair } 0°/180°\text{)}.$$

For pure axial tow force F_x, both channels respond with the same sign and similar magnitude. For bending about the plane through $0°-180°$, channel s_A is most sensitive while s_B is small; for bending

---

[1] Source: `https://www.amazon.co.jp/-/en/KFGS-5-120-C1-11-Strain-Gauges-Length-inches/dp/B0BPX52T5V?th=1`

about the orthogonal plane through $90° - 270°$, s_B dominates and s_A is small. A convenient linear combination is

$$s_{\mathsf{ax}} = \tfrac{1}{2}(s_A + s_B) \quad \text{(axial estimator)}, \qquad s_{\mathsf{b},x} \propto s_B, \quad s_{\mathsf{b},y} \propto s_A,$$

with proportionality constants obtained from calibration. Thus, the arrangement not only yields a robust axial channel for tow force estimation but also provides bending information in both orthogonal planes along the towbar axis.

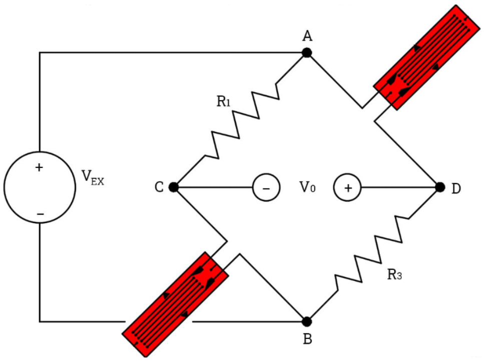

Figure 5.7: Diagonal half-bridge wiring with two active strain gauges[1]

The strain-gauge leads were routed through a connection board that fixed the bridge-to-ADC channel mapping. Because this mapping had to remain unchanged between calibration and field use, the detailed reassembly convention is provided in Appendix A.2.

IMU HAT (towbar/tug-mounted) The towbar/tug was instrumented with an IMU HAT that provided tri-axial acceleration and yaw rate. It was mounted rigidly on the towbar/tug chassis, with axes aligned with the vehicle frame (fore–aft x, starboard y, down z), and was used to characterise towing, braking, and turning manoeuvres.

GNSS HAT (towbar/tug-mounted) A GNSS HAT on the towbar/tug recorded position (ϕ, λ, h), ground speed and course over ground. Its PPS (pulse per second) output was used to discipline the Raspberry Pi clock, and an external roof-mounted active antenna with a 28 dB amplifier provided a clear sky view. The lever arm between the antenna and the IMU origin was measured for later kinematic reconstruction.

To further understand this setup, the following images show the instruments used: IMU (Figure 5.8a), GNSS (Figure 5.8b), and a 24-bit ADC HAT (Figure 5.8c).

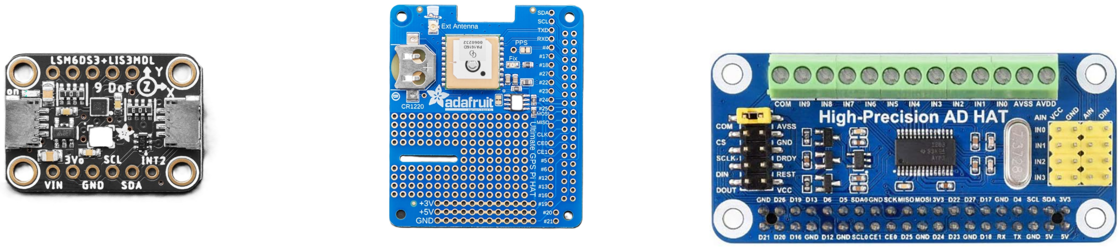

(a) IMU HAT[2]

(b) GNSS receiver + antenna[3]

(c) 24-bit ADC[4]

Figure 5.8: Field instruments used in towing measurements

iPhone 15 Pro (aircraft-side auxiliary) As an aircraft-side auxiliary logger, an iPhone 15 Pro recorded phone IMU data and GNSS via a logging application (Physics Toolbox Sensor Suite). The phone was mounted in a rigid cockpit cradle with recorded orientation and lever arm to the nose-wheel landing gear reference. Time alignment with the tug system was achieved through a step-based synchronisation, followed by cross-correlation and clock-drift correction during longer runs.

---

[1] Source: `https://www.iqsdirectory.com/articles/load-cell/strain-gauge.html`

[2] Source: `https://learn.adafruit.com/assets/123020`

[3] Source: `https://www.amazon.com/Adafruit-Ultimate-GPS-Raspberry-ADA2324/dp/B00SK696NS`

[4] Source: `https://www.amazon.nl/Coolwell-Waveshare-Precisie-Compatibel-Raspberry/dp/B08SJQQWML`

Additional components Power was supplied by a $10\,000$ mAh power bank, which provided approximately 5.5 hours of operating time during field use. This was sufficient for the planned test duration, and the remaining battery level could be monitored directly on the unit.

All electronics (Raspberry Pi, ADC, IMU, GNSS HATs, and power distribution) were housed in a single watertight enclosure mounted on a dedicated frame that was screwed rigidly to the towbar or tug chassis. The frame fixed the instruments' orientation and allowed the enclosure to be quickly removed as a unit and reinstalled on the towbarless tug with the same reference geometry.

Uncertainty and traceability The main sources of uncertainty are associated with the towbar strain bridge (gauge factor tolerance, bonding quality, bridge temperature effects, and ADC noise), the kinematic channels (IMU bias and scale drift, GNSS multipath), and auxiliary measurements such as aircraft mass. Time alignment between the Raspberry Pi stack and the aircraft-side phone introduces additional uncertainty, especially for short, transient events.

To keep these effects traceable, each channel was tied to a simple calibration or reference: the towbar bridge was calibrated using static pull and checked in the field using a shock load for traceable time calibration and pre- and post-zero readings. The IMU and GNSS performance was monitored using repeated straight, level towing passes, and the phone data were aligned by cross-correlation with tug signals and corrected for clock drift.

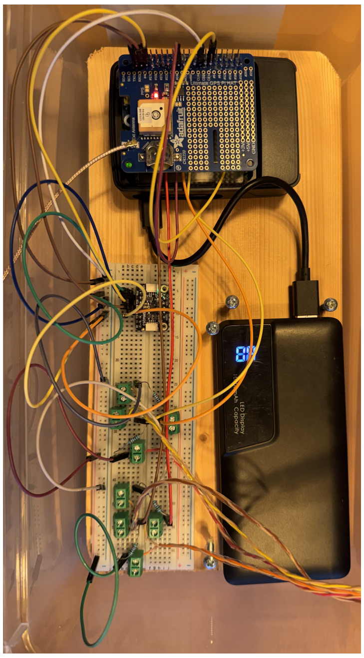

Figure 5.9: Complete field setup picture: Raspberry Pi, IMU, GNSS, 24-bit ADC, and powerbank

Figures 5.9 and 5.10 show the actual overview of the instruments used at the airfield. Figure 5.9 shows the assembled instruments used during in-field testing, including the Raspberry Pi host, IMU, GNSS with PPS, 24-bit ADC, towbar strain bridges and power distribution. Figure 5.10 focuses on the towbar, illustrating the entire setup when connected to the aircraft.

Figure 5.10: Wireless connection initialisation before towing manoeuvres

5.3. Towbar Calibration

Calibration of the instrumented towbar established the relation between strain-gauge output and axial tow force, and documented the test setup, signal processing, and selected force channel.

5.3.1. Setup and Test Overview

Calibration of the towbar strain gauges was carried out in the TU Delft Aircraft Hall using a 250 kN servo-hydraulic load frame equipped with a traceable load cell. The instrumented towbar was mounted vertically in axial tension/compression grips via pin adapters to replicate the in-service axial load path. Before loading, the system was allowed to stabilise thermally, and the zero was recorded with the towbar unloaded. The load cell provided the reference force F, while the ADC logged the bridge output at 16.2 Hz for two axial channels (A and B). A representative photo of the setup is shown in Figure 5.11. The towbar was vertical in the machine, whereas it operates horizontally. The self-weight introduces an axial bias, which was accounted for in the tare procedure.

For all tests, the towbar was set to its maximum extension. The screw-on tow ends could not be installed because their added length exceeded the available load frame fixture/travel, and were therefore left off. Consequently, the clevis pins at the head were loaded in a slightly non-standard manner relative to in-service use. AOG4Jets specified a provisional 10 kN axial limit for this prototype towbar in the complete configuration [7]; to maintain a conservative margin under the altered pin loading, tension steps were restricted to $+5$ kN. Under compression, small geometric tolerances caused noticeable out-of-plane bending, so the calibration was limited to -3 kN.

Calibration used bipolar step sequences with dwells to allow signal settling. The sequences were:

- **Tension series:** $0 \to 1.0 \to \cdots \to 5.0$ kN, then $5.0 \to 4.0 \to \cdots \to 1.0$ kN.
- **Compression series:** $0 \to -1.0 \to \cdots \to -3.0$ kN, then $-3.0 \to -2.0 \to -1.0$ kN.

Each series was repeated five times. Tension is defined as positive; compression is negative. The dwell period at each load plateau was set at 10 seconds. After each series, the machine was manually returned to 0 kN.

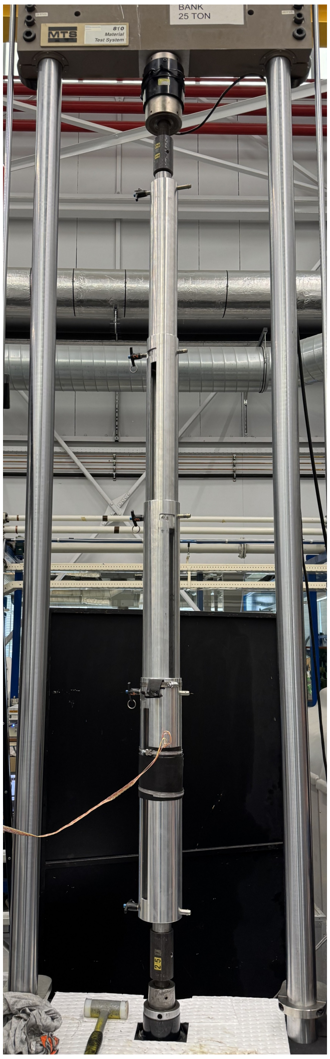

Figure 5.11: Towbar mounted in the 250 kN servo-hydraulic load frame for static step calibration

Logged signals and plateau detection

The following were logged: UTC timestamp, UTM force F (N), channel A and B differential voltages $V_{\text{diff},A/B}$ (V), and bridge excitation V_{ex} (V). Processing was ratiometric per channel,

$$r_k = \frac{V_{\text{diff},k}}{V_{\text{ex}}}, \qquad k \in \{A, B\}. \tag{5.1}$$

where,

- r_k ratiometric bridge signal for channel k [-]
- $V_{\text{diff},k}$ differential bridge voltage measured on channel k [V]
- V_{ex} measured excitation voltage used for ratiometric processing [V]

A single time-lag between UTM and ADC was then estimated per sheet using a fast, plateau-based method and applied once to the ADC series. Force plateaus were detected in the UTM trace using robust range/variance thresholds, with short gap bridging. For each accepted plateau $[t_1, t_2]$, means were computed over the tail of the dwell:

$$\bar{F} = \text{trimmed mean}\big(F(t)\big)_{t\in[t_2-\Delta,\, t_2]}, \qquad \bar{r}_k = \text{trimmed mean}\big(r_k(t)\big)_{t\in[t_2-\Delta,\, t_2]},$$

with $\Delta \approx 1.5$ s and a 5% trimmed mean. Plateaus with residual ramping or insufficient duration were rejected. Channels A and B were processed independently on the same set of detected plateaus.

Calibration is linear in strain form:

$$\text{Strain form :}\quad F \;=\; C'_k \;+\; K'_k\,\mu\bar{\varepsilon}_k, \quad \text{with} \quad \mu\bar{\varepsilon}_k \approx \frac{2\times10^6}{\text{GF}}\,\bar{r}_k \quad \text{(two-active half-bridge).} \tag{5.2}$$

where,

- $\overline{\mu\varepsilon}_k$ mean microstrain on channel k [$\mu\varepsilon$]
- GF strain-gauge factor [-]
- F applied axial force (reference from UTM load cell) [N]
- C'_k calibration intercept for channel k [N]
- K'_k calibration slope for channel k [N$/\mu\varepsilon$]
- k channel index (A or B) [-]

Least-squares fits were performed on plateau pairs $(\bar{r}_k, \bar{F})$, separately for tension and compression to expose any asymmetry; outliers were removed by a robust residual threshold. Results are reported N per $\mu\varepsilon$.

Channel behaviour and selection

Channel A exhibited inconsistent sensitivity and intercepts across repeats. Inspection of the instrumented section shows that A's gauges lie close to the longitudinal slot in the towbar tube (see Figure 5.12), which perturbs the local stiffness and shifts the neutral axis. In addition, the altered load introduction during the servo-hydraulic load frame setup (towbar end-fittings removed) leads to a pin force path that is slightly offset *and* more aligned with the Channel B gauge line. Together, the slot proximity and the pin-load eccentricity bias A's local strain field, making its response more susceptible to additional effects. In contrast, Channel B is aligned with the dominant load path and yields stable, repeatable fits. Therefore, Channel B is adopted as the sole calibration channel, while Channel A is retained mainly as a backup.

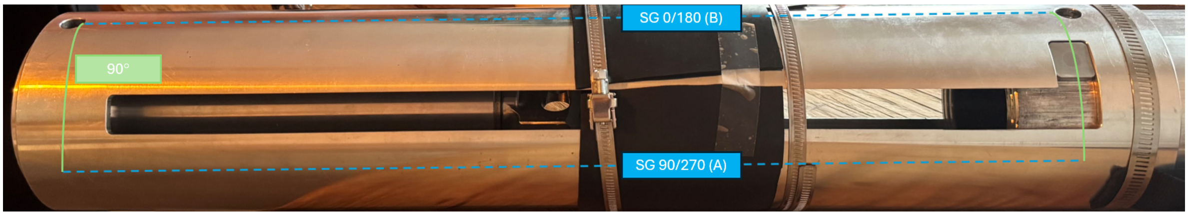

Figure 5.12: Towbar slotted region near the gauge stations. The slot and pin load path explain the A/B response difference

The impact of the slot on Channel A is visible in Figure 5.13, where the F–μ_ϵ relationship displays a clear asymmetry between tension and compression and a mild deviation from linearity in the tension markers at each plateau. This behaviour confirms that Channel A is less suitable as a primary force channel and is best used for qualitative cross-checks.

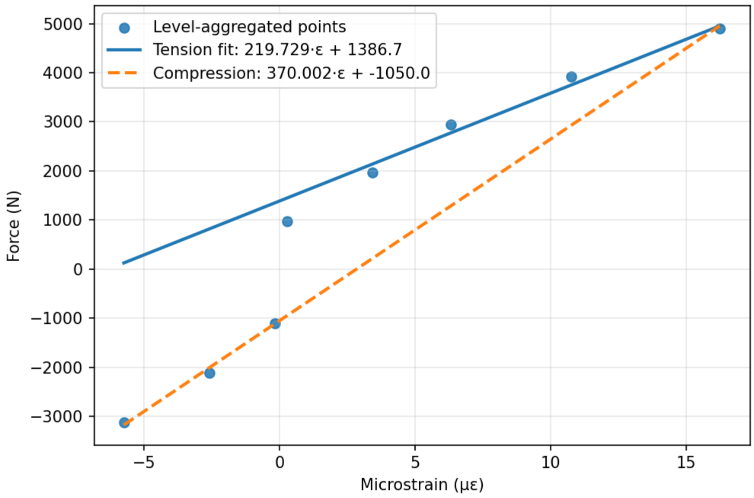

Figure 5.13: Channel A output showing the local slot-induced effects

5.3.2. Towbar Calibration Output

Representative plots for Channel B are shown in Figure 5.14 and 5.15, overlaying the applied force and the measured microstrain. Figure 5.14a and 5.14b correspond to one representative run from the five repeated tension runs and the five repeated compression runs. The other runs exhibited the same behaviour and yielded very similar results. The tension/compression fits for Channel B are summarised in Table 5.3.

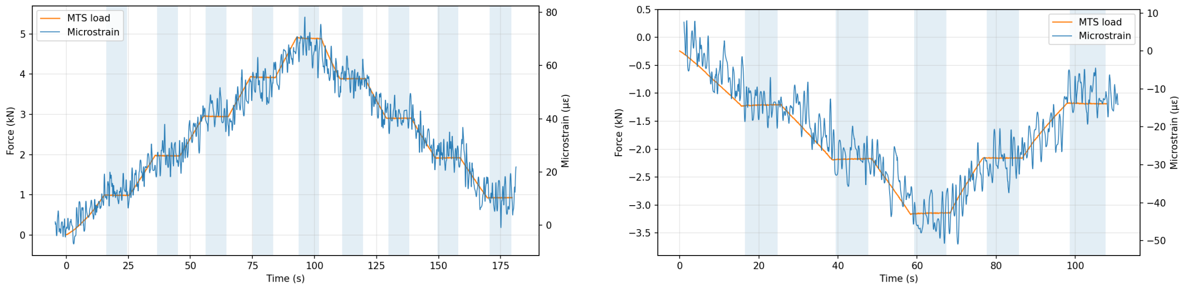

(a) Tension

(b) Compression

Figure 5.14: Calibration plots for Channel B

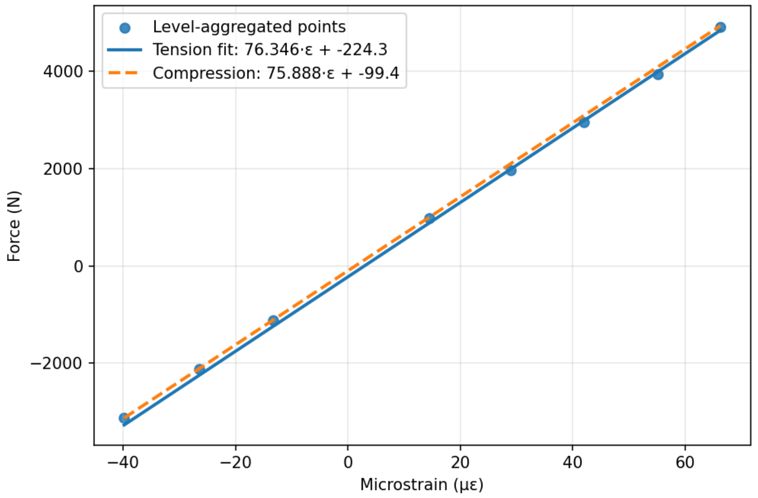

Figure 5.15: Plateau aggregation and residuals for Channel B

Calibration summary table

Because the towbar was tested vertically, gravity contributes a constant axial component of the towbar's self-weight along the load line. This introduces a bias of approximately $W_{\text{ax}} \approx 110$ N (compression-directed). The strain channels were tared at zero load, so tension plateaus are already referenced to the correct zero. Compression plateaus, however, carry the additional gravitational component. To report forces comparable to in-service horizontal operation and to keep tension/compression symmetry, a constant correction was applied to compression plateaus:

$$F_{\text{eq}} = \begin{cases} F_{\text{UTM}}, & \text{tension series,} \\ F_{\text{UTM}} - W_{\text{ax}}, & \text{compression series,} \end{cases} \qquad W_{\text{ax}} \simeq 110 \text{ N.} \tag{5.3}$$

The table below lists the linear fit constants obtained for Channel B after applying this correction to the compression data. These constants were used for implementation.

Table 5.3: Towbar calibration constants using Channel B for force estimation

Channel	Sign	K (N/$\mu\varepsilon$)	C (N)	R^2	N plateaus
B	Tension	76.3	-224.3	0.995	9
B	Compression	75.9	-209.4	0.997	5

5.4. In-Field Towing Campaigns and Dataset Roles

WP1 combined two complementary in-field towing datasets with distinct roles. The first campaign, conducted at Charleroi using an instrumented towbar on a Pilatus PC-12, provided the measured towbar force histories that define the baseline TB manoeuvre set. The second campaign, conducted at Rotterdam The Hague Airport using the TU Delft laboratory aircraft PH-LAB (Cessna Citation II), provided a comparative TB–TBL kinematic dataset used to identify relative differences between towing concepts.

Accordingly, the TBL manoeuvres used later in this thesis were not measured directly in force on the PC-12. Instead, they were reconstructed by applying the Rotterdam-derived TB–TBL differences to the measured PC-12 TB baseline from Charleroi. In this way, Charleroi provided the absolute force baseline, while Rotterdam provided the relative correction trends used for the TB-to-TBL translation.

Figure 5.16 summarises the WP1 measurement, reconstruction, and scaling chain by which the two field datasets were converted into the canonical TB and reconstructed TBL manoeuvre sets, the resulting WP1 load spectra, and the load input passed to WP2.

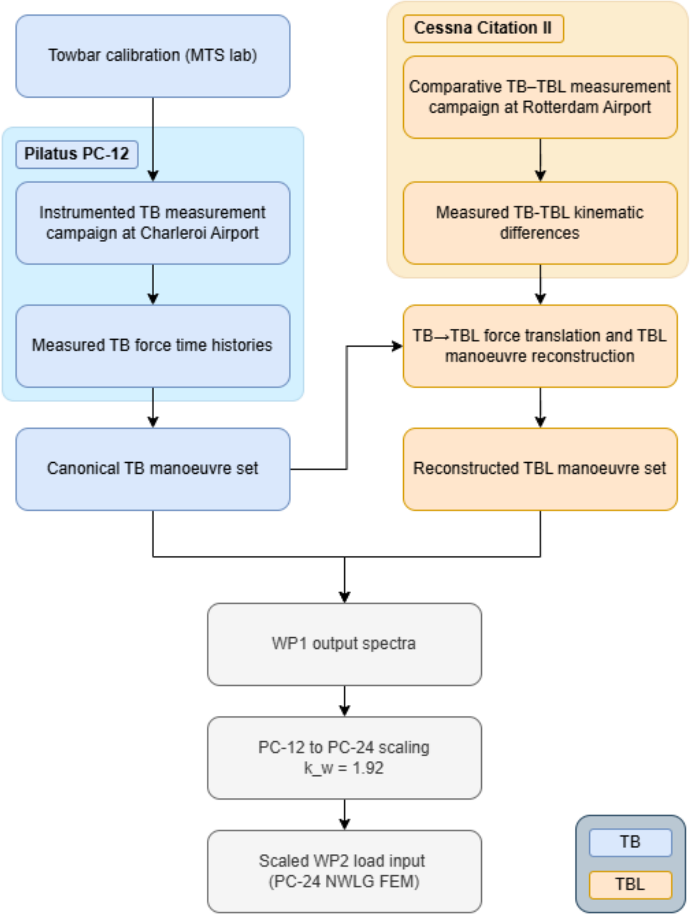

Figure 5.16: WP1 test campaigns, data-processing, reconstruction, and scaling chain

Table 5.4: Role of the two WP1 in-field campaigns

Campaign	Aircraft	Recorded data	Role in WP1
Charleroi	Pilatus PC-12	Instrumented towbar force histories and kinematics during TB manoeuvres	Provides the measured TB baseline manoeuvre set and the effective towing-resistance identification
Rotterdam	Cessna Citation II	Comparative TB and TBL kinematics only	Provides the relative TB–TBL correction terms used to reconstruct TBL manoeuvres from the Charleroi TB baseline

5.4.1. Instrumented Towbar Campaign (Pilatus PC-12 at Charleroi Airport)

The aircraft used for towing was a Pilatus PC-12 NGX, empty of payload but fully fueled. This resulted in a mass of ≈ 4300 kg. The objective of the Charleroi campaign was to measure representative towbar-towing loads acting on the NWLG of the PC-12 NGX and to provide the baseline dataset required for the later TB-to-TBL reconstruction.

Charleroi Airport (EBCI) — Friday, 12 December 2025. All towing tests at Charleroi were conducted on the morning of Friday, 12 December 2025, using a Pilatus PC-12. Operations took place both inside and outside a maintenance hangar. Ambient conditions were calm and dry, with no precipitation or significant wind influence. Given the sheltered setting and low towing speeds, effects from temperature variation or weather were negligible.

The surface was dry concrete, characterised as smooth, with limited surface irregularities. This combination resulted in a relatively smooth rolling interface and a low friction coefficient, representative of favourable operational ground conditions. As such, the measurements were expected to reflect a best-case scenario for rolling resistance and towing effort, serving as a baseline for subsequent load reconstruction and comparison.

5.4.2. Comparative TB–TBL Campaign (Cessna Citation II at Rotterdam The Hague Airport)

The TU Delft laboratory aircraft PH-LAB is a Cessna Citation II used for research and teaching purposes and was selected here as a practical platform for a controlled exploratory TB–TBL comparison.

Rotterdam The Hague Airport (EHRD) — Tuesday, 20 January 2026. The Rotterdam towing session was performed on Tuesday, 20 January 2026, using the TU Delft laboratory aircraft (Cessna Citation II, registration PH-LAB) based in a large hangar at Rotterdam The Hague Airport. Weather conditions were stable and favourable for testing: clear skies, cold ambient temperature, a dry surface, and no noticeable wind. These conditions minimised environmental variability and were therefore considered near-ideal for repeatable ground-handling measurements.

The towing surface at Rotterdam The Hague was in a very similar condition to Charleroi, consisting of dry, smooth asphalt with limited irregularities. Consequently, rolling-interface characteristics were considered to be comparable between the two sites, supporting cross-comparison of manoeuvre data without requiring additional correction for surface state.

5.4.3. In-Field Manoeuvres

The in-field campaign was originally designed around a set of twelve canonical towing manoeuvres identified in Table 5.1 as necessary to populate a representative towing cycle (straight push/pull, acceleration and braking transients, and tight and wide turns in both directions). Figure 5.17 shows the corresponding proposed test programmes at two candidate sites (Gray St. Adrien, and Charleroi), laid out such that the same manoeuvre set could be executed with consistent geometry and sequencing, enabling a direct comparison across sites and the later assembly of a complete, repeatable towing cycle.

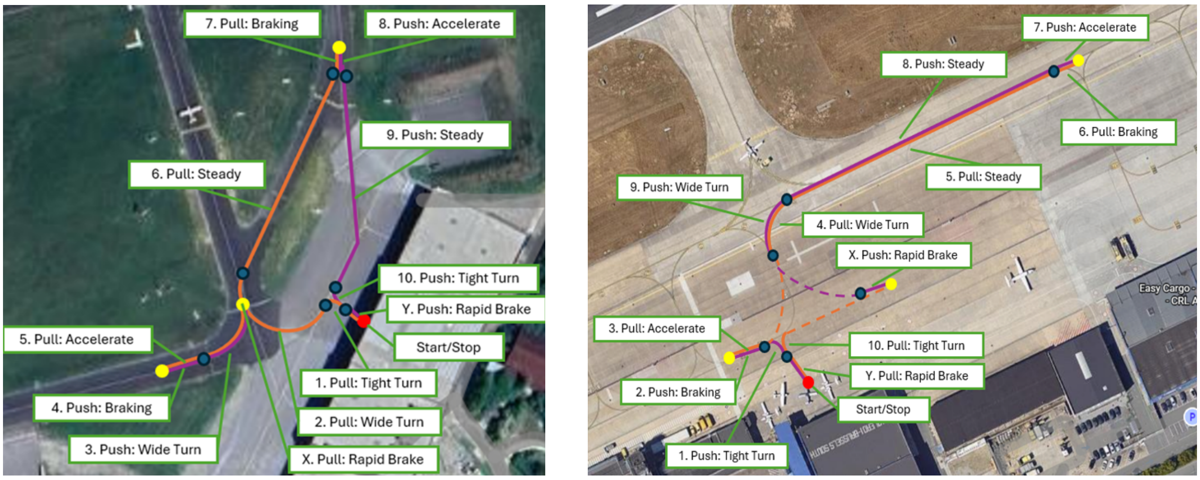

(a) Proposed test programme layout on Gray airfield

(b) Proposed test programme layout on Charleroi airfield

Figure 5.17: Proposed 12-manoeuvre towing test programmes [Google Maps & own work]

In practice, executing the full planned programme was not feasible due to operational and logistical constraints at active airports. Examples include restricted access to taxiways and apron areas, limited time windows and limited personnel availability during the test days, and the need to prioritise safe, non-disruptive operations amid ongoing airport activity. As a result, the test programme was adapted on-site, and the manoeuvres actually performed differ from the original plan. Figure 5.18, therefore, presents the actual towing programmes and measured paths from which the datasets in this thesis are derived.

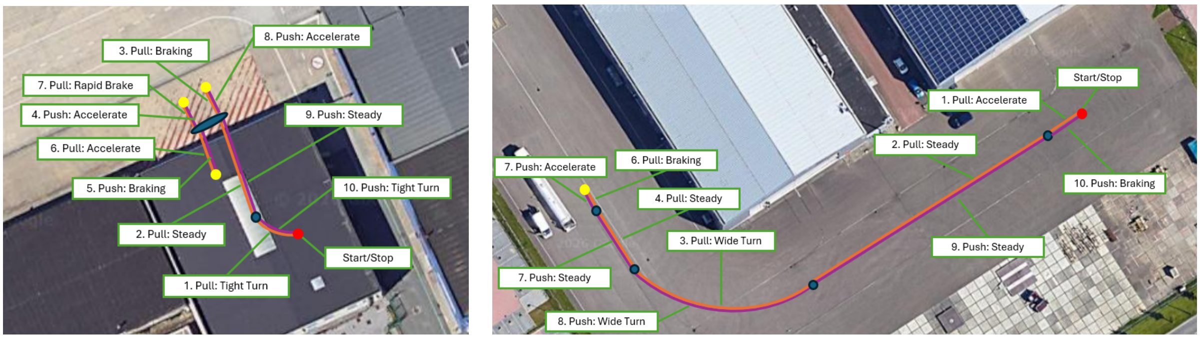

(a) Charleroi Airport (Instrumented TB)

(b) Rotterdam The Hague Airport (TB vs. TBL)

Figure 5.18: Actual towing programme and measured paths [Google Maps & own work]

Although the Charleroi campaign was performed earlier and provides the measured TB baseline, the next section first discusses the Rotterdam TB–TBL comparison because it motivates the translation from TB to TBL. The resulting Charleroi TB spectra and translated TBL manoeuvres are then presented in Section 5.7.

5.5. Rotterdam TB–TBL Comparison Used for Translation

Initial TB and TBL towing manoeuvres were compared at Rotterdam The Hague Airport using the TU Delft laboratory aircraft (Cessna Citation II, registration PH-LAB)[1]. The campaign remained exploratory and was used to compare towbar and towbarless towing interfaces, manoeuvrability, and potential mechanisms for load peaks before a controlled measurement campaign. The measurement architecture followed the approach introduced earlier (see Section 5.2). An aircraft-mounted smartphone logger (denoted AP) was placed near the cockpit, and a Raspberry Pi-based sensor package (denoted PI) was mounted on the towing equipment. In this campaign, the towbar used at the airport was not instrumented with strain gauges; the instrumented towbar could not be deployed, and retrofitting the new towbar would have required a full recalibration.

Performed test sequence:

- Partial repositioning: approximately half a turn out of the hangar. (TBL)
- Two TBL missions.
- One TB mission.
- Repositioning back into the hangar. (TBL)

Tow vehicle and operational configuration. Both TB and TBL manoeuvres were conducted using the same towing vehicle. The difference between the experiments was therefore primarily the towing interface: for TB, the vehicle coupled through a towbar connected to the aircraft nose-wheel landing gear axle, whereas for TBL, the vehicle engaged the nose-wheel/axle region via its towbarless capture mechanism. As a result, the maximum speed and acceleration were expected to be similar from a vehicle-capacity perspective, although operator confidence and interface constraints could still affect the realised manoeuvre. The towing vehicle used was a LEKTRO 86 Tow Tractor, as seen in Figure 5.19b.

---

[1] `https://www.tudelft.nl/lr/organisatie/afdelingen/control-and-operations/facilities/laboratory-aircraft`

(a) Towing vehicle configured for TB operation

(b) Towing vehicle configured for TBL operation

Figure 5.19: Same towing vehicle used for both experiments, shown in TB and TBL configurations

Interface location and load path. TB was attached to the nose-wheel axle. TBL engaged the gear at a pin location for pull manoeuvres, while push manoeuvres applied load primarily through the wheel (and thus into the axle). No “hard” clamping was observed for the TBL interface (no direct rigid clamping comparable to a dedicated clamp); the engagement appeared to rely on geometric capture and contact.

Informal discussions with local ground-handling staff and experienced maintainers indicated that axle-based towbar engagement of this type is considered an outdated towing arrangement and is not commonly applied in routine operations. In current practice, towbar towing is more commonly implemented via dedicated tow pins/lugs, which provide a clearer, more repeatable attachment interface.

A practical advantage of these pin-based arrangements is operational, as they are typically compatible with a single tug operator under standard procedures. By contrast, axle-based towing without a distinct load-limiting element (e.g. a shear pin) was described as formally requiring a second operator in the cockpit. This requirement was also stated during the Rotterdam The Hague Airport operation, but it was reported to be rarely implemented in day-to-day practice across the industry.

Moreover, this was backed up by an operator statement during the Rotterdam The Hague Airport towing tests (translated from Dutch): “I have seen axle towing very little over the last 20 years because you need more personnel for it, the towbar is heavy, it requires more handling steps, and you can park fewer aircraft in one hangar than with towbarless, which is more user-friendly. The manufacturer determines the requirements, and in the manuals you only find towbar procedures (it may be different for other manufacturers, or in newer manuals/revisions). Towbarless is just a hype: more productive, but without any deep research into safety for both aircraft and personnel. In short, the towbarless unit you tested on the Cessna has no shear pin, no safety like a tow strap if the engine/brake fails, and no damping.”

Aircraft-/gear-specific notes (Citation). The Citation’s front wheel assembly was perceived as comparatively light, which facilitated manual repositioning and alignment during the trials. For towbarless operation, an additional adapter was required on the towbarless vehicle to engage the Citation nose-wheel geometry, preventing the nose-wheel from lifting. Figure 5.20 documents the two towing interfaces used: the towbar connection at the axle (Figure 5.20a) and the towbarless engagement, which acts at the crown in pull and primarily through tyre contact in push (Figure 5.20b).

(a) Towbar interface

(b) Towbarless interface

Figure 5.20: Comparison of towing interfaces to NWLG for TB vs. TBL operation

Manoeuvre overview on the airfield (GPS overlay)

Figure 5.21 provides a map-based overview of the measured paths for one TB run and two TBL runs. The TB manoeuvre is visually shorter and includes limited pushback, consistent with the operational constraint observed during testing. During push, the towbar–tractor–aircraft configuration tended to "scissor" under certain conditions, limiting safe reverse distance and reducing manoeuvre consistency. By contrast, both TBL runs were executed as a complete cycle from point A to point B, back to point A, including a stop and reorientation. It should be noted that the run in Figure 5.21b is shorter after the turn manoeuvre and thus the distance covered during the TBL4 run is shorter than that covered during the TBL5 run.

(a) TB (`TB5`)

(b) TBL (`TBL4`)

(c) TBL (`TBL5`)

Figure 5.21: GPS overlay of the towing manoeuvres on the airfield (AP track)

Heading behaviour and qualitative manoeuvre smoothness

The AP–PI heading comparison (Figure 5.22) provides a direct view of the heading evolution during the manoeuvres. For the towbar run, the heading response indicates comparatively larger heading excursions, especially during pushback. These increased steering angles are consistent with the practical observation that pushback is more difficult to execute smoothly with a towbar, and may also reflect greater operator familiarity with towbarless procedures during this session. During the towbar pull, the aircraft's heading is relatively stable until the transition into pushback. Moreover, the PI shows inconsistent heading data. This inconsistency was expected to be due to the much higher vibrations experienced by the towbar compared to those experienced by the instruments on the towbarless vehicle. Therefore, these PI headings did not appear to reflect the actual test performed, based on visual verification.

For both towbarless runs, the aircraft heading remained comparatively steady. The towbarless vehicle exhibited more frequent small corrections (as expected with active guidance), whereas the aircraft followed them more smoothly.

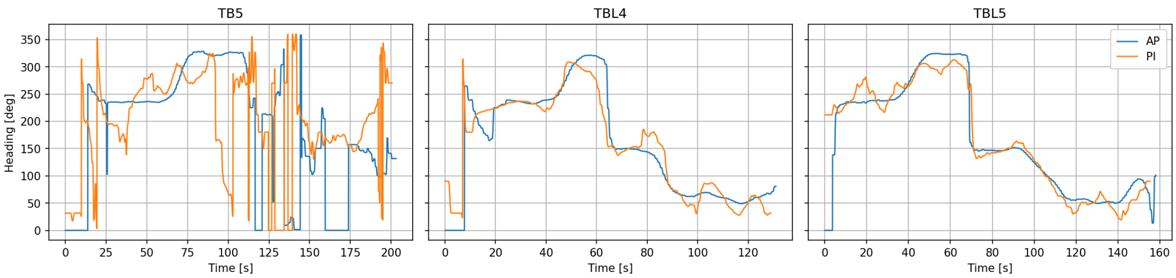

Figure 5.22: Heading comparison (AP in aircraft vs. PI on towing equipment)

Speed comparison and manoeuvre duration

TB towing was noticeably slower, particularly in push manoeuvres, attributed to the "scissor" effect. The towing vehicle used for both TB and TBL operations at Rotterdam The Hague Airport was the same, capable of towing TBL on one end and TB on the other. Hence, from a capacity standpoint, the achievable maximum speed and acceleration were expected to be similar across both methods. The operating speed was sufficiently high that the operator needed to stand on the vehicle during operation. This operational constraint differs from a remote-controlled TBL vehicle (e.g. Mototok-type), where human speed may limit the manoeuvre.

Figure 5.23 compares the AP-derived GPS speed for the three runs. A direct speed-time comparison over an identical path was not possible because the towbar run covered only a partial manoeuvre (predominantly pull with limited pushback), and the two towbarless runs differ slightly in total path length (as seen in the GPS overlays). However, comparing runs of similar overall distance for the pull part of the spectrum (here, `TB5` versus `TBL5`), suggested that the towbarless manoeuvre was completed faster: the towbarless run completed the corresponding cycle in approximately $70\,\mathrm{s}$, whereas the towbar run spanned roughly $95\,\mathrm{s}$ of active measurement for a comparable distance. This time difference indicated a lower average speed for the towbar case.

In the same figure, typical speed levels were approximately $2\,\mathrm{m/s}$ for towbarless towing and around $1.5\,\mathrm{m/s}$ for the towbar case. Short-duration spikes in the towbar speed trace were attributed to GPS artefacts rather than true vehicle dynamics. Operationally, lower towbar speed was consistent with increased caution against scissoring during braking and pushback: in towbar towing, the aircraft could overrun the tractor under braking, creating an unsafe geometry, whereas the towbarless capture interface constrained this relative motion more effectively.

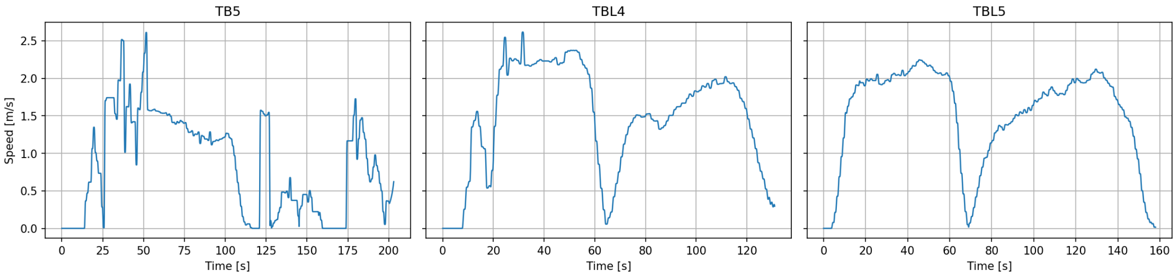

Figure 5.23: AP GPS speed for towing runs

Aircraft vibration response (AP residual acceleration)

To compare the high-frequency content experienced by the aircraft during towing, the AP IMU signals were decomposed into a low-frequency manoeuvre component and a high-frequency residual component, used as a vibration proxy. Figure 5.24 shows the residual longitudinal and lateral accelerations for the three runs.

Overall, the towbarless runs exhibited larger residual acceleration envelopes in the aircraft, with longitudinal residual peaks of approximately $0.2\,\mathrm{m/s^2}$–$0.3\,\mathrm{m/s^2}$ and $0.3\,\mathrm{m/s^2}$–$0.4\,\mathrm{m/s^2}$, respectively. Part of this difference was expected to be driven by the higher average towing speed in towbarless operation.

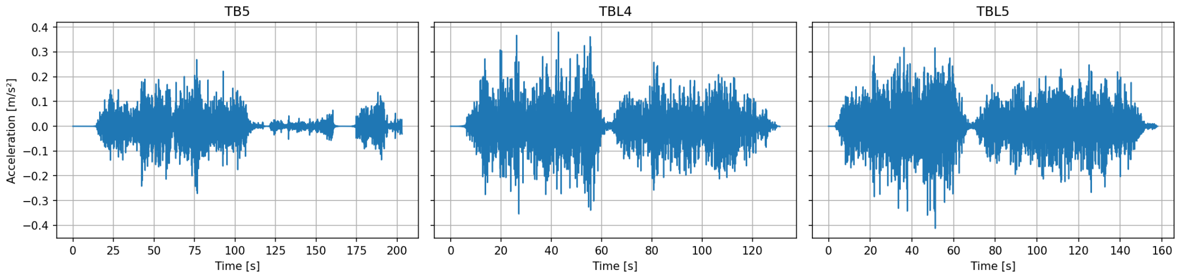

Figure 5.24: AP residual accelerations for towing runs (vibration proxy)

Using the vibration proxy amplitude AP, the measured envelopes were approximately $AP_{\text{TB}} \approx 0.2\,\text{m/s}^2$ and $AP_{\text{TBL}} \approx 0.4\,\text{m/s}^2$. For a TB→TBL comparison, the relevant incremental vibration magnitude is therefore

$$\Delta AP = AP_{\text{TBL}} - AP_{\text{TB}} \approx 0.2\,\text{m/s}^2. \tag{5.4}$$

where,

- ΔAP incremental vibration proxy amplitude between TBL and TB $[\text{m/s}^2]$
- AP_{TBL} vibration proxy amplitude for towbarless towing $[\text{m/s}^2]$
- AP_{TB} vibration proxy amplitude for towbar towing $[\text{m/s}^2]$

Converting this increment to an equivalent inertial force at the nose load path,

$$\Delta F_{\text{vib}} \approx m_N\,\Delta AP, \qquad m_N = \lambda_N m_{\text{MTOW}}, \tag{5.5}$$

where,

- ΔF_{vib} equivalent incremental vibration-induced inertial force $[\text{N}]$
- m_N effective nose-load-path mass $[\text{kg}]$
- ΔAP incremental vibration proxy amplitude $[\text{m/s}^2]$
- λ_N nose-load fraction of the aircraft mass $[-]$
- m_{MTOW} aircraft mass at maximum take-off weight $[\text{kg}]$

with $m_{\text{MTOW}} = 4313\,\text{kg}$ and $\lambda_N = 0.127$, yields:

$$\Delta F_{\text{vib}} \approx 0.127 \times 4313 \times 0.2 \approx 0.11\,\text{kN}. \tag{5.6}$$

Expressed as a nominal axial stress amplitude in the $3\,\text{mm}$ diameter gauge section used in WP3 ($A = \pi d_g^2/4 = 7.07\,\text{mm}^2$),

$$\Delta\sigma_{a,\text{vib}} \approx \frac{\Delta F_{\text{vib}}}{A} \approx \frac{110}{7.07 \times 10^{-6}} \approx 16\,\text{MPa}. \tag{5.7}$$

where,

- $\Delta\sigma_{a,\text{vib}}$ = equivalent incremental vibration-induced stress amplitude $[\text{MPa}]$
- A = specimen gauge-section area $[\text{m}^2]$

This increment was a magnitude below the WP3 endurance threshold. Moreover, before rainflow counting, a moving-window filter was applied to suppress small-amplitude content. With a window threshold of $\sigma_{a,\text{win}} = 8\,\text{MPa}$, the inferred vibration-induced increment ($\Delta\sigma_{a,\text{vib}} \approx 16\,\text{MPa}$) fell in the regime of cycles that were either removed outright by the filtering step or, if retained, contributed negligibly relative to the dominant towing load content. Consequently, the TB–TBL difference in measured vibration content was neglected in the fatigue initiation accounting.

Low-frequency manoeuvre accelerations (AP)

Figure 5.25 shows the low-frequency (manoeuvre) acceleration components. For the towbar run, longitudinal manoeuvre acceleration fluctuated within approximately $-0.2\,\text{m/s}^2$ to $0.2\,\text{m/s}^2$ but was comparatively irregular, consistent with a less fluid manoeuvre and repeated small corrections. For the towbarless runs, the longitudinal signal showed a clearer and smoother braking event at the mid-run stop/turn, reaching about $-0.8\,\text{m/s}^2$ for `TBL4` and about $-0.6\,\text{m/s}^2$ for `TBL5`, aligned with the stop event visible in the speed trace.

In the lateral manoeuvre acceleration, all runs showed a peak associated with turning. The towbar run almost reached $0.3\,\text{m/s}^2$, while the towbarless runs showed larger turn peaks (beyond $0.4\,\text{m/s}^2$ in

TBL4, and above $0.3\,\mathrm{m/s^2}$ in TBL5). This was consistent with towbarless runs executing full turns at higher speeds and should be interpreted in conjunction with the path geometry and speed history.

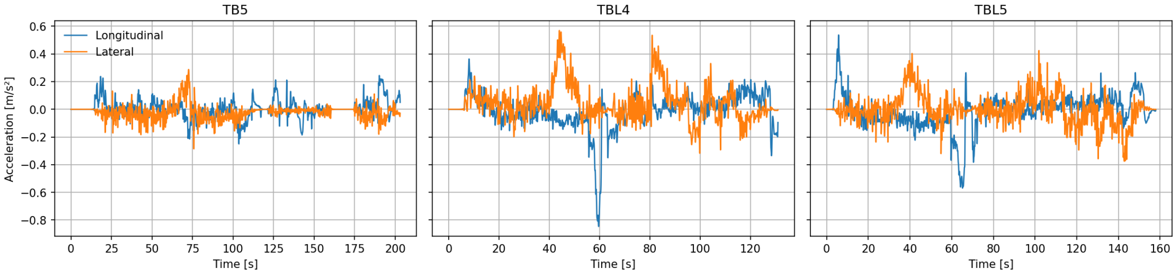

Figure 5.25: AP manoeuvre accelerations for towing runs (low-frequency components)

Towing-equipment response (PI acceleration)

PI acceleration histories provided an additional perspective on equipment-side excitation. A direct TB–TBL comparison is not strictly valid because the PI location and mounting stiffness differ between the towbar and towbarless configurations (Section 5.5). Nevertheless, the towbar-mounted PI recorded a distinct high-magnitude event in the longitudinal channel during braking/transition, consistent with mechanical play in the towbar ring interface producing an impact-like load transfer when the direction of force changes. A corresponding lateral component was also observed, indicating that the impact is not purely axial. In contrast, the towbarless PI signals were more consistent over the manoeuvre, reflecting a smoother force transfer through the capture interface and a more continuous towing cycle.

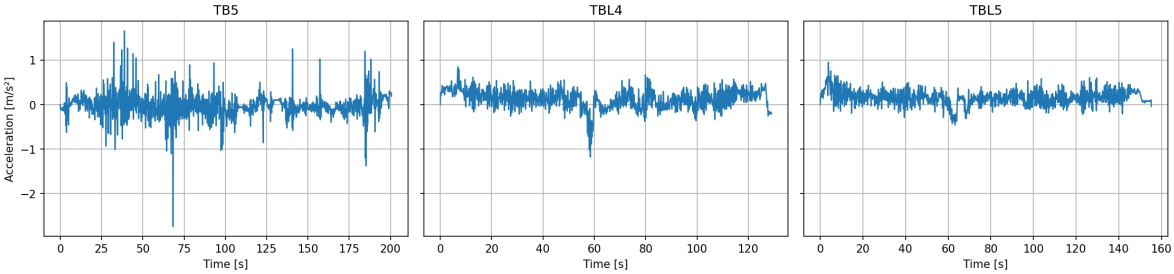

Figure 5.26: PI acceleration comparison for towing runs (note: different mounting locations)

Instrumentation mounting and interface play

Figure 5.27 documents the PI mounting configurations. For the towbarless vehicle, the PI package could be positioned on a relatively flat surface and restrained using a strap, providing a stable mounting. The towbarless vehicle itself includes wheels and tyres, which can attenuate certain high-frequency inputs transmitted to the instrument package.

For the towbar case, the PI package was mounted on the towbar (similar in concept to the original towbar trials), but the towbar was uninstrumented in strain. In addition, the towbar-to-vehicle connection used an oversized ring interface. This geometric play introduced a plausible mechanism for shock loading during reversals of towing direction (push-to-pull or pull-to-push): load transfer can occur through contact/impact within the ring, which was particularly noticeable during push manoeuvres and may contribute to a more "jerky" towing response.

Figure 5.27: Towbar connection to towing vehicle via oversized ring (mechanical play)

An illustrative example of this effect was visible in the TB Pi dataset. During push manoeuvres, the measured longitudinal shock peak reached approximately $-2.4\,\mathrm{m/s^2}$ for the towbar case, whereas the towbarless runs showed smaller negative peaks of roughly $-1.0\,\mathrm{m/s^2}$ and $-0.5\,\mathrm{m/s^2}$. Consistently, the spectrum comparison in Figure 5.26 exhibited more pronounced peak content for TB than for TBL. While this was mechanistically interesting, it was not interpreted as an intrinsic effect of the towing concept. As observed in the earlier trials with the

AOG4Jets towbar, which featured a tight (low-clearance) interface with little to no tolerance, such shock peaks were not observed. The present shocks were therefore attributed to towbar/interface play and treated as towbar-dependent artefacts. Given that their order of magnitude was similar to the vibration levels already shown to be negligible relative to the WP3 endurance threshold, this phenomenon was documented but not investigated further.

Additional in-field notes

A consideration was that towbar towing could be faster than towbarless towing. Based on the in-field observations, this appeared to hold when the towbarless alternative was a remote-controlled vehicle, for which the achievable towing speed was practically constrained by human walking/running speed and response time. However, the hypothesis did not appear to hold universally across towbarless implementations. When the towbarless vehicle is ride-on or stand-on, the towbar configuration is often slower in push manoeuvres due to kinematic and control constraints associated with the towbar interface and operator handling.

Two recurring observations were noted during the in-field work. First, the pin connecting the retraction/over-centre mechanism was identified as a critical element, as loss of this connection would remove structural support and could lead to collapse. Second, a practitioner's rule of thumb indicated that general-aviation operations may involve on the order of two towing activities per flight cycle (e.g., $\sim$2000 tows per 1000 flight cycles), implying comparatively high towing exposure compared to commercial aviation.

The observed towing behaviour exhibited some operator dependence. The tug operator available for the Rotterdam The Hague Airport session did not routinely handle general-aviation aircraft, which may have resulted in a comparatively cautious driving style. In addition, the operator indicated that recent operations were predominantly performed with the towbarless vehicle and that using the towbar configuration required a short re-familiarisation period. These factors introduce a plausible bias towards conservative manoeuvre execution, particularly for the towbar runs.

A further practical boundary condition observed during the test sequence was gradual battery depletion of the towing vehicle. The battery level decreased over the course of the session, accompanied by a perceived reduction in attainable top speed during the final run (the towbar run). While this may have affected the peak speed reached in that specific run, it was not expected to alter the qualitative conclusions of the in-field comparison, as the primary findings were based on the relative presence and magnitude of peaks and load features across repeated manoeuvres rather than on absolute top-speed capability in a single trial.

5.6. TB-to-TBL Reconstruction of the PC-12 Manoeuvres

This section reconstructs the PC-12 towbarless manoeuvre set from the two complementary WP1 datasets introduced in Section 5.4. The reconstruction combines the measured Charleroi PC-12 towbar force histories with the towbar–towbarless kinematic differences observed during the Rotterdam The Hague Airport campaign. To make this translation physically consistent, the section first establishes the nominal NWLG vertical reaction and the effective longitudinal towing-resistance coefficient. It then defines the TB$\rightarrow$TBL force-translation model, summarises the manoeuvre-specific corrections, and introduces the scaled reconstructed TBL signal set used for the downstream FEM and fatigue analyses.

Symbol summary and aircraft data

The following table, Table 5.5, summarises the symbols and parameters used in the kinematics analysis.

Table 5.5: Parameters used for kinematics analysis

m	aircraft mass
g	gravity
l_n, l_m	CG to nose/main lever arms
h_{cg}	CG height above ground
a_x, a_y	acceleration
δ	nose-wheel steer angle
C_{rr}	rolling-resistance coefficient
$F_{\text{tb},x}$	towbar axial at the NWLG pin

The aircraft weights, geometry and operational parameters used in the in-field tests are listed in Table 5.6.

Table 5.6: PC-12 NGX data sheet used during in-field testing

Parameter	Symbol	Value	Unit
Maximum Take-Off Weight	MTOW	46.5	kN
Current Weight	W	42.3	kN
Centre of Gravity location	x_{CG}	5.94	m
Centre of Gravity height	h_{CG}	≈ 1.1	m
Wheelbase (nose-main gear span)	L_{wb}	3.57	m
Nose-wheel landing gear longitudinal position	x_{NG}	2.83	m
Nose-wheel landing gear load fraction	λ_{NG}	12.7	%
Turning radius outside main gear (min)	R_{turn}	5.03	m

5.6.1. Reference NWLG Vertical Reaction for Load Reconstruction

The NWLG vertical reaction was estimated to define the nominal nose-wheel landing gear load fraction, which was used later when assigning aircraft-level inertial effects to the nose-wheel landing gear load path. The estimate considered the aircraft standing on level ground in static equilibrium. The main-gear reactions were treated as a single resultant acting at the mean main-gear axle station. For the PC-12 NGX, Pilatus lists a basic operating weight m_{BOW} and full usable fuel m_f of: [61]

$$m_{\text{BOW}} = 3086\,\text{kg}, \qquad m_f = 1227\,\text{kg},$$

hence the “empty + full fuel (no further payload)” mass was

$$m = m_{\text{BOW}} + m_f = 4313\,\text{kg}. \tag{5.8}$$

To obtain a representative longitudinal CG for the “basic aircraft + full fuel” condition, a published PC-12/47E weight-and-balance sheet was used for the basic aircraft mass and moment, and a fuel load moment chart was used for the fuel moment [62]. From the weight-and-balance sheet:

$$m_0 = 3031\,\text{kg}, \qquad M_0 = 18\,061\,\text{kg}\,\text{m}.$$

From the fuel-load moment chart (given in lb in), the fuel moment at 2704 lb was found by linear interpolation between 2600 and 2700 lb:

$$M_f(2704) = 628029 + (2704 - 2700)\frac{628029 - 604724}{2700 - 2600} = 628\,961\,\text{lb}\,\text{in}.$$

Using 1 lb in $= 0.45359237 \cdot 0.0254 = 0.011\,521\,246$ kg m, this is

$$M_f \approx 628961 \cdot 0.011521246 \approx 7.25 \times 10^3\,\text{kg}\,\text{m}.$$

Thus,

$$m_{\text{rep}} = m_0 + m_f \approx 4.26 \times 10^3\,\text{kg}, \qquad M_{\text{rep}} = M_0 + M_f \approx 2.53 \times 10^4\,\text{kg}\,\text{m}, \tag{5.9}$$

and the resulting CG station was

$$x_{\text{CG}} = \frac{M_{\text{rep}}}{m_{\text{rep}}} \approx 5.94\,\text{m}. \tag{5.10}$$

From the same weight-and-balance sheet, the distances from the reference line to the gear axles were

$$x_N = 2.83\,\text{m}, \qquad x_M = 6.39\,\text{m},$$

where x_M is the mean of left and right main-gear axle stations. Let R_N be the NWLG vertical reaction and $W = mg$ the aircraft weight. Static equilibrium yields

$$\frac{R_N}{W} = \frac{x_M - x_{\text{CG}}}{x_M - x_N} \tag{5.11}$$

where,

- R_N nose-wheel landing gear vertical reaction force [N]
- W aircraft weight, $W = mg$ [N]

- x_M main-gear station [m]
- x_N nose-wheel landing gear station [m]
- x_{CG} centre-of-gravity station [m]

so that

$$\frac{R_N}{W} \approx 0.127 \quad \Rightarrow \quad \text{NWLG share} \approx 12.7\,\%. \tag{5.12}$$

Reporting the NWLG reaction as:

$$R_N = mg\frac{x_M - x_{\text{CG}}}{x_M - x_N} \approx 4313 \cdot 9.80665 \cdot 0.127 \approx 5.37\,\text{kN}. \tag{5.13}$$

Vertical load transfer

Longitudinal acceleration redistributes vertical load between nose and main gear through pitch equilibrium, as partially discussed in Subsection 2.4.2. With the centre of gravity at height h_{cg} above the ground, and longitudinal distances l_n and l_m from the CG to the nose and main gear contact points, the quasi-static vertical reactions were written as expressed in Equation 5.14:

$$F_{z,n}(t) \approx W\,\frac{l_m}{L} - m\,a_x(t)\,\frac{h_{\text{cg}}}{L}, \qquad F_{z,m}(t) = W - F_{z,n}(t), \tag{5.14}$$

where,

- $F_{z,n}(t)$ nose-wheel landing gear vertical reaction time history [N]
- $F_{z,m}(t)$ main-gear vertical reaction time history [N]
- W aircraft weight [N]
- m aircraft mass [kg]
- $a_x(t)$ longitudinal acceleration time history [m s^{-2}]
- h_{CG} centre-of-gravity height above ground [m]
- l_m CG-to-main-gear lever arm [m]
- L wheelbase ($L = l_n + l_m$) [m]

Using the measured weight $W = 42.3\,\text{kN}$ and the nominal nose-wheel landing gear fraction $\lambda_{\text{NG}} = 12.7\,\%$, the quasi-static nose reaction is $F_{z,n,0} \approx \lambda_{\text{NG}}W \approx 5.37\,\text{kN}$. The acceleration-induced variation about this level follows directly from the second term in Equation 5.14:

$$\Delta F_{z,n} \approx m\,a_x\,\frac{h_{\text{CG}}}{L_{wb}} \;=\; W\,\frac{a_x}{g}\,\frac{h_{\text{CG}}}{L_{wb}}. \tag{5.15}$$

With $h_{\text{CG}} \approx 1.1\,\text{m}$ and $L_{wb} = 3.57\,\text{m}$, the fractional load transfer is $\Delta F_{z,n}/W \approx (a_x/g)\,(h_{\text{CG}}/L_{wb}) \approx 0.308\,(a_x/g)$. Even with a conservative upper-bound towing acceleration of $a_x = 1\,\text{m/s}^2$, this gives $\Delta F_{z,n} \approx 1.33\,\text{kN}$ (about $3.1\,\%$ of W). For more typical towing accelerations below $1\,\text{m/s}^2$, the corresponding variation is smaller (order $0.4 - 0.7\,\text{kN}$ for $a_x = 0.3 - 0.5\,\text{m/s}^2$).

In the context of this work, the fatigue-relevant stress ranges are governed primarily by the measured longitudinal towing/braking and turning-related loads that drive the local load path. The quasi-static vertical redistribution mainly modulates strut compression and is treated as a second-order effect for the initiation analysis. Accordingly, vertical load transfer is not propagated explicitly in the fatigue accounting, and the nose-wheel landing gear vertical reaction is approximated using the nominal fraction $\lambda_{\text{NG}}W$.

Even if longitudinal load transfer redistributes the vertical reactions between nose and main gear, the total rolling resistance is unchanged to first order if a common rolling resistance coefficient C_{rr} is assumed for all wheels:

$$F_{\text{rr}} = \sum_{i=1}^{n} C_{rr}F_{z,i} = C_{rr}\sum_{i=1}^{n} F_{z,i} = C_{rr}W. \tag{5.16}$$

In reality, C_{rr} may differ slightly between nose-wheel and main landing gear (pressure, condition, surface), so small deviations are possible, but quantifying this is beyond the present scope. Since the objective was a relative TB–TBL comparison under comparable conditions, $F_{\text{rr}} \approx C_{rr}W$ was retained, and load-transfer effects on total rolling drag were neglected.

5.6.2. Effective Longitudinal Towing-Resistance Estimation

At the low speeds involved in towing, the longitudinal resistance is represented here by a single effective coefficient:

$$F_{\text{long,res}}(t) = C_{\text{tow,eff}}\,W, \tag{5.17}$$

where,

- $F_{\text{long,res}}(t)$ effective longitudinal resistance force time history [N]
- $C_{\text{tow,eff}}$ effective longitudinal towing-resistance ratio [-]
- W aircraft weight [N]

The coefficient $C_{\text{tow,eff}}$ is not interpreted as a pure tyre rolling-resistance coefficient C_{rr}. Instead, it is used as a lumped parameter representing the overall low-speed longitudinal resistance under the tested towing conditions and serves as the effective longitudinal resistance parameter used throughout the remainder of the analysis. As such, it may include contributions from rolling resistance, tyre deformation, local scrub, bearing losses, residual brake drag, and other quasi-static resistance effects.

During testing, a slight slope was present along the towing path. This incline introduces an offset between pull and push efforts, for which towing uphill requires a slightly higher force than towing downhill. To correct for this, two quasi-steady manoeuvres were selected: a straight pull into the slope and a straight push back along the same path. Their average longitudinal forces were then compared. The measured towbar force during the pull was consistently higher than during the push, as shown in the side-by-side plots in Figure 5.28.

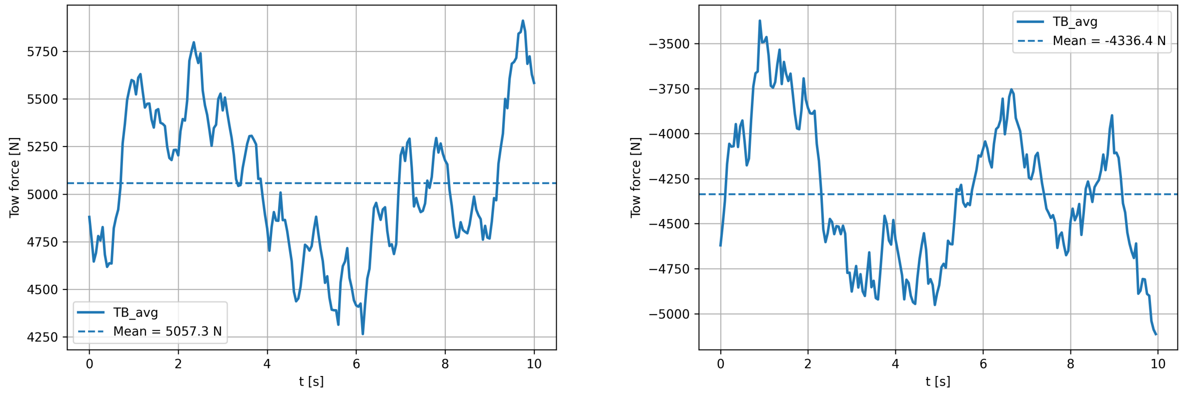

Steady pull (upslope)

Steady push (downslope)

Figure 5.28: Towbar force comparison for steady pull and push on a slight slope

From this offset, the contribution of the slope to the towing force could be estimated and removed. The corrected pull and push forces then yielded a common estimate of the effective longitudinal resistance:

$$F_{\text{long,res,corrected}} = \frac{F_{\text{pull}} + F_{\text{push}}}{2} = \frac{5057 + 4336}{2} \approx 4.7\ \text{kN} \tag{5.18}$$

Using the known aircraft weight W, the corresponding effective coefficient became

$$C_{\text{tow,eff}} = \frac{F_{\text{long,res,corrected}}}{W} = \frac{4700}{4313 \cdot 9.80665} \approx 0.11 \tag{5.19}$$

This value was adopted for the remainder of the analysis to reconstruct low-speed longitudinal tow loads. It should therefore be interpreted as a measured effective towing-resistance ratio for the tested aircraft, surface, tyre state, and operational conditions, rather than as a universal nominal value of tyre rolling resistance.

This interpretation is consistent with aircraft ground-handling practice, where towing demand is affected by more than rolling resistance alone. ISO 7717 explicitly treats aircraft breakaway resistance, grade resistance, and acceleration-related resistance as separate contributors in the establishment of towing performance requirements [63]. In addition, EASA RuFAB documentation reports that rolling friction on paved surfaces correlates with inflation pressure, vertical load, and speed [64]. During the present tests, noticeable tyre deformation was observed, which may indicate suboptimal inflation pressure, possibly due to the high fuel load, and thus could contribute to an elevated effective towing-resistance ratio.

Towing vehicles also indicate the required towing forces. For example, Goldhofer specifies the SHERPA D8 with a drawbar pull of $10{,}100$ lbf for aircraft up to $110{,}000$ lb MTOW, corresponding to 0.092 [65]. Similarly, BL Advanced Ground Support Systems specifies the ATT-2 towbarless tug with a drawbar pull of $6{,}500$ kg for aircraft up to $40{,}000$ kg, corresponding to 0.163 [66]. The value adopted here should therefore be regarded as a conservative, test-specific longitudinal resistance parameter.

Assuming that the only difference between the steady pull and push is the component of the aircraft's weight along the slope, the tow forces can be written as

$$F_{\text{pull}} = F_{\text{rr}} + W \sin\theta, \tag{5.20}$$

$$F_{\text{push}} = F_{\text{rr}} - W \sin\theta, \tag{5.21}$$

where,

- F_{pull} towing force required during uphill pulling [N]
- F_{push} towing force required during downhill pushing [N]
- F_{rr} rolling-resistance force [N]
- W aircraft weight [N]
- θ ground slope angle [rad]

Moreover, θ is positive when pulling uphill. Subtracting these two relations gives

$$F_{\text{pull}} - F_{\text{push}} = 2W \sin\theta, \tag{5.22}$$

so that

$$\sin\theta = \frac{F_{\text{pull}} - F_{\text{push}}}{2W} = \frac{5057 - 4336}{2 \cdot 4313 \cdot 9.80665} \approx 8.5 \times 10^{-3}. \tag{5.23}$$

This corresponds to a slope angle

$$\theta \approx \arcsin(8.5 \times 10^{-3}) \approx 0.49^\circ, \tag{5.24}$$

Even such a small longitudinal gradient already introduces a weight component.

$$W \sin\theta \approx W\,\theta = 4313 \cdot 9.80665 \cdot \frac{\pi}{180} \approx 0.74 \text{ kN} \approx 1.7\%\, W \text{ per degree.} \tag{5.25}$$

This means that each degree of slope adds roughly 1.7% of the aircraft weight as an additional towing force component, which is of the same order as the quasi-steady towing force level in the steady-pull/push case, and therefore cannot be neglected in the analysis.

Moreover, as discussed in Chapter 2, the surface condition also influences the rolling resistance and, consequently, the loads transmitted to the towbar and landing gear. While the differences between dry, wet, and icy paved surfaces appear modest in terms of the effective loads measured during towing, rough and deformable surfaces such as gravel or wet grass can lead to significantly higher C_{rr} values and thus towing forces. For general-aviation aircraft, which operate from remote or unpaved airfields far more frequently than commercial transport aircraft, such surface effects can therefore be an important contributor to the towing loads.

5.6.3. TB-to-TBL Force Translation

A first-order method was defined to translate towbar tow-force demand into a towbarless estimate using the measured kinematics and manoeuvre accelerations. The method is intentionally conservative and transparent: tyre scrub losses are neglected in the baseline translation, and differences between TB and TBL were introduced through measured differences in acceleration and turning severity, as observed in the Rotterdam The Hague Airport dataset (Section 5.5). The translation is based on the following assumptions for low-speed, controlled towing:

1. **No scrub in the baseline force translation:** turning-related tyre scrub is neglected in the tow-force estimate; its influence is treated separately through turning-severity metrics.
2. **Aircraft-level force balance:** the towing force acts primarily in the horizontal plane and is approximated along the direction of travel.
3. **Low-frequency accelerations only:** manoeuvre accelerations are used for force estimation; high-frequency residual accelerations (vibration) were analysed separately and not mapped into the tow-force estimate.

Longitudinal force model

The longitudinal towing force along the direction of travel is approximated as

$$F_{\text{tow}}(t) \approx F_{\text{steady}} + m\, a_t(t), \tag{5.26}$$

where,

- $F_{\text{tow}}(t)$ towing force along the travel direction [N]
- F_{steady} steady towing force required for constant-speed towing [N]
- m aircraft mass state during towing [kg]
- $a_t(t)$ low-frequency longitudinal acceleration of the aircraft along the travel direction [m/s^2]

For a given manoeuvre, the TB and TBL force estimates become

$$F_{\text{tow}}^{\text{TB}}(t) \approx F_{\text{steady}} + m\, a_t^{\text{TB}}(t), \qquad F_{\text{tow}}^{\text{TBL}}(t) \approx F_{\text{steady}} + m\, a_t^{\text{TBL}}(t), \tag{5.27}$$

and the incremental difference per manoeuvre is

$$\Delta F_{\text{acc}}(t) = F_{\text{tow}}^{\text{TBL}}(t) - F_{\text{tow}}^{\text{TB}}(t) \approx m\left(a_t^{\text{TBL}}(t) - a_t^{\text{TB}}(t)\right). \tag{5.28}$$

An example calculation is given below. Consider an aircraft with mass $m = 4313$ kg and a steady towing force $F_{\text{steady}} = 4697$ N (constant-speed pull). Using Eq. (5.26):

- TB acceleration case: for $a_t = 0.2$ m/s^2,

  $$\Delta F_{\text{acc}} = m a_t = 4313 \times 0.2 = 862.6\,\text{N} \tag{5.29}$$

  thus,

  $$F_{\text{tow}} \approx 4697 + 862.6 = 5560\,\text{N} \quad \text{(rounded)}$$

- TBL acceleration case: for $a_t = 0.5$ m/s^2,

  $$\Delta F_{\text{acc}} = m a_t = 4313 \times 0.5 = 2157\,\text{N}$$

  thus,

  $$F_{\text{tow}} \approx 4697 + 2157 = 6854\,\text{N} \quad \text{(rounded)}$$

The difference between these two acceleration demands is:

$$\Delta F = 4313\,(0.5 - 0.2) \approx 1.3\,\text{kN}, \tag{5.30}$$

Thus, approximately 1.3 kN higher towing force during the higher-acceleration TBL case, relative to the lower-acceleration TB case, for the same assumed steady-force baseline F_{steady}.

Lateral kinematics comparison

Turning is characterised using the low-frequency lateral acceleration of the aircraft, denoted $a_n(t)$ [m/s^2]. In this first-order method, turning is not mapped into an additional force term. Instead, TB and TBL manoeuvres are compared directly based on their measured lateral acceleration histories, using

$$\Delta a_n(t) = a_n^{\text{TBL}}(t) - a_n^{\text{TB}}(t) \tag{5.31}$$

Observed TB vs. TBL differences

Based on Section 5.5, the following qualitative differences are relevant when interpreting the per-manoeuvre force translation:

- **Acceleration/braking severity:** the TBL runs exhibited clearer and larger low-frequency braking events than the TB run, consistent with more continuous motion and a distinct stop/turn event. This directly increases the inertial term $m a_t(t)$ in Eq. (5.26).
- **Turning severity:** the TBL runs showed larger lateral manoeuvre acceleration peaks during turning, consistent with executing the full turn at higher speed and with fewer interruptions. This is captured through $\Delta a_n(t)$, and is reported separately from the baseline force estimate.
- **Vibration/impulsiveness:** TB showed stronger signatures consistent with interface play (notably during push/pull transitions), whereas TBL showed more continuous behaviour. These effects are treated as vibration/impulsiveness metrics and are not included in the force translation.

5.6.4. Overview of Manoeuvre-Level Translation Treatment

Table 5.7 summarises, for each canonical towing manoeuvre (`EventCode`), the main qualitative TB versus TBL differences observed in the in-field data, and states how each difference is handled in the baseline TB→TBL force translation model (Section 5.6.3). The resulting translated force histories and the corresponding load spectra used for subsequent analysis are presented in Section 5.7.

Table 5.7: Summary of TB vs. TBL differences per manoeuvre and applied correction in the TB→TBL force translation

`EventCode`	Observed TB vs. TBL difference	Treatment in TB→TBL translation	Applied correction
`SP_STEADY_PULL`	Typically similar steady behaviour; different speeds measured, mainly operator-dependent	No systematic correction. Use $F_{\text{TB\_steady\_pull}}$ as baseline.	–
`SP_STEADY_PUSH`	TB push often constrained (scissoring risk); TBL typically more continuous	No change to $F_{\text{TB\_steady\_push}}$. Push time is minimised for the TB case.	–
`ACC_PULL_SMOOTH`	TBL exhibits higher $\lvert a_t\rvert$ and smoother profile	Apply inertial correction (Eq. (5.28)).	$\Delta a_t = +0.2$ m/s^2
`BRK_PULL_SMOOTH`	TBL shows clearer braking event; TB more stop–start/irregular and less deceleration due to scissor risk	Apply inertial correction.	$\Delta a_t = -0.5$ m/s^2
`ACC_PUSH_SMOOTH`	TB push is typically less stable; TBL can accelerate more consistently, mainly operator-dependent	Same correction used as in `ACC_PULL_SMOOTH`.	$\Delta a_t = +0.2$ m/s^2
`BRK_PUSH_SMOOTH`	TBL may brake more decisively; TB includes additional jerkiness from interface play	No inertial correction due to low speeds and no scissor risk; mainly operator-dependent.	–
`TURN_PULL_TIGHT`	No direct differences measured; tighter turns are possible for TBL towing	No correction.	–
`TURN_PUSH_TIGHT`	No direct differences measured; TB performed slower; tighter turns possible for TBL towing	No correction.	–
`TURN_PULL_WIDE`	TBL often turns at a higher speed	Baseline: no extra force term. Report turning severity via Δa_n.	$\Delta a_n = +0.2$ m/s^2
`TURN_PUSH_WIDE`	TB push turn not clearly observed, while TBL is similar to the `TURN_PULL_TIGHT` case	Conservative turning-severity correction via Δa_n.	$\Delta a_n = +0.35$ m/s^2
`BRK_PULL_RAPID`	TBL tends to show a larger peak braking magnitude; TB runs are hazardous if not aligned with the tug/towbar	Apply inertial correction using peak/percentile.	$\Delta a_t = -0.5$ m/s^2
`BRK_PUSH_RAPID`	A corresponding TB case was unlikely to occur due to low TB push speeds	No correction; `BRK_PUSH_SMOOTH` is used for the TB case.	–

TB to TBL scaled reconstruction with inertial correction

The `TBL_scl` signal set was constructed directly from the measured TB time histories by superimposing manoeuvre-specific inertial differences between TB and TBL via prescribed acceleration increments Δa_t (tangential) and Δa_n (normal/lateral). The inertial correction was applied only within predefined time windows to adjust peak dynamic content without altering the window endpoints. Within each window, the force signal was decomposed into a linear baseline $L(t)$ connecting the endpoint values and a dynamic remainder $D(t) = F(t) - L(t)$, which was zero at the boundaries by construction. The correction was then imposed by scaling the dynamic remainder,

$$D_{\text{new}}(t) = \big(1 + k\big)\, D(t), \qquad k = \frac{m\,\Delta a}{\max_{t\in\text{window}} \lvert D(t)\rvert}, \tag{5.32}$$

where,

- $D_{\text{new}}(t)$ corrected dynamic remainder within the selected window [N]
- $D(t)$ original dynamic remainder [N]
- k dimensionless scaling factor applied to the dynamic remainder $[-]$
- m effective mass associated with the inertial correction [kg]
- Δa prescribed acceleration increment for the considered correction direction $[\text{m/s}^2]$
- $\max_{t\in\text{window}} |D(t)|$ maximum absolute dynamic remainder within the selected window [N]

and reconstructing $F_{\text{new}}(t) = L(t) + D_{\text{new}}(t)$, where,

- $F_{\text{new}}(t)$ corrected reconstructed force time history [N]
- $L(t)$ linear baseline connecting the window endpoint values [N]

For longitudinal adjustments, Δa_t acted on the towing (clamp) force. Lateral adjustments used Δa_n in the same baseline–dynamic formulation for the lateral NWLG reaction; in the current implementation, this correction was weighted by the assumed nose-wheel landing gear load fraction to reflect that only a portion of the aircraft inertia was reacted at the NWLG.

- Δa_t prescribed tangential acceleration increment $[\text{m/s}^2]$
- Δa_n prescribed normal/lateral acceleration increment $[\text{m/s}^2]$

5.7. Canonical WP1 Load Spectra and Output to WP2

This section presents the canonical TB manoeuvre spectra used in WP2 together with their reconstructed TBL counterparts. Measured manoeuvres are presented first, followed by manoeuvres estimated from related measured cases.

5.7.1. Measured Manoeuvres

Before presenting the load spectra, a brief note on signal processing is warranted. To account for minor timebase irregularities in the Raspberry Pi logging system (as seen in Figure 5.14), a moving average filter was applied to the raw data. Based on calibration results, a 9-point window was selected, corresponding to approximately 0.56 s at the nominal sampling rate of 16.2 Hz. This filter balances the suppression of high-frequency fluctuations caused by mechanical tolerances and logging jitter while preserving key features, such as abrupt changes in load.

For each manoeuvre below, the TB and TBL spectra are presented as overlaid traces in a single figure to enable direct visual comparison on the same axes. The TB loads are taken directly from the measured Charleroi instrumented-towbar dataset, whereas the TBL loads are reconstructed by applying Rotterdam-derived TB–TBL correction terms to the measured PC-12 TB baseline. For the turning manoeuvres, two plots are shown (longitudinal and lateral) because these events exhibit coupled loading.

Straight pull at constant speed (`SP_STEADY_PULL`)

Figure 5.29 shows the measured load spectra for the towbar and towbarless configurations during straight pull at constant speed. The manoeuvre curve is mean-shifted to the absolute mean over the push–pull overlap window and plotted with a positive sign. Because the TB and TBL spectra were treated as identical for this manoeuvre, the plotted curves coincide.

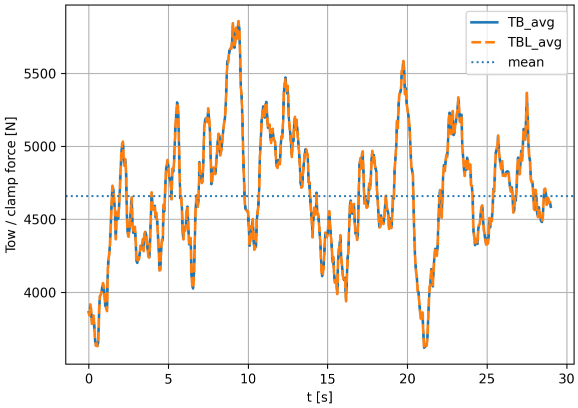

Figure 5.29: Measured TB and reconstructed TBL load spectra for straight pull at constant speed (TB and TBL considered identical)

Straight push at constant speed (`SP_STEADY_PUSH`)

Figure 5.30 depicts the measured spectra during straight push at constant speed for both towing methods. The manoeuvre curve is mean-shifted to the absolute mean over the push–pull overlap window and plotted with a negative sign. As the TB and TBL spectra were considered identical for this manoeuvre, the two curves overlap.

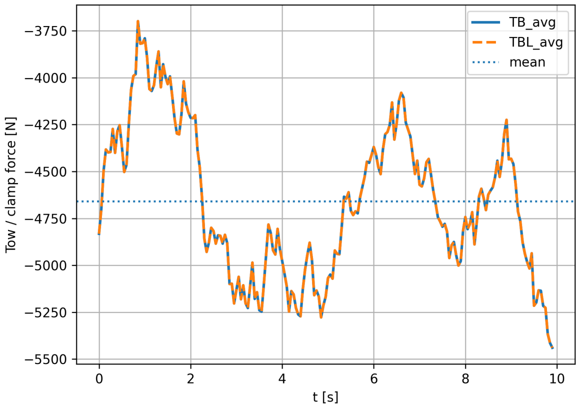

Figure 5.30: Measured TB and reconstructed TBL load spectra for straight push at constant speed (TB and TBL considered identical)

Smooth pull acceleration (`ACC_PULL_SMOOTH`)

During smooth forward acceleration in pull, the NWLG undergoes increasing tensile force. Figure 5.31 compares the measured spectra under both configurations.

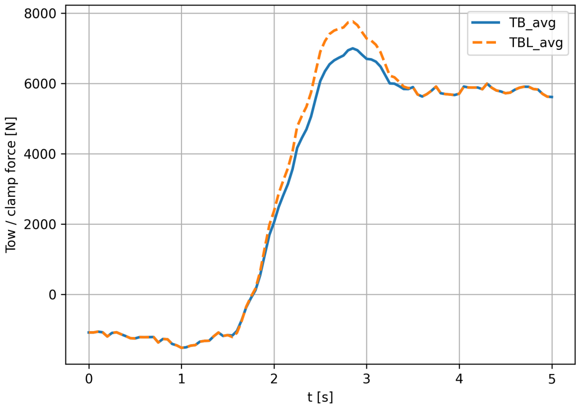

Figure 5.31: Measured TB and reconstructed TBL load spectra for smooth pull acceleration (TB and TBL overlaid)

Smooth pull braking (`BRK_PULL_SMOOTH`)

In braking while pulling, the NWLG transitions from tensile to compressive loading. Figure 5.32 compares the measured spectra.

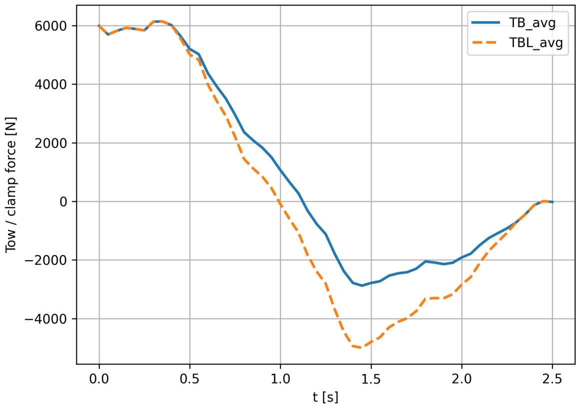

Figure 5.32: Measured TB and reconstructed TBL load spectra for smooth pull braking (TB and TBL overlaid)

Smooth push acceleration (`ACC_PUSH_SMOOTH`)

The spectra in Figure 5.33 reflect compressive loading during smooth push acceleration under both towing concepts.

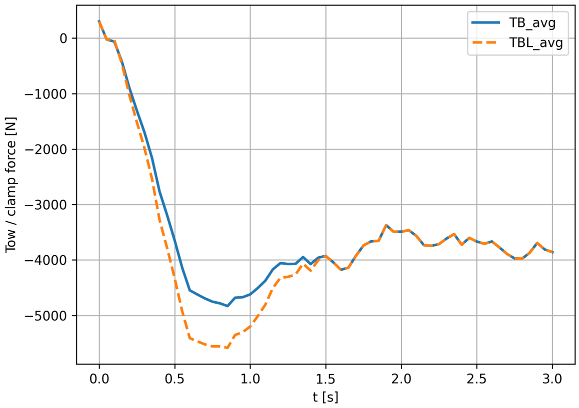

Figure 5.33: Measured TB and reconstructed TBL load spectra for smooth push acceleration (TB and TBL overlaid)

Smooth push braking (`BRK_PUSH_SMOOTH`)

Compressive braking under push is shown in Figure 5.34, based on measured manoeuvre data.

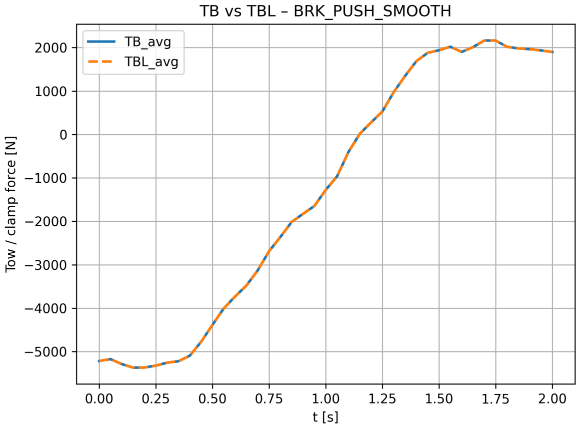

Figure 5.34: Measured TB and reconstructed TBL load spectra for smooth push braking (TB and TBL considered identical)

Tight-radius pull turns (`TURN_PULL_TIGHT`)

Tight-radius pull turns induce combined longitudinal and lateral loading at the NWLG. To preserve interpretability, the comparison is shown using separated longitudinal and lateral spectra in Figure 5.35a and Figure 5.35b, respectively. For tight turns, the steering angle is assumed to decrease from $45°$ to $0°$.

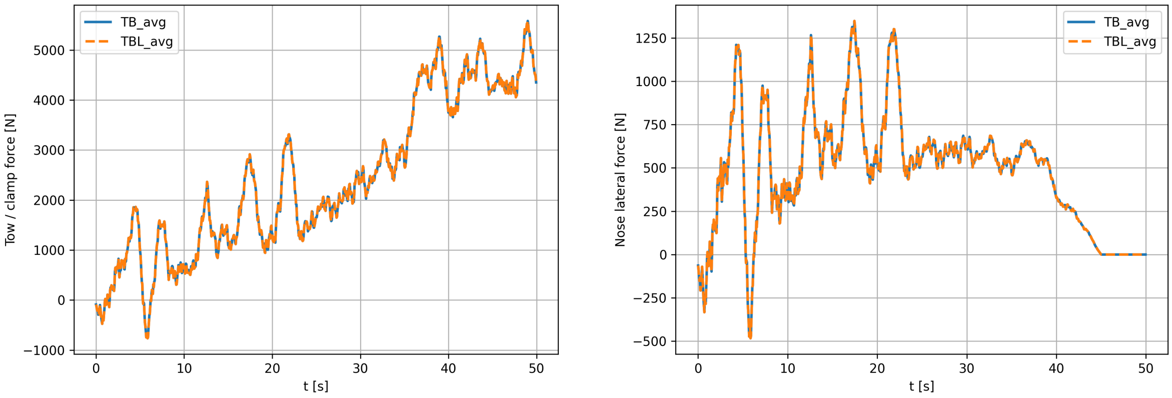

(a) Longitudinal **(b)** Lateral

Figure 5.35: Measured TB and reconstructed TBL load spectra for tight-radius pull turn (TB and TBL considered identical)

Controlled pull rapid tug brake input (`BRK_PULL_RAPID`)

An abrupt braking action during pulling generates a compressive spike, as shown in Figure 5.36.

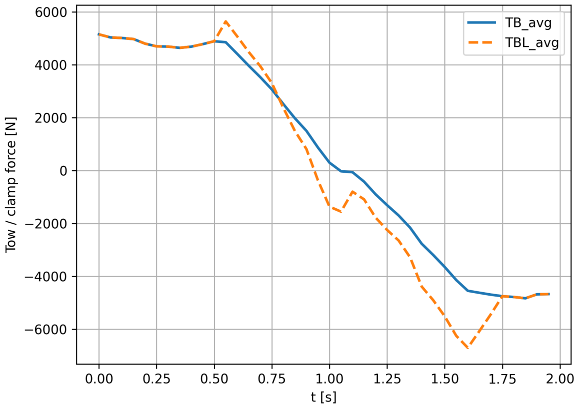

Figure 5.36: Measured TB and reconstructed TBL load spectra for controlled rapid brake input in pull (TB and TBL overlaid)

5.7.2. Estimated Manoeuvres

The following manoeuvres were not executed during the test campaign. Instead, representative load spectra were estimated from analogous measured events, applying conservative assumptions where appropriate to ensure reliable fatigue assessment.

Tight-radius push turns (`TURN_PUSH_TIGHT`)

The `TURN_PUSH_TIGHT` load history was not measured directly, but estimated to be identical to the measured tight-radius pull turn (Figure 5.35) in terms of time history and absolute load levels. To convert the pull case to a push case under the adopted sign convention, both the longitudinal and lateral force components were sign-flipped, $F_x^{\text{push}}(t) = -F_x^{\text{pull}}(t)$ and $F_y^{\text{push}}(t) = -F_y^{\text{pull}}(t)$. This preserves the manoeuvre severity while representing the reversed direction of operation.

Wide-radius pull turns (`TURN_PULL_WIDE`)

Spectra for wide-radius pull turns were obtained by scaling down the lateral loads from tight-radius pull turns to reflect reduced turning severity, while maintaining axial load features. For wide turns, the steering angle is assumed to decrease from $20°$ to $0°$. In addition, a speed-scaling assumption is applied. A higher speed yields smoother (less jerky) longitudinal and lateral force histories, and the manoeuvre duration is correspondingly shorter. The impact of lateral loading on the derived spectra is expected to be limited, as the nose-wheel landing gear carries only 12.7% of the aircraft weight, reducing the effective contribution of lateral forces relative to the primary longitudinal towing/braking content. The resulting spectra can be seen in Figure 5.37

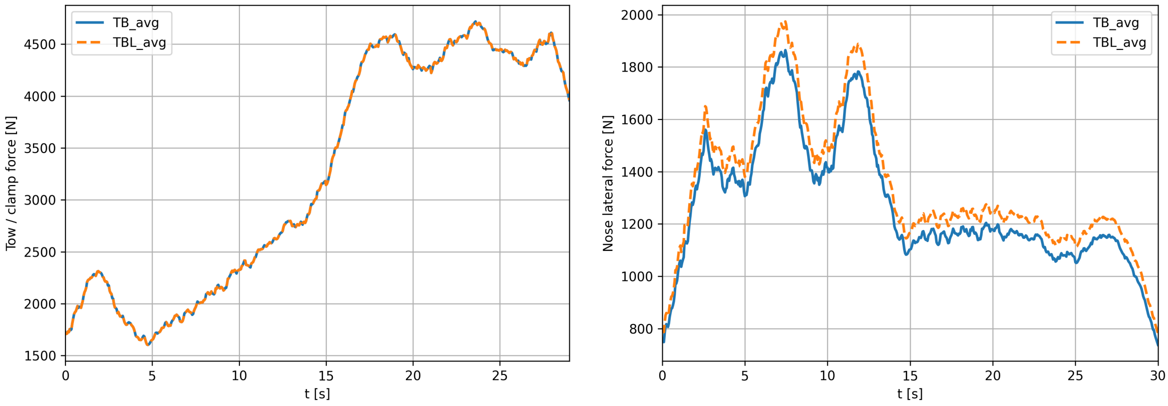

(a) Longitudinal

(b) Lateral

Figure 5.37: Estimated spectra for wide-radius pull turn (TB and TBL overlaid)

Wide-radius push turns (`TURN_PUSH_WIDE`)

The `TURN_PUSH_WIDE` load history was derived from the estimated wide-radius pull turn (Figure 5.37) by sign-flipping the longitudinal and lateral force components. Although the underlying manoeuvre template is the same, the resulting TB and TBL estimates are not strictly identical in magnitude, because the TBL case applies a slightly higher scaling to reflect towbarless-specific characteristics. The corresponding estimated spectra are therefore shown explicitly in Figure 5.38.

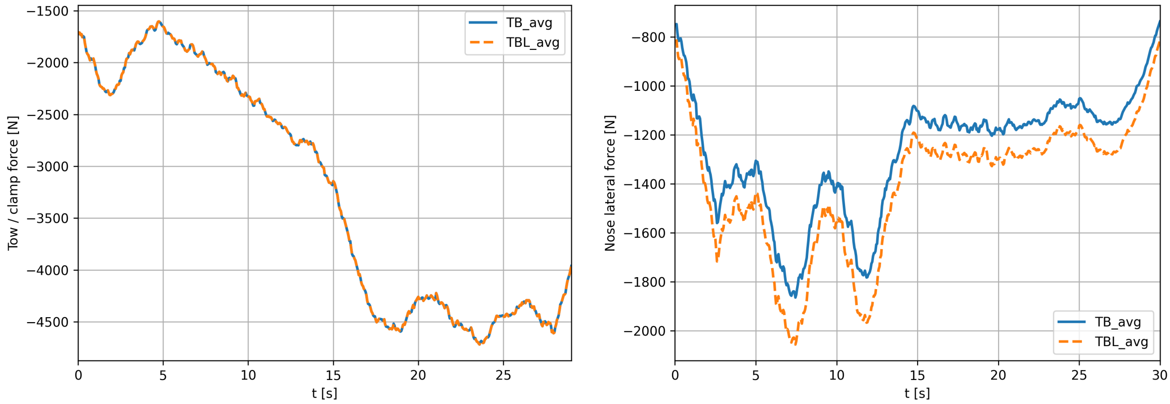

(a) Longitudinal

(b) Lateral

Figure 5.38: Estimated spectra for wide-radius push turn (TB and TBL overlaid)

Controlled push rapid tug brake input (`BRK_PUSH_RAPID`)

This case was treated as equivalent to the smooth push braking case (Figure 5.34). Given the low push speeds during towing, a distinct rapid braking event was not expected in practice; consequently, `BRK_PUSH_RAPID` was assumed to have the same load history as the smooth braking manoeuvre.

5.7.3. Further Notes from In-Field Testing

To complement the literature discussed in this chapter, informal interviews were conducted with several maintenance professionals active in the general-aviation sector. The observations reported below are not treated as quantitative evidence. Rather, they provide context that helps motivate specific modelling and inspection considerations addressed in later chapters.

Fatigue indications and inspection constraints. It was reported that, on certain Cessna Citation models, fatigue indications in the drag brace are encountered with some regularity. The interviewee was unable to specify the exact variants. However, the issue was associated with a configuration featuring a forward-folding NWLG with an aft-mounted drag brace, which is seen on the 680A model[1].

A particular area of concern was the lug-and-pin region connecting the strut barrel lugs to the drag brace. The inspection challenge arises from limited visual access. Several critical surfaces are partially obscured in the assembled condition and become fully inspectable only when the connecting pin is removed. In practice, pin removal requires unloading the NWLG (the aircraft must not be resting on the nose-wheel landing gear), which is not typically performed during routine line maintenance.

Operation manual notes It is noted that the following operational points are derived from the towing manual of an undisclosed GA aircraft type. The manual states that, during towing, the nose-wheel landing gear should be raised no more than 100 mm above the tarmac, indicating a relatively limited geometric margin during lifting and manoeuvring. In addition, the manual specifies a maximum allowable mass for the towbarless towing vehicle, prohibits the use of aircraft brakes during towing, and recommends that towing operations be conducted with a team of five personnel. These instructions indicate that towing is treated operationally as a constrained and carefully managed procedure, particularly for towbarless handling, and further show that aircraft manufacturers themselves recognise the importance of strict operational limits and procedural control during towing manoeuvres.

Towbarless tug interaction and manoeuvre characteristics. Finally, observations were noted regarding the TBL tug used during the reported operations at Charleroi Airport. The specific tug employed was capable of rotating the aircraft tie-down clamps during manoeuvring. As a result, no

---

[1] Source: `https://www.aircraftrecognitionguide.com/cessna-680a-citation-latitude`

appreciable steering angle was imposed on the NWLG. Instead, the tug primarily introduced a lateral load into the gear. This behaviour differs from many TBL systems that clamp the wheel directly, thereby enforcing a steering angle at the NWLG during turning manoeuvres. In addition, a qualitative asymmetry in manoeuvring capability was reported. The tug was observed to operate at noticeably higher speed in a forward (pull) manoeuvre than in a backwards (push) manoeuvre.

Overall, WP1 established the empirical loading basis for the remainder of the thesis. Despite the practical constraints of in-field testing and the limited possibility of direct towbarless force measurement, the campaign provided a calibrated towbar force channel, representative manoeuvre-resolved kinematic data, and a consistent route to reconstruct towbarless loading histories from the measured towbar baseline. These results enabled the definition of a set of representative TB and TBL manoeuvre spectra that captured the dominant longitudinal, braking, and turning characteristics relevant to towing-induced fatigue. The chapter, therefore, translated real towing practice into analysis-ready loading input, which forms the basis for the structural hotspot assessment in WP2 and the fatigue-spectrum implementation in WP3.

6

WP2 – Finite-Element Model Analysis

The finite-element modelling framework developed in WP2 translated the towing loads obtained in WP1 (Chapter 5) into fatigue-relevant stresses in the nose-wheel landing gear and, subsequently, into specimen-level loading for the laboratory programme of WP3 (Chapter 7). A staged global–local–specimen approach was adopted for this purpose.

Section 6.1 first introduces the overall WP2 methodology and modelling strategy. Section 6.2 then presents the global NWLG model, including the structural idealisation, applied towing loads, and hotspot screening used to identify the governing fatigue-critical regions. Section 6.3 subsequently develops the refined local submodel of the critical drag-brace region, enabling more detailed stress resolution and evaluation of the relevant hotspot response. Finally, Section 6.4 defines the translation from the local drag-brace response to an equivalent uniaxial loading of the laboratory dog-bone specimen, thereby establishing the link between the FEM results and the fatigue tests discussed in the following chapter.

6.1. WP2 – Methodology

WP2 followed a staged global–local–specimen finite-element approach. The purpose of this approach was first to represent the main towing load paths in the full landing-gear assembly, then to resolve the governing hotspot with higher local fidelity, and finally to transfer that hotspot response into a laboratory-relevant uniaxial specimen loading.

A single global NWLG model was constructed to represent the primary structural load path under towing. The model included the outer and inner strut, crown/fork, axle, torque links, steering collar, and the trunnion/drag-brace assembly. A representative reference configuration used for sizing and geometric idealisation is shown in Figure 6.1. Jointed connections were idealised using contact pairs and/or connector elements, with rotational compliance introduced where needed to represent the effective stiffness of the real assembly. Local refinement was applied at known stress raisers, including fork-crown transitions, axle fillets, torque-link lugs and pins, and drag-brace lugs. The trunnion/drag-brace assembly was connected to a fuselage proxy via boundary conditions that represent the aircraft-side support.

(a) Front view **(b)** Side view

Figure 6.1: NWLG reference for FEM analysis

The loading applied in WP2 was taken directly from WP1. For towbar manoeuvres, the measured longitudinal force history was applied at the tow-point representation in the global model. For towbarless manoeuvres, the towbar interface was absent, and the reconstructed interface load was instead introduced at wheel–axle height, consistent with the towbarless configuration considered in WP1. Tyre–ground interaction was represented by equivalent reactions at the axle according to the manoeuvre considered. Stress recovery was performed using linear-elastic material properties, with Young's modulus E and Poisson's ratio ν taken from certified material data and authoritative literature values.

Staged Global–Local–Specimen Workflow

Stage G — Global NWLG model The global model was used to replay the towing manoeuvres and to identify the governing fatigue-critical regions under comparable loading conditions. For each manoeuvre, stresses were extracted at predefined hotspot sets, including the drag brace, torque links, crown lugs, and fork–crown transitions, using consistent averaging and path definitions. These outputs were condensed into manoeuvre-wise hotspot metrics, which enabled a ranked comparison of candidate fatigue-critical locations and events.

Stage L — Local hotspot model Based on the Stage G ranking, a refined local model was built around the governing hotspot to resolve geometric details, local contact conditions, and stress gradients that were not efficiently captured by the global model. Representative loading was transferred from the global model to the local model by extracting the interface wrench, i.e. the resultant forces and moments, at a defined cut or interface in the global assembly and reapplying it to matching reference-point definitions in the local model while keeping the upper boundary conditions consistent. This global-to-local transfer yielded detailed hotspot stress histories for the governing manoeuvres, from which stress extrema, ranges, and relative severity could be evaluated.

Stage S — Specimen equivalence Finally, the local hotspot response was translated into an equivalent uniaxial loading for the dog-bone specimen used in Chapter 7. The baseline equivalence rule was to match the hotspot-driving σ_1 quantity to the nominal specimen stress under axial loading. This yielded manoeuvre-specific transfer factors from aircraft-interface tow force to specimen force, which were then applied to the measured time histories from WP1 to construct an equivalent specimen spectrum that preserved the relative amplitudes and sequencing of the original towing histories.

6.2. Stage G — Global NWLG Model

Stage G aimed to construct a global finite-element model of the nose-wheel landing gear that was sufficiently detailed to capture the main load paths and joint flexibility, yet efficient enough for systematic screening of towing load cases. Finite-element modelling is well established as a tool for resolving landing-gear load paths and identifying local fatigue-critical stress concentrations under complex ground-load cases. [67, 68]

The global NWLG assembly followed the layout shown in Figure 6.2a. The model included the oleo strut, the crown block, both fork legs, the wheel axle, the upper and lower torque links, the V-strut and V-brace members, and the towing lugs with their associated pins. Figure 2.1 shows a general layout of a general-aviation NWLG layout, including the names of the parts for reference.

Core FEM parameters

The NWLG geometry used in this work was an approximate representation of a Pilatus PC-24 NWLG. The model is not intended as a certified geometry reproduction; rather, it provides a consistent, physically plausible basis for load-path assessment and hotspot ranking within the scope of WP2. In Table B.1 of Section B.1, an overview of the key geometric and interface parameters is provided. These parameters were approximated from a 3D scan acquired using the Scaniverse application on an iPhone 15 Pro, as shown in Figure 6.2b. The scan provided a dimensionally consistent reference from which distances and lever arms were extracted for the Abaqus build and subsequent load application.

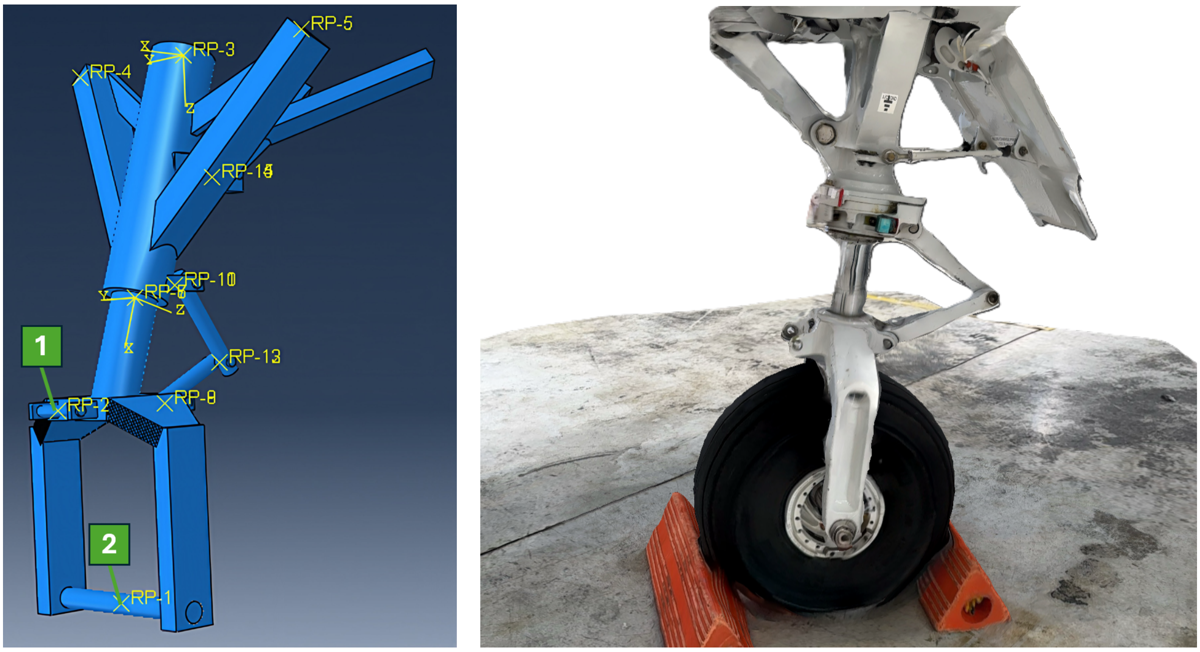

(a) Abaqus model NWLG

(b) Reference NWLG 3D scan

Figure 6.2: Visual comparison of reference NWLG to Abaqus model

The numbered callouts in Figure 6.2a identify the two principal load-introduction locations adopted in the FEM:

1. **Tow-lug application point:** location used for applying the TB loads, consistent with towbar load introduction through the towing pin.
2. **Axle application point:** location used for applying the TBL loads, with the axle used as a simplified representation of wheel-level load introduction.

The drag-brace arrangement in the Abaqus model was implemented as an aft-folding architecture. Based on the configuration overview presented in Section 2.5.3, Configuration C, with its additional lock strut and more complex attachment layout, is primarily representative of larger general-aviation and commuter-class aircraft and therefore lies near the upper end of the scope considered in this work. Configurations A and B, corresponding to aft- and forward-folding drag-brace layouts respectively, are more commonly encountered on light and medium GA nose-wheel landing gears. For the present study, Configuration A was selected as the representative reference geometry, particularly because it also supported the subsequent laboratory fatigue testing described in Chapter 7.

The laboratory programme relied on uniaxial loading of a dog-bone specimen, which favoured a drag-brace layout, with a clear translation from the component load path to the specimen stress state. The nearly straight load path and predominantly axial force transmission of the selected arrangement provided the most direct mapping between the structural component and the WP3 laboratory specimen, without introducing additional bending or multi-axial effects solely due to geometric differences. Moreover, this layout, or closely related variants, is widely used on GA aircraft such as the Pilatus PC-12, Beechcraft King Air 200, and Piper Arrow. It was therefore adopted as the reference drag-brace layout for the subsequent local modelling and specimen-equivalence steps.

Abaqus (finite-element modelling)

Abaqus/CAE was used to model the nose-wheel landing gear as a three-dimensional solid assembly. Boundary conditions were defined to allow compression along the oleo strut and rotation about the pin connections. The geometry was meshed with reduced-integration continuum elements, with local refinement at fillets and lug bores. Pins were idealised using kinematic couplings, while the fork–axle interfaces were modelled with surface-to-surface contact including friction.

The loading was taken directly from WP1. Longitudinal and lateral components were applied either at the tow-lug interface or through the wheel–ground interface, depending on whether towbar or towbarless loading was considered, with independent cases for braking and turning. Material properties corresponded to 300M steel for all components except the pins, which were modelled as 17-4PH (H900) stainless steel. Both materials were treated as linear elastic for the strain-transfer analysis; the corresponding material data are listed in Table 6.1.

Table 6.1: Core materials for global screening

Component	Material	E [GPa]	ν	σ_y [MPa]	σ_u [MPa]
Primary structure	300M steel[1,2]	205	0.29	≈ 1680	≈ 2030
Pins	17-4PH (H900)[3]	200	0.28	≈ 1250	≈ 1400

6.2.1. Boundary Conditions and Joints

The global NWLG model used idealised hinges, couplings, and connector constraints to reproduce the main kinematics and load paths without explicitly modelling all local contact interactions.

Fuselage-side supports. At the lower trunnion, a small patch of the barrel was rigidly coupled to a reference point and constrained as a local Z-axis hinge. Therefore, all translations and rotations were fixed except UR$_3$, which remained free. This reference point also served as the attachment location for the oleo spring acting in the Z-direction. The upper strut and V-strut tips were each rigidly coupled to their own reference points and hinged about global Y, such that all translations were fixed while UR$_2$ remained free. In contrast, the aft brace tips were fixed in translation and rotation to represent a stiff fuselage-side attachment.

Load introduction at axle and tow-pin. The axle and crown tow-pin were modelled as separate cylindrical solids whose lateral surfaces were tied to the corresponding bores in the fork legs and crown. External loads were applied through reference points coupled to these pin and axle surfaces. In practice, the towbar force may have a small vertical inclination due to height differences between the tug and NWLG. This effect mainly perturbs the vertical reaction and was therefore neglected in the present model, since it has little influence on the axial towing load and the resulting fatigue response. Effects associated with towing on slopes were treated separately in the in-field load analysis.

Oleo idealisation. The oleo was represented by friction patches on the barrel and piston, each coupled to its own reference point located on the common oleo axis. Equation constraints enforced cylindrical-joint-type behaviour by suppressing relative motion normal to the axis. At the same time, an axial two-point spring between the two reference points provided the oleo stiffness. The crown region was rigidly coupled to the piston-side reference point so that the crown, fork, and axle moved together with the piston in the axial direction.

Torque-link and brace pin joints. The torque-link and brace-pin joints were represented using the same generalised idealisation. For each pin, small patches on the lugs and bar eyes were coupled to two reference points on the joint axis. Equation constraints enforced equal translations and equal rotations UR$_1$ and UR$_3$, while leaving UR$_2$ free, thereby reproducing an ideal hinge about global Y. The solid pins were kinematically slaved to a reference point to ensure geometric continuity in the deformed configuration.

6.2.2. Load Spectrum Definition

This subsection defines the global towing load cases used in Stage G by translating the WP1 manoeuvre spectra into representative FEM force levels and by benchmarking their severity against conventional ground operations. To assess the relative severity of towing versus conventional operations, it is useful to compare the longitudinal forces transmitted through the drag brace during

1. landing roll and taxiing under own thrust, and
2. towbar / towbarless towing.

The comparison below is intentionally simplified and uses order-of-magnitude estimates suitable for guiding the FEM load cases and subsequent fatigue interpretation. For the present GA light-jet application, an aircraft mass of $m = 4000$ kg is assumed, and braking is provided by the main landing gear only, while the nose-wheel is non-braking and free-rolling.

---

[1] Source: `https://www.matweb.com/search/DataSheet.aspx?MatGUID=df0c08b0008749f0b84bf1fa44e49378`

[2] Source: `https://www.matweb.com/search/datasheet.aspx?MatGUID=2a074c62a3f0478ca305352a96ec78f6`

[3] Source: `https://www.matweb.com/search/DataSheet.aspx?MatGUID=c91b550de2b24b5ea70da0cc4575504d`

Longitudinal drag in landing roll/taxiing

The order-of-magnitude estimate is based on the following parameters:

- m aircraft mass [kg]
- g gravitational acceleration $[\mathrm{m/s^2}]$
- λ_N static fraction of weight carried by the nose-wheel landing gear on the ground $[-]$
- $R_N = \lambda_N mg$ static vertical reaction at the nose-wheel [N]
- C_{rr} effective rolling-resistance coefficient at the nose-wheel $[-]$

For a $m = 4000$ kg light jet with a representative nose-load fraction $\lambda_N = 0.12$, one obtains

$$mg = 4000 \times 9.81 \approx 39.2 \text{ kN}, \qquad R_N \approx 0.12\, mg \approx 4.71 \text{ kN}. \tag{6.1}$$

For taxiing with a free-castering, unbraked nose-wheel, the longitudinal force at the nose-wheel due to rolling resistance is approximately

$$F_{\text{drag,taxi}} \approx C_{\text{rr}} R_N. \tag{6.2}$$

With a representative $C_{\mathrm{rr}} \approx 0.11$, derived in WP1, this gives

$$F_{\text{drag,taxi}} \approx 0.11 \times 4.71 \approx 0.52 \text{ kN}. \tag{6.3}$$

Thus, the taxi-drag force at the nose-wheel is approximately 0.5 kN, which is small compared to structural capacity and to the towing loads measured in Chapter 5. During landing-roll braking, the nose-wheel in the present configuration remains unbraked. The main gear, therefore, provides essentially all wheel-braking drag, such that the longitudinal reaction at the nose-wheel landing gear remains of the same order as the rolling-resistance level above, with only modest changes due to dynamic load transfer. The majority of the total aircraft drag and braking loads are transmitted through the main gear, while the nose-wheel landing gear carries only a small fraction of the overall longitudinal reaction.

Longitudinal drag during towing

During towing, the longitudinal load at the nose-wheel landing gear is primarily determined by the tug's capability and the aircraft's resistance (rolling resistance of all gears, slight slopes, steering, and dynamic effects). A simple quasi-static balance for straight towing on a gentle slope can be written as

$$F_{\text{tow}} \approx F_{\text{rr,tot}} + m a_x + W \sin\theta, \tag{6.4}$$

where,

- F_{tow} towing force along the towing direction (longitudinal component) [N]
- $F_{\text{rr,tot}}$ total rolling-resistance force [N]
- m aircraft mass [kg]
- a_x longitudinal acceleration/deceleration $[\mathrm{m\,s^{-2}}]$
- W aircraft weight, $W = mg$ [N]
- θ ground slope angle (positive uphill in towing direction) [rad]

For a $m = 4000$ kg aircraft with $C_{\mathrm{rr}} \approx 0.11$ and weight $W \approx 3.9 \times 10^4$ N, the total rolling resistance is of order

$$F_{\text{rr,tot}} \approx C_{\text{rr}} W \approx 0.11 \times 3.9 \times 10^4 \approx 4.3 \text{ kN} \tag{6.5}$$

A modest towing acceleration of $a_x \approx 0.02\, g$ adds an inertial contribution $m a_x \approx 0.8$ kN, giving F_{tow} of order 5.1 kN on level ground. A slight uphill gradient ($\theta \sim 1^\circ$) adds a further $W \sin\theta \approx 0.7$ kN, so that realistic towing forces for this configuration fall naturally in the 4.4–5.8 kN range. These values remain well below the CS-23 towing limit of $0.3\, W \approx 11.8$ kN for a 4000 kg aircraft, but are about an order of magnitude larger than the nose-wheel landing gear drag during taxiing or landing roll.

Simplifications and scaling of measured towing loads

To translate the measured towing manoeuvres into a manageable set of Abaqus load cases for the global screening, a single external load combination was assigned to each manoeuvre family. Specifically, for every manoeuvre, the most extreme measured combination (in terms of the governing load components) was selected and applied as a static-equivalent load case. This reduction was used only for the global hotspot ranking. In WP3, the full measured load histories of each manoeuvre were reintroduced for the fatigue assessment.

PC-12 measurements scaled to a PC-24 global model

The global NWLG geometry modelled in this work was based on a Pilatus PC-24, while the towing manoeuvres were measured on a PC-12. To obtain a conservative proxy for PC-24 towing loads, all measured towing forces were scaled by the ratio of PC-24 MTOW to the PC-12 full weight:

$$k_W \;=\; \frac{W_{\text{PC24,MTOW}}}{W_{\text{PC12}}} \;=\; \frac{81400}{9.80665 \times 4313} \;\approx\; 1.92. \tag{6.6}$$

where,

- k_W weight-scaling factor $[-]$
- $W_{\text{PC24,MTOW}}$ PC-24 weight at maximum take-off weight [N]
- W_{PC12} PC-12 aircraft weight used in the reference case [N]

From the earlier rolling-resistance estimate for the PC-12, the total rolling-resistance force is taken as

$$F_{\text{rr,tot}} = 4.7 \text{ kN}$$

Using the measured/assumed nose-load fraction $\lambda_N = 12.7\%$, the corresponding longitudinal drag at the free-rolling nose wheel is

$$F_{\text{rr,kN}} \;=\; \lambda_N \, F_{\text{rr,tot}} \;=\; 0.127 \times 4.7 \;\approx\; 0.6 \text{ kN}. \tag{6.7}$$

For consistency with the PC-24 scaling applied to the towing forces, this nose-wheel drag is scaled as

$$F_{\text{rr,N,PC24}} \;\approx\; k_W \, F_{\text{rr,kN}} \;\approx\; 1.92 \times 0.6 \;\approx\; 1.15 \text{ kN}. \tag{6.8}$$

Turning manoeuvre assumptions

For turning manoeuvres, a representative steering angle is assumed to decompose the resultant towing effort into longitudinal and lateral axle forces:

$$F_{x,\text{axle}} = F_{\text{req}} \cos \delta, \qquad F_{y,\text{axle}} = F_{\text{req}} \sin \delta. \tag{6.9}$$

where,

- $F_{x,\text{axle}}$ longitudinal force component [N]
- $F_{y,\text{axle}}$ lateral force component [N]
- F_{req} required resultant towing force [N]
- δ steering angle of the NWLG [rad]

The following angles are used:

$$\delta_{\text{tight}} = 45^\circ, \qquad \delta_{\text{wide}} = 20^\circ.$$

These assumptions provided a consistent and conservative mapping from measured manoeuvre families to a limited set of Abaqus load cases, while preserving the full time-history fidelity for WP3 fatigue calculations.

Reference vertical loads and load mapping for global FEM cases

For all towing load cases (TB and TBL), the PC-12 test aircraft was assumed to be at MTOW,

$$m_{\text{MTOW}} = 4313 \text{ kg}, \qquad g = 9.80665 \text{ m/s}^2,$$

so that

$$W_{\text{PC12}} = m_{\text{MTOW}} g \approx 4.23 \times 10^4 \text{ N} \;\; (\approx 42.3 \text{ kN}). \tag{6.10}$$

Measured PC-12 force levels are mapped to the PC-24-based global model by the weight ratio $k_W = 1.92$ so that, for any measured force component,

$$F_{\text{PC24}} = k_W \, F_{\text{PC12}}. \tag{6.11}$$

The effective nose-load fraction during the towing tests is taken as $\lambda_N = 0.127$, giving the static PC-12 nose reaction

$$N_{N,\text{PC12}} = \lambda_N W_{\text{PC12}} \approx 5.4 \text{ kN}. \tag{6.12}$$

For consistency with the force scaling, the vertical reaction applied in the global model is

$$F_{z,N} = N_{N,\text{PC24}} = k_W \, N_{N,\text{PC12}} \approx 10.3 \text{ kN}, \tag{6.13}$$

applied as a constant compressive load at the wheel/axle region for all manoeuvres.

6.2.3. Applied Force Components in FEM

The preceding subsections defined how the measured WP1 towing loads were reduced, scaled, and mapped to the PC-24-based global FEM model. The resulting external load components applied in Abaqus are summarised in Tables 6.2 and 6.3. For each manoeuvre family, a single representative static-equivalent load combination was retained for the Stage G hotspot screening, with the towbar and towbarless cases distinguished by their respective load-introduction points and by the corresponding axle-force decomposition used for turning manoeuvres. Together, these tables provide the final set of global FEM load cases used for the comparative hotspot analysis.

At this Stage G level, the comparison was deliberately constructed such that TB and TBL cases were matched primarily in overall manoeuvre demand, while differing mainly in load-introduction location and axle-force decomposition. In other words, the absolute TB–TBL force differences inferred in WP1 from the operational kinematics were not yet fully imposed in the global hotspot screening. This choice was made to isolate the effect of the changed load path on hotspot ranking and redistribution in the Stage G comparison. The manoeuvre-dependent differences in absolute applied force level were reintroduced only in the subsequent stages, where the objective shifted from comparative hotspot screening to local stress quantification and specimen-level mapping for WP3.

Table 6.2: TB load magnitudes at towbar pin and nose-wheel axle for global NWLG FEM (scaled by $k_W = 1.92$)

ID	Manoeuvre	EventCode	$\lvert F_{x,\text{pin}}\rvert$ [kN]	$\lvert F_{x,\text{axle}}\rvert$ [kN]	$\lvert F_{y,\text{axle}}\rvert$ [kN]
1	Straight pull at constant speed	`SP_STEADY_PULL`	9.02	-1.15	0.00
2	Straight push at constant speed	`SP_STEADY_PUSH`	-9.02	1.15	0.00
3	Smooth pull acceleration	`ACC_PULL_SMOOTH`	13.44	-1.15	0.00
4	Smooth pull braking	`BRK_PULL_SMOOTH`	-5.52	-1.15	0.00
5	Smooth push acceleration	`ACC_PUSH_SMOOTH`	-9.28	1.15	0.00
6	Smooth push braking	`BRK_PUSH_SMOOTH`	4.15	1.15	0.00
7	Tight radius pull turns (const. speed)	`TURN_PULL_TIGHT`	2.80	-0.81	-0.81
8	Tight radius push turns (const. speed)	`TURN_PUSH_TIGHT`	-2.80	0.81	0.81
9	Wide-radius pull turns (const. speed)	`TURN_PULL_WIDE`	3.57	-1.08	2.52
10	Wide-radius push turns (const. speed)	`TURN_PUSH_WIDE`	-3.57	1.08	-2.52
11	Controlled pull rapid tug brake	`BRK_PULL_RAPID`	-9.28	-1.15	0.00
12	Controlled push rapid tug brake	`BRK_PUSH_RAPID`	4.15	1.15	0.00

The TB tow-force levels $|F_{x,\text{pin}}|$ in Table 6.2 were also used as the required towing force for the TBL cases. This table considers an MTOM of 4313 kg, scaled by a factor of 1.92, so that a constant vertical nose reaction $F_{z,N} = 10.3$ kN was always applied. The signs of F_x and F_y in the model were chosen according to pull/push direction and to excite the tension-critical drag-brace configuration. For a given manoeuvre, the aircraft therefore "feels" the same overall towing effort F_{req} in both TB and TBL towing, minus the drag of the front tyre for TBL towing. Only the load introduction at the NWLG changes (pin + axle for TB, axle only for TBL).

Towing forces at wheel axle for towbarless towing

For TBL towing, the tug clamps directly to the nose wheels. There is no force at a towbar pin, thus

$$F_{x,\text{pin}} = F_{y,\text{pin}} = 0.$$

The external loads on the NWLG are therefore the forces applied at the nose-wheel axle. For direct comparability with the TB cases, the manoeuvre demand level is taken from the corresponding TB pin-force magnitude, with the (PC-24-equivalent, scaled) values read from Table 6.2.

$$F_{\text{req}} = \left|F_{x,\text{pin}}\right|_{\text{TB}}, \tag{6.14}$$

In TB towing, the front wheel remains free-rolling and contributes a longitudinal rolling-resistance drag, which is reacted through the towing system. In the TBL configuration, the nose-wheel is clamped and does not roll. Therefore, the rolling-resistance contribution of the nose-wheel is removed from the required towing effort transmitted through the axle. Accordingly, the longitudinal axle load applied in the TBL cases is reduced by the PC-24-equivalent nose-wheel rolling-resistance level $F_{\text{rr,N,PC24}}$,

$$|F_{x,\text{axle}}|_{\text{TBL}} \;=\; F_{\text{req}} - F_{\text{rr,N,PC24}}, \qquad F_{\text{rr,N,PC24}} \approx 1.15 \text{ kN}. \tag{6.15}$$

This adjustment is applied consistently across the straight towing and longitudinal transient manoeuvres, and yields the axial force levels listed in Table 6.3. For turning manoeuvres, the required force is applied at the axle, decomposed into longitudinal and lateral components. For a representative steering angle δ,

$$F_{x,\text{axle}} = F_{\text{req}} \cos \delta, \qquad F_{y,\text{axle}} = F_{\text{req}} \sin \delta. \tag{6.16}$$

For the adopted tight and wide turn cases, the applied axle components in the global FEM are

$$\left(|F_{x,\text{axle,tight}}|,\ |F_{y,\text{axle,tight}}|\right) = (1.99,\ 2.37)\ \text{kN},$$

$$\left(|F_{x,\text{axle,wide}}|,\ |F_{y,\text{axle,wide}}|\right) = (2.67,\ 3.81)\ \text{kN},$$

with all manoeuvre-specific TBL axle loads collated in Table 6.3. The towbarless load cases are obtained from the refined towbar load-case table (Table 6.2) by applying a fixed component mapping in the model coordinate system:

$$F_{\text{TBL},x,axle} = F_{\text{TB},x,pin} + F_{\text{TB},x,axle}, \qquad F_{\text{TBL},x,pin} = 0 \tag{6.17}$$

This mapping collapses the TB in-plane components into the TBL primary towing direction, preserves the lateral component, and suppresses the pin loading component to reflect the assumed TBL load-path constraint in the FEM.

Table 6.3: TBL load magnitudes at the nose-wheel axle for global NWLG FEM (scaled by $k_W = 1.92$)

ID	Manoeuvre	`EventCode`	$\lvert F_{x,\text{axle}}\rvert$ [kN]	$\lvert F_{y,\text{axle}}\rvert$ [kN]
1	Straight pull at constant speed	`SP_STEADY_PULL`	7.87	0.00
2	Straight push at constant speed	`SP_STEADY_PUSH`	-7.87	0.00
3	Smooth pull acceleration	`ACC_PULL_SMOOTH`	13.76	0.00
4	Smooth pull braking	`BRK_PULL_SMOOTH`	-10.74	0.00
5	Smooth push acceleration	`ACC_PUSH_SMOOTH`	-11.72	0.00
6	Smooth push braking	`BRK_PUSH_SMOOTH`	5.30	0.00
7	Tight radius pull turns (const. speed)	`TURN_PULL_TIGHT`	1.99	2.37
8	Tight radius push turns (const. speed)	`TURN_PUSH_TIGHT`	-1.99	-2.37
9	Wide-radius pull turns (const. speed)	`TURN_PULL_WIDE`	2.67	3.81
10	Wide-radius push turns (const. speed)	`TURN_PUSH_WIDE`	-2.67	-3.81
11	Controlled pull rapid tug brake	`BRK_PULL_RAPID`	-14.02	0.00
12	Controlled push rapid tug brake	`BRK_PUSH_RAPID`	5.30	0.00

Reaction-force equilibrium verification

Static equilibrium of the global NWLG model was verified by extracting the reaction forces at the five reference points (RP1–RP5) used to represent the aircraft-side supports and kinematic constraints. For each load case, the summed reaction-force components were compared with the externally applied load components in the global X, Y, and Z directions. For a converged static solution, the model should satisfy:

$$\sum RF_x + \sum F_x^{\text{app}} \approx 0, \qquad \sum RF_y + \sum F_y^{\text{app}} \approx 0, \qquad \sum RF_z + \sum F_z^{\text{app}} \approx 0. \tag{6.18}$$

where,

- $\sum RF_x$ sum of reaction-force components at RP1–RP5 in global X direction [N]
- $\sum RF_y$ sum of reaction-force components at RP1–RP5 in global Y direction [N]
- $\sum RF_z$ sum of reaction-force components at RP1–RP5 in global Z direction [N]
- $\sum F_x^{\text{app}}$ sum of externally applied force components in global X direction [N]
- $\sum F_y^{\text{app}}$ sum of externally applied force components in global Y direction [N]
- $\sum F_z^{\text{app}}$ sum of externally applied force components in global Z direction [N]

In addition, moment equilibrium about a common reference point was reviewed as a consistency check. For the distributed support system, the support contribution was evaluated as the sum of the reaction moments at the support reference points and the moments generated by the support reaction forces about the chosen reference. Because the applied towing forces act at an offset from the restrained fuselage-side supports, non-zero reaction moments are expected. Their order of magnitude was therefore checked against simple lever-arm estimates of the form,

$$M \approx F \cdot l, \tag{6.19}$$

where,

- M reaction moment [Nm]
- F applied force component [N]
- l perpendicular lever arm from the support reference to the applied force line of action [m]

A final consistency check concerned the released hinge degrees of freedom used in the boundary conditions. At reference points where a rotation was intentionally left free, the corresponding reaction moment was required to remain small relative to the restrained components. This confirmed that the idealised joints behaved as intended.

Table 6.4 gives one representative example of this verification procedure for load case `TBL_SP_STEADY_PULL`. The same check was applied to the remaining load cases, with similarly small equilibrium residuals. For the global model, the expected reaction moment was evaluated about the lower trunnion reference point: $M_{y,\text{exp}} \approx z_{\text{axle}} F_x - x_{\text{axle}} F_z$,

Table 6.4: Representative equilibrium check for load case `TBL_SP_STEADY_PULL`

Force quantity	X **[kN]**	Y **[kN]**	Z **[kN]**
Applied load sum, $\sum F^{\text{app}}$	7.87	0.00	-10.34
Reaction force sum, $\sum RF$ fuselage	-7.87	0.00	10.34
Moment quantity	X **[kNm]**	Y **[kNm]**	Z **[kNm]**
Estimated moment, $\sum M^{\text{est}}$	0.00	5.28	0.0
Support reaction moment sum about TRUN, $\sum (RM + r \times RF)$	0.00	5.30	0.00

The difference between the estimated and extracted support moment about the global Y-axis was only 0.02 kNm, which was considered sufficiently small for the present verification purpose and therefore confirmed satisfactory moment equilibrium of the global model.

6.2.4. Hotspot Screening

The global NWLG model was used to screen candidate fatigue hotspots under the full set of towbar and towbarless manoeuvres. This subsection summarises the adopted mesh and convergence checks, the stress measures used for fatigue-driven ranking, and the resulting identification of governing locations and manoeuvres for the subsequent local analyses.

Mesh and convergence

The NWLG was discretised in Abaqus using reduced-integration linear brick elements (C3D8R), with local refinement in the identified hotspot regions. Simple bar parts (axle and all pins) were meshed using 32 elements circumferentially and a nominal axial element size of ≈ 5 mm to obtain smooth cylindrical coupling surfaces. The fork legs, crown block, barrel and piston were initially meshed as sweep hex solids with a comparable target size. After drilling all bores and merging the forks, crown, barrel, lugs, V-struts, brace, and torque-link rods into a single host body, the merged geometry was remeshed.

Local edge-based refinements were then applied in bounding boxes around the identified hotspot regions (lug bores, pin eyes, drag brace, axle–fork interfaces and crown/fillet transitions). A brief mesh-convergence study was performed by halving the local element size in these boxes; the resulting changes in von Mises stress at each hotspot (volume-averaged over the corresponding element set) remained within $\approx 5\%$, while halving the mesh size. Further refinement had little effect on the hotspot stress levels but substantially increased the computational cost. The converged mesh was therefore adopted as the baseline for all screening analyses, with the axle and pins kept as separate, finely meshed C3D8R parts, kinematically coupled to the surrounding bores via distributing couplings.

Hotspot metrics and damage indicator

For fatigue screening, post-processing focused on a compact set of geometric hotspots: (i) crown lug bores (front and back), (ii) torque-link lug bores and bar eyes, (iii) axle–fork bores, (iv) brace lug bores and brace-base eye, and (v) selected fork–crown fillet corners. Each region was represented by an assembly element set on the merged host structure. For each TB and TBL load case, stress and volume fields were extracted from these sets at the final increment.

Because the screening was fatigue-driven, the assessment was based on the maximum principal stress, σ_1, rather than the von Mises equivalent stress, σ_{vM}. The governing initiation mechanism at the selected hotspots was tensile crack opening (Mode I), so σ_1 provided the most direct measure of the local tensile response relevant for fatigue. By contrast, σ_{vM} is primarily a yield-oriented scalar that combines normal and shear components and is therefore more suitable for strength screening than for identifying tensile fatigue-critical locations under predominantly elastic loading.

From the Abaqus stress field `S`, a scalar field of maximum principal stress was formed using the `MAX_PRINCIPAL` invariant and combined with the element volumes (`EVOL`) to obtain a volume-averaged value $\bar{\sigma}_1$ for each hotspot and manoeuvre. The resulting matrix

$$\bar{\sigma}_1\big(\text{hotspot, manoeuvre}\big)$$

provided a direct comparison of all candidate locations across the TB and TBL load cases. To relate these stresses to fatigue utilisation, the peak $\bar{\sigma}_1$ value for each hotspot and manoeuvre combination was normalised into a scalar damage indicator

$$D\big(\text{hotspot, manoeuvre}\big),$$

which was subsequently scaled by the global maximum over all combinations, such that $D = 1.0$ corresponds to the most highly utilised location in the complete screening set.

Ranking by manoeuvre

Rather than reporting the full D-matrix, the results were condensed into a per-manoeuvre ranking that highlights only the dominant contributors. For each TB and TBL manoeuvre, the three most critical hotspots were identified and listed in Table 6.5, together with their normalised damage indicator D.

Because the ranking is based on $\bar{\sigma}_1$, multiple hotspots can appear very similar when rounded, even though small differences remain in the underlying values. For example, in `TB_SP_STEADY_PULL`, two candidate locations differed only slightly in σ_1 (257.5 versus 254.8 MPa), while their corresponding von Mises values differed more strongly (240.5 versus 204.6 MPa), indicating a different degree of local multiaxiality. Consequently, Table 6.5 should be interpreted primarily as a fatigue-oriented ranking of tensile hotspot severity rather than as a comparison of general multi-axial stress state. This distinction is consistent with the definition of von Mises stress,

$$\sigma_{\text{vM}} = \sqrt{\frac{(\sigma_1 - \sigma_2)^2 + (\sigma_2 - \sigma_3)^2 + (\sigma_3 - \sigma_1)^2}{2}}, \tag{6.20}$$

where,

- σ_{vM} von Mises equivalent stress [MPa]
- σ_1 first (maximum) principal normal stress [MPa]
- σ_2 second (intermediate) principal normal stress [MPa]
- σ_3 third (minimum) principal normal stress [MPa]

so that for a more hydrostatic-like local stress state, σ_{vM} can remain substantially below σ_1 even when the maximum tensile principal stress is high. [69]

Table 6.5: Dominant hotspots per manoeuvre, ranked by normalised damage indicator D

(a) TB hotspot ranking

Manoeuvre	Rank 1 hotspot	D	Rank 2 hotspot	D	Rank 3 hotspot	D
TB_SP_STEADY_PULL	DRAG_BRACE_V_BASE	0.71	BR_LUGS	0.70	BR_BASE_EYE	0.61
TB_SP_STEADY_PUSH	TL_BARREL_LUGS	0.21	DRAG_BRACE_V_BASE	0.19	TL_MID_LOWER	0.18
TB_ACC_PULL_SMOOTH	DRAG_BRACE_V_BASE	1.00	BR_LUGS	1.00	BR_BASE_EYE	0.86
TB_BRK_PULL_SMOOTH	DRAG_BRACE_V_BASE	0.19	BR_LUGS	0.19	FK_CROWN	0.12
TB_ACC_PUSH_SMOOTH	DRAG_BRACE_V_BASE	0.97	BR_LUGS	0.96	BR_BASE_EYE	0.69
TB_BRK_PUSH_SMOOTH	BR_LUGS	0.63	DRAG_BRACE_V_BASE	0.60	BR_BASE_EYE	0.45
TB_TURN_PULL_TIGHT	TL_LOWER_EYE	0.55	TL_BARREL_LUGS	0.55	TL_BACK_LUGS	0.48
TB_TURN_PUSH_TIGHT	TL_UPPER_EYE	0.52	TL_MID_UPPER	0.52	TL_BACK_LUGS	0.51
TB_TURN_PULL_WIDE	DRAG_BRACE_V_BASE	0.68	BR_LUGS	0.67	BR_BASE_EYE	0.49
TB_TURN_PUSH_WIDE	TL_BARREL_LUGS	0.32	TL_MID_LOWER	0.32	TL_LOWER_EYE	0.32
TB_BRK_PULL_RAPID	BR_LUGS	0.36	DRAG_BRACE_V_BASE	0.22	TL_BARREL_LUGS	0.21
TB_BRK_PUSH_RAPID	BR_LUGS	0.63	DRAG_BRACE_V_BASE	0.62	BR_BASE_EYE	0.54

(b) TBL hotspot ranking

Manoeuvre	Rank 1 hotspot	D	Rank 2 hotspot	D	Rank 3 hotspot	D
TBL_SP_STEADY_PULL	BR_LUGS	0.62	DRAG_BRACE_V_BASE	0.58	BR_BASE_EYE	0.50
TBL_SP_STEADY_PUSH	FK_CROWN	0.47	FK_AXLE	0.40	BR_LUGS	0.24
TBL_ACC_PULL_SMOOTH	BR_LUGS	0.99	DRAG_BRACE_V_BASE	0.92	FK_CROWN	0.82
TBL_BRK_PULL_SMOOTH	FK_CROWN	0.40	FK_AXLE	0.34	BR_LUGS	0.20
TBL_ACC_PUSH_SMOOTH	DRAG_BRACE_V_BASE	0.87	BR_LUGS	0.68	FK_CROWN	0.66
TBL_BRK_PUSH_SMOOTH	BR_LUGS	0.46	DRAG_BRACE_V_BASE	0.43	BR_BASE_EYE	0.37
TBL_TURN_PULL_TIGHT	TL_UPPER_EYE	0.98	TL_MID_UPPER	0.98	TL_BACK_LUGS	0.98
TBL_TURN_PUSH_TIGHT	TL_MID_LOWER	1.00	TL_BARREL_LUGS	1.00	TL_LOWER_EYE	1.00
TBL_TURN_PULL_WIDE	BR_LUGS	0.69	DRAG_BRACE_V_BASE	0.66	FK_CROWN	0.46
TBL_TURN_PUSH_WIDE	FK_CROWN	0.42	FK_AXLE	0.36	TL_BARREL_LUGS	0.27
TBL_BRK_PULL_RAPID	FK_CROWN	0.64	FK_AXLE	0.56	BR_LUGS	0.35
TBL_BRK_PUSH_RAPID	DRAG_BRACE_V_BASE	0.87	BR_LUGS	0.87	FK_CROWN	0.66

Torque-link modelling and towing steering state

In the present global NWLG finite-element model, the torque-link assembly was modelled as connected and effectively constraining relative rotation between the sliding and fixed members of the oleo about the strut axis. Consequently, steering was not represented as a free degree of freedom and strut-axis torsion generated during turning was reacted through the torque-link load path.

This steering assumption did not match the typical towing configuration. Operational guidance notes that towing/pushback can damage the nose-wheel steering system if it remains hydraulically pressurised. Therefore, a steering lockout pin is used to depressurise the nose-wheel steering system during towing/pushback [70]. More generally, it is noted that for towing/pushback, the steering linkage may be disconnected to allow the nose-wheel to freely castor, or a hydraulic bypass may be pinned to disable the steering actuator [71]. These findings establish that the “steering free/steering disabled” towing configuration is a realistic operational condition which was not represented by the current model formulation.

Moreover, turning-load demand is strongly speed-dependent. ISO 20683-2:2016 defines pushback (including a turn) with typical speed not exceeding 10 km h^{-1}, and maintenance towing with speeds up to 32 km h^{-1} [72]. In contrast, published flight-deck operating guidance quoted in an accident investigation report gives “normal maximum taxi speed” values of 30 kt in a straight line and 10 kt for a sharp turn [73]. From uniform circular motion, the centripetal-acceleration magnitude is

$$a_r = \frac{v^2}{r}, \tag{6.21}$$

where,

- a_r centripetal acceleration [m/s^2]
- v vehicle speed [m/s]
- r turn radius [m]

and, via Newton's second law, the required radial force satisfies $F_r = ma_r$ [74]. Therefore, for a given turn radius, the lateral force demand scales with v^2, and the low-speed towing regimes defined in this research inherently reduce turning-induced lateral demand relative to higher-speed ground operations.

Given this mismatch, turn-case torque-link forces and local stresses from the present model were treated as non-representative indicators of towing fatigue. The cited towing configuration allowed strut-axis rotation (free castoring or disabled steering), whereas the current model suppressed this degree of freedom, so any turn-induced steering demand was redirected into the torque-link load path. Therefore, the turning results were not used for quantitative fatigue ranking.

6.2.5. Summary of Governing Locations

To avoid a large per-location table, the global screening across all hotspot sets is condensed into a short ranking of the most critical details. For each hotspot, the damage indicator $D(\text{hotspot}, \text{manoeuvre})$ is first averaged over all manoeuvres in the towing spectrum to obtain a spectrum-mean value,

$$\bar{D}(\text{hotspot}) \;=\; \big\langle D(\text{hotspot}, \text{manoeuvre}) \big\rangle_{\text{spectrum}}$$

To enable comparison on a common scale, these values are normalised by the damage over the highest-rated hotspot over the spectrum,

$$D^*(\text{hotspot}) \;=\; \frac{\bar{D}(\text{hotspot})}{\big\langle \bar{D}(\text{hotspot}) \big\rangle_{\text{max}}} \tag{6.22}$$

Table 6.6 reports the hotspots, their structural role, and the resulting normalised spectrum-mean metric D^* used for ranking.

Table 6.6: Summary ranking of most critical hotspots (normalised D^*)

(a) TB

Rank	hotspot set	D^*_{TB} [-]
1	`DRAG_BRACE_V_BASE`	1.00
2	`BR_LUGS`	0.87
3	`TL_BARREL_LUGS`	0.60
4	`BR_BASE_EYE`	0.59
5	`TL_MID_UPPER`	0.44
6	`TL_LOWER_EYE`	0.42
7	`TL_BACK_LUGS`	0.39
8	`FK_CROWN`	0.33
9	`TL_MID_LOWER`	0.26
10	`TL_UPPER_EYE`	0.21
11	`FK_AXLE`	0.20

(b) TBL

Rank	hotspot set	D^*_{TBL} [-]
1	`DRAG_BRACE_V_BASE`	1.00
2	`FK_CROWN`	0.61
3	`BR_LUGS`	0.54
4	`TL_BACK_LUGS`	0.53
5	`TL_BARREL_LUGS`	0.50
6	`FK_AXLE`	0.42
7	`BR_BASE_EYE`	0.41
8	`TL_LOWER_EYE`	0.41
9	`TL_MID_UPPER`	0.37
10	`TL_MID_LOWER`	0.27
11	`TL_UPPER_EYE`	0.21

Furthermore, the change in peak tensile stress between TB and TBL towing is summarised in Table 6.7. The ratios show that the maximum principal stress σ_1 increases for all listed hotspots when averaged over the full towing spectrum, with particularly large increases in the fork and axle regions (`FK_CROWN` and `FK_AXLE`). This trend is consistent with the altered load introduction in TBL operations: instead of being applied through a towbar interface at the towing pin/crown region, the towing forces are transmitted through the wheel–tyre contact and consequently drive higher stresses in the fork–axle load path. Several other components also show moderate increases, indicating a generally higher tensile-stress level throughout the assembly under TBL towing.

It should be noted that Table 6.7 represents a spectrum-averaged comparison and does not imply that σ_1 is higher for TBL in every individual manoeuvre. For example, in the turning manoeuvres, the drag-brace hotspot `DRAG_BRACE_V_BASE` exhibits lower σ_1 in TBL than in TB, reflecting the manoeuvre-specific redistribution of load paths. Overall, the consistent increase in spectrum-mean σ_1 across hotspots supports the hypothesis that TBL towing increases the loads experienced by the NWLG relative to conventional TB towing.

Table 6.7: Stress ratio between TBL and TB towing for selected hotspots

Hotspot (part)	$\sigma_{\text{TBL}}/\sigma_{\text{TB}}$ [-]
`TL_BACK_LUGS`	2.18
`TL_UPPER_EYE`	1.44
`TL_BARREL_LUGS`	1.36
`TL_LOWER_EYE`	1.64
`TL_MID_LOWER`	1.74
`TL_MID_UPPER`	1.49
`BR_LUGS`	1.56
`BR_BASE_EYE`	1.53
`DRAG_BRACE_V_BASE`	1.55
`FK_AXLE`	4.28
`FK_CROWN`	3.97

Global conclusions and implications for local modelling

The global towing analysis demonstrated that towing constituted a distinct and more severe loading mode for the NWLG than conventional ground operation. For the load levels used, the characteristic longitudinal forces transmitted through the drag brace during towing were of order 5 kN, whereas the nose-wheel landing gear drag associated with taxiing and landing roll was of order 0.5 kN; the resulting drag-brace axial force was therefore approximately an order of magnitude higher in towing-dominated conditions.

Across the analysed towing spectrum, the drag-brace assembly governed fatigue utilisation. Both the per-manoeuvre ranking (Table 6.5) and the spectrum-mean ranking (Table 6.6) consistently placed the drag-brace hotspots at the top of the damage hierarchy, with torque-link joints and fork/crown details forming a secondary tier. The configuration discussion further indicated that aft-folding architectures with forward-offset nose wheels are unconservative from a fatigue perspective because the static weight introduces a tensile bias in the brace, which is augmented by towing-induced tensile cycles, especially during forward (pull) manoeuvres.

Towbarless towing modified load introduction by applying the required towing effort at the axle rather than through the tow-pin, thereby redistributing internal force paths. Consistent with this, the spectrum-mean tensile stress σ_1 increased across all listed hotspots in Table 6.7, with the largest increases occurring in the fork and axle load path. Despite this redistribution, the drag brace remained the governing component: in Table 6.6, the drag-brace metric retained $D^* = 1.0$ while the separation to the next-ranked locations increased in the TBL case, indicating that the drag-brace utilisation became more dominant relative to the remainder of the structure.

Finally, turn cases were not used for quantitative fatigue ranking because the present global model does not represent the towing steering state. Operational towing may disable steering and permit strut-axis rotation, whereas the current model suppresses this degree of freedom, redirecting turn-induced demand into strut torsion and the torque-link load path. Within the low-speed towing regimes considered, turning demand is also inherently limited by the v^2 scaling of lateral acceleration.

On this basis, the subsequent local submodelling and specimen design focused on the drag-brace assembly for an aft-folding NWLG configuration with forward-offset nose wheels.

6.3. Stage L — Local Hotspot Submodel

Based on the Stage G screening, Stage L developed a high-fidelity local submodel of the governing drag-brace region in the selected aft-folding configuration, suitable for fatigue-oriented stress analysis and subsequent specimen mapping.

6.3.1. Submodel Cut-Out and Geometry Fidelity

The local drag-brace model was extracted as a submodel from the global NWLG assembly used in Stage G. The cut boundary was chosen such that the entire brace, including the barrel-side lugs, knee region and base eye, was enclosed with a buffer of at least two to three characteristic section thicknesses in all directions.

Within this cut-out, the idealised Stage G solid representation was replaced by a more detailed drag-brace geometry. At the critical load-transfer interfaces (lug–pin and eye–pin), the contact was resolved by surface-to-surface contact with finite friction, so that local bearing, shear and secondary bending stresses were captured rather than idealised by constraints. Boundary conditions for the submodel were supplied by interpolating the global Stage G displacements onto the cut surface for the relevant TB and TBL load cases, thereby ensuring consistency between global and local response.

The end/connecting regions of the local drag-brace subcomponents were not reproduced by direct geometric scaling from the real drag-brace dimensions. This was intentional. A strict size match at the connecting ends would cause the local stress field to be dominated by geometry-specific attachment effects and local interface hotspots, making it more difficult to isolate the representative axial and bending load flow through the brace members themselves. For that reason, the connecting regions in the local model were deliberately over-dimensioned relative to the real geometry, so that stress concentrations would not localise prematurely at the interfaces. This modelling choice shifted the governing stress development towards the straighter load-carrying regions of the drag brace, in particular the base and V-brace regions, from which the hotspot stress histories could then be extracted in a more controlled and comparable manner.

The drag brace considered in Stage L corresponds to the compact, almost straight over-centre brace (Configuration A in Figure 2.10) embedded in an aft-folding NWLG with forward-offset nose wheels, as selected in the global analysis. The local model was based on the pictures seen in Figure 6.3. The resulting local stress fields formed the basis for the fatigue checks in Stage L and for the mapping to the dog-bone specimen geometry in Chapter 7.

(a) Drag brace close-up

(b) Drag Brace V, bottom view

Figure 6.3: Photos of the drag brace on which the local model is based

Figure 6.4 provides an overview of the constructed local drag-brace geometry used in the Abaqus analyses. The overall model layout, including the primary members and attachment interfaces, is shown in Figure 6.4a, while Figure 6.4b provides a detailed view of the section governing local load transfer and is therefore expected to control the development of hotspot stress.

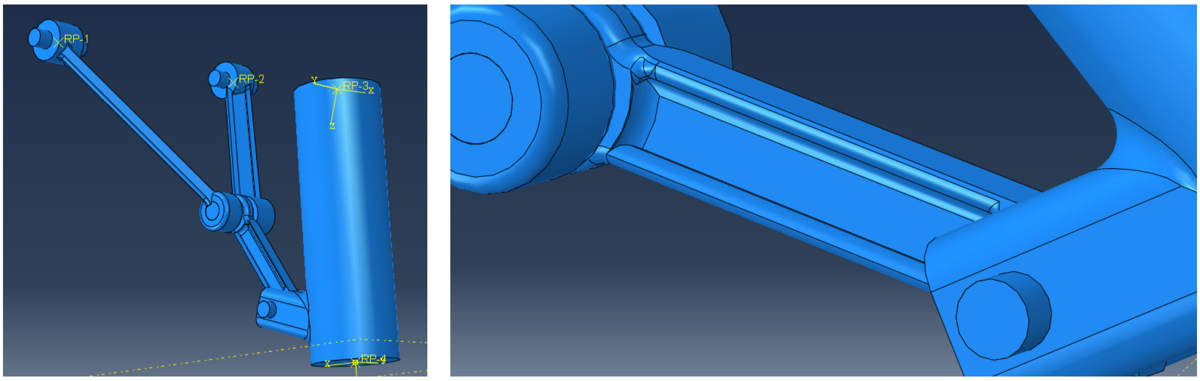

(a) Overall

(b) Detail view

Figure 6.4: Abaqus drag brace local model geometry

6.3.2. Boundary-Condition, Mesh and Element Choices for Local Model

The local model was constructed to remain mechanically consistent with the global NWLG model, while providing increased discretisation fidelity in the drag-brace load path. Accordingly, the boundary conditions applied to the retained attachment interfaces in the local model were taken to be identical to those defined for the global model in Subsection 6.2.1.

With the boundary conditions held fixed, the principal modelling difference between the global and local analyses was the discretisation level. The local model was meshed more finely than the global model, with targeted refinement in regions where high stress gradients were expected and where fatigue-relevant hotspots were evaluated. Outside these areas, a coarser mesh was used to limit computational cost, while maintaining smooth transitions in element size to avoid abrupt stiffness changes and degraded element quality. The refinement strategy was therefore local, which increases spatial resolution where stress extraction was required, without modifying the global load path or the imposed boundary conditions. The model was discretised using reduced-integration linear brick continuum elements (C3D8R), with variable mesh density to balance computational cost and local stress resolution. Global seeding was kept coarse on the barrel, refined on the lugs and drag-brace members, and locally refined at the brace base where peak stresses were expected. Pins were kept slightly coarser because they were not considered critical components (due to shear loading rather than tension-compression cycles). The adopted target seed sizes were:

- Barrel: `SEED_BARREL` = 15 mm,
- Lugs and remaining brace components: `SEED_OTHER` = 4 mm,
- Pins: `SEED_PIN` = 6 mm,
- Brace base (local refinement): `SEED_BASE` = 2 mm,
- Base-refinement capture radius: `SEED_BASE_RAD` = 30 mm.

The element formulation and element family used in the local model follow those adopted in the global model to ensure comparability of stress results and numerical behaviour. The only intentional change was the reduction of the characteristic element size in the local model, enabling more detailed stress fields and improved hotspot resolution for the drag-brace assessment. For reference, the global NWLG model also used reduced-integration linear brick elements (C3D8R), with a global seed of approximately 6 mm.

Figure 6.5 shows the meshed local drag-brace model together with a representative stress contour from an applied loading case. The overall distribution and global load path through the brace are visible in Figure 6.5a, while Figure 6.5b zooms in on a region, highlighting the local stress amplification at geometric transitions.

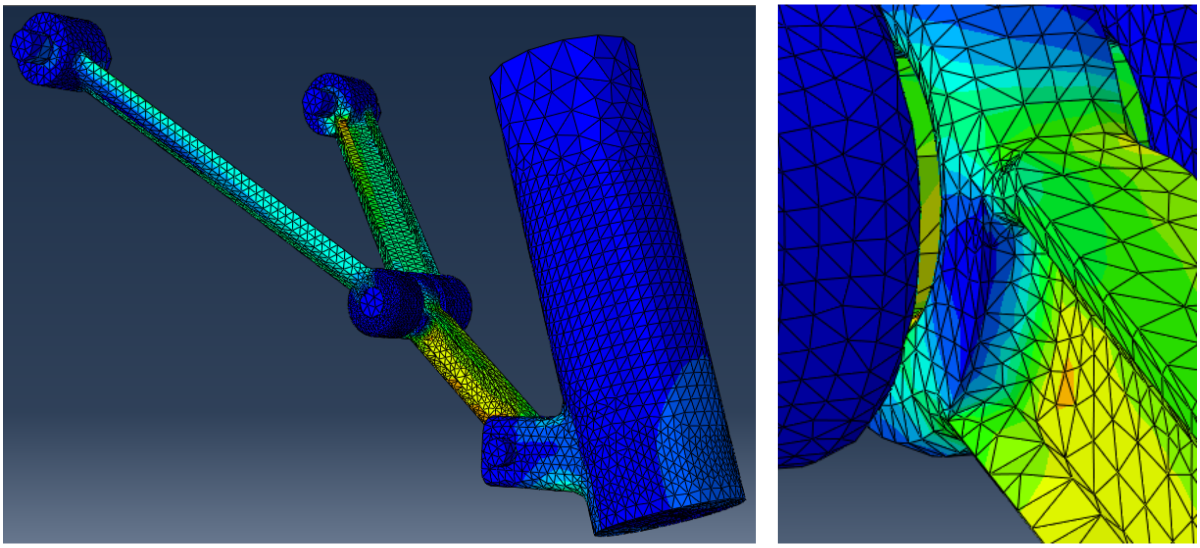

(a) Overall **(b)** Detail view

Figure 6.5: Abaqus drag brace local model: mesh and representative stress contour

6.3.3. Global–Local Load Transfer

The local finite-element model considered in this work retained the barrel and drag-brace subassembly, while the piston and the components below it (crown, fork, axle and towing interfaces) were omitted. In the global NWLG model, however, towing loads are naturally introduced through the tow-pin and/or at the wheel axle. Since these load application points were not present in the local model, a direct reapplication of the original external forces was not possible. It would, in any case, have risked altering the barrel's deformation state, which governs the drag-brace load path. To maintain physical consistency between global and local analyses, the reduced model was therefore driven by an equivalent set of interface actions extracted from the global solution.

The transfer concept was based on replacing the omitted lower assembly with its net mechanical action on the retained structure. A cross-section of the barrel was selected as the port plane at a prescribed axial station, which is geometrically reproducible in both models. Because the barrel dimensions and the coordinate system definition are identical in the global and local models, the same port plane could be constructed at the same axial location in each model without requiring any coordinate transformation. A moment reference point O was defined on the barrel axis at the port plane. The global solution was then post-processed to determine the resultant force and moment transmitted across this section. Together, these defined the section wrench that the omitted lower assembly applied to the retained barrel/drag-brace subassembly.

For each towing load case, the global NWLG model was solved with external loads applied at the tow-pin and/or axle according to the relevant manoeuvre. The transmitted actions at the port plane were then obtained from the resulting ODB using a free-body cut across the corresponding barrel cross-section. Moments were reported about the reference point O, yielding the resultant force vector

$$\mathbf{F}_{\text{port}} = \begin{bmatrix} F_x & F_y & F_z \end{bmatrix}^{\mathsf{T}}$$

and the resultant moment vector

$$\mathbf{M}_{\text{port}} = \begin{bmatrix} M_x & M_y & M_z \end{bmatrix}^{\mathsf{T}}$$

In the present application, each manoeuvre is represented by a single static-equivalent load level. Accordingly, the free-body cut was evaluated for the manoeuvre load case, and the transmitted actions at the port plane were retained as a single set of resultant components rather than as a time history. The exported dataset for each load case was therefore the six-component wrench,

$$\mathcal{W}_{\text{port}} = \{F_x,\ F_y,\ F_z,\ M_x,\ M_y,\ M_z\}_O\,,$$

which represented the net load transfer from the omitted lower assembly into the retained structure at the chosen axial station.

In the local model, the same port plane and the same reference point O were recreated. A reference point RP_{port} was placed at O, and the cut cross-section was coupled to RP_{port} using a distributing coupling so that forces and moments were introduced over the barrel section rather than concentrated at a single node. For each load case, the corresponding globally extracted wrench $\mathcal{W}_{\text{port}}$ was applied at RP_{port} as concentrated forces (F_x, F_y, F_z) and moments (M_x, M_y, M_z). The boundary conditions at the top of the barrel and at the fuselage-side attachment of the drag brace were kept consistent with the global model. With this setup, the local analysis reproduced the global model's net load transfer into the retained subassembly, while avoiding the need to impose axle or tow-pin loads on absent geometry.

Load Transfer Verification

To verify that the global-to-local load transfer was implemented consistently, the local drag-brace model was checked for static equilibrium under the reapplied port-section wrench. The verification procedure is analogous to that used for the applied force components in the global model in Section 6.2.3, but is here performed on the reduced local submodel.

For each load case, the summed reaction forces at the three constrained reference points in the local model were compared with the applied port-force components (F_x, F_y, F_z), with the summed reaction moments checked against the applied port moments (M_x, M_y, M_z) as a consistency check. Table 6.8 gives one representative example for load case `TBL_SP_STEADY_PULL`. The same procedure was applied to the remaining load cases, with similarly small residuals, confirming that the transferred port wrench was reproduced consistently in the local model.

For the moment verification, the expected reaction moment was decomposed into the directly applied port moment and the additional moment generated by the applied port force acting at an offset from the constrained reference points, such that $\mathbf{M}_{\text{tot}} = \mathbf{M}_{\text{port}} + \mathbf{r} \times \mathbf{F}_{\text{port}}$.

Table 6.8: Representative local equilibrium check for reapplied port wrench, load case `TBL_SP_STEADY_PULL`

Force quantity	X **[kN]**	Y **[kN]**	Z **[kN]**
Applied port force $\mathbf{F}_{\text{port}}$	7.87	0.00	-10.34
Summed reaction force at fuselage RP	-7.85	0.00	10.33
Moment quantity	X **[kNm]**	Y **[kNm]**	Z **[kNm]**
Applied wrench moment $\mathbf{M}_{\text{port}}$	0.00	3.10	0.00
Force-arm moment $\mathbf{r} \times \mathbf{F}_{\text{port}}$	0.00	2.14	0.00
Total expected moment $\mathbf{M}_{\text{tot}}$	0.00	5.24	0.00
Summed reaction moment	0.00	-5.24	0.00

The applied and recovered force components differed only slightly and were therefore deemed sufficiently accurate for the present verification. The same held for the moment balance, for which the agreement was likewise considered sufficient; when rounded to two decimal places, both values reduce to a magnitude of 5.24 kNm.

6.3.4. Local Outputs and Hotspot

The local drag-brace model provided stress outputs at the identified hotspot location for each towing manoeuvre considered in the load set. A single reference hotspot location was adopted for all manoeuvres, defined by the most severe case (`ACC_PULL_SMOOTH`). Although the peak element could vary slightly between manoeuvres, the corresponding hotspot regions remained very close, and a uniform reference location was therefore retained to ensure consistent comparison of local stress histories across the full load set. To interpret these results, the stresses were first summarised in terms of peak stress σ_{pk} and a normalised damage indicator D, which allowed the relative severity of the manoeuvres to be compared within each towing concept. Table 6.9 therefore ranks all manoeuvres for both TB and TBL towing, highlighting which operational events dominate the local drag-brace loading and are expected to contribute most strongly to fatigue damage. A notable outcome was that the most severe manoeuvre remained `ACC_PULL_SMOOTH` for both towing concepts. The intermediate ordering, however, was not identical. Several manoeuvres changed position between the TB and TBL rankings, indicating that the local drag-brace response was not only amplified under TBL towing, but also redistributed across the manoeuvre set.

Table 6.9: Dominant local drag-brace hotspot indicator per manoeuvre, ranked by normalised damage indicator D

(a) TB ranking

Rank	Manoeuvre	D [-]	σ_{pk} [MPa]
1	`TB_ACC_PULL_SMOOTH`	1.00	483
2	`TB_SP_STEADY_PULL`	0.71	342
3	`TB_BRK_PUSH_RAPID`*	0.62	300
4	`TB_BRK_PUSH_SMOOTH`	0.62	300
5	`TB_TURN_PULL_WIDE`	0.40	191
6	`TB_TURN_PULL_TIGHT`	0.32	153
7	`TB_BRK_PULL_RAPID`	0.29	138
8	`TB_ACC_PUSH_SMOOTH`	0.16	76
9	`TB_SP_STEADY_PUSH`	0.15	72
10	`TB_BRK_PULL_SMOOTH`	0.14	70
11	`TB_TURN_PUSH_TIGHT`	0.14	65
12	`TB_TURN_PUSH_WIDE`	0.13	61

(b) TBL ranking

Rank	Manoeuvre	D [-]	σ_{pk} [MPa]
1	`TBL_ACC_PULL_SMOOTH`	1.00	784
2	`TBL_SP_STEADY_PULL`	0.64	498
3	`TBL_BRK_PUSH_RAPID`*	0.47	372
4	`TBL_BRK_PUSH_SMOOTH`	0.47	372
5	`TBL_BRK_PULL_RAPID`	0.41	319
6	`TBL_TURN_PULL_WIDE`	0.35	273
7	`TBL_ACC_PUSH_SMOOTH`	0.33	256
8	`TBL_BRK_PULL_SMOOTH`	0.29	229
9	`TBL_TURN_PULL_TIGHT`	0.29	227
10	`TBL_SP_STEADY_PUSH`	0.19	151
11	`TBL_TURN_PUSH_TIGHT`	0.05	33
12	`TBL_TURN_PUSH_WIDE`	0.03	27

*The `BRK_PUSH_RAPID` manoeuvre is implemented with the same applied spectrum as `BRK_PUSH_SMOOTH` (see Section 5.7).

In addition to the absolute rankings in Table 6.9, Table 6.10 directly compares the stress response between TB and TBL towing for the same manoeuvres. The table therefore reports the ratio $\sigma_{\text{TBL}}/\sigma_{\text{TB}}$ at the hotspot. This comparison quantifies how much higher, or lower, the local stresses become when towbarless towing is used instead of a conventional towbar. Together, Tables 6.9 and 6.10 provide both the internal ranking of manoeuvre severity and a direct measure of the relative amplification of drag-brace stresses under TBL operation, which forms the basis for the subsequent fatigue and damage assessment.

Table 6.10: Peak stress ratio between TBL and TB towing for the local drag-brace hotspot

Rank	Manoeuvre	$\sigma_{\text{TBL}}/\sigma_{\text{TB}}$ [-]
1	`ACC_PUSH_SMOOTH`	3.35
2	`BRK_PULL_SMOOTH`	3.28
3	`BRK_PULL_RAPID`	2.32
4	`SP_STEADY_PUSH`	2.10
5	`ACC_PULL_SMOOTH`	1.62
6	`TURN_PULL_TIGHT`	1.49
7	`SP_STEADY_PULL`	1.45
8	`TURN_PULL_WIDE`	1.43
9	`BRK_PUSH_RAPID`*	1.24
10	`BRK_PUSH_SMOOTH`	1.24
11	`TURN_PUSH_TIGHT`	0.55
12	`TURN_PUSH_WIDE`	0.45
Average		1.7

*The `BRK_PUSH_RAPID` manoeuvre is implemented with the same applied spectrum as `BRK_PUSH_SMOOTH` (see Section 5.7).

As a verification step, the average TBL-to-TB stress ratio obtained from the local drag-brace model in Table 6.10 was compared with the corresponding average ratio from the global NWLG model. For the three drag-brace-related hotspot locations considered in the global model (Table 6.7), the mean ratio was 1.55, whereas the local model yielded an average value of 1.71. The local-model value was therefore somewhat higher, which may reflect a limited influence of local geometry and stress redistribution in the refined drag-brace representation. Nevertheless, the difference remained modest, and the overall agreement in trend and order of magnitude supported the conclusion that the TB-to-TBL load translation to the local drag-brace model was plausible and sufficiently representative for the subsequent hotspot and fatigue assessment.

Local hotspot stress extrema for compression-dominated manoeuvres

While Table 6.9 ranks the manoeuvres using the local peak hotspot stress σ_{pk}, the compression-dominated cases additionally require verification of the local minimum stress at the same fixed hotspot location. This check is only carried out for manoeuvres in which the overall drag brace is driven into compression, such that local bending may still produce a tensile region on one side and a compressive region on the other. These manoeuvres are summarised in Table 6.11 for both TB and TBL towing.

For each listed manoeuvre, the local response is characterised by the peak stress σ_{pk} and the minimum stress σ_{min}, where,

- σ_{pk} local peak hotspot stress during the manoeuvre [MPa]
- σ_{min} minimum local hotspot stress during the manoeuvre [MPa]

For consistency, σ_{pk} and σ_{min} are both evaluated at the plane perpendicular to the brace beam at the fixed hotspot location.

Table 6.11: Local hotspot stress extrema for compression-dominated manoeuvres

	TB		**TBL**	
Manoeuvre	σ_{pk} **[MPa]**	σ_{min} **[MPa]**	σ_{pk} **[MPa]**	σ_{min} **[MPa]**
`ACC_PUSH_SMOOTH`	76	-44	256	-154
`SP_STEADY_PUSH`	72	-42	151	-92
`BRK_PULL_SMOOTH`	70	-11	229	-138
`BRK_PULL_RAPID`	138	-81	319	-189

The push-turn manoeuvres were excluded from this compression-branch check, as they do not enter compression at the fixed hotspot location used consistently for all manoeuvres. Although these cases contain a relatively larger lateral load component, the detected hotspot in the present study is governed primarily by the longitudinal drag-brace response. As a result, the push-turn cases do not drive the local hotspot stress through zero at the governing location and therefore remain outside this additional check.

6.4. Stage S — Local to Specimen Mapping for Laboratory Test Correlation

Stages G and L identified the drag brace as the governing fatigue hotspot in the NWLG under towing. Stage S provided the final link from these structural hotspots to the laboratory dog-bone specimen used in Chapter 7. The aim was to construct a mechanically meaningful equivalence between the local response in the drag brace and the uniform axial response of the specimen, so that measured towing loads on the NWLG could be translated into an equivalent axial stress spectrum in the dog-bone.

6.4.1. Specimen Finite-Element Model

The model was created in Abaqus as a three-dimensional solid, with the gauge section, fillet radius and grip transition detailed according to the machining drawing (Figure 7.1a). The specimen was intended to represent a smooth, uniaxial reference for the drag-brace hotspot. The specimen FEM model is shown in Figure 6.6.

Boundary conditions represented symmetric axial gripping. The end faces were kinematically coupled to reference points at the jaw locations, and an axial displacement or force was applied at one jaw while the other was fixed in translation. This enforced a nearly uniform axial strain in the gauge, so that the gauge stress, with A_{db} the net cross-section of the dog-bone, is well approximated by:

$$\sigma_{\text{spec}} = \frac{F_{\text{spec}}}{A_{\text{db}}} \tag{6.23}$$

where,

- σ_{spec} nominal axial stress in the specimen gauge section [Pa]
- F_{spec} applied axial force in the specimen (through machine) [N]
- A_{db} net cross-sectional area of the dog-bone gauge section [m^2]

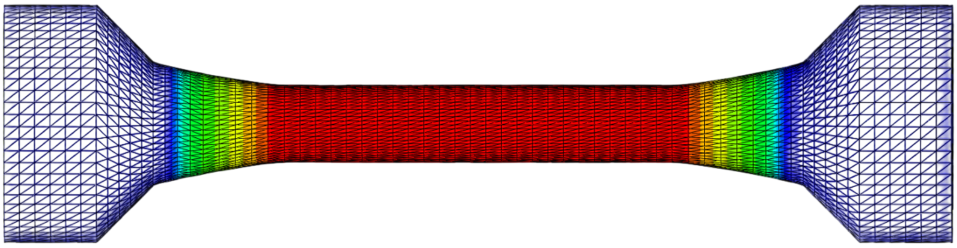

Figure 6.6: Dog-bone specimen Abaqus model

6.4.2. Hotspot to Specimen Equivalence

The drag-brace submodel from Stage L provided local hotspot stress measures for each towing manoeuvre. For each manoeuvre, the hotspot response was characterised by the volume-averaged maximum principal stress, which was used as the local stress measure for subsequent specimen mapping.

$$\bar{\sigma}_{1,\text{local}} = \bar{\sigma}_1\big(\text{hotspot, manoeuvre}\big)$$

The equivalence between drag brace and specimen was defined by mapping the local hotspot stress history to an equivalent axial stress history in the dog-bone specimen. In this way, the specimen reproduced the local stress cycle associated with each towing manoeuvre, while the peak local stress remained available as a calibration quantity.

$$\sigma_{\text{spec},m}(t) = \frac{F_{\text{spec},m}(t)}{A_{\text{db}}} \approx \sigma_m(t) \tag{6.24}$$

so that the local hotspot stress history, and therefore the corresponding stress range, was reproduced in the specimen gauge. For each manoeuvre m, WP1 provided a measured tow-force time series $F_m(t)$. First, the baseline hotspot stress under zero tow load (weight only) was defined as

$$\sigma_0 = \sigma(F = 0).$$

Next, for each manoeuvre m, the specimen model was evaluated at the signed peak force level $F_{\text{pk},m}$ used in the corresponding FE calibration case, to obtain the associated hotspot stress

$$\sigma_{\text{pk},m} = \sigma(F_{\text{pk},m}).$$

To map measured towing-force time histories to hotspot stresses, a linear force–stress relation was assumed to hold over the operating range of each manoeuvre. The reconstructed hotspot stress history for manoeuvre m is then:

$$\sigma_m(t) = \sigma_0 + k_m\, F_m(t) \tag{6.25}$$

where,

- $\sigma_m(t)$ reconstructed hotspot stress time history for manoeuvre m [MPa]
- σ_0 baseline hotspot stress at $F_m(t) = 0$ [MPa]
- k_m manoeuvre-specific linear scaling coefficient [MPa/kN]
- $F_m(t)$ towing-force time history for manoeuvre m [kN]
- t time [s]
- m manoeuvre index [-]

The scaling coefficient k_m was identified from a baseline state ($F = 0$) and a peak-load state, such that the linear model reproduced the corresponding peak hotspot stress:

$$k_m = \frac{\sigma_{\text{pk},m} - \sigma_0}{F_{\text{pk},m}} \tag{6.26}$$

where,

- $\sigma_{\text{pk},m}$ hotspot stress evaluated at peak tow force for manoeuvre m [MPa]
- $F_{\text{pk},m}$ signed peak force level used in the FE calibration case for manoeuvre m [kN]

For manoeuvres that remain tension-dominated at the hotspot, the linear stress–force relation of Eq. (6.25) was used directly. For compression-dominated manoeuvres, however, the local hotspot response may pass through zero and enter compression due to nominal section compression and bending of the drag brace. In those cases, the tensile and compressive parts of the local response were treated separately by introducing an additional compression-branch scaling coefficient. For these compression-dominated manoeuvres, the reconstructed hotspot stress history was written as

$$\sigma_m(t) = \begin{cases} \sigma_0 + k_m\, F_m(t), & F_m(t) > F_{\sigma=0,m} \\ \sigma_0 + k_{m,\text{comp}}\, F_m(t), & F_m(t) \le F_{\sigma=0,m} \end{cases} \tag{6.27}$$

where $F_{\sigma=0,m}$ denoted the signed applied towing force at which the reconstructed hotspot stress passed through zero for manoeuvre m, such that the compression-branch relation became active.

6.4.3. Lab Specimen Stress per Manoeuvre

From the reconstructed stress time history $\sigma_m(t)$, the stress spectrum for each manoeuvre was computed. These resulting spectra defined the specimen loading for the subsequent fatigue and damage analyses. The maximum applied towing force levels were kept identical to those used in the global NWLG model, so that the local drag-brace stress response remained directly traceable to the previously defined global load cases.

Table 6.12 summarises the manoeuvre-specific stress scaling parameters used to translate the measured and reconstructed towing-force histories into local hotspot stress histories. For each manoeuvre, the baseline stress σ_0, the peak hotspot stress σ_{pk}, the corresponding applied force F_x, and the resulting linear scaling coefficient k_m are reported for both TB and TBL. These coefficients were then used in Eq. (6.25) to reconstruct the full hotspot stress histories from the WP1 towing-force signals.

Table 6.12: Specimen stress scaling parameters at the hotspot

(a) TB and TBL manoeuvre scaling

		TB			TBL		
Manoeuvre	σ_0 [MPa]	σ_{pk} [MPa]	F_x [kN]	k_m [MPa/kN]	σ_{pk} [MPa]	F_x [kN]	k_m [MPa/kN]
`SP_STEADY_PULL`	109	342	9.02	25.8	498	7.87	49.4
`SP_STEADY_PUSH`†	109	72	-9.02	4.2	151	-7.87	-5.2
`ACC_PULL_SMOOTH`	109	483	13.44	27.8	784	13.76	49.0
`BRK_PULL_SMOOTH`†	109	70	-5.52	7.2	229	-10.74	-11.1
`ACC_PUSH_SMOOTH`†	109	76	-9.28	3.6	256	-11.72	-12.5
`BRK_PUSH_SMOOTH`	109	300	4.15	45.9	372	5.30	49.5
`TURN_PULL_TIGHT`	109	153	2.80	15.6	227	1.99	59.3
`TURN_PUSH_TIGHT`	109	65	-2.80	15.7	36	-1.99	36.9
`TURN_PULL_WIDE`	109	191	3.57	23.0	273	2.67	61.4
`TURN_PUSH_WIDE`	109	61	-3.57	13.7	27	-2.67	30.7
`BRK_PULL_RAPID`†	109	138	-9.28	-3.1	319	-14.02	-15.0
`BRK_PUSH_RAPID`*	109	300	4.15	45.9	372	5.30	49.5

†Partial compression manoeuvre; additional compression-branch parameters are reported in Table 6.13.
*The `BRK_PUSH_RAPID` manoeuvre is implemented with the same applied spectrum as `BRK_PUSH_SMOOTH` (see Section 5.7).

For the compression-dominated manoeuvres marked in Table 6.12, an additional compression-branch calibration was introduced. The corresponding minimum hotspot stresses and compression-side scaling coefficients are reported in Table 6.13.

Table 6.13: Additional compression-branch scaling parameters at the hotspot

	TB			TBL		
Manoeuvre	$F_{\sigma=0,\text{pin}}$ [kN]	σ_{min} [MPa]	k_{comp} [MPa/kN]	$F_{\sigma=0,\text{axle}}$ [kN]	σ_{min} [MPa]	k_{comp} [MPa/kN]
`ACC_PUSH_SMOOTH`	-6.62	-44	16.5	-4.86	-154	22.5
`SP_STEADY_PUSH`	-6.52	-42	16.8	-4.27	-92	25.6
`BRK_PULL_SMOOTH`	-5.02	-11	21.8	-4.75	-138	23.0
`BRK_PULL_RAPID`	-5.33	-81	20.5	-5.14	-189	21.3

Here, $F_{\sigma=0}$ denotes the signed applied towing force at which the hotspot stress crosses zero, such that the compression-branch relation becomes active. For TB, this force is referenced at the tow-pin interface, whereas for TBL it is referenced at the axle interface. The coefficient k_{comp} denotes the linear compression-side scaling between the applied force increment beyond $F_{\sigma=0}$ and the corresponding local hotspot stress response. Table 6.13 shows that the TBL cases generally enter the compression branch at lower force magnitudes and with higher compression-side scaling coefficients than the corresponding TB cases, consistent with the stronger local stress sensitivity already observed for the TBL load introduction.

CS-23 reference case and specimen-scaling check

To anchor the specimen-level stress translation against a structural upper-bound reference, three additional reference cases were evaluated: a stationary case and two CS-23 towing-envelope cases, as summarised in Table 6.14. The longitudinal CS-23 towing cases were defined from the towing-load criterion of $0.3W$, applied in pull and push, and were not treated as representative manoeuvres within the towing spectrum. Instead, they were used as reference cases to assess whether the specimen stress levels derived from the WP2 mapping remained within a realistic severe-loading range.

Table 6.14: CS-23 reference towing cases used for specimen scaling

ID	`EventCode`	$\lvert F_{x,\text{axle}}\rvert$ [kN]	$\lvert F_{y,\text{axle}}\rvert$ [kN]
1	`MAX_STATIONARY`	0.00	0.00
2	`MAX_PULL_CS23`	23.34	0.00
3	`MAX_PUSH_CS23`	-23.34	0.00

For the present drag-brace-based specimen translation, `MAX_PULL_CS23` was retained as the governing reference case. Although the push case produced a slightly higher local hotspot stress, this result was strongly influenced by an additional geometric bending effect associated with the drag brace's over-centre locking condition. In the deployed configuration, the brace is rotated slightly past $180°$, which stabilises the mechanism in tension but also makes it more sensitive to bending once the global brace load is driven into compression during push-type manoeuvres. As a result, the `MAX_PUSH_CS23` case generated a stronger local bending response than would be expected from a purely axial load translation, and the corresponding hotspot stress became more dependent on the idealised brace geometry than on the general towing load level itself.

For that reason, the push case was noted as a useful bounding result but was not adopted as the governing specimen-scaling reference. The pull case provided a more robust and less geometry-sensitive upper-bound reference for the subsequent laboratory scaling, while remaining directly relevant to the drag-brace load path identified as governing in WP2.

In accordance with CS-23.2230, ultimate loads are defined as the limit loads multiplied by a factor of 1.5, while CS-23.2235 requires that the structure support limit loads without detrimental permanent deformation and support ultimate loads [9]. Taking the present specimen ultimate strength as $\sigma_u = 1379$ MPa, the corresponding limit-load-equivalent reference stress is

$$\sigma_{\text{ref}} = \frac{\sigma_u}{1.5} = 919 \text{ MPa}. \tag{6.28}$$

For `MAX_PULL_CS23`, the nominal specimen stress was approximately 934 MPa, while the corresponding local hotspot stress reached approximately 1190 MPa. The nominal value, therefore, remained close to the reference level, while the local value stayed below the material yield strength of approximately 1225 MPa. In this context, the higher local stress should be interpreted as a hotspot amplification arising from the local geometry rather than as the nominal section stress carried by the specimen gauge. The selected specimen scaling was therefore severe, but still mechanically plausible for a conservative GA-relevant fatigue assessment.

To convert the measured towing-force histories from Section 5.7 into specimen-relevant stress histories, the linear stress–force relation identified for the reference manoeuvre `SP_STEADY_PULL` was used as an example mapping. In this formulation, the local hotspot stress was expressed as in Equation 6.25. For the present local model, this relation was evaluated separately for TB and TBL using the `SP_STEADY_PULL` calibration case, after which the same linear mapping was applied to the full measured manoeuvre force histories. To translate the measured PC-12 towing loads to a representative PC-24 level, all force histories were scaled by the previously defined weight-scaling factor

$$k_W = 1.92$$

Because the local FE response was assumed to be linear elastic, the tow-force-induced hotspot stress varied proportionally to the applied force. Therefore, scaling the force histories by k_W also scaled the corresponding tow-induced stress variations and stress ranges by the same factor. The resulting TB and TBL stress spectra are shown in Figure 6.7.

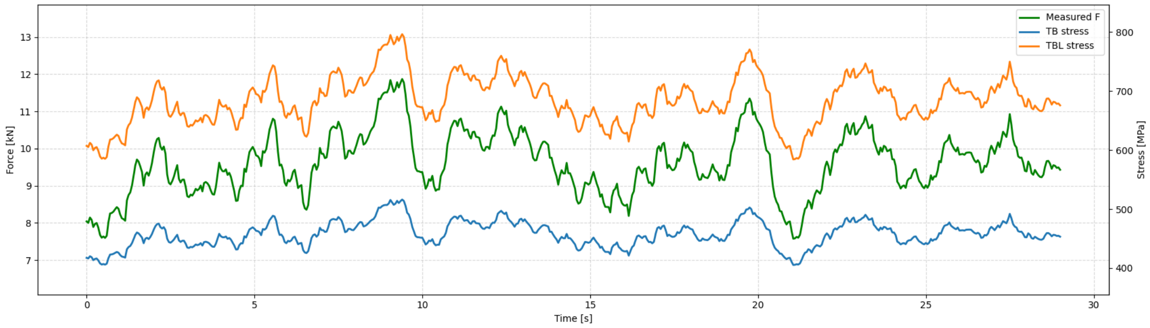

Figure 6.7: `SP_STEADY_PULL` for TB and TBL stress spectra obtained from the linear force-to-stress translation

Figure 6.7 shows that the translation scales the spectrum amplitude while preserving the cycle sequence and time-history shape. On that basis, the linear mapping was considered a sufficiently accurate and traceable method to translate the measured manoeuvre forces from Section 5.7 into local drag-brace stress histories. These translated stress histories are subsequently used as the basis for the laboratory fatigue spectrum definition in WP3.

Overall, WP2 identified the drag brace as the governing structural location for the present towing-load comparison and established the corresponding translation from towing load histories to specimen-relevant hotspot stress spectra. Based on the local drag-brace model and the linear force–stress relations summarised in Tables 6.12 and 6.13, the measured and reconstructed WP1 manoeuvres were converted into equivalent local stress histories representative of the drag-brace fatigue response. These translated spectra provide the structural basis for the laboratory fatigue programme developed in WP3.

7

WP3 – Laboratory Fatigue Testing

WP3 comprised the laboratory fatigue-testing work package, in which the towing-induced drag-brace hotspot response obtained in WP2 was translated into machine-executable axial-fatigue programmes for smooth dog-bone specimens. The main objective was to compare, under controlled laboratory conditions, the relative fatigue severity of towbar and towbarless towing spectra, including the effect of a single early overload insertion to probe load-sequence sensitivity.

The chapter is organised as follows. Section 7.1 introduces the WP3 methodology, including the translation from WP2 hotspot stresses to nominal specimen stresses and force-controlled machine inputs, the adopted test matrix, and the overload-insertion variant. Section 7.2 describes the fatigue test setup, specimen geometry, proxy material selection, and the relevant rig and control constraints. Section 7.3 then defines the manoeuvre missions and assembles them into representative towing blocks based on the assumed lifetime usage mix. Section 7.4 reduces these variable-amplitude histories by rainflow counting and discretisation into a finite set of executable stress levels, after which Section 7.5 converts them into machine-ready loading programmes subject to the imposed tension–tension and stress-cap constraints. Section 7.6 provides the pre-test severity ranking and fatigue-life framework used for internal consistency assessment. The executed laboratory tests and measured fatigue results are documented in Section 7.7. Finally, Section 7.8 discusses the main uncertainty sources and the limitations of the lab-to-service interpretation.

7.1. WP3 – Methodology

WP3 translated the towing-derived drag-brace hotspot response from WP2 into a laboratory axial-fatigue programme that could be executed on a 15 kN servo-hydraulic test frame. The central requirement was damage relevance. Therefore, the variable-amplitude towing spectra (TB and TBL) had to be represented in the laboratory by an axial loading programme that, as closely as practicable, reproduced the stress ranges and mean-stress effects that governed fatigue damage at the structural hotspot. Accordingly, the WP2 hotspot stress histories were mapped to a nominal specimen stress history and then to a machine force history using the dog-bone geometry in Figure 7.1.

Specimen representation and nominal stress definition. The laboratory specimens were smooth, round dog-bones loaded in axial tension–tension. With d_g the gauge diameter, the net cross-sectional area is

$$A = \frac{\pi d_g^2}{4} \tag{7.1}$$

and the nominal gauge stress corresponding to an applied force history $F(t)$ is

$$\sigma_{\text{nom}}(t) = \frac{F(t)}{A} \tag{7.2}$$

where,

- $\sigma_{\text{nom}}(t)$ nominal axial stress in the specimen gauge section [MPa],
- $F(t)$ applied axial force history [N],
- A net cross-sectional area of the gauge section [mm^2].

This definition provided a direct, traceable conversion between the commanded machine force and the specimen stress, and was used consistently for both the TB- and TBL-derived programmes.

Hotspot-to-specimen spectrum mapping. $\sigma_{\text{HS}}(t)$ denotes the manoeuvre-resolved hotspot stress history obtained in WP2 for the governing drag-brace location. Each towing spectrum was expressed as a hotspot-equivalent nominal specimen stress history, $\sigma_{\text{spec}}(t)$, using the same mean-stress correction framework as adopted in WP2 (modified Goodman), such that tension–tension cycles with non-zero mean stress were treated consistently across modelling and test. In the smooth-specimen fallback case, $\sigma_{\text{spec}}(t)$ was obtained by back-calculating the nominal stress required to reproduce the hotspot driving quantity under the WP2 model. The corresponding machine force history was then defined by

$$F_{\text{spec}}(t) = A\,\sigma_{\text{spec}}(t), \tag{7.3}$$

and was implemented in force control. The frame capacity constrained the commanded history, $|F_{\text{spec}}(t)| \leq 15\,\text{kN}$. In practice, specimen failure occurred below this machine limit, and thus, an additional force cap was introduced later in the test implementation, as discussed in the following subsections.

Mission editing, block construction, and test matrix. The towing-derived time histories (WP1) were condensed into mission-level blocks representative of ground-towing usage. Rainflow counting was used to identify the cycle ranges and means, after which the variable-amplitude histories were edited into machine-executable blocks. Separate blocks were constructed for TB and TBL.

A retardation variant was generated by appending a single overload/retardation event once, before the first 100-mission block only (therefore, the overload is not repeated in subsequent block repetitions). This insertion enabled a direct assessment of whether a one-time overload produced a measurable change in the subsequent response compared to the corresponding baseline spectra (TB, TBL). In total, four spectra were tested (TB, TB+RET, TBL, TBL+RET), with three repetitions for the clean spectrum and two replicate specimens per retardation case, resulting in a comparison matrix of 10 specimens. In addition, two separate specimens were used during machine calibration and programme verification, resulting in a total of 12 specimens tested across the full WP3 campaign.

Actuation and control. All tests were performed on a $15\,\text{kN}$ servo-hydraulic fatigue frame in load control, using real-time force limits to prevent accidental overload. The frame was operated at 40 Hz. The applied stress ratio $R = \sigma_{\text{min}}/\sigma_{\text{max}}$ followed the edited mission definition and remained within $0.1 \leq R \leq 0.9$, ensuring tension–tension loading without crossing zero load, consistent with both specimen gripping and machine capability.

For both towing concepts, the reported outputs comprised the cycles and mission blocks required to fracture for each specimen, the corresponding TB/TBL life and damage ratios, and post-mortem observations (fractography) confirming fatigue-dominated failure characteristics. Given the test-frame constraints (tension–tension loading, force capacity, and controlled force tracking) and the use of smooth dog-bone specimens, these results were interpreted primarily in terms of relative spectrum severity rather than absolute operational life. They therefore provided an experimental anchor for the spectrum-damage evaluation and bounded the uncertainty of the relative fatigue demand between towbar and towbarless towing.

Candidate approaches for laboratory fatigue tests

The WP3 fatigue campaign compared towbar and towbarless towing by varying what was held constant between the two concepts. The core distinction was the comparison definition: whether the test isolates towing dynamics and spectrum build-up or intentionally includes the geometric load-path difference (towing location/moment arm).

Table 7.1 summarises three candidate approaches. In brief, Approach (1) provides the cleanest isolation of spectrum build-up and dynamic effects by holding the tow point fixed, but may under-represent the true TBL load path if towbarless towing effectively loads closer to the axle. Approach (2) is more representative because it allows the tow point to differ (pin vs. axle), but it mixes geometric effects with spectral and dynamic differences. Approach (3) extends Approach (2) by inserting a single rare maximum-load event to probe overload/retardation sensitivity. Therefore, it is inherently more uncertain and is therefore positioned as an additional case rather than a baseline comparison.

Table 7.1: Summary of three possible WP3 fatigue-test approaches

Approach	Comparison basis	Main differences	Primary insight / main drawback
(1) Same tow point	TB spectrum vs. TBL spectrum at the same towing location (pin location)	Only (A) spectrum build-up differences (e.g. mitigating push segments for TB) and (B) dynamic differences (speed/acceleration profiles)	Insight: isolates dynamic/spectrum effects with minimal geometric confounding. Drawback: may underrepresent the true TBL load path if TBL acts closer to the axle/wheel capture and induces larger moments. Outcome: expected small difference; limited experimental value.
(2) Different tow point	TB spectrum vs. TBL spectrum at different towing locations (pin vs. axle)	(C) towing location and resulting moment arm (M expected larger for TBL), plus (A) spectrum build-up and (B) dynamics	Insight: captures the representative geometric/load-path difference between TB and TBL. Drawback: mixes geometric effects with dynamics/spectrum effects, making attribution less clean, but more representative. Outcome: expected a clear contrast by design due to intentionally different tow points and spectra.
(3) Extreme-load insertion	TB spectrum vs. TBL spectrum with an added extreme event	(D) Single maximum towing load event (retardation/overload effect) inserted before variable-amplitude cycles, (C) combined with towing location, (A) spectrum build-up, and (B) dynamics	Insight: probes sensitivity to rare overloads (retardation/acceleration of crack growth). Drawback: overload/retardation response is difficult to predict a priori and requires careful justification of the "limit" level (σ_{lim} vs. σ_y Outcome: sensitivity case to evaluate whether the effect is larger on the TBL spectrum than on the TB spectrum.

Operational scenarios (mission context)

To translate the manoeuvre-level spectra into a finite and reproducible laboratory programme, the towing operation was idealised into four canonical mission types (A–D). Each mission represents a typical ground-handling "task" defined by a prescribed sequence of measured manoeuvre segments (straight towing, turns, braking, etc.) and a characteristic duration. The missions are ordered by increasing operational complexity and expected loading severity, such that A/B represent short repositioning actions near the hangar area, C represents longer airfield repositioning on open tarmac, and D represents a full-airport repositioning into the hangar with the highest manoeuvre count and interaction complexity. Mission B is identical to Mission A in structure, but includes an explicit rapid-brake segment to represent a rare, short-duration high-severity input within an otherwise light cycle. The manoeuvre sequences are grouped by operational complexity/duration:

- **A–B:** simple tarmac-to-hangar repositioning (TB and TBL assumed identical in manoeuvre sequence).
- **C:** airfield repositioning on tarmac (TB primarily pull, while TBL includes push capability).
- **D:** full-airport repositioning into the hangar (TB primarily pull, while TBL includes push capability).

This led to the following working hypotheses, combining the approaches and operational scenarios:

- **Approach (1):** TB and TBL responses are expected to be close for pull-dominated manoeuvres, thus differences are mainly due to dynamics (TBL often higher) and spectrum construction.
- **Approach (2):** TBL is expected to be more damaging due to towing at/near the axle (larger induced moments), hence shorter life.
- **Approach (3):** The net effect of a single early overload is ambiguous under variable-amplitude loading. The overload level is therefore treated as a sensitivity input. The aircraft is designed for a certain load case, so it could either be that the TB is over- or the TBL is under-designed. Its magnitude is justified relative to the governing towing limit case and is kept identical across TB and TBL to preserve interpretability.

Within this mission framework, Approach (2) was adopted as the baseline because it preserved the representative geometric load-path distinction between TB and TBL, while still retaining the measured manoeuvre content and spectrum build-up. Approach (3) was included as a sensitivity case by applying a single early overload insertion, applied only once, to probe load-sequence effects without altering the background mission content. Approach (1) was not pursued further because it would intentionally suppress the tow-point difference central to the practical distinction between the two towing concepts.

Sources of Scatter

In both laboratory testing and service operation, fatigue data exhibit significant scatter that must be accounted for when interpreting fatigue test results. Table 7.2 summarises the main sources of scatter in material, production, loading, environment and human factors for tests and in-service structures.

Table 7.2: Sources of scatter in fatigue testing and service, adapted from TU Delft AE4ASM005 course materials [75] and Schijve [52]

	Possible sources of scatter	
Aspects considered	**Laboratory test series**	**Structures in service**
Material	Material structure	Material from different batches and manufacturers
Production	Specimen production Specimen surface quality	Production of structures over years Surface quality of fatigue critical notches in structure
Fatigue load	Type of fatigue load (CA, VA) Test frequency Accuracy of test equipment	Load spectra in service Different users of structure Fatigue life covers years
Environment	Laboratory environment, controlled temperature and humidity	Service environment, possibly aggressive
Personal aspects	Skill of laboratory technicians	Different users

Within WP3, three analytical levels were kept distinct. First, the WP2 hotspot histories were translated into nominal specimen stresses and then conditioned into machine-executable tension–tension blocks. This step used the adopted mean-stress treatment and machine constraints, but did not itself constitute a life prediction. Second, the resulting discrete block levels were evaluated using an MMPDS-style S–N framework to obtain a pre-test severity ranking and to assess internal consistency across spectra. Third, the laboratory tests provided the decisive result of WP3 through the measured cycles and missions to fracture. The modelling in this chapter is therefore used primarily to define comparable input spectra and to support relative interpretation, whereas the experimental lives remain the governing basis for the final TB–TBL comparison.

7.2. Fatigue Test Setup

This section defines how the towing-derived hotspot spectra from WP2 could be translated into an executable laboratory fatigue programme. It first justifies the use of 17-4PH (H900) as a practical proxy material for 300M, then describes the specimen geometry, stress scaling, machine constraints, and allocation of specimens across the TB, TBL, TB+RET, and TBL+RET spectrum variants.

7.2.1. Material Selection: 17-4PH (H900) as Proxy for 300M

For the laboratory programme, 17-4PH stainless steel in condition H900 was selected as the proxy material because it was the strongest option available within the project timeframe and budget, whereas 300M was not practically obtainable under these constraints. The two alloys differ in class and application: 300M is an ultra-high-strength low-alloy steel (quenched and tempered) used for primary load-bearing landing-gear forgings, while 17-4PH (H900) is a precipitation-hardened stainless steel commonly used on aircraft for pins, lugs, and fittings, which is an aerospace-grade material, but not typically selected for the highest load-bearing forgings. Representative room-temperature yield strengths are $\sigma_{y,\text{300M}} = 1.68$ GPa and $\sigma_{y,\text{17-4PH(H900)}} = 1.23$ GPa which gives a yield-strength ratio

$$k = \frac{\sigma_{y,\text{17-4PH(H900)}}}{\sigma_{y,\text{300M}}} \approx \frac{1.23}{1.68} \approx 0.73 \tag{7.4}$$

These values are given in Table 6.1, while the corresponding supplier material datasheet for the 17-4PH (H900) specimens used in the laboratory programme is provided in Appendix C.1. Elastic moduli are similar (~ 200 GPa), so stiffness effects are minor. Nonetheless, differences in microstructure behaviour imply that absolute fatigue lives may differ.

Moreover, the Abaqus drag-brace model was developed using 300M material assumptions, while the laboratory specimens are 17-4PH (H900). The translation from the component-level hotspot stresses to a specimen-level stress spectrum, therefore, requires an explicit scaling assumption, since the absolute stress level predicted by the 300M-based model does not necessarily match the target maximum stress level for 17-4PH (including the intended safety margin) in a one-to-one manner.

To ensure that the laboratory programme was most likely to produce a decisive comparative outcome within a feasible cycle budget, the TBL spectrum was scaled such that its maximum stress level reaches the 17-4PH yield stress at the prescribed ultimate towing load. The TB spectrum was then scaled using the same multiplicative factor to preserve the relative TB–TBL severity and spectrum shape. This procedure resulted in an amplitude scaling factor of

$$\text{AMP\_SCALE} = 1.10$$

7.2.2. Laboratory Programme

All fatigue tests were performed on ten 17-4PH (H900) dog-bone specimens with identical geometry on a 15 kN servo-hydraulic frame, as shown in Figures 7.1 and 7.2. The laboratory programme evaluated four spectrum variants: TB and TBL, each tested both without retardation and with the applied retardation (RET) treatment. The corresponding nominal axial stress spectra were denoted S_{tb}, S_{tbl}, $S_{\text{tb+ret}}$, and $S_{\text{tbl+ret}}$. In total, three baseline specimens were tested for each of the TB and TBL spectra, while two specimens were tested for each retardation variant. The full specimen identification and spectrum allocation are provided in Appendix C.2, Table C.1.

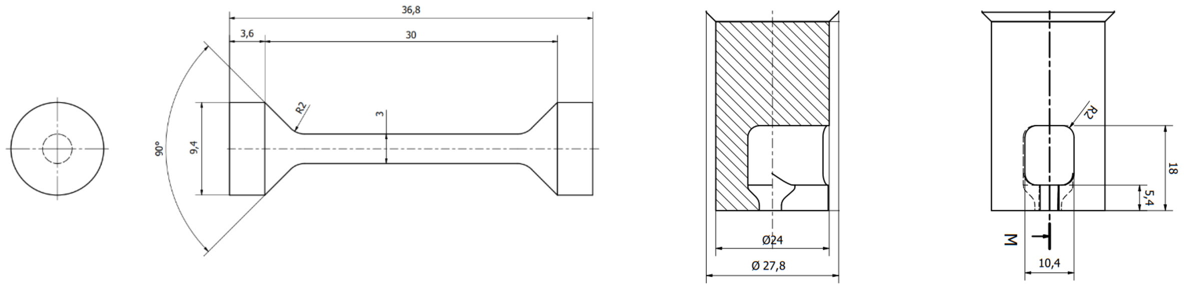

(a) 17-4PH (H900) axial-fatigue specimen **(b)** Clamps used to load specimen

Figure 7.1: Clamp and specimen technical drawings [received from laboratory staff]

For a smooth, round tensile/fatigue specimen, the axial force at a certain stress level is

$$F = \sigma_u \, A = \sigma_u \, \frac{\pi d^2}{4} \tag{7.5}$$

With diameter $d = 3$ mm and ultimate strength $\sigma_u = 1379$ MPa $= 1379$ N/mm^2:

$$A = \pi \left(\frac{d}{2}\right)^2 = \pi(1.5\ \text{mm})^2 = 7.0686\ \text{mm}^2, \qquad F_u = \sigma_u A = 1379 \times 7.0686 \approx 9748\ \text{N} \approx 9.8\ \text{kN} \tag{7.6}$$

The test frame was rated to approximately 15 kN, which exceeded the theoretical yield load of the specimen. A force limit was therefore imposed in the machine control to prevent accidental overloading, even though the planned programme applied fatigue loading at nominal stress levels well below yield. The machine was operated in the range 40 Hz with a load ratio $0.1 \leq R \leq 0.9$ (tension–tension, without crossing zero load). This operating window is acceptable, as the present tests were intended to characterise fatigue behaviour under tensile loading only, rather than fully reversed loading.

(a) Overall view of the 15 kN servo-hydraulic fatigue machine

(b) Zoomed view of the specimen and wedge grips

Figure 7.2: Laboratory setup for the 17-4PH (H900) axial fatigue programme in the 15 kN servo-hydraulic fatigue machine

7.3. Specimen Loading Spectra

Chapter 5 and 6 provide manoeuvre-resolved axial stress histories at the governing drag-brace hotspot for all canonical towing events (see Section 6.4.3). In WP3, these hotspot histories were converted into machine-executable force-controlled spectra by applying the same translation chain for each mission:

$$\text{hotspot stress} \rightarrow \text{nominal specimen stress} \rightarrow \text{material/amplitude scaling} \rightarrow \text{actuator force}$$

7.3.1. Hotspot Stress Translated to Manoeuvre Missions (A–D)

For each manoeuvre type, the Abaqus hotspot output was mapped to a representative drag-brace stress time history $\sigma(t)$ (hotspot metric, nominal section stress: S_1). A manoeuvre, therefore, became a stress trace over its duration, such that the complete operational set could be reconstructed as a concatenation of manoeuvre traces. Four manoeuvre missions were constructed:

- **Mission A–D:** missions represent increasing towing “severity” (operational heaviness), each built as a prescribed sequence of manoeuvre segments.
- **Configurations:** each mission was generated for towbar and towbarless, resulting in eight stored mission time histories: {A,B,C,D}×{TB,TBL}.

An example mission (A-TBL) stress history / stress-range evolution is shown in Figure 7.3. The signal was predominantly tensile with occasional compressive excursions. This stress history was consistent with a forward-facing drag-brace offset, resulting in a quasi-static tensile bias (linked to the net load path and aircraft weight contribution), while compressive minima were comparatively limited. In other words, the mission spectra were tension-dominated by design, with bounded compression.

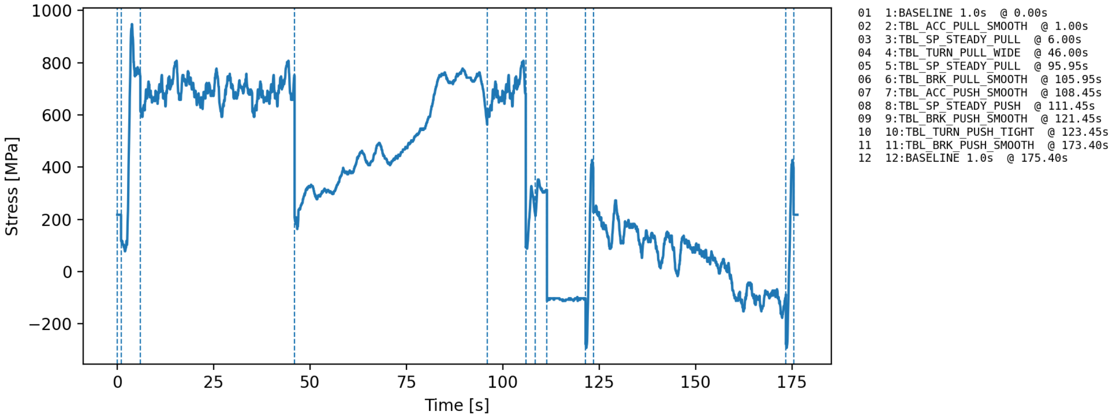

Figure 7.3: Mission A-TBL drag-brace hotspot section nominal stress history (not scaled by 1.1)

7.3.2. Towing Mission Schedules and Spectrum Assembly

The airport ground cycle was modelled as a sequence of canonical towing manoeuvres, including smooth acceleration, steady straight towing, turns, and braking. For each manoeuvre m, a reference load spectrum $S_m(t)$ was available from the measured towing data. A ground-towing mission was then defined by prescribing, for each manoeuvre in the sequence, whether it was run for a fixed time interval (time-controlled) or for a fixed number of occurrences (event-controlled). The lightest representative schedule, Mission A, is shown in Table 7.3. The remaining schedules, Mission B and the paired TB/TBL schedules for Missions C and D, are provided in Appendix C.3.

The four mission schedules defined representative archetypes of ground-towing usage. The mission definitions were established through repeated airfield observations and discussions with towing operators and were intended to reflect realistic manoeuvre sequencing and dwell times for typical ground-handling tasks. For spectra A and B, the prescribed mission schedule was identical for TB and TBL, because these cycles represent short repositioning tasks in which the operational sequence is not materially affected by the towing concept. Differences between TB and TBL were therefore expressed through the measured manoeuvre spectra $S_m(t)$ and the resulting hotspot stresses, rather than through different mission scheduling. For spectra C and D, TB and TBL mission schedules differed to reflect the greater operational flexibility of towbarless towing, notably through the use of push-capable repositioning strategies.

For spectra C and D, TB and TBL mission schedules are reported in paired tables (Tables C.3–C.4) to make the operational differences explicit. Airfield observations and operator feedback indicate that towbar towing generally aims to avoid push manoeuvres where possible. This typically leads to alternative repositioning approaches that require longer straight segments and/or additional pull-turn-brake manoeuvres to achieve the same end position. Towbarless towing provides greater operational flexibility (notably push capability with different turn and brake combinations), which is reflected in the dedicated TBL schedules for spectra C and D.

NASA Ames research shows that the pushback process time, defined as the duration from off-block after pushback clearance until the aircraft begins taxiing under its own power, averages 4.72 minutes with a standard deviation of 2.27 minutes over 20,595 departures. These statistics, drawn from NASA's ATD-2 operational dataset of commercial airline departures, provide an empirical basis for modelling pushback-time variability in departure sequencing [76]. The resulting mission duration of spectrum A (order of 3 min for the lightest scenario) is therefore deemed realistic for a short repositioning/pushback-type ground-towing cycle.

Table 7.3: Representative mission schedule for spectrum A (light ground-towing cycle, identical for TB and TBL)

#	Manoeuvre m	Control	Value
1	Stationary baseline	time	1 s
2	Smooth pull acceleration	event	–
3	Straight pull (constant speed)	time	40 s
4	Wide-radius pull turn	event	–
5	Straight pull (constant speed)	time	10 s
6	Smooth pull braking	event	–
7	Smooth push acceleration	event	–
8	Straight push (constant speed)	time	10 s
9	Smooth push braking	event	–
10	Tight-radius push turn	event	–
11	Smooth push braking	event	–
12	Stationary baseline	time	1 s

Mission lifetime usage mix

Based on the four towing operations, Table 7.4 defines a simplified usage mix for the full towing lifetime of the nose-wheel landing gear. The fractions α_i specify what proportion of all towing missions is assumed to follow each spectrum. Most missions are light or medium (A and C), a smaller share is heavy (D), and only a very small fraction contains an explicit rapid brake input (B). When constructing the lifetime load spectrum, missions of type A–D are repeated in these proportions so that the cumulative number of manoeuvres and load cycles reflects an entire operational life rather than a single ground-towing event.

Table 7.4: Usage mix of spectra A–D over the NWLG towing lifetime

Spectrum	Description	Share α_i [%]
A	Light spectrum	49.0%
B	Light spectrum + rapid brake input	1.0%
C	Medium spectrum	35.0%
D	Heavy spectrum	15.0%
	Total	**100%**

7.3.3. Implementation of Retardation

In addition to the baseline TB and TBL spectra, WP3 included a retardation variant in which a single overload event was inserted into the otherwise unchanged variable-amplitude block. The purpose was to probe whether the TB–TBL comparison was sensitive to load-sequence effects. As discussed in the Literature Study, Subsection 2.7.3, an overload can increase short-term damage but also induce local plasticity and residual stresses that reduce subsequent crack-growth rates, thereby extending the effective life. This makes the overload case a targeted check on the applicability of linear damage summation under spectra that contain rare high-amplitude events.

Retardation level selection and placement. The retardation cycle was applied once, before the first 100-mission block. A single absolute retardation level was used for both the TB and TBL spectra. This choice was motivated by operational representation, as the aircraft is expected to experience both towing configurations in service, and a towbarless event is plausibly the governing factor for the maximum nose-wheel landing gear load during ground towing. Using the same retardation level, therefore, allows evaluation of whether an early high-load event can influence subsequent damage accumulation in both configurations, including any potential life-extension or reduction effect in the TB spectrum after a TBL-governed maximum event.

Defining the retardation level instead as a fixed multiplier of each spectrum maximum (e.g. $\times 1.2$ or $\times 1.3$) would lead to an asymmetric comparison. The TB retardation may become too mild to produce an observable effect, while the TBL retardation becomes substantially more severe. Therefore, the shared absolute retardation level yielded a more interpretable and comparable sensitivity study across TB and TBL.

Overload magnitude. The overload level was anchored to the CS-23 towing requirement. As stated in Table 2.4, the maximum longitudinal towing force was taken as $0.3W$, which corresponds to approximately 24 kN for the PC-24. This level was adopted as the representative extreme towing event for the retardation case.

Interpretation for smooth specimens. Within the present smooth dog-bone setup, the overload can have two competing effects. First, it can increase immediate fatigue damage by introducing a high-amplitude cycle early in the block. Second, if the overload drives local plasticity (even if limited), it may introduce beneficial residual stresses and strain hardening that delay subsequent crack initiation and/or reduce subsequent crack growth. The experiment, therefore, provides a practical check on whether the relative conclusions from a Miner-type framework remain stable when a rare extreme event is introduced.

7.4. Load Spectra Simplification

The towing load cases defined in Chapter 5, 6 and Section 7.3.2 provide variable-amplitude hotspot stress histories for the mission spectra A–D. For fatigue-life evaluation and for the subsequent laboratory translation, these histories had to be reduced to a compact representation that preserved the cycle range and mean-stress characteristics that drove damage. This section, therefore, assembled a representative towing block from the lifetime usage mix, extracted the corresponding cycle population using rainflow counting, and discretised the cycle set into a limited number of stress-range levels. The resulting discretised cycle description was used directly in the damage calculations and was passed to Section 7.5 for conversion into a machine command programme.

Lifetime usage mix and block assembly

Let α_i denote the lifetime share (in percent) of mission type $i \in \{A, B, C, D\}$ from Table 7.4. For a planning horizon of M missions (here $M = 100$), the corresponding number of missions of each type is

$$N_i = \text{round}\left(\frac{\alpha_i}{100} M\right), \qquad \sum_i N_i = M, \tag{7.7}$$

where,

- α_i lifetime share of mission type i [%]
- i mission-type index, with $i \in \{A, B, C, D\}$ $[-]$
- M total number of missions in the planning horizon $[-]$
- N_i number of missions of type i in the assembled block $[-]$

Each mission of type i yields a hotspot stress history $\sigma_i^{(k)}(t)$ at the critical drag-brace location, obtained as described in Chapter 5 and 6. The representative block history was then constructed by time concatenation,

$$\sigma_{\text{blk}}(t) \;=\; \bigoplus_{i\in\{A,B,C,D\}} \; \bigoplus_{k=1}^{N_i} \sigma_i^{(k)}(t) \tag{7.8}$$

where,

- $\sigma_{\text{blk}}(t)$ assembled block stress history [MPa]
- t time [s]
- $\oplus$ concatenation in time $[-]$
- $\sigma_i^{(k)}(t)$ hotspot stress history of the k-th mission of type i [MPa]
- k mission counter within mission type i, with $k = 1, \ldots, N_i$ $[-]$

The block construction was performed separately for the two towing concepts, yielding two base block histories with identical mission mixes but different mission stress traces.

Rainflow counting and cycle descriptors

The block history $\sigma_{\text{blk}}(t)$ was reduced to a set of fatigue cycles using rainflow counting. Rainflow identified closed cycles by pairing turning-point maxima and minima and closing nested reversals, thereby separating small embedded cycles from larger excursions. The method was standard for variable-amplitude fatigue analysis and was described by Schijve [52]. Figure 7.4 illustrates the counting principle.

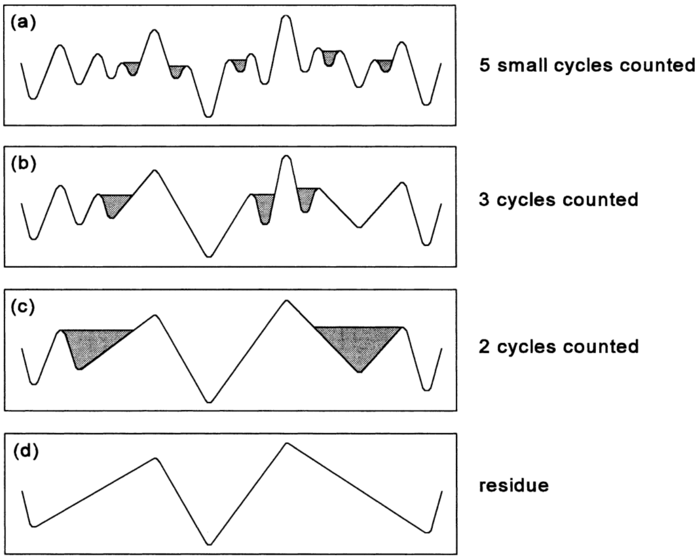

Figure 7.4: Rainflow counting example [52]

The rainflow output was stored cycle-by-cycle in terms of extrema and derived quantities. For each counted cycle j:

$$\Delta\sigma_j = \sigma_{\text{max},j} - \sigma_{\text{min},j}, \tag{7.9}$$

$$\sigma_{m,j} = \frac{\sigma_{\text{max},j} + \sigma_{\text{min},j}}{2}, \tag{7.10}$$

$$R_j = \frac{\sigma_{\text{min},j}}{\sigma_{\text{max},j}} \tag{7.11}$$

where,

- $\Delta\sigma_j$ stress range of counted cycle j [MPa]
- $\sigma_{\text{max},j}$ maximum stress in counted cycle j [MPa]
- $\sigma_{\text{min},j}$ minimum stress in counted cycle j [MPa]
- $\sigma_{m,j}$ mean stress of counted cycle j [MPa]
- R_j stress ratio of counted cycle j $[-]$
- j cycle index $[-]$

These descriptors were used consistently in the subsequent damage evaluation and in the laboratory translation.

Discretisation and compact spectrum representation

The raw cycle population typically contained many distinct stress ranges. To obtain a compact, repeatable spectrum description, stress ranges were discretised to fixed bins with bin width $\Delta\sigma_{\text{bin}}$. This reduced the number of unique levels and yielded an ordered cycle list that was more tractable to interpret and report, while the discretised cycle set remained fully defined in terms of $(\sigma_{\text{max}}, \sigma_{\text{min}})$ and therefore retained the associated $\Delta\sigma$, σ_m, and R distributions.

With this approach, very small stress excursions of less than approximately one bin width were effectively filtered out or merged, since their fatigue contribution was negligible while they would otherwise inflate the cycle count and reduce the compactness of the spectrum representation. Moreover, the discretised cycle set could be represented in a mean–range rainflow matrix. Figure 7.5 shows an ordered cycle list for the discretised A–TBL mission example.

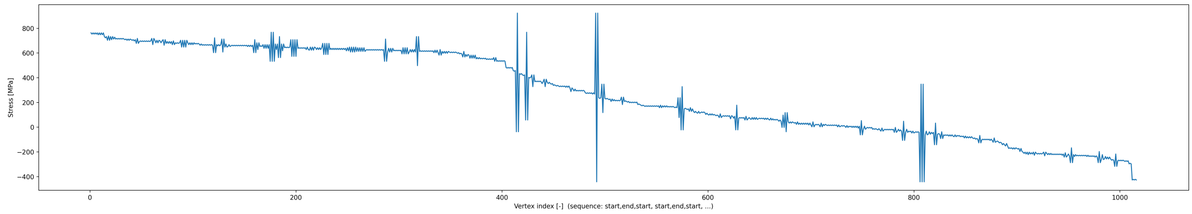

Figure 7.5: Ordered cycle list for the discretised A–TBL mission example (= 390 cycles)

Table 7.5 shows a simplified example layout to illustrate the matrix structure, where $n_{i,j}^{\text{RF}}$ denotes the number of cycles whose (normalised) range lies in row i and whose (normalised) mean lies in column j. In the actual implementation, the discretisation produced a much finer grid (exceeding 100×100 bins), which was impractically large to reproduce in this document.

Table 7.5: Illustrative example of a rainflow mean–range matrix layout

Range	$[0.0, 0.2)$	$[0.2, 0.4)$	$[0.4, 0.6)$	$[0.6, 0.8)$	$[0.8, 1.0]$
$[0.0, 0.2)$	N/A	$n_{1,2}^{\text{RF}}$	$n_{1,3}^{\text{RF}}$	$n_{1,4}^{\text{RF}}$	$n_{1,5}^{\text{RF}}$
$[0.2, 0.4)$	$n_{2,1}^{\text{RF}}$	N/A	$n_{2,3}^{\text{RF}}$	$n_{2,4}^{\text{RF}}$	$n_{2,5}^{\text{RF}}$
$[0.4, 0.6)$	$n_{3,1}^{\text{RF}}$	$n_{3,2}^{\text{RF}}$	N/A	$n_{3,4}^{\text{RF}}$	$n_{3,5}^{\text{RF}}$
$[0.6, 0.8)$	$n_{4,1}^{\text{RF}}$	$n_{4,2}^{\text{RF}}$	$n_{4,3}^{\text{RF}}$	N/A	$n_{4,5}^{\text{RF}}$
$[0.8, 1.0]$	$n_{5,1}^{\text{RF}}$	$n_{5,2}^{\text{RF}}$	$n_{5,3}^{\text{RF}}$	$n_{5,4}^{\text{RF}}$	N/A

Cycles with $R < 0$ may occur due to compressive excursions in the original histories. These cycles were retained at this stage and explicitly treated during fatigue-machine translation, where the tension–tension constraint was enforced. The choice of $\Delta\sigma_{\text{bin}}$ used in the final implementation is justified below.

Sensitivity to discretisation step size

A sensitivity study was conducted to quantify the effect of the discretisation step size on the computed Palmgren–Miner damage and thereby to select $\Delta\sigma_{\text{bin}}$. The complete levelling–rainflow–damage workflow was repeated for $\Delta\sigma \in \{20, 15, 12, 10, 8, 6, 4\}$ MPa. For each $\Delta\sigma$, the stress history was discretised and rainflow-counted. Moreover, total damage D was evaluated using the same mean-stress correction and $S-N$ parameters as in the final life model. Table 7.6 reports the resulting values for the three cases and provides the basis for selecting $\Delta\sigma_{\text{bin}} = 8$ MPa.

Table 7.6: Convergence of total damage D with stress-levelling step size $\Delta\sigma$

$\Delta\sigma$ [MPa]	Damage D [-]		Step change $\|\Delta D_{\%}\|$ [%]		$\|\Delta D_{\%}\|$ [%]
	TB	TBL	TB	TBL	
20	2.067E-05	3.855E-04	–	–	–
15	2.342E-05	4.137E-04	13.30	7.32	10.31
12	2.582E-05	3.905E-04	10.25	5.61	7.93
10	2.366E-05	3.897E-04	8.37	0.20	4.29
8	2.289E-05	3.953E-04	3.25	1.44	2.35
6	2.334E-05	3.938E-04	1.97	0.38	1.17
4	2.303E-05	3.874E-04	1.33	1.63	1.48

TB exhibited the more stable convergence behaviour across the tested step sizes. The TB damage varied only modestly and converged in absolute percentage, whereas TBL showed greater sensitivity to the chosen stress-levelling resolution. From $\Delta\sigma = 8$ MPa down to 4 MPa, the average step-to-step change was already below ≈ 2 %, which is a respectable level of numerical stability given that some variability is inherent to any discretisation/levelling procedure.

At the same time, the computational cost increased disproportionately as $\Delta\sigma$ was reduced. In practice, the runtime approximately doubled with each refinement step, such that $\Delta\sigma = 2$ MPa required almost forty minutes for only a marginal improvement in the damage estimate. Therefore, $\Delta\sigma_{\text{bin}} = 8$ MPa was selected as a pragmatic and defensible compromise between accuracy/stability and computation time.

7.5. Fatigue Machine Translation

The discretised spectrum description from Section 7.4 was translated into a laboratory programme that satisfied the mechanical and operational constraints of the fatigue test frame. The translation was performed cycle-wise and preserved the stress range wherever possible, while enforcing a tension–tension load ratio and explicit limits on maximum stress levels. The resulting machine-ready level tables and block visualisations are reported at the end of this section.

The test frame was operated in tension–tension load control. To avoid loss of grip and to maintain a practical minimum load, all cycles were conditioned such that

$$R = \frac{\sigma_{\text{min}}}{\sigma_{\text{max}}} \geq 0.1 \tag{7.12}$$

For each counted cycle with extrema $(\sigma_{\text{max},i}, \sigma_{\text{min},i})$, a constant offset was applied to both extrema,

$$\sigma'_{\text{max},i} = \sigma_{\text{max},i} + k_i, \qquad \sigma'_{\text{min},i} = \sigma_{\text{min},i} + k_i, \tag{7.13}$$

where k_i was selected such that $R'_i = \sigma'_{\text{min},i}/\sigma'_{\text{max},i} = 0.1$ for cycles violating the limit of a lower value, and $k_i = 0$ otherwise. This operation preserved the stress range,

$$\Delta\sigma'_i = \sigma'_{\text{max},i} - \sigma'_{\text{min},i} = \Delta\sigma_i \tag{7.14}$$

while increasing the mean stress of originally low-R cycles. For the present spectra, the conditioning did not introduce non-physical wrap-around artefacts in the counted cycle population. The shifted ordered-cycle list is shown in Figure 7.6 for the ABCD–TBL 100-mission block.

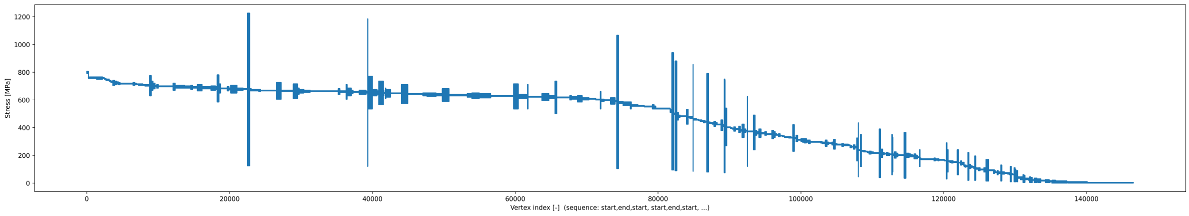

Figure 7.6: Ordered cycle list after conditioning to enforce $R \geq 0.1$ for the ABCD–TBL 100-mission block (= 73120 cycles)

Moreover, the specimens were tested at 40 Hz, as stated earlier. This rate is a balance between speed and minimising the heating effects on the specimen caused by energy passing through it. The exact rate was decided through calibration of the fatigue machine, and validating that against the reference fatigue test data obtained from ARMCO 17-4PH, which was tested at 1800 CPM (cycles per minute), which is 30 Hz. [77]

Block composition, overload insertion, and stress caps

A baseline block contained 100 towing manoeuvres with composition consistent with Table 7.4. The retardation variants were formed by inserting a dedicated overload event once per block, at the prescribed location defined in the WP3 methodology. To reserve the overload corner for the retardation event, non-retardation cycles were capped at an explicit maximum stress level,

$$\sigma_{\text{max}}^{\text{nonRET}} \leq \sigma_{\text{max,cap}} \tag{7.15}$$

while the overload peak was assigned a higher maximum stress,

$$\sigma_{\text{max}}^{\text{RET}} = \sigma_{\text{max,ovl}} \tag{7.16}$$

In the current implementation, $\sigma_{\text{max,cap}}$ was set equal to the nominal yield strength used in the material model, and $\sigma_{\text{max,ovl}}$ was selected below the ultimate strength to avoid immediate net-section failure while remaining sufficiently high to trigger a sequence effect.

If a cycle exceeds the cap after R-conditioning, it is shifted downward to enforce the cap while preserving stress range where feasible. If enforcing both the cap and $R \geq 0.1$ cannot be achieved simultaneously with range preservation, $R \geq 0.1$ is enforced at the capped maximum, implying a reduced stress range for that cycle.

7.5.1. 17-4PH (H900) Endurance Strength Translated to R=0.1

For 17-4PH in condition H900, the Cliffs/ARMCO product bulletin reported a rotating-beam (R.R. Moore) fatigue strength of [77]

$$S_{e,-1}(N = 10^7) = 621\,\text{MPa}$$

for polished specimens, and an ultimate tensile strength of $S_u = 1379\,\text{MPa}$. The quoted $S_{e,-1}$ thus originated from an R.R. Moore rotating-beam test and represented a bending endurance strength under approximately fully reversed loading ($R \approx -1$), rather than a directly measured axial endurance limit. It was therefore translated here to the machine-relevant tension–tension ratio $R = 0.1$ using a mean-stress correction. The stress ratio was defined as $R = \sigma_{\text{min}}/\sigma_{\text{max}}$, with

$$\sigma_m = \frac{\sigma_{\text{max}} + \sigma_{\text{min}}}{2}, \qquad \sigma_a = \frac{\sigma_{\text{max}} - \sigma_{\text{min}}}{2} \tag{7.17}$$

where,

- σ_m mean stress [Pa]
- σ_a stress amplitude [Pa]
- σ_{max} maximum stress in the cycle [Pa]
- σ_{min} minimum stress in the cycle [Pa]

For a prescribed R, these imply

$$\sigma_m = \sigma_a \frac{1+R}{1-R} \tag{7.18}$$

A linear Goodman constant-life relation was used at $N = 10^7$,

$$\frac{\sigma_a}{S_{e,-1}} + \frac{\sigma_m}{S_u} = 1 \tag{7.19}$$

where,

- R stress ratio, defined as $R = \sigma_{\text{min}}/\sigma_{\text{max}}$ $[-]$
- $S_{e,-1}$ endurance strength under fully reversed loading ($R \approx -1$) [Pa]
- S_u ultimate tensile strength [Pa]
- N number of cycles to the constant-life point $[-]$

which yields the allowable alternating stress at a given R:

$$\sigma_{a,\text{lim}}(R) = \left(\frac{1}{S_{e,-1}} + \frac{1+R}{1-R}\frac{1}{S_u}\right)^{-1} \tag{7.20}$$

For $R = 0.1$ with $S_{e,-1} = 621\,\text{MPa}$ and $S_u = 1379\,\text{MPa}$, the translated $N = 10^7$ constant-life values are

$$\sigma_{a,\text{lim}}(0.1) = 401\,\text{MPa}, \qquad \sigma_{m,\text{lim}}(0.1) = \sigma_{a,\text{lim}}\frac{1+0.1}{1-0.1} = 490\,\text{MPa} \tag{7.21}$$

Equivalently,

$$\sigma_{\text{max,lim}} = \sigma_m + \sigma_a = 890\,\text{MPa}, \qquad \sigma_{\text{min,lim}} = \sigma_m - \sigma_a = 89\,\text{MPa}$$

Because the source endurance value was obtained from a rotating-beam test, its direct use for the present axial specimen configuration required caution. In an R.R. Moore test, the specimen was rotated under a constant bending moment, so the surface experienced fully reversed stress while the stress decreased toward the interior because of the bending stress gradient. In axial testing, by contrast, the gauge section was ideally stressed more uniformly, so a larger material volume was exposed to the maximum stress. In the present case, the loading was furthermore tension–tension with a positive mean stress. Consequently, endurance limits reported from rotating-bending tests were generally higher than those from axial push–pull tests, and direct use of rotating-beam data for axial design could therefore be non-conservative unless an appropriate load-mode correction were applied to account for stress-gradient and stressed-volume effects. [78]

Endurance-strength filtering

After machine conditioning, a runout-style filter was applied using an $N = 10^7$ constant-life endurance threshold. Using Eq. (7.20), the smooth-specimen $R = 0.1$ endurance amplitude is $\sigma_{a,\text{lim}}(0.1) = 400.5\,\text{MPa}$. A local stress concentration factor, due to specimen geometry (Figure 7.9), was accounted for by reducing this limit, where K_t is the elastic stress concentration factor caused purely by the specimen geometry. For the present dog-bone specimen, a value of $K_t = 1.1$ was assumed, as introduced here and discussed in more detail later in this chapter.

$$\texttt{FATIGUE\_LIMIT\_R01\_AMP\_MPA} = \frac{\sigma_{a,\text{lim}}(0.1)}{K_t} = \frac{400.5\,\text{MPa}}{1.1} \approx 364\,\text{MPa} \tag{7.22}$$

For each (machine-shifted) cycle with (σ_a, σ_m), a Goodman utilisation was computed using the same reference parameters,

$$U = \frac{\sigma_a}{S_{e,-1}} + \frac{\sigma_m}{S_u} \tag{7.23}$$

and expressed as an equivalent $R = 0.1$ amplitude

$$\sigma_{a,\text{eq},R=0.1} = U\,\sigma_{a,\text{lim}}(0.1) \tag{7.24}$$

The filtering rule is then

$$\sigma_{a,\text{eq},R=0.1} < \texttt{FATIGUE\_LIMIT\_R01\_AMP\_MPA} \;\Rightarrow\; \text{cycle removed} \tag{7.25}$$

The value of 10^7 cycles was intentionally set high (and exceeds the planned laboratory cycle budget) but was adopted as a conservative runout criterion. It aligns with common high-cycle fatigue reporting practice, reduces the risk of declaring “infinite life” prematurely when the S–N curve has not fully stabilised, and ensures that any cycles retained as damaging are genuinely in the finite-life regime for the chosen mean-stress and R-ratio conditions.

After machine conditioning and application of the non-retardation stress cap, the discretised towing blocks were translated into a finite sequence of constant-amplitude levels that can be executed repeatably in load control. Figure 7.7 visualises the resulting machine-ready block for the TBL+RET case. The corresponding level definitions are reported in Tables 7.7 and 7.8, which list, for each level, the mean stress σ_m, stress amplitude σ_a, stress ratio R, and the number of applied cycles n within one block. For the RET variants, the overload cycle is included as a dedicated single-occurrence level.

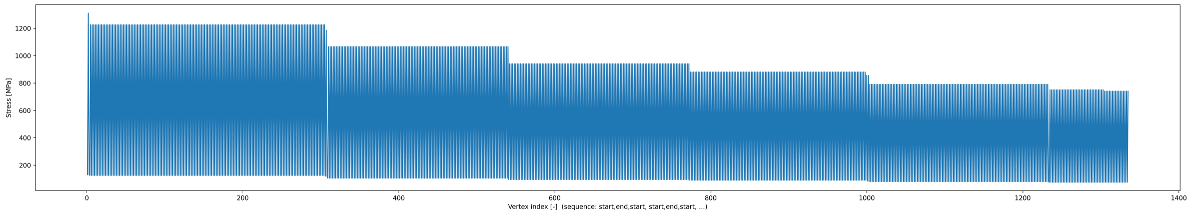

Figure 7.7: TBL + RET machine test block visualising the sequence of constant-amplitude levels in Table 7.8 (= 661 cycles)

Table 7.7: Machine input levels for the TB and TB + RET spectra

TB				TB + Ret			
Level	σ_m [MPa]	σ_a [MPa]	n [cycles]	Level	σ_m [MPa]	σ_a [MPa]	n [cycles]
1	434	354	1	1	434	354	1
2	442	362	113	2	442	362	113
3	568	464	65	3	568	464	65
4	602	494	1	4	602	494	1
–	–	–	–	RET	716	584	1

Table 7.8: Machine input levels for the TBL and TBL + RET spectra

TBL				TBL + Ret			
Level	σ_m [MPa]	σ_a [MPa]	n [cycles]	Level	σ_m [MPa]	σ_a [MPa]	n [cycles]
1	410	334	15	1	410	334	15
2	414	338	35	2	414	338	35
3	434	354	115	3	434	354	115
4	470	386	1	4	470	386	1
5	484	396	113	5	484	396	113
6	520	424	115	6	520	424	115
7	586	478	115	7	586	478	115
8	654	534	1	8	654	534	1
9	674	550	150	9	674	550	150
–	–	–	–	RET	716	584	1

7.5.2. Cycle-Count Reduction due to Endurance-Strength Filtering

The 100-mission block constructed in Section 7.4 contained a large number of rainflow-counted cycles, spanning a wide range of stress amplitudes. After successive filtering steps, only a comparatively small subset of cycles was retained for the machine-ready programme and for the subsequent Miner-type damage evaluation. The difference between the unfiltered and filtered cycle totals provided a compact measure of how strongly the lifetime block was dominated by a small number of damage-relevant excursions under the present S–N-based approach. For each case, the rainflow output was represented as a list of counted cycles with multiplicities n_j. The total number of cycles in the unfiltered block is

$$N_{\text{raw}} = \sum_j n_j, \tag{7.26}$$

and the total number of cycles retained after filtering is

$$N_{\text{kept}} = \sum_j n_j^{\text{kept}}, \tag{7.27}$$

where $n_j^{\text{kept}} \leq n_j$ accounts for cycles removed by the above criteria. The retained-cycle share and the reduction factor are then defined as

$$\eta_N = \frac{N_{\text{kept}}}{N_{\text{raw}}} \tag{7.28}$$

Values for N_{raw} and N_{kept} are reported for the two 100-mission blocks in Table 7.9. A low value of η_N indicates that most counted cycles fall into a low-amplitude regime that is treated as runout (or negligible damage) within the adopted endurance-strength filtering step. This interpretation is specific to the present modelling choices and should not be read as a general statement that the removed cycles are physically irrelevant. Rather, it reflects that they contribute negligibly to the predicted life under the chosen S–N curve, mean-stress correction, and runout threshold.

Table 7.9: Cycle-count reduction for the 100-mission block before and after endurance-strength filtering

Case	N_{raw} [cycles]	N_{kept} [cycles]	η_N [-]	Removed [%]
TB	49,076	179	0.0037	99.63
TBL	60,540	660	0.0109	98.91

7.6. Fatigue-Life Prediction

The previous sections define towing-derived load spectra at the drag-brace hotspot, map them to nominal axial stress in the 17-4PH (H900) specimens, and subsequently simplify them into a finite set of discrete stress levels suitable for repeated laboratory execution. The purpose of this section was to define the fatigue-life methodology used to interpret these spectra, provide a consistent pre-test severity assessment for the four spectrum variants (TB, TB+RET, TBL, TBL+RET), and clarify the limitations of absolute life prediction for the present smooth dog-bone specimens.

7.6.1. Choice of Fatigue-Life Methodology

The general fatigue background for metallic structures, including fatigue-driving mechanisms and life-assessment concepts, has already been introduced in Section 2.6. At the same time, the broader role of laboratory testing and finite-element modelling has been discussed in Section 2.7. For WP3, the additional point of importance is that the present comparison is fundamentally a variable-amplitude fatigue problem rather than a constant-amplitude strength problem.

The towing load cases defined in WP1 and translated in WP2 produce variable-amplitude hotspot stress histories at the governing drag-brace location. These histories are not characterised by a single stress level, but by a sequence of cycles with different stress ranges, mean stresses, stress ratios, and frequencies of occurrence across the representative mission mix. Accordingly, the relevant difference between TB and TBL was not defined solely by one peak stress or one extreme towing event, but by the full spectrum structure of the representative towing block, including the distribution of cycle magnitudes, the relative proportion of light and heavy manoeuvre content, and the placement of rare high-severity events within the loading sequence.

This distribution is particularly relevant to the present spectra because the towing blocks exhibit steep, variable-amplitude spectra, containing a comparatively small number of high-amplitude cycles and a much larger population of lower- and intermediate-amplitude cycles. Although many of these lower cycles contribute little individually in an S–N based damage calculation, they remain part of the original loading history and influence the overall spectrum composition, mean-stress content, and sequence context of the larger cycles. For that reason, the towing-derived histories were first assembled into representative mission blocks and then reduced, using rainflow counting and discretisation, to a finite set of constant-amplitude levels. This procedure did not preserve the full continuous-time history, but it retained the fatigue-relevant cycle population in a form suitable for machine execution and comparative assessment.

The S–N and Palmgren–Miner framework adopted in this section should therefore be interpreted primarily as a method for comparing the relative severity of two variable-amplitude spectra after translation into machine-executable laboratory blocks. It is not intended to imply that the towing problem can be represented adequately by a single constant-amplitude level, nor that all load-sequence effects are captured explicitly within the present formulation.

Fatigue-life estimation for metallic components can be approached in several ways. The classical stress–life (S–N) approach relates stress amplitude to cycles to failure on a logarithmic S–N curve, often represented by a Basquin law in the high-cycle regime. Variable-amplitude histories are reduced to an equivalent set of constant-amplitude cycles, and damage is accumulated using a rule such as Palmgren–Miner linear summation. This approach is widely used for components that operate elastically and fail after many cycles. Therefore, it is the basis of many design S–N curves and Goodman-type mean-stress diagrams for steels. [52]

In contrast, the strain–life (ε–N) approach combines elastic and plastic strain components (for example, via the Coffin–Manson relation) and is particularly suitable for low-cycle fatigue with significant local plasticity, notched components, and situations where crack initiation dominates life. Mean stress can be accounted for via parameters such as Morrow or Smith–Watson–Topper, and the method is often recommended when lives are below about 10^5 cycles or when local plastic strain is non-negligible. [79]

A third class of methods uses fracture mechanics and crack-growth laws. Here, life is expressed in terms of crack growth from an assumed initial defect size to a critical crack, using Paris-type relations for $\mathrm{d}a/\mathrm{d}N$ as a function of stress-intensity factor range. This approach is appropriate when inspection intervals, defect distributions, and crack-growth properties are known, and is frequently used in damage-tolerance assessments of primary aircraft structure [52]. For the present study, the following considerations are important:

- The laboratory specimens were smooth, polished dog-bones loaded in axial tension–tension, with spectra conditioned for machine feasibility.
- The main experimental objective was to make consistent comparisons between towing concepts and overload insertion (TB, TB+RET, TBL, TBL+RET) within an identical test framework.
- The drag brace is a feature-dominated component. Fatigue initiation in-service is expected at geometric details rather than in a uniform stress field.

In view of these remarks, an S–N based framework with rainflow cycle counting and Palmgren–Miner damage accumulation was adopted as the primary interpretation tool for spectrum severity. The S–N input was taken from MMPDS-style axial fatigue regressions for 17-4PH H900 at the relevant stress ratios. These relations provided the level-wise $N_{f,i}$ values used in the Palmgren–Miner summation, but did not constitute a separate damage-accumulation. The methodology was used primarily for internal consistency checks and relative comparisons among the four laboratory spectral variants, rather than as a definitive, absolute predictor of operational life.

7.6.2. Damage Calculation for the Discretised Towing Block

Each spectrum variant was reduced to a finite cycle population by rainflow counting and discretisation as described in Section 7.4. The output was a list of discrete, constant-amplitude levels, each with an associated cycle count per repeated laboratory block. For any fatigue model that maps each counted level i to a cycles-to-failure value $N_{f,i}$, the Palmgren–Miner damage per block is

$$D_{\text{blk}} = \sum_i \frac{n_i}{N_{f,i}}, \tag{7.29}$$

and the corresponding predicted number of identical blocks to failure is

$$N_{\text{blk,pred}} = \frac{1}{D_{\text{blk}}}. \tag{7.30}$$

This calculation was performed consistently for the four cases (TB, TB+RET, TBL, TBL+RET) to obtain a pre-test ordering of severity and an indicative range of expected lives in block units.

Fatigue-life prediction using an MMPDS-style model

In addition to the Basquin-style S–N representation, an MMPDS-style formulation was used to evaluate the counted loading levels in a compact, R-sensitive manner. For each counted cycle with maximum stress $\sigma_{\text{max},j}$ and stress ratio $R_j = \sigma_{\text{min},j}/\sigma_{\text{max},j}$, an equivalent stress was computed as

$$S_{\text{eq},j} = \sigma_{\text{max},j}\,(1 - R_j)^P, \tag{7.31}$$

where,

- $S_{\text{eq},j}$ equivalent stress parameter for counted cycle j [MPa]
- $\sigma_{\text{max},j}$ maximum stress in counted cycle j [MPa]
- R_j stress ratio of counted cycle j, defined as $R_j = \sigma_{\text{min},j}/\sigma_{\text{max},j}$ $[-]$
- $\sigma_{\text{min},j}$ minimum stress in counted cycle j [MPa]
- P exponent in the MMPDS-style equivalent-stress definition $[-]$

The corresponding S–N relation was written as

$$\log_{10}(N_{f,j}) = C - M\,\log_{10}(S_{\text{eq},j}), \tag{7.32}$$

where,

- $N_{f,j}$ cycles to failure at the severity of counted cycle j [cycles]
- C intercept parameter of the fitted MMPDS-style S–N relation $[-]$
- M slope parameter of the fitted MMPDS-style S–N relation $[-]$

The parameters P, C, and M were fitted for the selected 17-4PH H900 dataset. The resulting $N_{f,j}$ values were then substituted into the block-damage formulation above to obtain D_{blk} and $N_{\text{blk,pred}}$ for each assembled spectrum. This provided a consistent cycle-by-cycle severity measure that directly reflects the stress ratio of each counted level.

Block-wise damage contributions

Tables 7.10 and 7.11 summarise the block-wise damage contributions obtained from the MMPDS-based calculation. The main purpose of this breakdown was to identify which discrete stress levels dominate the predicted fatigue consumption within each mission spectrum, rather than considering only the total life estimate. The bold row corresponds to the inserted RET manoeuvre, which appeared as a distinct high-severity cycle and, in the prediction, contributed measurably to the accumulated fatigue damage.

For the TB-based spectra, the damage was strongly concentrated in a limited number of high-severity blocks. In the baseline TB case, the first major block at a mean stress of 568 MPa and amplitude of 464 MPa accounted for most of the total damage, after which the remaining blocks mainly completed the final fraction to unity. In the TB+RET case, this dominance remained, but the inserted overload block, defined by $(\sigma_m, \sigma_a) = (716, 588)$ MPa, introduced an additional distinct contribution early in the sequence, thereby shifting the cumulative damage development and increasing the total predicted severity relative to the baseline TB case, as shown in Table 7.10.

Table 7.10: Cycle blocks and cumulative fatigue damage for the TB and TB + RET cases using the MMPDS-based method

TB					TB+RET				
Cycles count	**Mean [MPa]**	**Amp. [MPa]**	**Damage [-]**	**Cum. [-]**	**Cycles count**	**Mean [MPa]**	**Amp. [MPa]**	**Damage [-]**	**Cum. [-]**
65	568	464	0.7638	0.7638	65	568	464	0.7303	0.7303
113	440	360	0.2177	0.9815	113	440	360	0.2082	0.9384
1	604	492	0.0169	0.9983	**1**	**716**	**588**	**0.0439**	**0.9823**
1	432	352	0.0016	1.0000	1	604	492	0.0162	0.9985
					1	432	352	0.0015	1.0000

For the TBL-based spectra, the damage was distributed over a larger number of blocks, although the highest-amplitude levels still dominated the cumulative total. The first few blocks in both TBL and TBL+RET already consumed the majority of the available damage, with subsequent medium-amplitude blocks providing a smaller but still non-negligible contribution. Compared with TB, the TBL spectra therefore exhibited a less concentrated but still clearly top-heavy damage distribution. The overload insertion in TBL+RET had only a modest effect on the block ranking and cumulative progression, as seen in Table 7.11.

Table 7.11: Cycle blocks and cumulative fatigue damage for the TBL and TBL + RET cases using the MMPDS-based method

TBL					TBL+RET				
Cycles count	**Mean [MPa]**	**Amp. [MPa]**	**Damage [-]**	**Cum. [-]**	**Cycles count**	**Mean [MPa]**	**Amp. [MPa]**	**Damage [-]**	**Cum. [-]**
150	672	552	0.6090	0.6090	150	672	552	0.6056	0.6056
115	584	480	0.2067	0.8158	115	584	480	0.2055	0.8111
115	520	424	0.0940	0.9098	115	520	424	0.0935	0.9046
113	484	396	0.0568	0.9666	113	484	396	0.0565	0.9611
115	432	352	0.0231	0.9898	**1**	**716**	**588**	**0.0057**	**0.9668**
1	656	536	0.0035	0.9932	115	432	352	0.0230	0.9898
35	408	336	0.0046	0.9978	1	656	536	0.0034	0.9933
15	404	332	0.0018	0.9996	35	408	336	0.0046	0.9978
1	472	384	0.0004	1.0000	15	404	332	0.0018	0.9996
					1	472	384	0.0004	1.0000

Overall, the block-wise results confirmed that the predicted fatigue response was governed primarily by a relatively small subset of the most severe stress states. These findings support the interpretation that differences in fatigue severity between the four spectra were driven mainly by the presence, magnitude, and ordering of the highest-stress blocks, rather than by the large number of lower-amplitude cycles.

7.6.3. Reference S–N Behaviour: Smooth vs. Notched Representation

Figure 7.8 compares two reference S–N representations used to contextualise the predicted behaviour under the present tension–tension machine constraint ($R \geq 0.1$). The smooth/unnotched representation (Figure 7.8a) exhibits a pronounced runout tendency under tension–tension loading, such that only a small number of high-stress cycles contribute materially to Miner damage. The notched/feature-sensitive representation (Figure 7.8b) retains a broader finite-life regime and is therefore more consistent with the localised initiation behaviour expected in the full-scale drag brace.

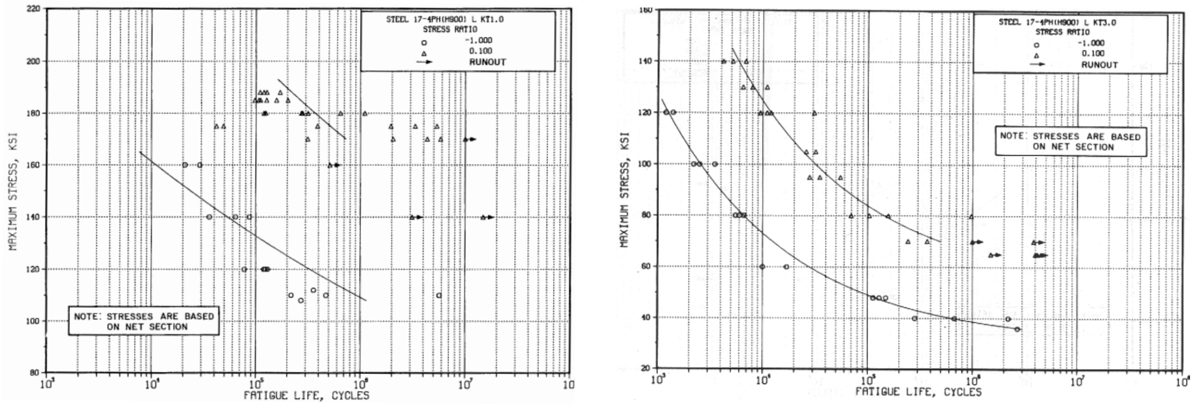

(a) Smooth/unnotched reference S–N behaviour

(b) Notched/feature-sensitive reference S–N behaviour

Figure 7.8: Comparison of reference S–N behaviour under the machine tension–tension constraint [80]

The notched representation is therefore the more informative indicator for where fatigue is expected to initiate in the actual component. However, the present laboratory programme uses smooth dog-bone specimens and could not introduce a representative notch geometry within the manufacturing and time constraints. As a result, any absolute life prediction based on a notched S–N curve is not directly testable with the current specimen set; instead, it is used to motivate the expectation that fatigue-critical locations in the drag brace are associated with geometric features, which is addressed explicitly in the next-step framing of the laboratory programme.

Specimen representativeness and residual stress concentration

Although the specimens are nominally smooth, a small geometric stress concentration remains at the shoulder transition. For the present dog-bone geometry, this is taken as approximately $K_t \approx 1.1$, consistent with smooth-specimen stress distributions reported by Schijve and seen in Figure 7.9. [52]

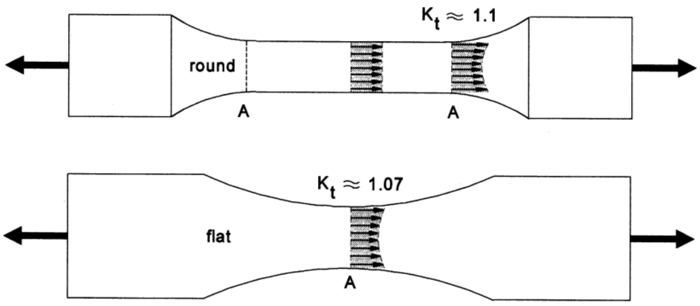

Figure 7.9: Stress concentration in unnotched specimens [52]

Specimen representativeness and expected initiation sites

Given the runout tendency associated with smooth tension–tension behaviour, the pre-test fatigue-life calculations were primarily used to verify internal consistency of the condensed spectra, identify the damage-dominant portion of each block, and provide a relative ranking between the four spectrum variants (TB, TB+RET, TBL, TBL+RET). The decisive outcome of WP3 is therefore experimental, yielding the number of blocks and the equivalent 100-operation mission blocks required till complete fracture for each specimen.

Figure 7.10 highlights representative pinned attachment features of the drag-brace linkage that may act as candidate fatigue-initiation regions in the actual component. These locations combine load transfer with local geometric discontinuities. The associated smooth-specimen versus component-representativeness limitation is discussed further in Section 7.8. The next section reports the measured lives and the observed differences between towing concepts and overload insertion under identical test conditions.

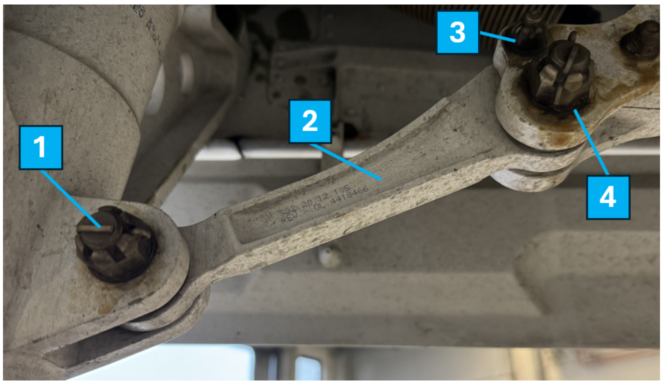

Figure 7.10: Representative drag-brace linkage of the NWLG, showing (1) the barrel-side attachment, (2) the drag-brace member, (3) the over-centre locking joint, and (4) the V-brace-side attachment

7.7. Performed Laboratory Tests and Results

All tests were conducted on twelve nominally identical specimens (at room temperature $\sim 20\,^\circ$C), of which two were used for calibration. The final fracture occurred when the specimen was split into two parts, causing the machine to reach its interlock settings and automatically stop the program. In Figure 7.11, the fully fractured dog-bone specimen is shown, while Figure 7.12 provides a zoomed-in view of the fatigue-growth and final-fracture surfaces.

Block scaling and machine settings

Fatigue tests were conducted at 40 Hz. This frequency was selected during the calibration phase (Specimen 2) as the highest setting at which the machine maintained stable force tracking without noticeable overshoot or resonant behaviour, while still providing sufficient test speed to reach the required cycle counts within practical laboratory time.

To improve machine execution stability, the 100-mission spectrum was repeated $\times 10$ within a single programme segment (1000 missions per segment). This extended segment length provided sufficient time for the controller to settle into steady sinusoidal tracking before interpreting the measured response, while also reducing the number of programme restarts required during a test. Throughout this work, cycle counts are reported using the machine convention of half-cycles. In addition, the programmed level order was inverted relative to the original plan, as, instead of stepping from high to low mean stress, the block was executed from low to high mean stress. This ordering was found to yield more stable machine behaviour and was therefore adopted for the final programme, as illustrated in Figure 7.7.

The retardation event was programmed at a target force of 9189 N. In practice, the machine frequently exhibited a modest overshoot, reaching approximately 9.4 kN. To minimise dynamic effects, the retardation event was applied quasi-statically using displacement control at 0.1 mm/min, with a typical application duration of about 4 min. After completion of the retardation event, the test proceeded directly into the repeated TB/TBL mission-block loading sequence.

Figure 7.11: Fractured dog-bone specimen after fatigue failure

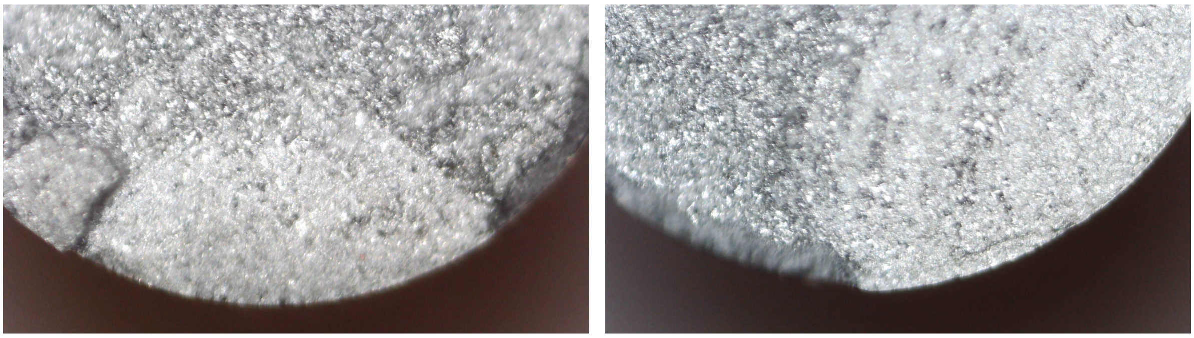

Figure 7.12: Microscope images of the fracture surface, separating the fatigue crack growth region (light grey) from the final fast-fracture region (darker grey)

Test matrix and outcomes

Table 7.12 summarises the laboratory fatigue runs and the measured number of cycles to complete fracture. Notes are used to flag non-standard events and to distinguish calibration runs from the nominal TB/TBL comparison matrix.

Table 7.12: Summary of laboratory fatigue runs and measured cycles to complete fracture

Run	N_f [cycles]	Notes
Cal1	1	Rapid failure due to machine overload at measured peak 10.8 kN
Cal2	4,999	Multiple overloads at 9.5 kN to 10.2 kN, with TBL spectrum applied till failure
TB1	58,506	–
TB2	23,246	Possible premature failure
TB3	49,957	–
TB1 RET	78,739	–
TB2 RET	125,666	–
TBL1	30,789	–
TBL2	25,088	–
TBL3	25,940	–
TBL1 RET	39,526	–
TBL2 RET	31,853	Shock overload to 10.2 kN after 678 cycles (machine error; no visible damage)

7.7.1. Test Results per Spectrum Variant

The laboratory programme yielded measured fatigue lives that can be linked back to the towing-derived spectra, their simplification, and the test matrix definition. Each test was executed in force control using the discrete-level block programmes defined earlier. Failure was defined as a complete fracture in the gauge section, thus, full separation of the specimen into two parts. The results are presented in a form that supports the two central comparisons of WP3: the difference between TB and TBL loading, and the influence of a single early overload insertion (retardation) for each towing concept.

For each spectrum variant $v \in \{\text{TB}, \text{TB+RET}, \text{TBL}, \text{TBL+RET}\}$ with $n_v = 2$ or 3 specimens, the mean missions to fracture and sample standard deviation are computed as:

$$\bar{N}_{\text{missions,exp},v} = \frac{1}{n_v} \sum_{j=1}^{n_v} N_{\text{missions,exp},v,j} \tag{7.33}$$

$$s_{N,v} = \sqrt{\frac{1}{n_v - 1} \sum_{j=1}^{n_v} \left(N_{\text{missions,exp},v,j} - \bar{N}_{\text{missions,exp},v} \right)^2} \tag{7.34}$$

where,

- v spectrum variant index ($v \in \{\text{TB}, \text{TB+RET}, \text{TBL}, \text{TBL+RET}\}$) [-]
- j specimen index within variant v ($j = 1, \ldots, n_v$) [-]
- n_v number of tested specimens (replicates) for variant v [-]
- $N_{\text{missions,exp},v,j}$ measured equivalent towing missions to complete fracture of specimen j in variant v [-]

- $\bar{N}_{\text{missions,exp},v}$ sample mean of $N_{\text{missions,exp},v,j}$ over the n_v specimens of variant v [-]
- $s_{N,v}$ sample standard deviation of $N_{\text{missions,exp},v,j}$ for variant v [-]

The coefficient of variation is reported as $\text{CoV}_v = s_{N,v}/\bar{N}_{\text{missions,exp},v}$ to provide a compact measure of relative scatter. The measured lives in cycles were converted to equivalent towing missions using the number of counted cycles per mission block. For the towbarless spectra, one mission contains approximately 660 counted cycles, whereas for the towbar spectra, one mission contains approximately 179 counted cycles. As a consequence, the separation between TB and TBL becomes more pronounced when life is expressed in terms of missions rather than cycles. For TB, each mission contributes substantially fewer fatigue-relevant cycles, so a given cycles-to-failure result translates into a larger number of missions to failure than for TBL. This conversion effect is therefore a structural difference in mission cycle density, rather than a purely material or specimen effect.

Figure 7.13 compiles the measured outcomes into a fatigue-life diagram, plotting the applied average peak stress level for each laboratory spectrum against the achieved life. The corresponding numerical results are summarised in Table 7.13, which reports the mean and sample standard deviation of life expressed in both equivalent towing missions and machine cycles, together with the coefficient of variation as a normalised scatter metric.

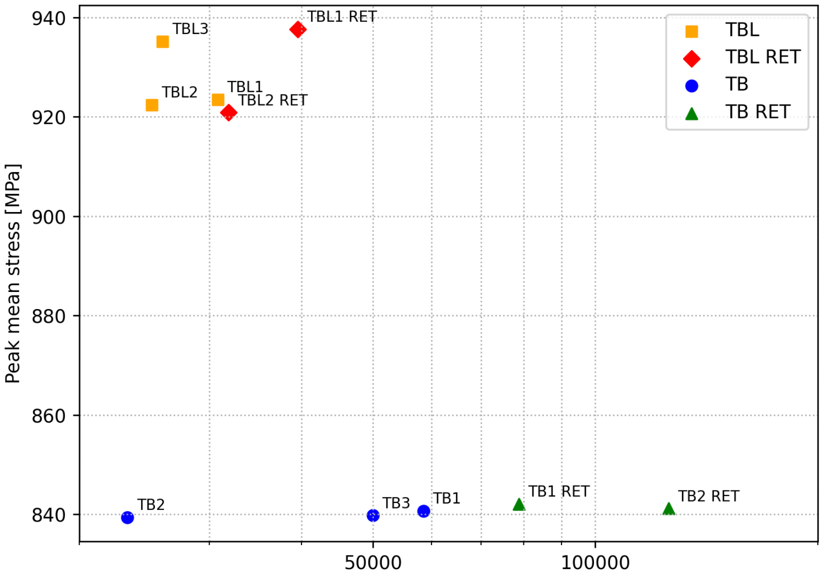

Figure 7.13: Fatigue-life scatter plot containing measured outcomes for the tested specimens

Table 7.13: Measured fatigue lives to complete fracture for each laboratory spectrum variant

Variant	Replicates [-]	$\bar{N}_{\text{missions,exp}}$ [-]	$s_{N,\text{missions}}$ [-]	CoV [-]	$\bar{N}_{\text{cycles,exp}}$ [-]	$s_{N,\text{cycles}}$ [-]
TBL	3	41	5	0.11	27,272	3,075
TBL+RET	2	54	8	0.15	35,690	5,426
TB	3	245	103	0.42	43,902	18,393
TB+RET	2	571	185	0.32	102,202	33,182

Finally, Figure 7.14 presents the same cycle-to-failure outcomes in a compact statistical form, showing the individual replicate points together with the variant mean and standard deviation on a linear axis. This plot is used to assess repeatability and to highlight potential outliers before any exclusion/sensitivity treatment in subsequent analysis.

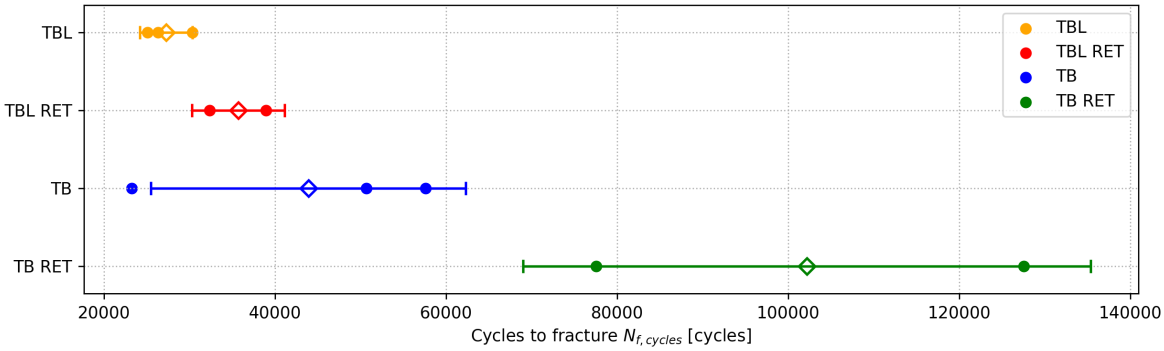

Figure 7.14: Measured cycles to failure per spectrum variant, including specimen-level replicates and mean ± standard deviation

Possible Premature Specimen (TB2) Failure

Specimen TB2 failed substantially earlier than the other TB specimens, despite being tested under the same nominal spectrum definition and machine settings. Given the limited number of available tests, a post-test fractographic screening was performed to assess whether TB2 exhibited an abnormal near-surface condition that could plausibly bias its fatigue life relative to the remaining population.

All fractured specimens were inspected using optical microscopy, with emphasis on the specimen perimeter and near-surface regions where fatigue crack initiation is expected under axial loading. For TB2, the fracture perimeter shows several sharp, re-entrant discontinuities at the free surface, from which multiple crack-like features extend radially inwards (Figure 7.15). In contrast to TB2, Figure 7.12 also shows two representative zoomed-in views of the fatigue crack-growth region from other tested specimens in which substantially fewer, pronounced edge-connected flaws are observed.

Sharp surface discontinuities can substantially reduce the crack initiation phase by acting as preferential nucleation sites with a small effective root radius and an increased effective initial defect size. Approximating such a discontinuity as an initial crack of characteristic size a_0, the local crack-driving force scales with the stress intensity range, [52]

$$\Delta K = Y\,\Delta\sigma\sqrt{\pi a} \tag{7.35}$$

where,

- ΔK stress-intensity-factor range $[\text{MPa}\sqrt{\text{m}}]$
- Y dimensionless geometry factor $[-]$
- $\Delta\sigma$ applied stress range $[\text{MPa}]$
- a crack length (or effective defect size) $[\text{m}]$

So a larger effective a_0 increases ΔK from the first loading cycles and can cause crack growth to commence with minimal microstructural initiation. In this case, the measured life is dominated by the propagation phase, which may remain broadly comparable across specimens once a dominant crack is established. In contrast, the shortened initiation period leads to earlier overall failure for TB2.

Figure 7.15: TB2 specimen showing multiple sharp, surface-connected discontinuities extending radially inwards from the specimen edge (highlighted)

Although the present optical microscopy does not provide definitive fractographic confirmation, the edge-connected, step-like features observed on TB2 are consistent with ratchet marks reported in fatigue failure analysis literature, where they are identified as fracture-surface features associated with fatigue and high local stress [81]. This literature supports the interpretation that TB2 failed prematurely due to specimen condition rather than to the severity of the TB spectrum. TB2 is therefore excluded from the fatigue-test result comparison from this point onward, as seen in Table 7.14.

Table 7.14: Measured fatigue lives to complete fracture for each laboratory spectrum variant (TB2 excluded)

Variant	Replicates [-]	$\bar{N}_{\text{missions,exp}}$ [-]	$s_{N,\text{missions}}$ [-]	CoV [-]	$\bar{N}_{\text{cycles,exp}}$ [-]	$s_{N,\text{cycles}}$ [-]
TBL	3	41	5	0.11	27,272	3,075
TBL+RET	2	54	8	0.15	35,690	5,426
TB	**2**	**303**	**34**	**0.11**	**54231**	**6045**
TB+RET	2	571	185	0.32	102,202	33,182

7.7.2. Fatigue Machine Observations and Limitations

During the WP3 campaign, two practical limitations were observed that could influence the interpretation of the measured lives. Firstly, force-tracking limitations during the initial APC (Amplitude Phase Control) tuner build-up, and secondly, local specimen settling during the retardation application.

At the start of selected runs, the APC compensator required a transient “build-up” period before the measured force closely matched the commanded sinusoidal waveform. Figure 7.16 illustrates the force-command build-up.

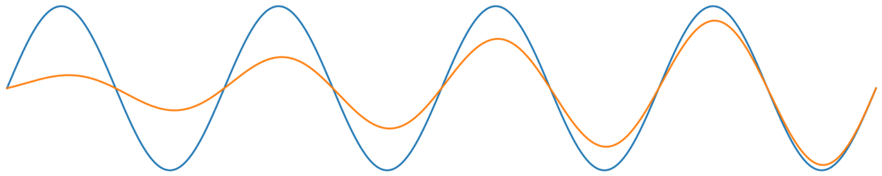

Figure 7.16: Example of force tracking during sinusoidal loading, illustrating APC compensator build-up

This behaviour is visible in the force–cycles records as a short initial interval with reduced amplitude, followed by stable tracking. The measured spectra for TB and TBL are partially shown in Figure 7.17. While this does not change the intended nominal spectrum definition, it introduces a brief non-stationary loading segment at the beginning of a programme segment. For consistency, the main fatigue-life interpretation therefore relies on the steady-state portion of the block repetitions after APC tracking has converged.

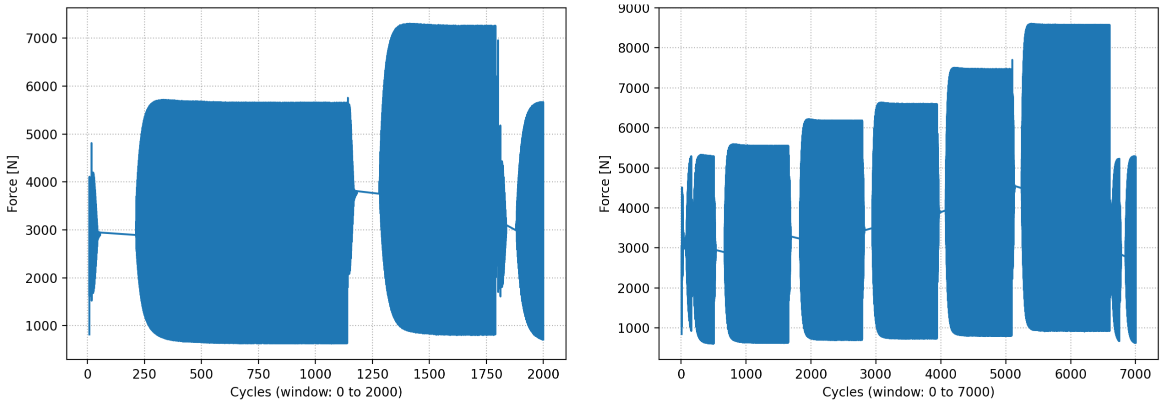

(a) Windowed view TB (0–2000 cycles)

(b) Windowed view TBL (0–7000 cycles)

Figure 7.17: Measured force versus cycles showing APC delay

The retardation cycle was applied quasi-statically (displacement-controlled ramp) to minimise dynamic overshoot. Nevertheless, a reproducible jump was observed in the measured displacement signal for all four retardation cycles, accompanied by a transient in the applied force. The event consistently occurred when the actuator displacement passed through 0 mm, indicating that the dominant mechanism is an LVDT zero-crossing artefact (offset/nonlinearity or signal conditioning around the reference point) rather than a physical transition from tension to compression, since the force remained tensile (between $2.2 - 7.0$ kN) at the time of the event. Notably, the same behaviour was not observed during force-controlled operation, which is consistent with the interpretation that the artefact is specific to displacement control. This caused a relatively high cycle, but not higher than the cycles applied in the spectra. Therefore, it was neglected as it most likely did not cause excessive damage.

A secondary effect is consistent with grip settling at the specimen ends. Post-test inspection revealed local surface damage near the grip-contact regions, suggesting seating and localised plasticity during load transfer. In the force–displacement records, this manifests as a local nonlinearity (deviation from the straight line expected for purely elastic response), and can therefore contribute to abrupt compliance changes during the retardation application. Moreover, a small jump is observed around 60 seconds, after which the graph becomes linear, suggesting that the specimen has finally settled.

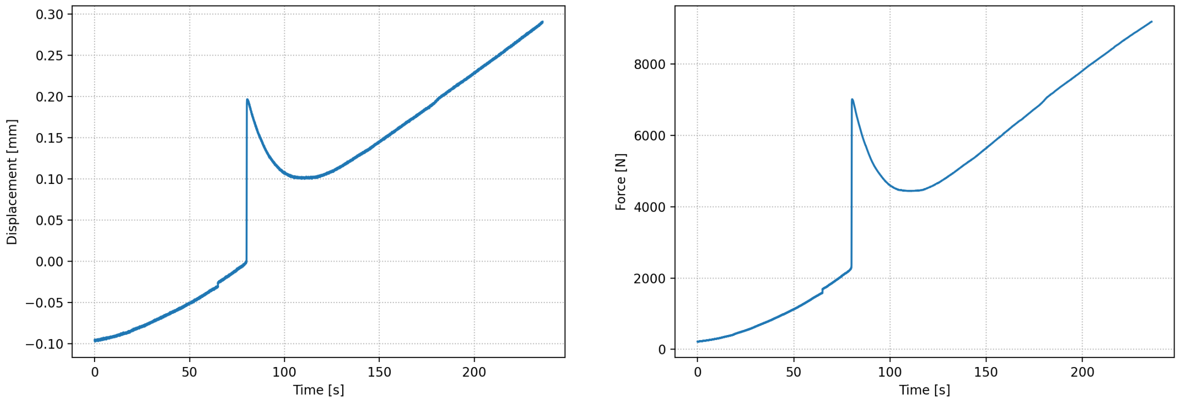

(a) RET1: displacement vs. time

(b) RET1: force vs. time

Figure 7.18: RET1 application event: displacement-controlled ramp and corresponding measured force response

Figure 7.19 shows the measured force history over the full programme, starting from the retardation event and continuing through the repeated mission-block loading until final failure. It can be seen that failure occurs after continued cycling, indicating that the remaining load capacity is progressively reduced.

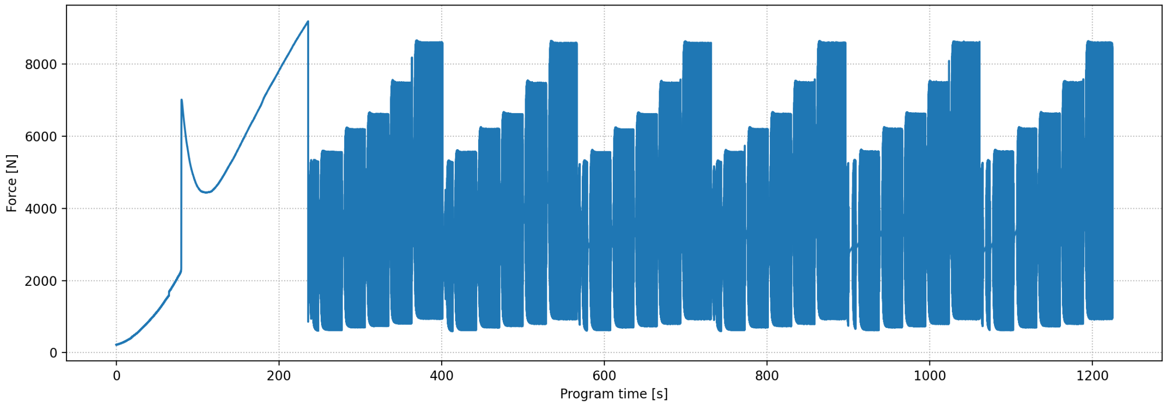

Figure 7.19: TBL + RET: measured force history over the retardation event and mission-block repetitions until final failure

7.7.3. MMPDS-based S–N Reference Curves and Effective Notch Severity

To benchmark the fatigue performance of the tested specimens, mean S–N reference curves were constructed from the MMPDS-01 (2003) axial fatigue regressions for 17-4PH H900 at fixed stress ratio $R = 0.1$, as seen in Figure 7.8. [80]

The MMPDS formulation is expressed in terms of an equivalent stress parameter S_{eq} (given in ksi) and relates S_{eq} to life N_f. For the unnotched condition ($K_t = 1$), MMPDS gives

$$\log_{10}(N_f) = 30.6 - 11.2 \log_{10}(S_{\text{eq}}) \, , \tag{7.36}$$

$$S_{\text{eq}} = S_{\text{max}}(1 - R)^{0.52} \tag{7.37}$$

while for the notched condition ($K_t = 3$) MMPDS gives

$$\log_{10}(N_f) = 9.10 - 2.79\,\log_{10}(S_{\text{eq}} - 48.4)\,, \tag{7.38}$$

$$S_{\text{eq}} = S_{\text{max}}(1 - R)^{0.67} \tag{7.39}$$

For a prescribed N_f and $R = 0.1$, Eqs. (7.36)–(7.37) and Eqs. (7.38)–(7.39) were inverted to obtain the corresponding $S_{\text{max}}(N_f)$ curves for $K_t = 1$ and $K_t = 3$, respectively, and converted from ksi to MPa for consistency with the experimental results. Additionally, the curves were truncated at the reported ultimate tensile strength $S_u = 1379$ MPa, such that no reference curve exceeds S_u.

Interpolation between $K_t = 1$ and $K_t = 3$

To obtain intermediate reference curves for $1 < K_t < 3$ (specifically $K_t = \{1.5, 2.0, 2.5\}$), an interpolation was performed between the two MMPDS anchor curves. At each life N_f, the interpolated maximum stress was defined via linear interpolation in log-stress,

$$\log_{10}\big(S_{\text{max}}(N_f, K_t)\big) = (1 - w)\,\log_{10}\big(S_{\text{max}}(N_f, 1)\big) + w\,\log_{10}\big(S_{\text{max}}(N_f, 3)\big), \qquad w = \frac{K_t - 1}{3 - 1} \tag{7.40}$$

where,

- $S_{\text{max}}(N_f, K_t)$ interpolated maximum stress at life N_f for stress concentration factor K_t [MPa]
- $S_{\text{max}}(N_f, 1)$ maximum stress at life N_f from the $K_t = 1$ MMPDS reference curve [MPa]
- $S_{\text{max}}(N_f, 3)$ maximum stress at life N_f from the $K_t = 3$ MMPDS reference curve [MPa]
- N_f number of cycles to failure [cycles]
- K_t stress concentration factor $[-]$
- w interpolation weight between the $K_t = 1$ and $K_t = 3$ reference curves $[-]$

This procedure enforces monotonic behaviour and guarantees that the intermediate curves remain bounded by the two MMPDS anchor curves. The resulting family of curves provides a convenient visual and quantitative reference, but should be interpreted as an interpolation-based estimate rather than an additional MMPDS allowables dataset.

Specimen-based fit and effective K_t estimate.

A specimen-specific mean curve was then fitted directly to the measured (S_{max}, N_f) points using an MMPDS-style relationship of the form

$$\log_{10}(N_f) = C - M\log_{10}(S_{\text{eq}})\,, \qquad S_{\text{eq}} = S_{\text{max}}(1 - R)^P, \tag{7.41}$$

with $R = 0.1$ fixed and $P = 0.52$ (consistent with the unnotched MMPDS exponent). The parameters C and M were identified by linear regression in $\log_{10}(S_{\text{eq}})$–$\log_{10}(N_f)$ space. As shown in Fig. 7.20, the MMPDS mean reference curves for $K_t = 1$ and $K_t = 3$ were augmented with interpolated intermediate curves ($K_t = \{1.5, 2.0, 2.5\}$) and compared against the measured TB/TBL results and the specimen-based fitted mean curve.

Finally, an “effective” notch severity for the specimens was estimated by comparing the five-specimen fitted curve to the interpolated K_t-family in Eq. (7.40) over the plotted life range (10^4 to 10^6 cycles). The best match corresponded to an effective value of approximately

$$K_{t,\text{eff}} \approx 2.3,$$

indicating that the overall fatigue behaviour of the tested geometry is intermediate between the MMPDS unnotched ($K_t = 1$) and notched ($K_t = 3$) reference cases when TB2 is excluded.

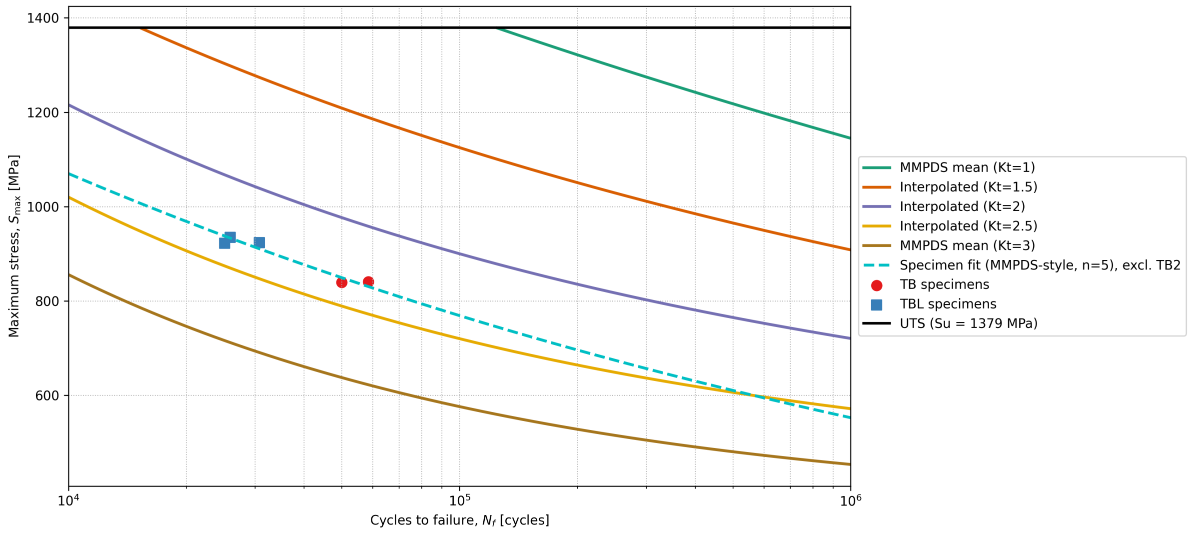

Figure 7.20: MMPDS reference curves with interpolated intermediate Kt curves, overlaid with TB/TBL test results

7.7.4. Comparison with Fatigue-Life Prediction and Retardation Effects

The fatigue-life prediction framework in Section 7.6 provided an expected ordering of the four spectrum variants and an indication of whether a meaningful life difference should be observable within a feasible cycle budget. Given the limitations discussed earlier for smooth specimens under tension–tension loading, the comparison was framed primarily in terms of relative agreement, whether the model captures the observed ranking between variants and the direction of the overload effect, rather than absolute life accuracy.

Table 7.15: Comparison of measured cycles to failure with MMPDS mean-life prediction ratios (TB2 excluded)

	Measured [-]	MMPDS $K_t = 1$ [-]	MMPDS $K_t = 2.3$ [-]	MMPDS $K_t = 3$ [-]
TB	54,321	7,862,952	30,414	7,644
TBL	27,272	1,669,539	13,939	4,630
TB/TBL	2.0	4.7	2.2	1.7

In the MMPDS-based predictions, inclusion of the retardation blocks reduced the predicted life for both the TB and TBL spectra. In contrast, the experiments did not show a corresponding reduction in life, indicating that retardation effects remain difficult to capture reliably within the present simplified prediction framework.

Table 7.16: Measured versus predicted fatigue lives, reported in equivalent towing mission blocks (= 100 towing operations) (TB2 excluded)

	Measured [-]	MMPDS $K_t = 1$ [-]	MMPDS $K_t = 2.3$ [-]	MMPDS $K_t = 3$ [-]
TB	302	43,683	169	42
TBL	41	2,530	21	7
TB/TBL	7.3	17.3	8.0	6.1

Retardation effects

To isolate the towing-concept effect and the overload-insertion effect from absolute scatter, results are additionally expressed as ratios of mean lives. Using missions to fracture as the reported metric, the towing-concept ratio was defined as

$$\rho_{\text{TBL/TB}} = \frac{\bar{N}_{\text{missions,exp,TBL}}}{\bar{N}_{\text{missions,exp,TB}}} \tag{7.42}$$

while the overload effect for each towing concept is captured by

$$\rho_{\text{RET,TB}} = \frac{\bar{N}_{\text{missions,exp,TB+RET}}}{\bar{N}_{\text{missions,exp,TB}}}, \qquad \rho_{\text{RET,TBL}} = \frac{\bar{N}_{\text{missions,exp,TBL+RET}}}{\bar{N}_{\text{missions,exp,TBL}}} \tag{7.43}$$

The ratios in Table 7.17 were evaluated directly from the measured mean missions to failure in Table 7.14 by substituting the corresponding $\bar{N}_{\text{missions,exp}}$ values into Equations 7.42–7.43.

Table 7.17: Life ratios quantifying the towing-concept effect and the effect of a single early overload insertion (TB2 excluded)

Metric	Computation	Ratio [-]
Towing concept effect, $\rho_{\text{TBL/TB}}$	$41/303$	0.14
Overload effect under TB, $\rho_{\text{RET,TB}}$	$571/303$	1.89
Overload effect under TBL, $\rho_{\text{RET,TBL}}$	$54/41$	1.32

These ratios were the most direct experimental indicators, because they compare like-for-like spectra under identical machine and specimen conditions.

Interpretation of results

The towing-concept ratio $\rho_{\text{TBL/TB}} = 0.14$ indicated that, in this programme (TB2 excluded), TBL reached fracture in ≈ 7.3 times fewer missions than TB. The overload-insertion ratios showed a life increase for both concepts: $+32\%$ for TBL ($\rho_{\text{RET,TBL}} = 1.32$) and $+89\%$ for TB ($\rho_{\text{RET,TB}} = 1.89$). The larger TB increase was consistent with the overload being defined at a TBL-representative stress range. Relative to the baseline TB spectrum, the overload ratio was higher (greater separation between the overload and subsequent-cycle maxima). Hence, any retardation mechanism persisted more strongly into subsequent TB cycles. Moreover, for TBL, subsequent high cycles lie closer to the overload level and could erode the retardation benefit more rapidly. Operationally, this implies that occasional TBL-like peak events during otherwise TB-dominated service could also increase life through retardation, so mixed TB/TBL usage may reduce the practical separation between the pure-TB and pure-TBL lives. In contrast, the MMPDS/Miner framework used here did not capture such sequence effects. It therefore predicted a reduction in life upon overload insertion, indicating that retardation effects would require an explicit crack-growth formulation for prediction.

7.7.5. Grip-Induced Load Asymmetry

Following the MMPDS comparison in Section 7.7.3, the remaining discrepancy between the smooth-specimen reference predictions and the measured lives indicated that the laboratory boundary condition itself contributed additional local severity beyond the nominal dog-bone geometry. The fracture surfaces and grip-contact patterns suggested that this effect was not random specimen scatter alone, but a systematic asymmetry in load introduction. The present subsection, therefore, treats grip-induced eccentricity as a candidate explanation for the elevated effective local severity inferred from the test results.

Baseline geometric K_t under uniform axial loading

In Section 7.6, the geometric stress concentration associated with the dog-bone shoulder transition was already discussed, and the baseline value was stated to be approximately $K_t \approx 1.1$. To verify this for the present specimen geometry and to separate the purely geometric contribution from any test setup artefacts, an additional Abaqus analysis was performed in which the axial load is introduced uniformly.

From this uniform-loading case, the effective stress concentration factor at the critical shoulder-to-gauge transition was extracted using the same definition as in Eq. (7.44), based on the maximum axial surface stress in the gauge region relative to the nominal stress F/A. For the present, as-modelled dog-bone geometry (Figure 7.22a), the resulting baseline value was

$$K_{t,\text{geom}} \approx 1.12$$

confirming the earlier estimate and demonstrating that the geometry alone produces only a modest local amplification of the nominal axial stress. Any increase beyond $K_{t,\text{geom}} \approx 1.12$ must originate from non-uniform load introduction in the grips, rather than from the specimen geometry itself.

Fractographic indication of asymmetric load introduction

A consistent feature across all failed specimens was that the dog-bone did not appear to be seated centrally in the grips. Instead, the imprint of the grip contact region formed an off-centred 'grip circle', indicating that the specimen effectively shifted during clamping. This implied that the axial load was introduced with a persistent eccentricity, such that one side of the cross-section carries a larger share of the applied load than the opposite side.

The fracture surfaces supported this interpretation. In the three examples shown in Fig. 7.21 (TB2, TB RET2, and TBL2), the crack-initiation side corresponds to the region where the grip imprint extends further inwards. Crack growth markings were then observed to propagate from this side across the section, consistent with a higher local tensile stress (and hence accelerated damage accumulation) on the loaded side. Taken together, the grip imprint and fracture morphology indicated that an asymmetric load introduction was a plausible root cause of the recurring one-sided damage pattern.

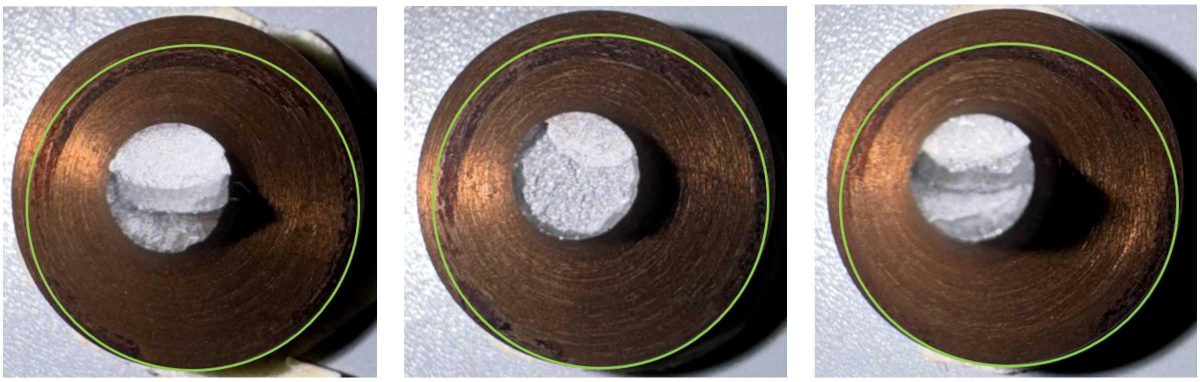

(a) TB2 **(b)** TB RET2 **(c)** TBL2

Figure 7.21: Examples of asymmetric grip damage pattern

Abaqus model and K_{t-grip} estimation under eccentric load sharing

To quantify the potential artificial stress concentration resulting from this off-centred seating, an Abaqus finite-element analysis was performed in which the specimen was loaded with an intentionally asymmetric load distribution across the grip contact region. The model was used to estimate an effective stress concentration factor,

$$K_{t-grip} = \frac{\sigma_{\text{max,surf}}}{\sigma_{\text{nom}}} \tag{7.44}$$

where,

- K_{t-grip} stress concentration factor at the considered location [-]
- $\sigma_{\text{max,surf}}$ maximum surface stress at the hotspot/location of interest [MPa]
- σ_{nom} nominal (net-section) stress used as the reference stress level [MPa]

The surface stress is used because crack initiation occurs at the free surface and is therefore governed by the local surface stress state. A parametric study was conducted by prescribing different left–right load-sharing ratios at the grips, ranging from symmetric loading (50–50) to increasingly eccentric cases up to 60–40. For each case, the resulting $\sigma_{\text{max,surf}}$ and corresponding K_{t-grip} were extracted from the Abaqus results, yielding a mapping between assumed grip load distribution and the implied stress concentration factor.

The resulting K_t values for all investigated load splits are summarised in Table 7.18. To aid interpretation, Figure 7.22 shows the corresponding Abaqus stress contour on the specimen, illustrating how grip-induced load asymmetry localises the surface stress field and drives $\sigma_{\text{max,surf}}$ above the nominal level σ_{nom}.

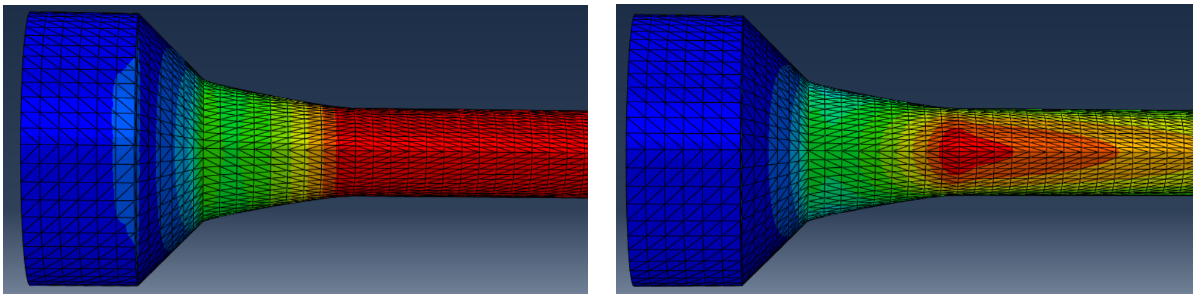

(a) Uniform grip load split (50/50) **(b)** Asymmetric grip load split (59/41)

Figure 7.22: Abaqus stress contours on the axial-fatigue specimen for two assumed grip load-sharing ratios

Table 7.18: Abaqus-derived stress concentration factors $K_{t\text{-}grip}$ for different assumed grip load-sharing ratios

Load split [%–%]	$K_{t\text{-}grip} = \sigma_{\text{max,surf}}/\sigma_{\text{nom}}$
50–50	1.12
51–49	1.25
52–48	1.38
53–47	1.50
54–46	1.63
55–45	1.76
56–44	1.89
57–43	2.02
58–42	2.15
59–41	2.28
60–40	2.41

Comparing the Abaqus-derived factors to the experimentally inferred value ($K_t \approx 2.3$), the best agreement occurred for a load-sharing ratio of approximately 59–41 %, which was considered plausible given the non-ideal force introduction between the two grip sides. The type of damage seen in Figure 7.21 is a distinct pattern of a smaller and a larger radius half circle on the specimen, potentially causing a distribution of the load as modelled for this specimen. With this inferred load distribution, the mapping from nominal to local stress was better constrained, enabling a more defensible comparison between the predicted spectrum severity and the measured fatigue lives.

In the Abaqus interpretation above, the grip-induced load asymmetry is treated as a net left–right load split at the specimen section. If the opposing grip is assumed to remain concentrically seated (it does not introduce additional eccentricity and maintains a stable, symmetric contact), the resulting $K_{t\text{-}grip}$ did not change much relative to the net-split representation, because the peak surface stress remains governed by the dominant side carrying the larger force fraction. Over the investigated range from 50–50 to 60–40, the corresponding increase for the opposite end of the specimen, was only $\Delta K_{t\text{-}grip} \approx 0.38$ to a value of $K_{t\text{-}grip} \approx 1.5$

7.8. Limitations and Uncertainty of Lab-to-Service Comparison

Although WP3 provided a controlled comparative assessment of TB and TBL fatigue severity, the lab-to-service interpretation remained subject to several important limitations. These uncertainties stem from the experimental setup, specimen and material representativeness, spectrum simplification, and the difference between laboratory and operational boundary conditions.

Test-Frame and Control

APC stabilisation effects

At the start of a programme segment of cycles, the APC compensator required a short stabilisation period before the measured force matched the commanded sinusoidal waveform. As a result, the first cycles of a segment were occasionally applied at a slightly reduced amplitude relative to the intended spectrum. This affects the absolute fidelity of the executed loading history. However, because this build-up behaviour was consistent across runs, and because the TB and TBL programmes contain a comparable level-transition structure, its influence is expected to be broadly similar for both spectra. The APC stabilisation effect is therefore considered a secondary source of uncertainty for absolute life, but not one that is likely to alter the comparative TB–TBL interpretation in a significant way.

Grip alignment and load-introduction asymmetry

Grip alignment and the resulting non-uniform load introduction constitute a major limitation of the present laboratory campaign. The observed off-centred seating of the specimens likely introduced a persistent eccentricity in the applied load path, which increased the local surface stress and probably reduced the measured lives relative to an ideally concentric setup. This effect is therefore important for the absolute life level obtained in WP3. At the same time, the same grip concept and boundary conditions were used throughout the full test matrix, and the grips were not free to rotate about their own axis. The resulting asymmetry is therefore considered systematic rather than random, such that the comparative differences between spectrum variants remain defensible, even if the absolute lives were biased downward. For future work, this uncertainty should preferably be reduced by introducing a central notch geometry that forces crack initiation away from the grip region and at a more predictable location.

Load-ratio constraint and mean-stress representativeness ($R = 0.1$)

The machine requirement to maintain tension-tension loading imposed a lower bound of $R \geq 0.1$, whereas the original towing-derived stress histories also contained cycles with negative stress ratios. To make the spectra executable, cycles violating this constraint were shifted upward in stress while preserving the stress range where possible. Although this procedure retains an important fatigue-driving quantity, it modifies the original mean-stress distribution and therefore does not exactly reproduce the operational loading state. This is a limitation because fatigue damage depends not only on stress range, as captured by rainflow counting, but also on mean stress. The adopted $R = 0.1$ conditioning was therefore a practical compromise required to connect the towing spectra to the available MMPDS-style reference data and the limitations of the test setup, rather than an ideal physical representation of the full mission loading. Future experiments would benefit from a setup that allows zero-crossing, such that the original stress-ratio content of the towing spectra can be reproduced more directly.

Specimen Characteristics

Surface condition

The surface condition of the tested specimens is a relevant source of uncertainty, but could not be quantified explicitly in the present campaign. No detailed manufacturing or finishing records were available, and no formal pre-test surface metrology or microscopic inspection dataset was performed. Although no obvious defects were visible to the naked eye before testing, this does not exclude the presence of small surface discontinuities, machining marks, or incipient defects that could locally accelerate crack initiation. The post-test observations on TB2 suggest that such specimen-specific surface or edge imperfections may indeed have contributed to its premature failure. As a result, the specimen surface condition should be regarded as an uncontrolled scatter source in the measured lives. For future work, this uncertainty should be reduced by documenting the full manufacturing route, specifying the finishing procedure, and performing pre-test surface inspection at a suitable magnification, preferably supplemented by roughness measurements or other surface-quality controls.

Geometric representativeness: smooth specimen versus feature-controlled initiation

A more fundamental limitation is that the present specimens are smooth dog-bone specimens, whereas fatigue initiation in the actual drag brace is expected to be feature-controlled. In service, cracking is more likely to initiate at local geometric discontinuities such as holes, fillets, lug transitions, or contact interfaces, where the stress field is highly concentrated, and the initiation phase is shorter than in a uniform, smooth gauge section. The present specimen geometry, therefore, does not reproduce the true local initiation condition of the component, but instead provides a simplified axial-fatigue representation that is suitable mainly for relative spectrum comparison. Within the constraints of the available grips, machine capacity, and test setup, a representative notched specimen was not pursued because this would have introduced additional uncertainties related to notch manufacture, alignment, and load introduction. Consequently, the link to component-level behaviour had to be made indirectly, including comparison against MMPDS reference curves and interpolation between $K_t = 1$ and $K_t = 3$. Future work should preferably focus on specimens or subcomponents that more directly reproduce the actual geometric initiation features, so that the fatigue response is governed by a representative local stress concentration rather than being inferred from smooth-specimen behaviour.

Material representativeness: 17-4PH H900 vs. 300M steel

Fatigue specimens were manufactured from 17-4PH in condition H900, whereas primary landing-gear components are commonly produced from ultra-high-strength steels such as 300M. This material substitution adds systematic uncertainty when translating laboratory life to in-service relevance, because fatigue response depends on alloy system and heat treatment.

The main effect is on absolute life interpretation rather than within-test repeatability. Differences in S–N behaviour, mean-stress sensitivity, notch sensitivity, and crack initiation mechanisms imply that life measured on 17-4PH H900 cannot be assumed directly representative of 300M without additional material-specific calibration. The test programme is therefore used primarily to compare relative towing-spectrum severity under a consistent specimen material condition, while absolute life transfer to 300M is treated as a limitation.

Spectrum Simplification

Mission block simplification

The laboratory loading programme is based on a simplified representation of towing usage rather than on a direct replay of full operational histories. First, the original variable-amplitude hotspot histories were reduced through discretisation, rainflow counting, and conversion into a finite set of constant-amplitude machine levels. The selected discretisation width of $\Delta\sigma_{\text{bin}} = 8$ MPa was shown to provide acceptable numerical convergence, but it nonetheless replaces a continuous stress history by a levelled approximation.

A second simplification arises from block construction and execution order. The representative towing usage is condensed into a fixed 100-operation reference block, which was repeated ten times per machine programme segment based on the adopted A–D mission mix, after which this block is repeated in the machine programme. For execution stability, the final laboratory programme was ordered from relatively low to high mean stress and amplitude, rather than preserving the exact original sequence of the towing histories. This ordering may influence sequence-sensitive behaviour and could slightly delay failure relative to a less ordered spectrum. However, because failure occurred only after multiple repeated programme segments, the influence of this start-up ordering is expected to be secondary relative to the overall difference in retained TB and TBL spectrum severity.

Finally, the adopted mission set $\{A, B, C, D\}$ and its fixed usage mix remain operational idealisations. Real towing practice depends on airport layout, aircraft positioning tasks, local procedures, and operator behaviour, so the true mission distribution in service will vary. The present block definition is therefore not intended as a complete statistical representation of all possible towing operations, but as a structured and comparable approximation for relative TB–TBL assessment. Future work would benefit from expanding the operational database and more explicitly examining the extent to which the measured differences between TB and TBL are robust across operators, manoeuvre strategies, and airfield contexts.

Neglected multiaxiality: torsion and out-of-plane effects

A further limitation is that WP3 reduces the drag-brace response to an equivalent axial specimen loading, whereas the actual component is subjected to a more complex multi-axial stress state. In service, the drag brace can experience combined axial force, local bending, secondary torsion, and out-of-plane loading arising from geometric offsets, joint flexibility, wheel-ground interaction, and changes in towing direction. Even if one stress component is dominant at the selected hotspot, these additional components can influence both the crack-initiation location and the subsequent development of fatigue damage. The current smooth axial-fatigue setup cannot directly reproduce such multi-axial effects.

This simplification was accepted because the objective of WP3 was to obtain a controlled and repeatable laboratory comparison between TB and TBL using a feasible specimen and machine configuration. Nevertheless, it limits the tests' physical representativeness at the component level. In particular, any interaction among normal stress, shear stress, and local non-proportional loading is not explicitly captured, and the resulting lives should therefore not be interpreted as a complete representation of drag-brace fatigue behaviour in service. Future work would ideally include a more direct subcomponent or full-scale test configuration, or a dedicated multi-axial specimen concept, such that torsional and out-of-plane effects can be introduced and their contribution to the TB–TBL difference can be assessed explicitly.

Revised endurance-strength filtering due to grip-induced stress concentration

The geometric stress concentration associated with the dog-bone shoulder transition was already discussed in Section 7.6, and the baseline value was stated to be approximately $K_t \approx 1.1$ (Figure 7.9). Post-test inspection and the observed grip "locking" behaviour indicate that this assumption was non-conservative for the laboratory configuration. The effective stress concentration at the specimen ends during load transfer was higher than assumed. As a result, the fatigue-limit threshold used in the filtering step was set too high, which removed an excessively large fraction of the cycle population. This removal will likely shift the predicted fatigue lives because cycles that are currently neglected may, in fact, contribute non-negligible damage once the effective local stresses are accounted for.

To reflect the effective laboratory boundary condition, the present analysis therefore adopts an updated specimen factor of

$$K_t = 2.3$$

which revises the peak-to-peak fatigue-limit threshold used for cycle removal. Since the original filtering used $\Delta\sigma_{\text{FL}} = 364$ MPa at $K_t = 1.1$, the updated threshold becomes

$$\Delta\sigma_{\text{FL,new}} = \Delta\sigma_{\text{FL,old}} \frac{K_{t,\text{old}}}{K_{t,\text{new}}} = 364\,\text{MPa}\,\frac{1.1}{2.3} \approx 174\,\text{MPa} \tag{7.45}$$

Implementing $\Delta\sigma_{\text{FL,new}}$ in the MMPDS-style filtering framework would increase the number of retained damage-relevant cycles in the representative block from 179 to 546 for TB and from 660 to 1447 for TBL. This indicates that the original filtering based on $K_t = 1.1$ was too strict, particularly given the later-observed effective notch severity caused by the grips. Although the revised filtering would admit a substantially larger population of intermediate cycles into the laboratory representation, the comparative trend remains unchanged. Overall, the towbarless spectrum still retains more damaging content than the towbar spectrum. Importantly, the revised K_t would also have improved the laboratory programme representativeness, because an unconservative fatigue-limit threshold would no longer have excluded cycles that plausibly contribute to fatigue damage.

Environmental Effects on Service Life.

The present fatigue programme is conducted in laboratory air on smooth specimens, while operational landing-gear parts may experience chloride-containing environments and crevice conditions at joints. Published data show that such environments can materially reduce fatigue resistance for 17-4PH. The ARMCO 17-4PH product data bulletin reports corrosion-fatigue limits at 5×10^7 cycles in flowing seawater (rotating cantilever-beam specimens) of approximately 207 MPa to 276 MPa for conditions H925 and H1150, which is only about 15–20% of the listed UTS for H925. [77]

In a separate study performed in 3.5% NaCl at $R = -1$, the fatigue limit decreased from about 700 MPa in air to about 415 MPa in the corrosive environment, corresponding to a reported reduction of up to 40 %. [82]

These magnitudes demonstrate that laboratory air tests alone do not fully capture service-relevant damage mechanisms (notch and pit initiation, environment-assisted cracking). Therefore, laboratory results should be interpreted primarily as a benign reference for relative spectrum comparisons rather than a direct service-life prediction.

8

Results

This chapter presents the study's main findings and relates them directly to the research questions defined in Chapter 4. The results are organised by work package, while the relation between the individual sections and the research questions addressed is summarised in Table 8.1. The final sections synthesise these findings into explicit answers to the sub-research questions and, ultimately, the main research question.

Table 8.1: Relation between Results chapter sections and research questions

Section	Main focus	Research questions addressed
Section 8.1	In-field towing results and spectra	SRQ1, SRQ2, SRQ4
Section 8.2	Finite-element hotspot and stress results	SRQ3, SRQ5, SRQ6
Section 8.3	Laboratory fatigue results	SRQ7
Section 8.4	Overall synthesis	SRQ1–SRQ7 + MRQ
Section 8.5	Expert-observation comparison	Qualitative triangulation of the integrated findings

8.1. In-Field Towing Results

This section presents the WP1 in-field towing results and the final manoeuvre set carried forward into the finite-element and laboratory work packages. It addresses SRQ1, concerning which representative towing load cases populate the measured ground-loading spectrum, SRQ2, concerning how towbar and towbarless towing differ at the manoeuvre level, and SRQ4, concerning how representative towing spectra should be constructed for fatigue assessment. These questions are addressed by first defining the usable manoeuvre dataset, then comparing the retained TB–TBL differences at the manoeuvre level, and finally identifying the governing spectral features passed to WP2 and WP3.

8.1.1. Measured Manoeuvre Set and Usable Dataset

WP1 delivered a canonical library of 12 towing manoeuvres for downstream analysis, based on the event definitions in Table 5.1 and the executed programme shown in Figure 5.18. Table 8.2 distinguishes between directly measured, estimated, and proxy cases. Of the 12 manoeuvres, eight were available as directly measured towbar force histories, three were estimated from related measured cases, and one was represented by a proxy case. The downstream WP1 spectrum definition was therefore based predominantly on measured towbar data, with only limited supplementation required to complete the canonical manoeuvre set.

Table 8.2: Summary of the WP1 manoeuvre set used in the downstream analysis

EventCode	Status	TB basis	Downstream use
`SP_STEADY_PULL`	Measured	Direct towbar force history	Baseline pull case
`SP_STEADY_PUSH`	Measured	Direct towbar force history	Baseline push case
`ACC_PULL_SMOOTH`	Measured	Direct towbar force history	Longitudinal transient case
`BRK_PULL_SMOOTH`	Measured	Direct towbar force history	Longitudinal transient case
`ACC_PUSH_SMOOTH`	Measured	Direct towbar force history	Longitudinal transient case
`BRK_PUSH_SMOOTH`	Measured	Direct towbar force history	Longitudinal transient case
`TURN_PULL_TIGHT`	Measured	Direct towbar force history	Baseline turning case
`BRK_PULL_RAPID`	Measured	Direct towbar force history	Overload-like transient case
`TURN_PUSH_TIGHT`	Estimated	Sign-reversed from tight pull turn	Estimated turning case
`TURN_PULL_WIDE`	Estimated	Reduced variant of tight pull turn	Estimated turning case
`TURN_PUSH_WIDE`	Estimated	Sign-reversed from wide pull turn	Estimated turning case
`BRK_PUSH_RAPID`	Proxy	`BRK_PUSH_SMOOTH`	Proxy braking case

The corresponding TBL force histories were obtained through the WP1 TB–TBL translation framework rather than through direct force measurement.

8.1.2. Towbar vs. Towbarless Differences at Manoeuvre Level

At the manoeuvre level, the TB–TBL difference was limited for steady towing and remained secondary for the turning cases, but became more pronounced in acceleration and especially braking manoeuvres. This pattern is consistent with the Rotterdam The Hague Airport comparison in Figures 5.23–5.25, which showed faster and more continuous TBL execution, clearer braking events, and larger lateral manoeuvre-acceleration peaks during turning. Figure 8.1 shows four manoeuvres, with different severities between the two towing methods.

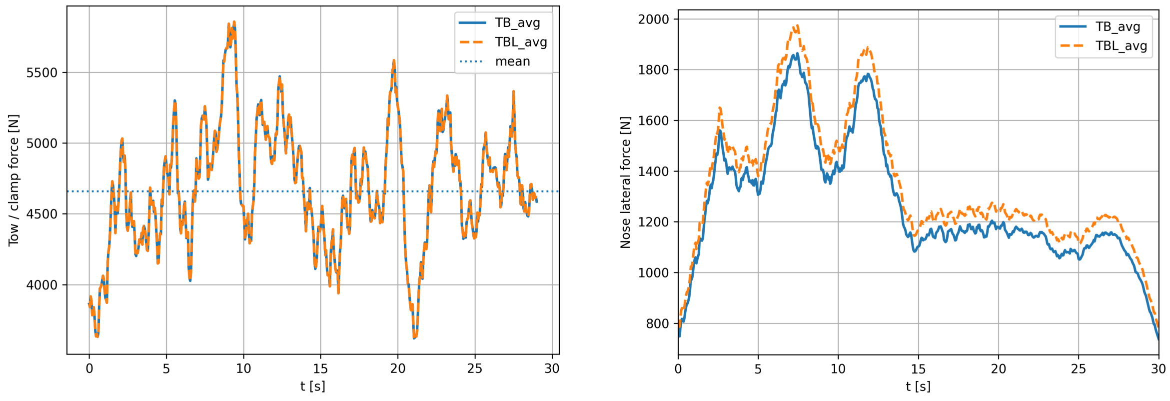

(a) `SP_STEADY_PULL`: Negligible

(b) Lateral `TURN_PULL_WIDE`: Minor

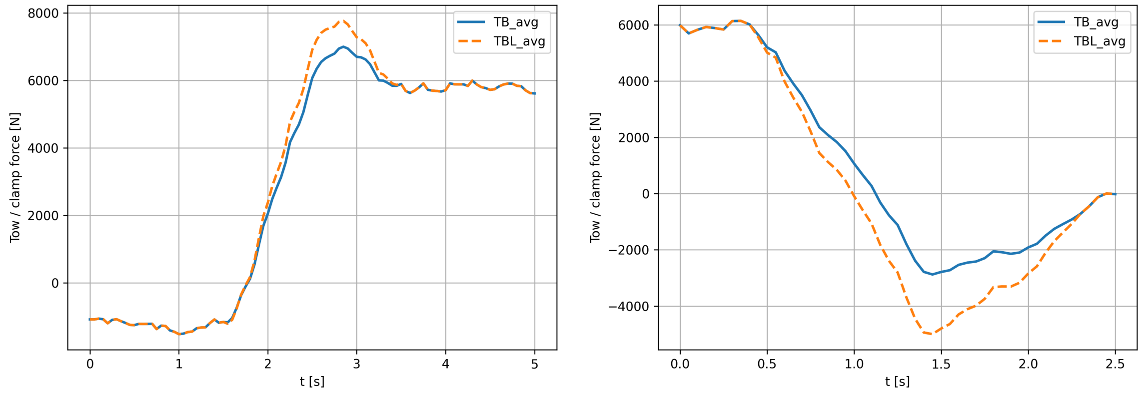

(c) `ACC_PULL_SMOOTH`: Moderate

(d) `BRK_PULL_SMOOTH`: Strong

Figure 8.1: Representative TB–TBL manoeuvre-level spectra used to illustrate the main in-field differences

Table 8.3 summarises the retained relative severity per `EventCode`, consistent with the detailed manoeuvre-level treatment in Table 5.7.

Table 8.3: Summary of retained TB–TBL manoeuvre-level differences in WP1

EventCode(s)	TB–TBL effect	Downstream relevance
`SP_STEADY_PULL` `SP_STEADY_PUSH`	Negligible	Baseline tensile/compressive towing level
`ACC_PULL_SMOOTH` `ACC_PUSH_SMOOTH`	Moderate	Retained as transient-sensitive longitudinal cases
`BRK_PULL_SMOOTH`	Strong	Retained as a key braking-sensitive comparison case
`BRK_PULL_RAPID`	Strong	Retained as overload-like peak-content case
`BRK_PUSH_SMOOTH` `BRK_PUSH_RAPID`	Negligible	Push braking not treated as a primary discriminator

`TURN_PULL_TIGHT`
`TURN_PUSH_TIGHT`
`TURN_PULL_WIDE`
`TURN_PUSH_WIDE`
	Minor	Turning retained for completeness, but not as a primary TB–TBL discriminator in WP1

A final cross-manoeuvre observation concerns the high-frequency response content. Although the aircraft IMU residuals showed somewhat larger high-frequency acceleration envelopes in the TBL runs, the inferred increment remained small relative to the dominant towing load content. It was therefore neglected in the fatigue-initiation accounting. At the towing-equipment side, the TB configuration showed more pronounced shock-like peaks during braking and push–pull reversals, consistent with geometric play in the towbar ring interface (Figures 5.26 and 5.27). These peaks were treated as interface-dependent artefacts rather than as an intrinsic towing-concept effect and were therefore not propagated as governing spectral features.

8.1.3. Resulting Towing Spectra and Governing Spectral Features

The resulting spectra indicated that the main TB–TBL distinction lay not in the baseline towing level but in a smaller subset of transient-sensitive longitudinal manoeuvres. The steady pull and push levels are quantified in Figure 5.28, from which the corrected effective longitudinal resistance was obtained as $F_{\text{long,res,corrected}} = 4.7$ kN with $C_{\text{tow,eff}} = 0.11$. The manoeuvre spectra presented in Section 5.7, particularly Figures 5.31–5.38, showed that the most relevant TB–TBL differences occurred in pull braking, rapid pull braking, and, to a lesser extent, pull and push acceleration, whereas the turning cases remained effectively unchanged in the longitudinal direction under the adopted WP1 treatment.

Figure 8.2 summarises this result across the canonical manoeuvre set using the max–min force range and time-weighted mean force of each event. The steady towing cases remained nearly unchanged between TB and TBL, while `BRK_PULL_SMOOTH` and `BRK_PULL_RAPID` showed the clearest increase in TBL severity. `ACC_PULL_SMOOTH` and `ACC_PUSH_SMOOTH` exhibited a more moderate increase, whereas the push-braking and turning cases remained comparatively similar under the adopted WP1 treatment.

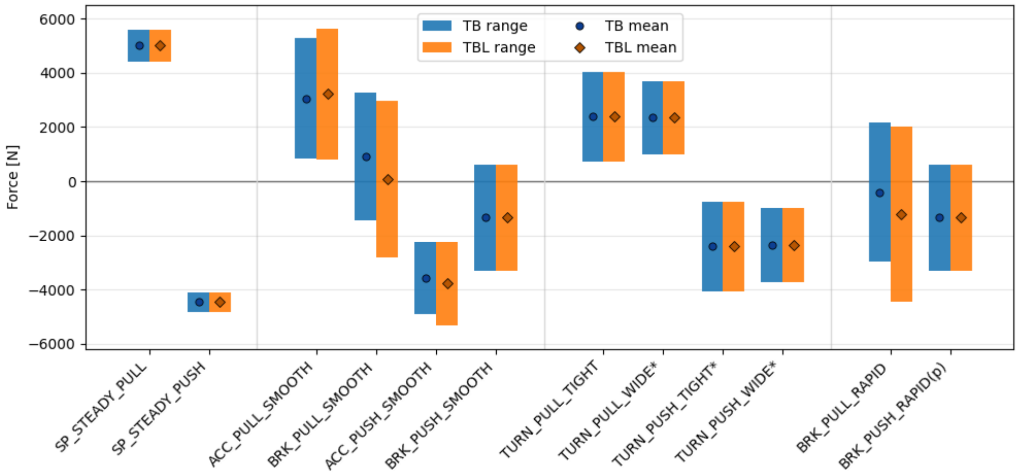

Figure 8.2: Cross-manoeuvre comparison in terms of peak-to-peak force range and mean force for TB and TBL

Accordingly, WP1 provided a structured set of representative towing events in which the steady manoeuvres defined the background load environment and a limited number of longitudinal transient-sensitive cases defined the concept-level separation between TB and TBL. These spectra were passed to WP2 and WP3 as a canonical event-based loading library rather than as a single continuous operational trace.

8.2. Finite-Element Results and Governing Critical Locations

This section presents the WP2 finite-element results for the towing-derived load cases. It addresses SRQ3, concerning which nose-wheel landing gear components and locations are most fatigue-critical, SRQ5, concerning which manoeuvres produce the largest TB–TBL stress differences and hotspot amplification, and SRQ6, concerning whether towbarless towing shifts the governing hotspot or suggests a different failure-mode tendency. These questions are addressed by first comparing the global hotspot rankings, then evaluating the refined local drag-brace hotspot response, and finally assessing whether the change in towing method alters the governing structural fatigue picture.

8.2.1. Global Hotspot Screening

The global screening results showed that the drag-brace-related hotspot `DRAG_BRACE_V_BASE` remained the highest-ranked location for both TB and TBL towing, while the relative importance of several other regions changed between the two concepts. In particular, the fork-and-axle load path became more prominent under TBL loading, while the drag-brace region remained the dominant global fatigue-critical location overall, consistent with the summary ranking reported in Table 6.6. The condensed ranking is shown in Figure 8.3 and Table 8.4.

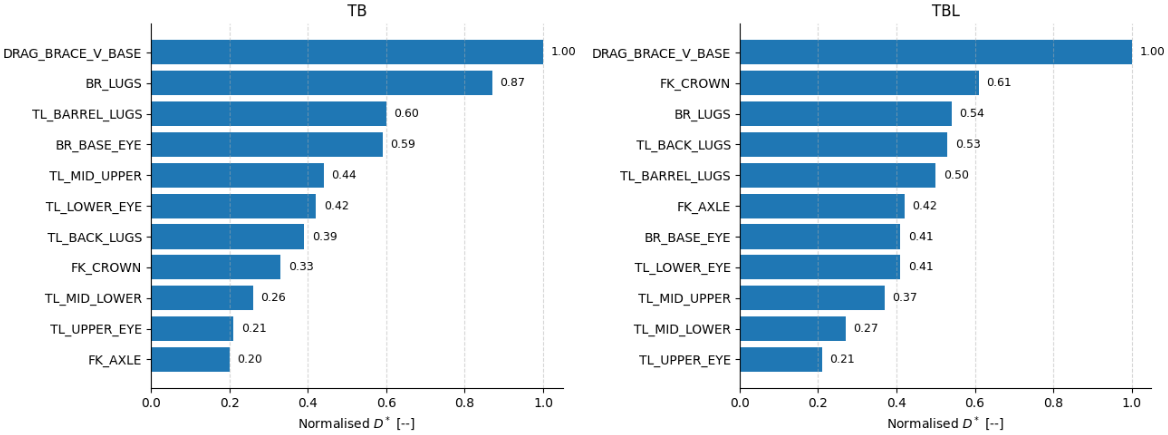

Figure 8.3: Global hotspot ranking of the NWLG under the canonical towing load set

Table 8.4: Condensed summary of the highest-ranked global hotspots, based on Table 6.5 (WP2)

Rank	TB	TBL
1	`DRAG_BRACE_V_BASE`	`DRAG_BRACE_V_BASE`
2	`BR_LUGS`	`FK_CROWN`
3	`TL_BARREL_LUGS`	`BR_LUGS`

Figure 8.3 and Table 8.4 show that `DRAG_BRACE_V_BASE` was already the governing global hotspot under TB loading and retained this position under TBL loading. In relative terms, its dominance increased further under TBL, even though the ranking of the other regions changed. The drag-brace base was therefore selected as the governing location for the subsequent local model refinement and specimen-level translation.

8.2.2. Local Drag-Brace Hotspot Result

The refined local drag-brace model confirmed that the drag-brace region remained the governing fatigue-critical location for downstream assessment. Figure 8.4 shows that, in terms of absolute local hotspot stress, `ACC_PULL_SMOOTH` was the dominant manoeuvre for both towing concepts, increasing from approximately 482.5 MPa in TB to 783.5 MPa in TBL. The same figure also shows that the local manoeuvre ranking is not preserved under towbarless towing: while the highest absolute severity remains associated with pull acceleration, several secondary TB manoeuvres increase substantially in the TBL case, including `BRK_PULL_SMOOTH` and `BRK_PULL_RAPID`. This is consistent with the local drag-brace bending response, causing manoeuvres that act more globally in compression, such as pull braking and selected push cases, generated tensile stress at the local hotspot because the brace was bent, thereby producing the large increases in maximum principal stress seen for these cases.

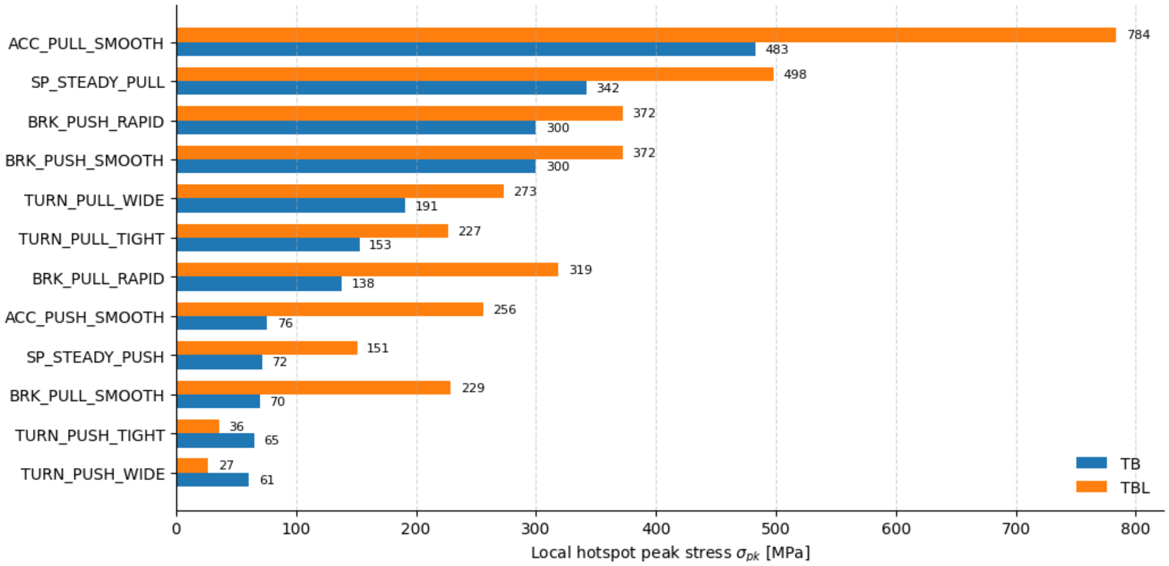

Figure 8.4: Local drag-brace hotspot severity per manoeuvre for TB and TBL

This redistribution becomes even clearer in Figure 8.5, which isolates the TBL-to-TB amplification ratio at the local drag-brace hotspot. The largest relative increases do not occur in the already-governing pull-acceleration case, but in `ACC_PUSH_SMOOTH` and `BRK_PULL_SMOOTH`, with stress ratios of 3.35 and 3.28, followed by `BRK_PULL_RAPID` at 2.32 and `SP_STEADY_PUSH` at 2.10. By contrast, the only manoeuvres for which the TBL response falls below the TB level are the push-turn cases `TURN_PUSH_TIGHT` and `TURN_PUSH_WIDE`. This behaviour is attributed to the adopted modelling and constraint treatment of the torque links, as discussed in Subsection 6.2.4, which results in a less representative load introduction for these specific cases. Since these manoeuvres are not fatigue-governing and the expected TB–TBL difference is limited, they do not affect the overall interpretation of the WP2 results.

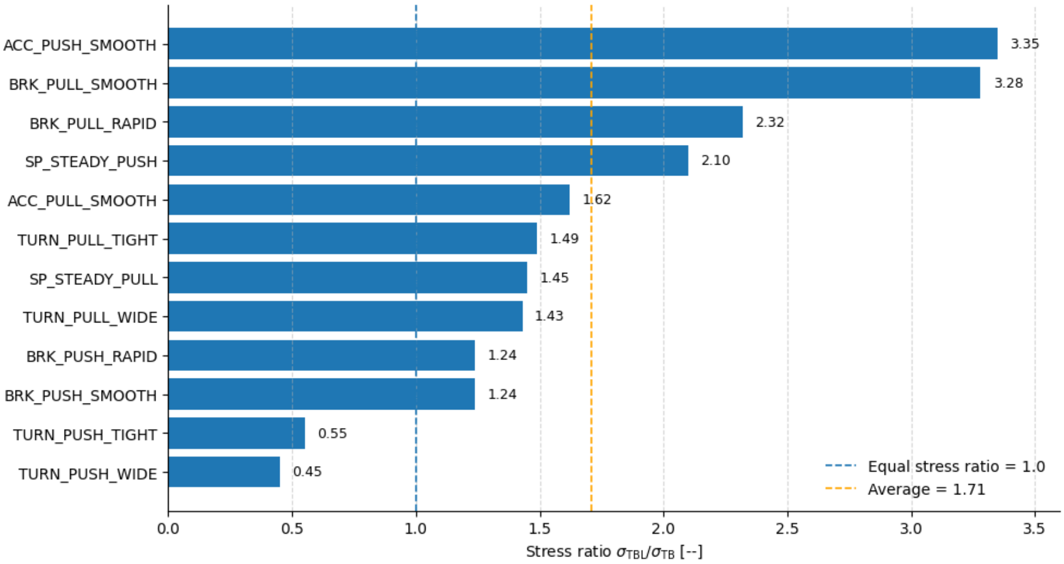

Figure 8.5: TBL-to-TB local drag-brace hotspot stress ratio per manoeuvre

Taken together, Figures 8.4 and 8.5 show that towbarless towing changes the local fatigue-driving manoeuvre mix at the existing drag-brace hotspot in a pronounced way. The local drag-brace response under TBL is therefore not characterised by a simple uniform scaling of the TB result. Instead, it reflects a strong redistribution of manoeuvre sensitivity, primarily driven by braking and selected longitudinal-transient manoeuvres. The lower ratios found for the push-turn cases are attributed to the adopted local modelling treatment and are not considered representative of the overall TB–TBL structural difference. This result provides the direct rationale for carrying the drag-brace hotspot forward into WP3 and for constructing the specimen spectra such that the amplified governing manoeuvre classes remain explicitly represented.

8.2.3. Hotspot Shift and Failure-Mode Implications

The WP2 results do not indicate a complete shift to a new globally governing fatigue location under towbarless towing. Instead, they show a redistribution of hotspot importance, such that the drag-brace remains the governing critical region in the staged global–local assessment, while the fork/axle path becomes more stressed under TBL loading and several local drag-brace manoeuvres experience strong amplification. The principal effect of changing the towing method is therefore not the replacement of one fatigue-critical component by another, but a change in relative hotspot ranking and manoeuvre sensitivity at the existing governing location.

For the downstream fatigue programme, this meant the local drag-brace hotspot output was retained as the final structural basis for defining specimen-level stresses. The implemented specimen stress ranges in WP3 were therefore derived from this local drag-brace result, rather than from the broader global hotspot screening, as summarised in Table 6.12. In that sense, WP2 serves not only to identify the governing fatigue-critical location but also to provide the direct quantitative bridge between the towing-derived aircraft loads and the machine-executable specimen stress levels used in the laboratory campaign.

8.3. Laboratory Fatigue Results

This section presents the WP3 laboratory fatigue results for the towing-derived specimen spectra. It addresses SRQ7, concerning the extent to which towbarless towing alters fatigue life relative to conventional towbar towing. This question is addressed by first comparing the measured lives of the tested spectrum variants, then expressing the difference in relative life ratios, and finally evaluating the extent to which the experimental ranking is consistent with the pre-test fatigue-life predictions and overload-insertion behaviour.

8.3.1. Measured Fatigue Lives per Spectrum Variant

The primary WP3 output was the measured fatigue life of the four tested spectrum variants, expressed in both raw machine cycles and equivalent 100-operation towing mission blocks. For the research-level comparison, the mission-block-equivalent representation was the more relevant comparative metric, since the TB and TBL spectra contain different numbers of counted cycles per mission. Table 8.5 summarises the mean lives and scatter per variant, disregarding one specimen tested under the TB spectrum (`TB2`), which was treated as a probable outlier because visual inspection indicated specimen-specific defects. The corresponding sensitivity analysis was discussed further in Section 7.7.1.

Table 8.5: Condensed experimental summary of the WP3 fatigue results

Variant	n	**Mean life [cycles (k)]**	**SD [cycles (k)]**	**Mean life [mission blocks]**	**SD [mission blocks]**	**Note**
TB	2	54.2	6.0	303	34	TB2-excluded
TB+RET	2	102.2	33.2	571	185	–
TBL	3	27.3	3.1	41	5	–
TBL+RET	2	35.7	5.4	54	8	–

Moreover, Figure 8.6 is shown in cycles to visualise specimen-to-specimen scatter directly, whereas the cross-variant severity comparison is interpreted primarily in equivalent towing missions.

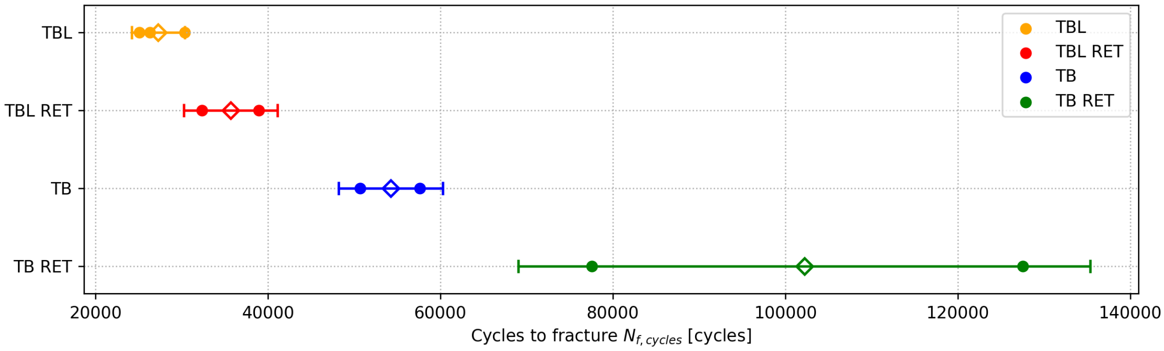

Figure 8.6: Measured cycles to failure per spectrum variant, including specimen-level replicates and mean ± standard deviation (TB2 excluded)

The measured results showed a clear separation between the towbar- and towbarless-derived laboratory spectra. For the base cases, using the TB2-excluded sensitivity case, the mean specimen life decreased from 54.2k cycles for TB to 27.3k cycles for TBL. When converted with the retained cycle content of the executed machine programmes, the same comparison corresponds to 303 equivalent 100-operation mission blocks for TB and 41 for TBL. These findings indicate that the TBL-derived specimen spectrum was experimentally more severe than the corresponding TB-derived spectrum. The mission-block-equivalent comparison is useful for comparing the executed spectra, but should not be read as a direct aircraft service-life prediction.

The same overall ranking was retained for the overload-insertion variants. The TB+RET specimens reached a mean life of 102.2k cycles, corresponding to 571 equivalent 100-operation mission blocks, whereas the TBL+RET specimens reached 35.7k cycles, corresponding to 54 equivalent 100-operation mission blocks. Although the RET variants outlived their respective base cases in the present dataset, the TBL-derived spectrum remained substantially more damaging than the TB-derived spectrum under both loading programmes.

8.3.2. Relative Fatigue Severity and Experimental Life Ratios

To express the experimental outcome more directly, the comparison is next cast in relative terms using the TB2-excluded mission means from Table 7.14. This prevents a potentially premature TB failure from dominating the principal severity ratios. Figure 8.7, therefore, compares the base and overload-insertion cases based on equivalent towing missions.

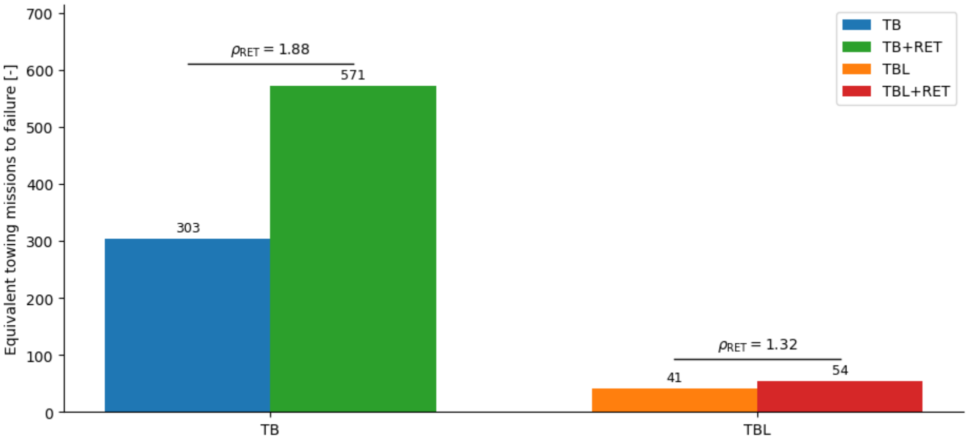

Figure 8.7: Equivalent towing mission blocks to failure for the base and overload-insertion variants, with the measured overload ratios ρ_{RET} indicated for TB and TBL

Overall, the mean life of the TBL base case is 41 mission blocks, compared with 303 equivalent 100-operation mission blocks for TB, corresponding to a relative life ratio of

$$\rho_{\text{TBL/TB}} = \frac{41}{303} \approx 0.14 \tag{8.1}$$

Thus, in equivalent mission-block terms, the TBL-derived spectrum reduced the converted laboratory life to approximately 14% of the TB value, or conversely, the TB-derived spectrum survived about 7.4

times as many equivalent 100-operation mission blocks as the TBL-derived spectrum under the present test conditions.

Figure 8.7 also shows that overload insertion produced a smaller effect than the towing-concept change itself. For the TB-derived spectrum, the overload-insertion case increased the mean life from 303 to 571 equivalent 100-operation mission blocks, corresponding to

$$\rho_{\text{RET,TB}} = \frac{571}{303} \approx 1.88 \tag{8.2}$$

For the TBL-derived spectrum, the corresponding increase is from 41 to 54 equivalent 100-operation mission blocks, giving

$$\rho_{\text{RET,TBL}} = \frac{54}{41} \approx 1.32 \tag{8.3}$$

The main experimental separation remained the difference between TB and TBL, while the overload-insertion effect served as a secondary modification within each towing concept.

These ratios showed that the fatigue consequence of towbarless towing is severe. At the same time, the overload-insertion cases indicated that sequence effects are present, but their magnitude is smaller than the underlying concept-level life separation.

8.3.3. Comparison with Fatigue-Life Prediction

The experimental lives were next compared with the pre-test fatigue-life prediction framework. Here, the principal question is not whether the model reproduces absolute life exactly, but whether it captures the correct ordering among spectrum variants and whether a plausible effective specimen severity can reconcile predictions with experiments. In this respect, the grip-induced load asymmetry discussed in Subsection 7.7.5 is important. The relevant comparison is not with the geometry-only stress concentration alone, but with an effective severity that reflects the actual specimen loading condition in the test frame.

For a discrete comparison, Figure 8.8 shows the converted mission-block-equivalent lives alongside predictions for selected assumed stress concentration factors.

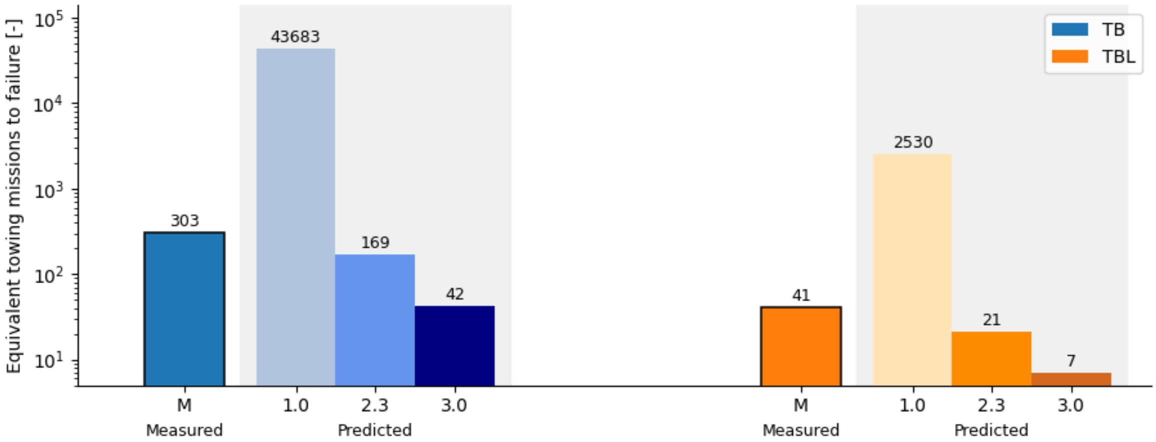

Figure 8.8: Measured and predicted equivalent towing mission blocks to failure for selected assumed stress concentration factors

Figure 8.8 shows that the model consistently predicts the correct ranking, namely that TB survives longer than TBL for all assumed K_t values considered. However, it also shows that absolute life is highly sensitive to the assumed stress concentration factor. At $K_t = 1.0$, the predictions are far above the measured lives, with 43,683 equivalent 100-operation mission blocks predicted for TB and 2,530 for TBL. Increasing the assumed severity to $K_t = 2.3$ reduces the predicted lives to 169 and 21 equivalent 100-operation mission blocks, respectively, while $K_t = 3.0$ reduces them further to 42 and 7 equivalent 100-operation mission blocks. The comparison, therefore, indicates that the geometry-only case is clearly non-conservative in life, whereas a much higher effective severity is required to bring the prediction into the same order of magnitude as the measurements.

The continuous dependence of the prediction on assumed K_t is shown in Figure 8.9, together with the measured means and standard-deviation bands from Table 8.5.

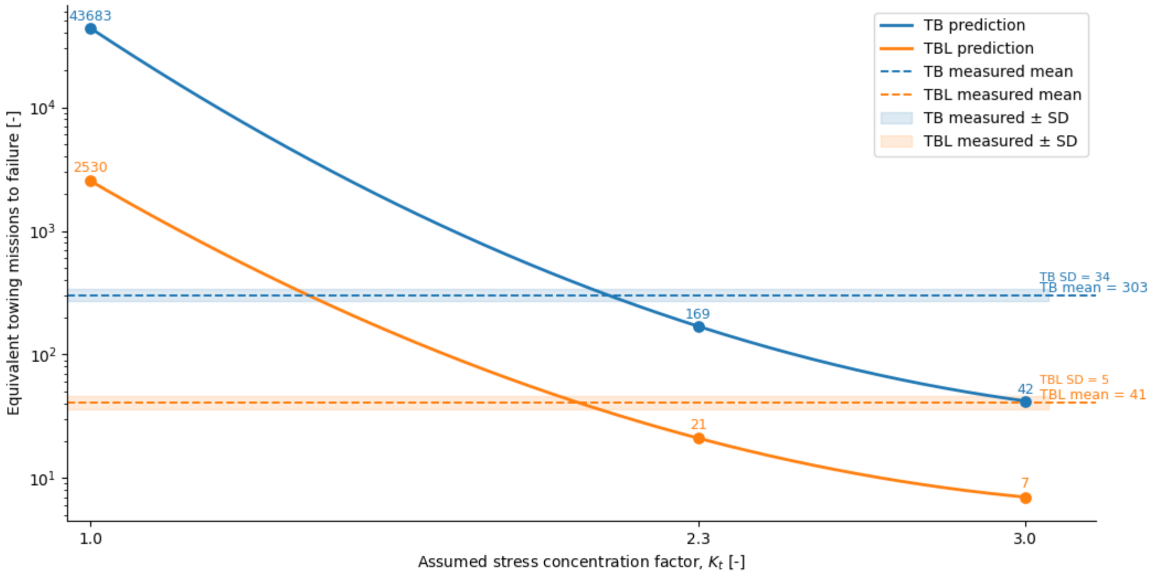

Figure 8.9: Predicted equivalent towing mission blocks to failure as a function of assumed stress concentration factor, compared with the measured mean $\pm$ standard deviation bands for TB and TBL

Figure 8.9 confirms the same overall conclusion. The prediction framework captures the direction of the towing-concept effect, but not a unique absolute life scale. In particular, no single low-K_t assumption simultaneously reproduces both measured means, and the correspondence improves only once an effective severity substantially above the geometry-only value is assumed. This behaviour is consistent with the interpretation from Subsection 7.7.5. Interpolating the prediction curves against the converted equivalent mission-block lives yields an effective severity of $K_t \approx 2.3$, whereas the geometry-only case yields $K_t \approx 1.12$. This shows that overall fatigue life is governed not only by the global loads and stress redistribution in the nose-wheel landing gear, but also by detailed local design and the manner in which the load is introduced into the critical detail. The specific contribution of those detailed design effects was not investigated separately in the present work. The predictive framework is therefore most reliable here as a tool for relative ranking and trend interpretation, rather than as a high-accuracy absolute life predictor.

8.3.4. Overload-Insertion and Sequence Effects

The overload-insertion results provided additional information on sequence effects. As already shown in Figure 8.7, the inserted overload block did not reduce the measured life in either towing concept. Instead, both TB and TBL showed longer lives in the RET variants, with the effect being stronger in TB than in TBL.

This outcome was important for two reasons. First, it shows that the experimental response to overload insertion is not equivalent to a simple life-shortening penalty. Second, it indicates that the sequence effect is sensitive to the underlying spectrum context, as the apparent life increase is substantial for TB $(\rho_{\text{RET,TB}} = 1.88)$, but much smaller for TBL $(\rho_{\text{RET,TBL}} = 1.32)$. In that sense, the experimental programme suggests that overload insertion modifies the effective fatigue response, but does not overturn the primary ranking between the towing concepts.

Taken together with the prediction comparison in the previous subsection, this implies that the simplified retardation treatment does not fully reproduce the measured overload behaviour. The experiments support the presence of sequence effects, but their observed expression is weaker and directionally different from what would be expected from a simple life-reduction assumption. For the present study, the overload result is therefore interpreted primarily as evidence that sequence matters, while the dominant fatigue-severity conclusion remains the experimentally shorter life under the TBL-derived spectra.

8.4. Consolidated Answers to the Research Questions

This section synthesises the results from WP1, WP2, and WP3 (Sections 8.1–8.3) into direct answers to SRQ1–SRQ7 and, ultimately, to the main research question on the consequences of towbarless towing for the loading and fatigue behaviour of general-aviation nose-wheel landing gear. It does so by first answering each sub-research question individually, then combining those answers into a single integrated research-level conclusion.

8.4.1. Consolidated Answer to the Sub-Research Questions

SRQ1: What are the primary ground-operation load cases on the nose-wheel landing gear, and how do they populate the measured ground-loading/fatigue spectrum? The primary towing-related ground-operation load cases identified in this study were steady pull, steady push, smooth pull and push acceleration, smooth pull and push braking, turning manoeuvres, and rapid braking transients. These were represented by a canonical library of 12 manoeuvre classes, of which eight were available as directly measured towbar force histories, three were estimated from related measured cases, and one was represented by a proxy case. The resulting spectrum is therefore not treated as a single continuous generic towing trace, but as a manoeuvre-resolved loading library. Within this library, the steady pull-and-push cases define the background towing level and much of the time occupancy, while a smaller subset of transient-sensitive manoeuvres, especially braking, rapid braking, and selected acceleration events, provides the fatigue-relevant peak content. The turning cases were retained as representative operational manoeuvres, but they contributed mainly secondary spectral content compared with the dominant longitudinal transients. In that sense, the measured ground-loading spectrum was populated by frequent low-severity baseline towing segments, together with a limited number of higher-severity transient events that govern the fatigue-relevant stress-range content.

SRQ2: How do towbar and towbarless towing differ in the forces and moments applied to the nose-wheel landing gear, and how do these differences alter the sequence, magnitude, and frequency content of the resulting usage spectra? Towbar and towbarless towing did not differ by a uniform increase in all loads. The steady pull and push cases remained broadly similar, while the main concept-level differences were concentrated in transient-sensitive manoeuvres, especially pull braking and selected acceleration cases. In addition, the towing concepts differed in load introduction. In the present framework, TB loads entered through the tow-lug path, whereas TBL loads were introduced at the axle. This changed the internal force path through the nose-wheel landing gear and increased the relative importance of the fork/axle region under TBL loading. The resulting usage spectra therefore differed primarily in the magnitude and sequencing of the fatigue-relevant transient events, rather than in the quasi-steady towing baseline.

SRQ3: Which critical nose-wheel landing gear components are most susceptible to fatigue damage from repeated towing and manoeuvring loads? For the investigated GA-type nose-wheel landing gear configuration, the drag-brace region emerged as the governing fatigue-critical structural location. In the global hotspot screening, `DRAG_BRACE_V_BASE` ranked first for both TB and TBL, as well as relative to all other hotspot locations, while the fork/axle load path became relatively more important under TBL loading. The refined local model then confirmed that the drag-brace hotspot remained the controlling location for downstream assessment. The main conclusion was therefore that the drag brace was the most fatigue-relevant component within the present comparison, even though the fork and axle became more stressed under towbarless towing.

SRQ4: How should representative ground operation spectra be constructed for GA aircraft to perform fatigue analysis? Representative ground-operation spectra should be constructed as a finite set of canonical manoeuvres, first identified at the aircraft level and then assembled into repeatable mission blocks for downstream structural and laboratory use. In the present study, this was implemented through the A–D mission structure, in which the measured and reconstructed towing events were grouped into a small number of representative manoeuvre classes and then discretised into machine-executable spectra. This approach preserves the fatigue-relevant distinction between background loading and transient-sensitive events, while remaining practical for repeated testing and comparison. Moreover, it allows comparison not only of stress magnitudes but also of operational differences between TB and TBL operations, taking practical considerations into account. In that sense, the A–D implementation provides a workable bridge between in-field towing measurements and fatigue assessment. It reduces complex ground-handling activity to a structured sequence of representative mission blocks without losing the manoeuvres that govern relative fatigue severity.

SRQ5: Which specific towing manoeuvres or conditions lead to the largest differences in peak stress ratio, rainflow damage ratio D_{TBL}/D_{TB}, and change in hotspot ranking between towbar and towbarless methods? The largest TB–TBL differences occur in transient-sensitive longitudinal manoeuvres, not in steady towing. In WP1, `BRK_PULL_SMOOTH` and `BRK_PULL_RAPID` showed the clearest increase in TBL severity, while `ACC_PULL_SMOOTH` and `ACC_PUSH_SMOOTH` showed more moderate increases. In WP2, this became stronger at the local hotspot on the drag-brace, where the largest TBL-to-TB amplification ratios occurred for `ACC_PUSH_SMOOTH` (3.35), `BRK_PULL_SMOOTH` (3.28), and `BRK_PULL_RAPID` (2.32). A key part of this redistribution is the different force-introduction locations in the FEM, with TB loads applied at the tow lugs and TBL loads applied at the axle. The tow location changes the structural load path. It helps explain why the fork/axle region becomes more prominent and why braking- and push-related transients amplify strongly at the local drag-brace hotspot.

SRQ6: Could switching the towing method *(from towbar to towbarless)* introduce new failure modes or shift the primary fatigue hotspots in the nose-wheel landing gear, thereby requiring updated maintenance or operational guidance? The present results do not support a complete shift in the globally governing fatigue location under towbarless towing. Instead, they show a redistribution of hotspot ranking and manoeuvre sensitivity within the existing structural system. Globally, the drag brace remained governing, while the fork/axle path became more prominent under TBL. Locally, the drag-brace hotspot remained controlling, but its internal manoeuvre ranking changed substantially, with braking- and push-related transients becoming disproportionately more severe. The most defensible conclusion is therefore not that towbarless towing introduces an entirely new governing failure mode, but that it changes the relative importance of existing components and load cases. In practical terms, this supports increased attention to braking transients, push-related manoeuvres, and those structural details most affected by the shift from tow-lug loading to axle loading.

SRQ7: To what extent does towbarless towing alter the fatigue life of nose-wheel landing gear components compared to towbar towing? The laboratory programme shows that the towing-derived TBL spectrum is markedly more fatigue-severe than the corresponding TB spectrum. Using the TB2-excluded sensitivity case, the measured mean life decreased from 54.2k cycles for TB to 27.3k cycles for TBL, or 303 equivalent 100-operation mission blocks for TB versus 41 for TBL. Under the present test conditions, the TBL-derived spectrum reduced the measured life to approximately 14% of the TB value, or equivalently, the TB spectrum survived about 7.4 times as many towing missions as the TBL spectrum. The fatigue-life prediction framework also reproduced this relative ranking, although the absolute life scale depended strongly on the assumed effective specimen severity and was influenced by grip-induced asymmetry.

At the same time, the overload-insertion results showed that sequence effects could modify this comparison. In the present programme, the RET variants did not reduce life, but instead produced longer measured lives than their respective base cases, with a stronger apparent effect for TB than for TBL. This indicated that an overload-like event could introduce retardation, thereby partially extending subsequent life. As a result, if real operation contains a mixture of TB and TBL towing events, and if some of the TBL-derived events act in a retardation-inducing manner similar to the present RET insertion, then the total fatigue-life difference between TB and TBL could be less severe than the pure base-spectrum comparison suggested. However, the present results did not overturn the main ranking: within the scope of this study, towbarless towing still produced a clearly shorter fatigue life than conventional towbar towing.

8.4.2. Integrated Answer to the Main Research Question

Main Research Question: What are the consequences of towbarless towing on the loading and fatigue behaviour of representative general-aviation turboprop and light- to midsize-jet nose-wheel landing gear compared to conventional towbar towing? Overall, the results showed that, in the general-aviation nose-wheel landing gear context examined in this study, towbarless towing was more fatigue-severe than conventional towbar towing. This conclusion did not arise because towbarless towing uniformly increases all loads, nor because it shifts the governing structural response entirely to a new component. Instead, it arose from a more specific mechanism. Relative to towbar towing, towbarless towing left the steady towing cases broadly similar, but amplified a limited set of transient-sensitive manoeuvres, particularly braking and acceleration cases. These amplified manoeuvres redistributed the local stress severity at the governing drag-brace hotspot and increased the effective fatigue severity of the towing spectrum.

A key part of this redistribution was the change in the force-introduction path. In the present FEM implementation, the towbar case applies the towing load at the tow lugs, whereas the towbarless case applies it at the axle. This shifts how loads are transferred through the nose-wheel landing gear and helps explain why the fork/axle path becomes more prominent under TBL, even though the drag-brace region remains the governing fatigue-critical location overall.

Experimentally, this translated into substantially shorter measured fatigue lives for the TBL-derived specimen spectra. The strongest fatigue consequence was observed when life was expressed in equivalent towing missions, which is the most operationally meaningful basis for comparison in the present work. This relative life reduction should, however, be interpreted primarily for the present base-spectrum comparison, since the overload-insertion tests indicate that retardation effects can partly mitigate the net life difference when overload-like events are mixed into the towing sequence. The main research question can therefore be answered as follows: for the investigated GA nose-wheel landing gear context, towbarless towing did not create a wholly different fatigue problem, but it did make the existing towing-related fatigue problem more severe by intensifying the transient manoeuvres that drive local stress and cumulative damage, and by shifting the structural load path from tow-lug loading toward axle-dominated loading. The principal consequence is a redistribution and amplification of fatigue-driving loading at the existing governing drag-brace region, resulting in a materially shorter relative fatigue life than under conventional towbar towing.

8.5. Comparison with Expert Technical Field Observations

The integrated research results were compared with the experience-based field observations presented in Chapter 3. The purpose is not to treat the expert account as an independent validation dataset, but to assess whether the mechanisms, directional trends, and practical implications inferred from WP1–WP3 are consistent with long-term in-service experience.

8.5.1. Points of Agreement

A first point of agreement concerns the towing load path itself. The expert observations describe towbarless towing as introducing load through the tyre and wheel interface, with increased effective lever arm effects, greater lateral and torsional cycling, and the absence of a towbar shear-pin load limiter. This is consistent with the structural interpretation developed in this study. In the present FEM implementation, the towbar case applies the towing load at the tow lugs, whereas the towbarless case applies it at the axle. The resulting change in force introduction path explains why the fork/axle region becomes more prominent under TBL loading, while the governing drag-brace hotspot remains highly fatigue-relevant.

A second point of agreement concerns which manoeuvres matter most. The expert account identifies braking, constrained turning, and demanding ground conditions as the situations most likely to amplify towbarless severity. The present results showed the same directional pattern within the investigated manoeuvre set. In WP1, the principal TB–TBL differences were not found in steady towing, but in transient-sensitive manoeuvres, especially pull braking and selected acceleration cases. In WP2, these differences became stronger at the local drag-brace hotspot, where braking- and push-related manoeuvres showed the largest TBL-to-TB amplification ratios. This increase supported the expert view that the main TBL effect lies in handling transients rather than in the steady-towing baseline.

A third point of agreement is the problem's cumulative nature. The expert chapter describes the reported degradation as cycle-dependent and progressive rather than linked to a single isolated overload event. The laboratory results of WP3 are consistent with this interpretation. The TBL-derived spectrum produced a markedly shorter measured fatigue life than the corresponding TB-derived spectrum, particularly when life was expressed in equivalent towing missions. Taken together, the experimental and numerical results therefore supported the broader field observation that repeated towbarless operation could increase cumulative structural severity over time.

8.5.2. Points Not Directly Resolved

Although the direction of the expert observations is broadly consistent with the research results, several reported in-service degradation signatures remain unresolved by the present work. In particular, the study does not experimentally verify shock-strut internal leakage, floating-piston seal wear, progressive free play in bushings and attachments, wear in mechanically interconnected nose-wheel landing gear door hardware, hidden tyre carcass damage, or fretting-driven corrosion. These findings are maintenance observations at the part or assembly level, whereas the present research focuses on towing load reconstruction, hotspot stress redistribution, and specimen-level fatigue comparison.

Similarly, the expert chapter places strong emphasis on demanding operational modifiers such as high aircraft mass, high fuel load, slopes, rough apron transitions, and uneven terrain. These effects are physically plausible and consistent with the load-path reasoning adopted here, but they were not systematically varied in the experimental programme. The in-field datasets used in WP1 were obtained under comparatively favourable dry and smooth-surface conditions, and the laboratory work in WP3 was based on reduced spectra derived from those canonical manoeuvres. The study, therefore, cannot quantify how much additional severity these operational modifiers would introduce in practice.

Finally, the expert observations suggest potential maintenance and inspection requirements at specific interfaces, such as torque-link hardware, steering-actuator attachments, drag-brace interfaces, and shimmy-damper mounts. The present WP2 results indicate increased stress in some of these load paths, particularly the fork/axle path and the local drag-brace region. Still, they do not provide direct evidence of crack initiation or service inspection thresholds for those individual hardware items.

8.5.3. Implication of the Triangulation

The comparison with expert technical field observations strengthens the external plausibility of the research findings, but primarily at the level of mechanisms and directional trends. The expert account independently pointed to towbarless towing as a loading concept with a less favourable load path, greater sensitivity to braking, constrained manoeuvres, and a tendency to promote cumulative degradation in nose-wheel landing gear components. These points are in clear agreement with the present findings that TBL does not uniformly scale all loads, but instead amplifies a limited set of fatigue-driving manoeuvres and redistributes structural severity within the existing nose-wheel landing gear system.

At the same time, the triangulation should not be overstated. The expert chapter does not validate the numerical stress levels, local hotspot magnitudes, or fatigue-life ratios obtained in WP2 and WP3. Conversely, the research does not directly confirm the specific maintenance findings reported from service experience. The most defensible interpretation is therefore that the expert observations provide qualitative external support for the research-level conclusion.

In practical terms, this triangulation supports greater operational and maintenance attention to towbarless braking events, constrained turning, rough ground transitions, and the interfaces most affected by axle-dominated load introduction. These implications remain directional rather than prescriptive, but they are sufficient to justify further in-service monitoring and aircraft-specific follow-on assessment.

9

Verification and Validation

This chapter outlines the verification and validation approach adopted in this study and the steps applied to each work package. In this context, verification refers to whether a method, model, translation, or test procedure was implemented correctly and consistently. Validation refers to whether the resulting approach reproduced the relevant physical behaviour with sufficient fidelity for the research objectives.

The verification and validation strategy followed the work package framework. Sections 9.1–9.3 summarise the verification and validation assessments for WP1, WP2, and WP3, respectively. Section 9.4 addresses external validity through comparison with operational experience.

Verification and validation framework

Table 9.1 summarises the verification and validation structure which was adopted in this study. In the assessment tables, ✓ indicates verified or validated status, $\sim$ indicates partial verification or validation, and $\times$ indicates that the item is not considered verified or validated.

Table 9.1: Verification and validation structure of the performed research

Stage	Verification focus	Validation focus
WP1	Measurement and translation chain	Physical plausibility of the obtained towing histories
WP2	Finite-element implementation and load-transfer chain	Resulting structural response and hotspot trends
WP3	Fatigue-spectrum construction and test translation	Relative fatigue behaviour against the laboratory results
External Validity	–	Comparison of the inferred mechanisms and trends with the expert field observations from Chapter 3

9.1. WP1 – In-Field Towing

For WP1, verification and validation were assessed by first examining the correctness and traceability of the in-field measurement and translation chain in Section 9.1.1, and then the physical credibility and downstream suitability of the resulting towing histories and spectra in Section 9.1.2.

9.1.1. Verification

Verification of WP1 focused on whether the in-field measurement and translation chain was implemented correctly and consistently, such that the manoeuvre-level spectra used in later chapters can be traced back to a documented set of measured and estimated inputs. To structure this assessment, the WP1 verification items are first defined in Table 9.2 and then assessed in Table 9.3.

Table 9.2: WP1 verification items

Identifier	Verification item
VER-WP1-01	Towbar instrumentation setup and signal chain
VER-WP1-02	Towbar calibration procedure and selected calibration channel
VER-WP1-03	Event segmentation and manoeuvre labelling procedure
VER-WP1-04	TB-to-TBL translation procedure, including rolling resistance, slope, and manoeuvre-specific assumptions
VER-WP1-05	Traceability of the final manoeuvre spectra used in later chapters

Table 9.3: WP1 verification assessment

Identifier	Method	Reported	Status
VER-WP1-01	Documented instrumentation layout, signal chain, field setup, and data-handling workflow demonstrating that the required channels could be recorded and processed consistently	Section 5.2	✓
VER-WP1-02	Controlled towbar calibration against a traceable servo-hydraulic load frame including a reference load cell, repeated loading steps, channel comparison, and justified selection of the primary calibration channel	Section 5.3	✓
VER-WP1-03	Documented event segmentation workflow and the use of a fixed manoeuvre-labelling structure for consistent grouping of towing events	Section 5.1 Subsection 5.4.3	✓
VER-WP1-04	Consistent application of the quasi-static translation procedure, including rolling-resistance treatment, slope correction, and manoeuvre-specific assumptions	Section 5.6	∼
VER-WP1-05	Documented construction of manoeuvre-wise spectra from measured TB cases and estimated TBL cases, such that the final spectra used in WP2 and WP3 remain traceable to their source inputs	Section 5.7	✓

The partial verification status of VER-WP1-04 requires some qualification. While the TB-to-TBL translation procedure was implemented consistently within the adopted quasi-static framework, its physical accuracy remains limited by the extent of the underlying assumptions. In particular, the adopted rolling-resistance treatment, the slope-related weight component, and the manoeuvre-specific translation assumptions were not independently validated over a broader range of towing conditions, aircraft mass states, pavement characteristics, and operational scenarios. Moreover, the translation is based on a limited set of towing exercises and therefore cannot be considered fully representative of towing behaviour in general. The resulting towing histories for TB and TBL are therefore regarded as first-order, comparative engineering estimates that are suitable for the present thesis scope, but not as fully verified or universally transferable representations of the manoeuvres considered during this study.

Taken together, the WP1 verification assessment indicated that the in-field measurement and translation chain was implemented in a traceable and internally consistent manner. The principal remaining limitation is the assumption-dependent nature of the decomposition of towing measurements, such that the absolute translated load magnitudes remain subject to uncertainty. Nevertheless, for comparative purposes in the present thesis, the reconstructed TBL histories were considered sufficiently robust as relative engineering estimates for use in downstream analyses.

9.1.2. Validation

Validation of WP1 concerned whether the measured and translated load histories provide a physically credible and suitable basis for the downstream comparative analyses. In contrast to verification, which focuses on the correct and consistent implementation of the measurement and translation chain, validation here focuses on the quality of the resulting loading histories and spectra for use in WP2 and WP3. The WP1 validation items are defined in Table 9.4 and assessed in Table 9.5.

Table 9.4: WP1 validation items

Identifier	Validation item
VAL-WP1-01	Physical plausibility of the measured and translated load histories for the tested towing manoeuvres
VAL-WP1-02	Suitability of the derived manoeuvre spectra for comparative downstream use in WP2 and WP3

Table 9.5: WP1 validation assessment

Identifier	Method	Reported	Status
VAL-WP1-01	Assessment of whether the measured TB histories and reconstructed TBL histories are physically consistent with the tested towing manoeuvres, measured tug kinematics, rolling-resistance treatment, slope correction, and manoeuvre-specific assumptions	Section 2.2 Section 5.5 Section 5.6	∼
VAL-WP1-02	Assessment of whether the derived manoeuvre spectra preserve the relevant manoeuvre classes, relative severity differences, and traceable source histories required for comparative downstream use in WP2 and WP3	Section 5.7	✓

The validation status of VAL-WP1-01 is taken as partial, since the physical plausibility of the measured TB histories and reconstructed TBL histories is supported within the tested manoeuvre set and the adopted first-order reconstruction framework, but remains limited by the assumption-dependent nature of the translation procedure. Moreover, aside from order-of-magnitude comparisons, no direct comparison of the measured values was possible, as only limited data were publicly available. By contrast, VAL-WP1-02 is considered validated within the scope of the present research, since the derived manoeuvre spectra were explicitly constructed and documented for downstream comparative use in WP2 and WP3, with traceable source histories and conservative estimates of unmeasured manoeuvres where required.

Therefore, these validation items assess whether WP1 provides loading histories and manoeuvre spectra that are physically credible and suitable for the subsequent finite-element and laboratory-fatigue work packages.

9.2. WP2 – Finite-Element Model Analysis

For WP2, verification and validation were assessed by first examining the correctness and consistency of the finite-element modelling and load-transfer chain in Section 9.2.1, and then the physical credibility and representativeness of the resulting structural response and hotspot trends in Section 9.2.2.

9.2.1. Verification

Verification of WP2 assessed whether the finite-element modelling chain was implemented correctly and consistently, ensuring that the structural response used in later chapters could be traced from the global model to the local hotspot submodel and finally to the specimen-equivalent representation. Verification, therefore, focuses on the model setup, load application, discretisation strategy, global-to-local transfer, and hotspot-to-specimen mapping. The WP2 verification items are defined in Table 9.6 and assessed in Table 9.7.

Table 9.6: WP2 verification items

Identifier	Verification item
VER-WP2-01	Global model setup, including geometry idealisation, material assignment, joints, and boundary conditions
VER-WP2-02	Applied TB and TBL load definitions and their points of introduction
VER-WP2-03	Mesh adequacy and hotspot screening at global level
VER-WP2-04	Local submodel setup, including cut-out definition, local mesh, and element choices
VER-WP2-05	Global-to-local load-transfer procedure
VER-WP2-06	Hotspot-to-specimen mapping procedure used for the laboratory correlation

Table 9.7: WP2 verification assessment

Identifier	Method	Reported	Status
VER-WP2-01	Documented definition of the global model, including the selected structural scope, material properties, joints, and aircraft-side boundary conditions	Subsection 6.2.1, Subsection 6.2.3	~
VER-WP2-02	Documented definition of TB and TBL load cases, including load components, load spectrum definition, and consistent points of force introduction in the FEM	Subsection 6.2.2, Subsection 6.2.3	✓
VER-WP2-03	Documented mesh strategy and hotspot screening procedure at the global level to identify candidate critical regions under comparable loading	Subsection 6.2.4	✓
VER-WP2-04	Documented definition of the local drag-brace submodel, including cut-out geometry, retained interfaces, local mesh refinement, and element choices consistent with the global model	Subsection 6.3.1, Subsection 6.3.2	✓
VER-WP2-05	Documented global-to-local load-transfer procedure based on the extraction and re-application of equivalent interface actions to preserve the deformation state of the retained structure	Subsection 6.3.3	~
VER-WP2-06	Documented hotspot-to-specimen mapping procedure, including specimen finite-element model definition, hotspot equivalence, and conversion to specimen-equivalent loading	Section 6.4	✓

The partial verification status for VER-WP2-01 and VER-WP2-05 reflects the modelling level adopted in WP2. For VER-WP2-01, the global model definition, boundary conditions, and load paths were documented and checked at the system level, including assessment of supports, applied loads, and resulting reaction-force consistency. However, the model was not intended as a fully detailed local representation of every NWLG feature. In particular, local properties such as joint details, contact behaviour, and exact fillet geometry were simplified to remain consistent with the global screening purpose. The resulting verification is therefore sufficient for identifying overall load transfer and candidate critical regions, but not for claiming full local geometric fidelity.

For VER-WP2-05, the global-to-local transfer procedure was verified primarily through consistency of the transferred interface actions and reaction forces. Deformation of the submodel was additionally inspected visually and did not show unexpected kinematic behaviour or unrealistic distortion. Nevertheless, deformation-field agreement was not verified in a more quantitative sense, for example, through direct displacement-field matching or a formal comparison of local compliance between global and local representations. The verification of the transfer procedure is therefore considered adequate for stress-based hotspot evaluation, but only partial with respect to full deformation equivalence.

Taken together, these verification items indicated that WP2 provides a traceable and internally consistent finite-element modelling chain from towing input to specimen-equivalent structural response.

9.2.2. Validation

Validation of WP2 concerned whether the finite-element modelling chain produces a physically credible structural response and whether the resulting hotspot trends and specimen-equivalent histories are sufficiently representative for the downstream comparative analyses. In this thesis, validation therefore focuses on the credibility of the predicted load paths, hotspot behaviour, TB–TBL severity differences, and the suitability of the specimen-equivalent stress histories for use in WP3. The WP2 validation items are defined in Table 9.8 and assessed in Table 9.9.

Table 9.8: WP2 validation items

Identifier	Validation item
VAL-WP2-01	Physical credibility of the global-model load paths and deformation behaviour under TB and TBL loading
VAL-WP2-02	Consistency of the identified critical region and hotspot trends between the global and local stages
VAL-WP2-03	Suitability of the specimen-equivalent stress histories as representative inputs for WP3

Table 9.9: WP2 validation assessment

Identifier	Method	Reported	Status
VAL-WP2-01	Assessment of whether the global model produces physically credible load paths and deformation behaviour under the applied TB and TBL loading conditions	Subsection 6.2.5	∼
VAL-WP2-02	Assessment of whether the governing critical region and hotspot ranking remain consistent between the global model and the refined local submodel	Subsection 6.3.4	✓
VAL-WP2-03	Assessment of whether the specimen-equivalent stress histories preserve the relevant structural severity trends and are suitable as representative inputs for WP3	Section 6.4	∼

The partial validation status for VAL-WP2-01 and VAL-WP2-03 reflects the interpretive scope of WP2. For VAL-WP2-01, the global model was validated mainly at a qualitative physical level by assessing whether the resulting stress patterns and load paths were consistent with the expected mechanics of TB and TBL loading. In particular, the model shows the largest stress increase in the region between the axle and the towing pin, which is physically credible because this region is directly affected by the altered force introduction and the associated moment arm. Regions above the pin also show increased stress under TBL loading, but to a lesser extent, consistent with the fact that these parts already carry the towing force in both concepts and are primarily influenced by the additional moment arm effect. This provides general confidence that the model captures the intended load-path differences. However, some structural assumptions, including the treatment of the torque links, were introduced in a simplified manner. The global model validation is therefore considered physically plausible at the system level, but not fully validated in detail for all local mechanisms.

The partial validation status of VAL-WP2-03 indicates that the hotspot-to-specimen translation was assessed primarily at the level required for relative spectrum transfer to WP3, rather than as a fully validated absolute stress conversion. In this assessment, both the nominal section stress and the local hotspot stress were compared, and the resulting amplification factor of approximately 1.28 was considered physically credible for the simplified geometry and loading representation adopted in WP2. This provided a reasonable basis for scaling the hotspot response into specimen-equivalent stress histories while preserving the relative TB–TBL severity trend. However, the translation was not validated in detail against more refined local geometric effects, such as exact fillet shapes, local contact conditions, or other small-scale stress-raising features that may influence the true hotspot magnitude. The resulting stress histories should therefore be interpreted as comparatively valid in relative scale and ordering, but not as fully validated absolute stress predictions. For this reason, an additional magnitude adjustment was required before the spectra could be used in WP3, and these stress levels should not be used directly for aircraft design or certification. They remain dependent on several simplifying assumptions introduced to make the WP2-to-WP3 transfer tractable within the scope of the present study.

Taken together, these validation items assessed whether WP2 provided a physically credible and sufficiently representative structural-response basis for the downstream comparative fatigue analyses.

9.3. WP3 – Laboratory Fatigue Testing

For WP3, verification and validation were assessed by first examining the correctness and traceability of the laboratory-fatigue spectrum construction and test-translation chain in Section 9.3.1, and then whether the resulting tests provide a physically credible basis for relative TB–TBL fatigue comparison in Section 9.3.2.

9.3.1. Verification

Verification of WP3 assessed whether the laboratory-fatigue translation chain was implemented correctly and consistently, such that the tested spectra and fatigue-life comparisons could be traced back to the hotspot-derived loading histories from WP2. In this thesis, verification therefore focused on the translation of hotspot responses into manoeuvre missions, the construction and simplification of the loading spectra, the machine-conditioning procedure, and the fatigue-life calculation framework. The WP3 verification items are defined in Table 9.10 and assessed in Table 9.11.

Table 9.10: WP3 verification items

Identifier	Verification item
VER-WP3-01	Spectrum assembly and lifetime usage-mix construction
VER-WP3-02	Rainflow counting, discretisation, and compact spectrum representation
VER-WP3-03	Machine translation, including stress-ratio conditioning, block composition, and overload insertion
VER-WP3-04	Fatigue-life calculation framework used for pre-test and post-test comparison

Table 9.11: WP3 verification assessment

Identifier	Method	Reported	Status
VER-WP3-01	Documented assembly of towing spectra and lifetime usage mix for block construction, including the adopted mission scheduling and overload variant definition	Section 7.3	✓
VER-WP3-02	Documented rainflow counting procedure, discretisation sensitivity study, and compact spectrum representation used to obtain machine-executable loading blocks	Section 7.4	✓
VER-WP3-03	Documented machine translation procedure, including conditioning to the minimum stress ratio, block composition, stress caps, and overload insertion	Section 7.5	✓
VER-WP3-04	Documented fatigue-life calculation framework used to compare spectra before and after testing, including the adopted damage model and reference S–N interpretation	Section 7.6	✓

Taken together, these verification items showed that WP3 was implemented as a traceable and internally consistent translation chain from hotspot-derived loading histories to the tested specimen blocks.

9.3.2. Validation

Validation of WP3 concerned whether the tested spectra and observed test outcomes provide a physically credible basis for comparing the relative fatigue severity of TB and TBL loading concepts. In this thesis, validation therefore focuses on whether the tested spectra reproduce the intended relative severity ordering, whether the observed failure behaviour remains consistent with the adopted specimen representation and loading concept, and whether WP3 is interpreted appropriately as a relative rather than absolute validation step. The WP3 validation items are defined in Table 9.12 and assessed in Table 9.13.

Table 9.12: WP3 validation items

Identifier	Validation item
VAL-WP3-01	Reproduction of the intended relative severity ordering between TB and TBL in the tested spectra
VAL-WP3-02	Consistency of the observed failure behaviour with the intended specimen representation and loading concept
VAL-WP3-03	Relative interpretation of WP3, rather than absolute laboratory-to-service life validation

Table 9.13: WP3 validation assessment

Identifier	Method	Reported	Status
VAL-WP3-01	Assessment of whether the tested TB and TBL spectra preserve the intended relative severity ordering established during the hotspot-to-spectrum translation	Section 7.5, Section 7.8	∼
VAL-WP3-02	Assessment of whether the fracture location, failure mode, and post-mortem observations remain consistent with the adopted specimen representation and intended loading concept	Section 7.7	✓
VAL-WP3-03	Assessment of whether the WP3 outcomes are interpreted consistently as a relative comparison between tested spectrum variants, rather than as direct absolute validation of operational life	Subsection 7.7.3, Subsection 7.7.4, Subsection 7.7.5	✓

The partial validation status for VAL-WP3-01 reflects a distinction between the intended spectrum construction and the behaviour of the executed laboratory setup. The simplification and translation steps used to derive the TB and TBL machine spectra were themselves implemented consistently and verified as described in Section 7.5. However, the subsequent validation of the intended relative severity ordering is less conclusive than desired because the laboratory execution introduced an additional effect that was not fully accounted for before the test. As discussed in the limitations section of WP3, the grips induced a local stress concentration that increased the effective specimen severity and caused failure to occur substantially earlier than would be expected from the nominal smooth-specimen interpretation.

This has two important implications for validation. First, although the experimental results still indicate that the TBL spectrum is more damaging than the TB spectrum, the precise magnitude of this difference is less certain than originally intended. Second, because the grip-induced concentration increased the effective local stresses, the fatigue-limit threshold used during the spectrum filtering stage was likely set too high. As a result, a substantial number of intermediate cycles may have been removed even though they could still contribute non-negligible damage under variable-amplitude loading. The relative severity ordering is therefore considered qualitatively preserved, with TBL remaining the limiting case, but the quantitative validation of the TB–TBL separation remains only partial.

9.4. External Validity from Operational Experience

As a final step, the main findings from WP1–WP3 were compared with the expert technical field observations presented in Chapter 3. This comparison does not directly validate numerical stress magnitudes or absolute fatigue life. Instead, it serves as an external qualitative validity check on whether the inferred load-path changes, severity modifiers, and degradation trends remain consistent with reported operational experience. The external validity items are defined in Table 9.14 and assessed in Table 9.15.

Table 9.14: External validation items

Identifier	Validation item
VAL-EXT-01	Comparison of the inferred TB–TBL load-path differences with the expert observations
VAL-EXT-02	Comparison of the identified severity drivers with the reported operational severity modifiers
VAL-EXT-03	Comparison of the predicted critical regions and relative fatigue implications with the reported degradation signatures

Table 9.15: External validation assessment

Identifier	Method	Reported	Status
VAL-EXT-01	Assessment of whether the inferred differences in TB and TBL load introduction, load path, and resulting structural response are consistent with the expert technical field observations	Section 8.5	✓
VAL-EXT-02	Assessment of whether the severity drivers identified in WP1–WP3 are consistent with the operational severity modifiers reported by the expert	Section 8.5	$\sim$
VAL-EXT-03	Assessment of whether the predicted critical regions and relative fatigue implications are consistent with the degradation signatures and maintenance observations reported in Chapter 3	Section 8.5	$\sim$

These external validation items assess whether the physical interpretation of the findings from WP1–WP3 remains consistent with reported operational experience, while recognising that this comparison is qualitative and does not constitute direct validation of numerical stress magnitudes or absolute fatigue life.

For VAL-EXT-02, the agreement is partial rather than complete. The research results and expert observations both indicate that the most severe effects occur during transient manoeuvres rather than during steady towing, particularly under braking, constrained manoeuvring, and other conditions that increase local demand. However, the expert also identifies additional operational severity modifiers such as high aircraft mass, high fuel load, slopes, rough apron transitions, and uneven terrain. These effects are physically consistent with the present framework, but they were not systematically varied in the WP1–WP3 programme. The agreement is therefore directional, but not comprehensive.

For VAL-EXT-03, the agreement is also partial. The expert chapter reports a range of service-level degradation signatures, including seal leakage, freeplay in bushings and attachments, wear in mechanically linked hardware, possible internal tyre damage, and fretting-related corrosion. The present thesis supports the broader interpretation that towbarless towing increases cumulative structural severity and redistributes local fatigue demand within the existing nose-wheel landing gear system, particularly in the drag-brace and fork/axle load paths. However, it does not directly verify those individual maintenance findings or establish one-to-one correspondence between the predicted hotspots and the reported in-service damage manifestations. The research, therefore, supports the direction of the reported degradation trends, but not their specific service-level forms.

Taken together, the external validity assessment strengthened the plausibility of the thesis's conclusions regarding physical mechanisms and directional trends. The expert observations independently support the central interpretation that towbarless towing does not create a wholly different fatigue problem, but does make the existing towing-related fatigue problem more severe by changing the load path, amplifying critical transients, and increasing cumulative structural demand in the governing nose-wheel landing gear components. At the same time, this triangulation remains qualitative and should not be interpreted as direct validation of the numerical stress magnitudes, life predictions, or specific maintenance outcomes.

10

Conclusion

The integrated results showed consistently that towbarless towing resulted in higher fatigue severity than conventional towbar towing in the investigated general-aviation turboprop and light- to midsize-jet nose-wheel landing gear context. This finding was supported across the full analysis chain, from the manoeuvre-level loading differences identified in the in-field assessment, through the staged global–local finite-element analysis, to the laboratory fatigue tests, in which the towbarless-derived spectra produced shorter measured lives than the corresponding towbar-derived spectra.

This increased fatigue severity did not arise from a uniform scaling of all towing loads, nor from a complete shift to a new globally governing structural region. Instead, it arose from a selective redistribution of load severity towards a limited set of transient manoeuvres. At the manoeuvre level, the TB–TBL difference was negligible for steady towing, minor for turning, moderate for acceleration, and strongest for pull-braking events. The principal discriminator between the two towing concepts was therefore not the quasi-steady towing baseline, but a limited number of transient longitudinal manoeuvres. This redistribution became more pronounced at the local drag-brace hotspot, where the largest TBL-to-TB amplification ratios were obtained for `ACC_PUSH_SMOOTH` (3.35), `BRK_PULL_SMOOTH` (3.28), and `BRK_PULL_RAPID` (2.32). Towbarless towing, therefore, primarily changed manoeuvre sensitivity and cumulative spectrum severity, rather than increasing all loads by a common factor.

At the structural level, this redistribution was linked to the changed force-introduction path, from tow-lug loading in towbar towing to axle-dominated loading in towbarless towing. As a result, towbarless towing increased the relative importance of the fork/axle load path, while the drag-brace region remained the governing fatigue-critical location throughout the global–local assessment. Towbarless towing did not introduce a new globally governing fatigue hotspot, but redistributed load transfer and hotspot ranking within the existing nose-wheel landing gear system. The principal structural consequence of changing the towing method was therefore an intensification of the existing towing-related fatigue problem, rather than the introduction of a different one.

The laboratory programme showed that this redistribution of load severity led to a substantial reduction in measured fatigue life for the TBL-derived spectra. The measured mean life decreased from 54.2k cycles for TB to 27.3k cycles for TBL, corresponding to a reduction from 303 to 41 equivalent 100-operation towing mission blocks. Because the TB- and TBL-derived machine blocks had different retained cycle counts per 100 operations, the cycle-life ratio and mission-block-life ratio are not identical. In this study, the mission-based comparison formed the most operationally meaningful basis for evaluating the fatigue consequence of the towing-method change. Under the present test conditions, the TBL-derived spectrum therefore reduced the converted equivalent mission-block life to approximately 14% of the TB value.

The overload-insertion results showed that sequence effects were present, but secondary to the towing-concept effect. In both towing concepts, the overload variants produced longer measured lives than the corresponding base spectra, with measured overload ratios of $\rho_{\text{RET,TB}} = 1.9$ and $\rho_{\text{RET,TBL}} = 1.3$. The overload insertion, therefore, did not act as a life-shortening penalty, but instead indicated retardation-type behaviour that partially modified the net life difference. This effect did not overturn the primary result that the TBL-derived spectra remained more severe than the TB-derived spectra, but it does indicate that overload events mixed into the towing sequence may partly reduce the net life difference relative to the retained base-spectrum comparison.

The fatigue-life prediction framework reproduced the correct relative ranking between towing concepts, namely that TB survived longer than TBL, but it did not define a unique absolute life scale. The geometry-only case was clearly non-conservative, and agreement with the measured lives improved only when a substantially higher effective severity was assumed. Interpolation against the converted equivalent mission-block lives gave an effective severity of approximately $K_t \approx 2.3$, substantially above the geometry-only value of approximately $K_t \approx 1.12$. This indicated that, in addition to the global stress and load-transfer effects captured here, detailed design characteristics are crucial to fatigue life. However, their specific contribution was not investigated separately in the present study. The predictive framework is therefore most reliable here as a tool for relative ranking and trend interpretation, rather than as a direct predictor of absolute in-service life.

Overall, the consequences of towbarless towing on the loading and fatigue behaviour of the investigated general-aviation turboprop and light- to midsize-jet nose-wheel landing gear can be stated as follows: Towbarless towing left the steady towing cases broadly similar, but amplified the transient manoeuvres that governed local stress and cumulative damage, particularly braking and selected acceleration cases, while shifting the structural load path from tow-lug loading towards axle-dominated loading. The principal consequence was a redistribution and amplification of fatigue-driving loading at the existing governing drag-brace region, resulting in a materially shorter relative fatigue life for the towbarless-derived loading spectrum than for the conventional towbar-derived loading spectrum.

11

Limitations and Recommendations

This chapter reflects on the principal limitations of the present research and, based on these, formulates recommendations for further work. The thesis established a structured relative comparison between towbar and towbarless towing for the investigated case, but not a universally transferable absolute prediction of in-service fatigue life. Its main contribution, therefore, lay in identifying relative severity differences, clarifying the governing mechanisms, and defining the bounds of interpretation of the results. Section 11.1 first discusses the main limitations of the present study, after which Section 11.2 presents the corresponding recommendations for future research.

11.1. Limitations of the Present Research

Although the present thesis provided a structured comparison between towbar and towbarless towing for the investigated case, several limitations must be recognised when interpreting the results.

Operational Representativeness

The operational representativeness of the analysed towing cases remained limited, because the comparison was based on a finite manoeuvre library rather than on a broad statistical database of real towing operations. Although the selected manoeuvres were chosen to cover the most relevant steady and transient cases, they cannot be regarded as fully representative of all operational conditions. In particular, differences in airport layout, surface conditions, slope, weather, and operator behaviour were not systematically addressed.

Much of the work was also carried out at MTOM, or on a basis scaled towards a relatively severe loading case. These extreme cases are useful for structural comparison, but not necessarily representative of routine towing practice. The conclusions should therefore be interpreted primarily as relative findings for the investigated severe case.

The applied spectra were further constructed through spectrum simplification, fixed block ordering, and a prescribed A–D usage mix. While this provided a consistent and traceable basis for comparison, it also idealised real operational variability, where mission sequencing, manoeuvre occurrence, and usage intensity may differ substantially.

TB–TBL Load Reconstruction

A key limitation of the present work is that TBL loading was not obtained from direct aircraft-side force measurements. Instead, the TBL histories used in the later work packages were reconstructed through a translation framework based on measured TB data, rolling-resistance estimates, and manoeuvre-specific assumptions. This approach is suitable for first-order comparative engineering analysis, but it introduces uncertainty in the absolute magnitude of the TBL load.

Moreover, the effect of operator behaviour was not explicitly quantified. Differences in braking style, steering input, and general towing practice may produce substantial scatter in towing-induced loading, but this was outside the scope of the present study.

Structural Modelling and Design Specificity

The finite-element work was suitable for identifying the governing hotspot and comparing TB and TBL load-path effects, but it did not fully resolve all local design features that may influence fatigue initiation. Contact conditions, local interfaces, manufacturing details, and other fine-scale geometric effects were simplified.

Only one selected nose-wheel landing gear architecture was assessed in detail. The present work, therefore, supported the conclusion that detailed design characteristics are important for fatigue behaviour. Still, it did not determine how strongly the observed TB–TBL effect depends on landing gear configuration.

Laboratory Representativeness and Fatigue-Life Interpretation

The laboratory programme was designed as a controlled, relative comparison rather than a full-scale reproduction of service loading on the real drag-brace detail. The tested specimens were smooth axial dog-bone specimens and therefore did not reproduce the actual fatigue-initiation features of the component, such as holes, fillets, lugs, and contact interfaces. In addition, the tests were performed under practical machine constraints, including tension–tension loading with $R \geq 0.1$, which required adaptation of the original spectra and limited direct laboratory-to-service transfer.

The use of 17-4PH (H900) as a proxy material, rather than a representative landing-gear steel such as 300M, further limited the interpretation of absolute life. Moreover, the executed laboratory loading was influenced by setup-specific effects, including grip-induced load asymmetry and test-frame control artefacts, which increased the effective local severity and introduced additional uncertainty in the realised stress state.

As a result, the fatigue-life framework was most reliable in the present work as a tool for relative ranking and trend interpretation, rather than as a direct predictor of absolute in-service life. The geometry-only severity was insufficient, and agreement with the measured lives improved only when a substantially higher effective severity was assumed. In addition, the applied fatigue-endurance threshold was likely unconservative for the present variable-amplitude assessment, so part of the lower-amplitude cycle population may have been treated as non-damaging even though it could still contribute to cumulative damage. Finally, the number of tested specimens per variant remained limited, sufficient to indicate the main trend but not to robustly characterise the statistical scatter.

Scope Boundary

The present work focused specifically on the structural fatigue consequences of towing-induced loading. Broader topics such as maintenance cost, inspection intervals, repairability, life-cycle economics, human factors, and systematic differences between towing-vehicle concepts were not assessed in detail. The conclusions should therefore be interpreted within the scope of a structural comparison, rather than as a complete operational assessment of towing practice and aircraft operations.

11.2. Recommendations for Further Research

The limitations identified above point directly to several targeted recommendations for further research. The items below focus on the most relevant next steps to reduce the main uncertainties in the present work and to improve the robustness, representativeness, and practical applicability of the results.

R1. **Direct instrumentation of the nose-wheel landing gear.** Future work should develop a dedicated measurement concept with sensors mounted directly on the nose-wheel landing gear, allowing towbar and towbarless towing to be compared directly for the same manoeuvres or towing operations. This would remove the need for an indirect translation framework and provide a stronger one-to-one comparison of the loads introduced by both towing concepts.

R2. **Expansion of the operational database.** A broader towing database should be developed, covering different aircraft mass states, fuel loads, pavement conditions, slopes, weather conditions, manoeuvre severities, and operators. This would allow operational scatter to be quantified and would show how robust the observed TB–TBL differences remain under different practical conditions.

R3. **Inclusion of human factors.** Since towing loads are likely influenced by operator behaviour, future work should quantify the role of training, handling style, and local procedures. This would help distinguish structural effects from operational variability.

R4. **Comparison of different TBL vehicles and interfaces.** The present thesis did not represent all towbarless systems. A useful extension is to compare different TBL vehicle concepts, wheel-clamp interfaces, and control strategies to determine how strongly towing-induced loads depend on the towing hardware.

R5. **Assessment of different NWLG architectures.** A natural extension of this work is a design-dependent comparison across different nose-wheel landing gear configurations. In particular, forward-folding drag-brace arrangements should be compared with the aft-folding configuration considered here, since their load path may remain more compressive and therefore potentially less fatigue-sensitive during towing.

R6. **Improved detailed structural modelling.** Future modelling should resolve the fatigue-critical local design features more explicitly, including contact, attachment details, and local stress raisers. This would help quantify how much of the observed increase in severity is due to detailed design effects rather than to global load transfer alone.

R7. **More representative fatigue tests.** A logical next step in WP3 would be to move from smooth specimens towards notched specimens, representative feature specimens, or subcomponent tests that better reproduce the real drag-brace geometry.

R8. **Assess overload-induced retardation more explicitly.** Future work should investigate whether overload events associated with towbarless towing can induce crack-growth retardation and thereby partially offset the increased damage from the regular towing spectrum. This would clarify whether the net fatigue-life effect of towbarless towing is less severe than suggested by the baseline mission-block comparison alone.

R9. **Link to inspection and maintenance practice.** Future research should investigate whether demanding towing events can be linked to specific inspection triggers or degradation indicators. This would help translate the present structural findings into practical maintenance guidance.

R10. **Investigate non-structural degradation mechanisms.** In addition to metal-fatigue effects, future work should also examine other towing-related degradation mechanisms identified in the expert observations, such as seal or O-ring wear and oleo-strut leakage.

R11. **Broadening beyond structural fatigue.** Finally, future studies could extend the present structural perspective towards a broader operational assessment by including operational efficiency, maintenance cost, inspection burden, repairability, and other life-cycle consequences of different towing methods.

Taken together, these recommendations define the most relevant next steps for building on the present thesis. In particular, they point to a more direct and representative definition of loading, improved resolution of design-specific structural effects, and a closer link between fatigue assessment and operational practice. Addressing these aspects would strengthen the transferability of the present findings and further clarify the fatigue implications of towbarless towing for nose-wheel landing gear structures.

References

[1] FAA Transport Airplane and Engine Issues Group, Loads and Dynamics Harmonization Working Group. *Final Report on Landing Gear Loads and Dynamics Harmonization*. Tech. rep. Federal Aviation Administration, Sept. 28, 2000. URL: `https://www.faa.gov/regulations_policies/rulemaking/committees/documents/media/TAEldhT20-9282000.pdf`.

[2] SAE International. *SAE ARP5283B: Nose Gear Towbarless Tow Vehicle Test Requirements*. 2022.

[3] Q. Lin et al. “Structural Strength Analysis and Optimization of Commercial Aircraft Nose Landing Gear under Towing Taxi-Out Conditions Using Finite Element Simulation and Modal Testing”. In: *Aerospace* 11.5 (2024), p. 414. URL: `https://www.mdpi.com/2226-4310/11/5/414`.

[4] Gordon F. Hayhoe and Jr. Patterson James. *Towbarless Towing Vehicle Operations—Evaluation of Braking Action and Vehicle Conspicuity*. Technical Note DOT/FAA/AR-TN09/44. Federal Aviation Administration, Aug. 2009. URL: `https://skybrary.aero/sites/default/files/bookshelf/3717.pdf`.

[5] Yan-kun Sun, Li Zhao, and Peng Wei. “Review on Aircraft Towing Taxi Technologies”. In: *Journal of Transport* 31.3 (2023). URL: `https://transport.chd.edu.cn/en/article/doi/10.19818/j.cnki.1671-1637.2023.03.002`.

[6] Snorri Gudmundsson. “The Anatomy of the Landing Gear”. In: *General Aviation Aircraft Design: Applied Methods and Procedures*. Butterworth-Heinemann (Elsevier), 2013.

[7] Lorenzo Tofoni. *Technical input on towbar and towbarless towing, and NWLG loads*. Personal communication. AOG4Jets.

[8] International Organization for Standardization. *ISO 20683-1:2016 — Aircraft ground support equipment — Towbarless aircraft towing vehicles — Part 1: General requirements*. 2016.

[9] European Union Aviation Safety Agency. *Easy Access Rules for Normal-Category Aeroplanes (CS-23), CS Amendment 5, AMC/GM Issue 3*. June 2023. URL: `https://www.easa.europa.eu/en/downloads/138114/en` (visited on 03/16/2026).

[10] Haihong Tang et al. “Fatigue Life Prediction and Experimental Study of Landing Gear Components via FKM Local Stress Approach”. In: *Aerospace* 12.11 (Nov. 19, 2025). DOI: `10.3390/aerospace12111026`. URL: `https://www.mdpi.com/2226-4310/12/11/1026`.

[11] L’Avionnaire. *Landing Gear*. 2025. URL: `https://www.lavionnaire.fr/AngLandingGear.php` (visited on 10/13/2025).

[12] Colleen E. Quinn. *Use of Towbarless Tractors at Airports—Best Practices*. Research Results Digest 15. Airport Cooperative Research Program, Transportation Research Board, 2012. URL: `https://skybrary.aero/sites/default/files/bookshelf/3716.pdf`.

[13] A. Hovmark and B. Andersson. “Measurements of Landing Gear Loads of a Commuter Airliner During Taxiing and Towing”. In: *ICAS-86 Congress Proceedings*. 1986. URL: `https://www.icas.org/icas_archive/ICAS1986/ICAS-86-5.9.3.pdf`.

[14] Y. Lu, H. Chen, and Q. Zhang. “Dynamic Modeling and Control of Towbarless Towing Vehicles for Aircraft Ground Handling”. In: *IEEE Transactions on Systems Engineering* 51.2 (2024), pp. 145–158.

[15] Hui Wang et al. “Study on Vibration Characteristics of the Towbarless Aircraft Taxiing System”. In: *SAE International Journal of Vehicle Dynamics, Stability, and NVH* 6.2 (2022).

[16] M. A. Gamon. *Evaluation of the Impact of Towing the L-1011 Airplane at Boston-Logan Airport*. Tech. rep. FAA-NA-80-24. Burbank, California: Lockheed-California Company, 1980. URL: `https://apps.dtic.mil/sti/tr/pdf/ADA086977.pdf`.

[17] H. Yang et al. “Finite Element Simulation of B727 Nose Landing Gear under Towing Taxi-Out Conditions”. In: *Journal of Aerospace Engineering* 38.5 (2024), pp. 1–15.

[18] EUROCONTROL and ACI-Europe Sustainable Taxiing Taskforce. *Sustainable Taxi Operations: Concept of Operations & Industry Guidance.* Tech. rep. Brussels: EUROCONTROL, Mar. 2024. URL: `https://www.eurocontrol.int/sites/default/files/2024-07/eurocontrol-sustainable-taxi-operations-conops.pdf`.

[19] Diamond Aircraft Industries. *DA20-32-02: Nose Gear Fork, Fatigue*. Jan. 8, 1999. URL: `https://support.diamond-air.at/fileadmin/uploads/Canada/Tech_Pubs_DA20-A1/Service_Bulletin/DA20-32-02-Rev-0.pdf`.

[20] M. Arif et al. “Structural Design Analysis of Torque Links of Nose Landing Gear on Light Aircraft”. In: *International Journal on Advanced Science, Engineering and Information Technology* 14.3 (2024).

[21] Federal Aviation Administration. *Airworthiness Directives; Pilatus Aircraft Ltd. Models PC-12 and PC-12/45 Airplanes*. Final rule AD 2003-14-07; Amendment 39-13226. U.S. Department of Transportation, July 16, 2003. URL: `https://www.govinfo.gov/content/pkg/FR-2003-07-16/pdf/03-17566.pdf`.

[22] Mohammed Abdo et al. “Optimisation of a Business Jet”. In: *Aircraft Design and Development Symposium, Canadian Aeronautics and Space Institute Annual General Meeting*. Toronto, Ontario, Canada, Apr. 2005.

[23] Jiahao Qin et al. “The Recovering Stability of a Towing Taxi-Out System from a Lateral Instability with Differential Braking Perspective: Modeling and Simulation”. In: *Electronics* 12.10 (2023), p. 2170.

[24] pritamashutosh. *Aircraft General Engineering and Maintenance Practices*. Apr. 14, 2014. URL: `https://pritamashutosh.wordpress.com/2014/04/14/aircraft-general-engineering-and-maintenance-practices/` (visited on 03/25/2026).

[25] MOTOTOK International GmbH. *Towing Tractor TWIN 6500 NG Flat (electric, towbarless)*. 2025. URL: `https://www.aeroexpo.online/prod/mototok-international-gmbh/product-168827-11043.html` (visited on 12/09/2025).

[26] European Union Aviation Safety Agency. *AMC 25.509 Towbarless Towing*. ED Decision 2013/010/R. 2013. URL: `https://www.easa.europa.eu/en/document-library/easy-access-rules/online-publications/easy-access-rules-large-aeroplanes-cs-25?page=18`.

[27] S. Kumar and R. Patel. “Multiaxial Fatigue Assessment of Landing Gear Fuse Pins and Cylinders”. In: *Engineering Failure Analysis* 90 (2018), pp. 120–134.

[28] X. Jiang, H. Wang, and P. Zhou. “Spectrum Synthesis and Miner-Rule Fatigue Assessment for Transport Landing Gear”. In: *International Journal of Fatigue* 176 (2025), p. 107053.

[29] Jerzy A. Ejsmont, Grzegorz Ronowski, and W. James Wilde. *Rolling Resistance Measurements at the MnROAD Facility*. Tech. rep. Minnesota Department of Transportation, 2012. URL: `https://dot.state.mn.us/research/TS/2012/201207.pdf`.

[30] Mohamad Heerwan Bin Peeie. *BMA4723 Vehicle Dynamics: Chapter 2 Fundamentals of Vehicle Dynamics (Dynamic Axle Loads)*. Universiti Malaysia Pahang, OpenCourseWare. URL: `https://ocw.ump.edu.my/mod/resource/view.php?id=557`.

[31] Euromotor. *Lecture 2: Lateral Dynamics*. URL: `https://euromotor.org/mod/resource/view.php?id=516`.

[32] Norman S. Currey. *Aircraft Landing Gear Design: Principles and Practices*. American Institute of Aeronautics and Astronautics (AIAA), 1988.

[33] Corporate Jet Investor. *Beechcraft King Air B200 – Buyers and Investors Guide*. 2021. URL: `https://www.corporatejetinvestor.com/aircraft/beechcraft-king-air-b200-buyers-investors-guide/` (visited on 11/24/2025).

[34] CMIG Online. *Cessna Citation Mustang C510 – Technical Data*. 2023. URL: `https://www.cmig.online/en/C510.html` (visited on 11/24/2025).

[35] Honda Aircraft Company. *HondaJet Elite S Brochure: Specifications & Performance*. 2021. URL: `https://www.hondajet.com/en/elite-s`.

[36] Pilatus Aircraft Ltd. *PC-24 Specifications*. 2018. URL: `https://www.pilatus-aircraft.com/en/fleet/pc-24` (visited on 10/13/2025).

[37] Jetcraft. *Cessna Citation Excel/XLS Overview*. 2022. URL: `https://www.jetcraft.com/jetstream/2022/01/cessna-citation-excel-overview-1998-2004-2/` (visited on 11/24/2025).

[38] Yuanbo Lv et al. "Reliability Evaluation of Landing Gear Retraction/Extension Accuracy Based on Bayesian Theory". In: *Aerospace* 12.4 (2025), p. 300.

[39] NASA Johnson Space Center. *Landing Gear Integration in Aircraft Conceptual Design*. 1997. URL: `https://www.nasa.gov/centers/johnson/pdf/586083main_Landing_Gear_Design.pdf`.

[40] J.Y. Du et al. "Planning towing processes at airports more efficiently". In: *Transportation Research Part E: Logistics and Transportation Review* 70 (2014), pp. 293–304.

[41] La Roche Spotters. *HK-5171 – Beechcraft B300 King Air 350i*. Dec. 30, 2020. URL: `https://www.jetphotos.com/photo/10067499` (visited on 01/12/2026).

[42] Aircraft Owners and Pilots Association (AOPA). *Beechcraft Bonanza*. 2025. URL: `https://www.aopa.org/go-fly/aircraft-and-ownership/aircraft-guide/aircraft/beechcraft-bonanza`.

[43] Temporal Engineering. *Cessna Skyhawk II / 100 Performance Assessment*. Tech. rep. 2003. URL: `https://www.temporal.com.au/c172.pdf`.

[44] Jerzy Pytka et al. "Determining Wheel Forces and Moments on Aircraft Landing Gear with a Dynamometer Sensor". In: *Sensors* 20.1 (2019), p. 227.

[45] National Transportation Safety Board. *Aircraft Accident Report: Aloha Airlines, Flight 243, Boeing 737-200, N73711, near Maui, Hawaii, April 28, 1988*. Tech. rep. NTSB/AAR-89/03. Washington, DC, 1989. URL: `https://www.ntsb.gov/investigations/AccidentReports/Reports/AAR8903.pdf`.

[46] National Transportation Safety Board. *Factual Report: Southwest Airlines Flight 2294, Rapid Decompression near Charleston, West Virginia, July 13, 2009*. Tech. rep. DCA09FA065. Washington, DC, 2010. URL: `https://data.ntsb.gov/Docket/Document/docBLOB?FileExtension=.PDF&FileName=Flight+Data+Recorder+10+-+Factual+Report+of+Group+Chairman-Master.PDF&ID=40333539`.

[47] Federal Aviation Administration. *Aging Airplane Program: Widespread Fatigue Damage; Final Rule*. Federal Register 75 FR 69746. Nov. 2010. URL: `https://www.federalregister.gov/documents/2010/11/15/2010-28363/aging-airplane-program-widespread-fatigue-damage`.

[48] Federal Aviation Administration. *AC 25.571-1D: Damage Tolerance and Fatigue Evaluation of Structure*. Tech. rep. AC 25.571-1D. Washington, DC: U.S. Department of Transportation, Federal Aviation Administration, 2011. URL: `https://www.faa.gov/documentLibrary/media/Advisory_Circular/AC_25_571-1D_.pdf`.

[49] European Union Aviation Safety Agency. *AMC 25.571: Damage tolerance and fatigue evaluation of structure (CS-25)*. EASA Easy Access Rules (online). 2023. URL: `https://www.easa.europa.eu/en/document-library/easy-access-rules/online-publications/easy-access-rules-large-aeroplanes-cs-25`.

[50] U.S. Department of Defense. *MIL-HDBK-1823A: Nondestructive Evaluation System Reliability Assessment*. Tech. rep. Washington, DC, 2009. URL: `https://statistical-engineering.com/wp-content/uploads/2017/10/MIL-HDBK-1823A2009.pdf`.

[51] ASTM International. *ASTM E647: Standard Test Method for Measurement of Fatigue Crack Growth Rates*. 2023. URL: `https://www.astm.org/e0647-23.html`.

[52] J. Schijve. *Fatigue of Structures and Materials*. 2nd ed. Dordrecht: Springer, 2009. URL: `https://link.springer.com/book/10.1007/978-1-4020-6808-9`.

[53] An Tang, Zhiguo Zhou, and Jie Cao. "A Technique of Landing Gear Loads Calibration with Strain Gages". In: *27th International Congress of the Aeronautical Sciences (ICAS)*. Nice, France, 2010.

[54] Zbigniew Skorupka. "Dynamic Testing and Fatigue Analysis of the I-31P Nose Landing Gear". In: *Fatigue of Aircraft Structures* 15 (2023), pp. 133–145.

[55] Pilatus Aircraft Ltd. *PC-24 Ground Servicing Guide*. 2020. URL: `https://www.pilatus-aircraft.com/assets/files/Technical-Publications/Ground-Servicing-Guide_PC-24.pdf`.

[56] SAE International. *SAE ARP5284: Towbarless Towing Vehicle Nose Gear Steering Interface and Stability*. 2019.

[57] National Transportation Safety Board. *Aviation Investigation Final Report: Piper PA-24-400, Des Moines, Iowa*. Accident Report CHI07CA088. Washington, DC: National Transportation Safety Board, Mar. 12, 2007. URL: https://data.ntsb.gov/carol-repgen/api/Aviation/ReportMain/GenerateNewestReport/65490/pdf.

[58] Piper Aircraft, Inc. *PA-46-600TP, M600 Maintenance Manual: Towing*. Nov. 30, 2020. URL: https://data.ntsb.gov/Docket/Document/docBLOB?FileExtension=pdf&FileName=Maintenance+Manual+Towing+Guidance-Rel.pdf&ID=12286438.

[59] Xiaofeng Cui and Yong Li. “A Test Method for Traction Load of Aircraft Nose Landing Gear”. In: *CSAA/IET International Conference on Aircraft Utility Systems (AUS 2022)*. 2022.

[60] Lorenzo Tofoni. *Equipment provided for experimental towing tests*. Equipment provided on loan for this study. AOG4Jets, Aug. 25, 2025.

[61] Pilatus Aircraft Ltd. *PC-12 NGX — Just the Facts*. 2024.

[62] National Transportation Safety Board. *Weight & Balance Data — N56KJ (PC-12/47E)*. 2013.

[63] *ISO 7717:1985 Aircraft — Four-wheel-drive tow tractors — Performance requirements factors for design*. Tech. rep. International Organization for Standardization, 1985. URL: https://cdn.standards.iteh.ai/samples/14546/6c48221bfc714bf2b4ec5fd63c69acc1/ISO-7717-1985.pdf.

[64] BMT Fleet Technology Limited. *Runway Friction Characteristics Measurement and Aircraft Braking (RuFAB), Volume 2: Documentation and Taxonomy*. Tech. rep. European Aviation Safety Agency, 2010. URL: https://www.easa.europa.eu/sites/default/files/dfu/Report%20Volume%202%20-%20Documentation%20and%20taxonomy.pdf.

[65] Goldhofer Aktiengesellschaft. *SHERPA D Family Technical Data*. July 2025. URL: https://www.goldhofer.com/fileadmin//downloads/BRO_AT/Data_Sheets/DSH_SHERPA-D-FAMILY_EN-imp.pdf.

[66] BL Advanced Ground Support Systems Ltd. *ATT-2 (Towbarless Tug) Product Specification*. 2025. URL: https://www.bl-il.com/wp-content/uploads/2025/09/1003-ATT-2-Leaflet-Rev-B-1.pdf.

[67] Thoai D. Nguyen. “Finite Element Analysis of a Nose Gear During Landing”. Master of Science in Mechanical Engineering (MSME) thesis. Jacksonville, FL: University of North Florida, 2010.

[68] V. Infante et al. “Failure analysis of a nose landing gear fork”. In: *Engineering Failure Analysis* 82 (2017), pp. 554–565. URL: https://www.sciencedirect.com/science/article/pii/S1350630716308792.

[69] Kelly Carney et al. *Development of a Generalized Yield Surface for Isotropic, Pressure-Insensitive Metal Plasticity With Differing Tension, Compression, and Shear Yield Strengths*. Final Report DOT/FAA/TC-19/42. U.S. Department of Transportation, Federal Aviation Administration (FAA), William J. Hughes Technical Center, Mar. 2020. URL: https://rosap.ntl.bts.gov/view/dot/57808/dot_57808_DS1.pdf.

[70] BEA (France). *Safety Investigation Report (TF-BBM)*. 2023. URL: https://bea.aero/fileadmin/user_upload/TF-BBM_EN.pdf.

[71] SKYbrary Aviation Safety. *Nose Wheel Steering*. URL: https://skybrary.aero/articles/nose-wheel-steering.

[72] *Aircraft ground support equipment — Towbarless towing tractors — Part 2*. ISO 20683-2:2016. 2016. URL: https://cdn.standards.iteh.ai/samples/68259/175c0a7eb40d4bf09f8fbc452fe46a3f/ISO-20683-2-2016.pdf.

[73] Accident Investigation Board Denmark. *Final Report HCLJ510-2012-172*. 2012. URL: https://skybrary.aero/sites/default/files/bookshelf/2468.pdf.

[74] MIT OpenCourseWare. *8.01SC Classical Mechanics: Chapter 6 – Circular Motion*. 2016. URL: https://ocw.mit.edu/courses/8-01sc-classical-mechanics-fall-2016/mit8_01scs22_chapter6.pdf.

[75] Delft University of Technology, Faculty of Aerospace Engineering. *AE4ASM005 Fatigue of Structures and Materials: Course notes*. Lecture notes, TU Delft. 2025.

[76] Hanbong Lee, William J. Coupe, and Yoon C. Jung. “Prediction of Pushback Times and Ramp Taxi Times for Departures at Charlotte Airport”. In: *AIAA Aviation 2019 Forum*. Dallas, TX: American

Institute of Aeronautics and Astronautics, June 2019. URL: `https://ntrs.nasa.gov/citations/20190027660`.

[77] *ARMCO® 17-4 PH® Stainless Steel: Product Data Bulletin*. October 2022. AK Steel International (Cleveland-Cliffs Inc.), 2022. URL: `https://www.aksteel.nl/files/downloads/clf_datasheet_armco_17-4_ph_pdb_euro_102022_89.pdf`.

[78] Richard G. Budynas and J. Keith Nisbett. *Fatigue Failure Resulting from Variable Loading (Chapter 6 excerpt, Mechanical Engineering Design)*. URL: `https://faculty.up.edu/lulay/me401/FatigueFailureChapter6-s10.pdf`.

[79] Norman E. Dowling. *Mechanical Behavior of Materials: Engineering Methods for Deformation, Fracture, and Fatigue*. 4th ed. Harlow: Pearson Education Limited, 2012.

[80] R. C. Rice et al. *Metallic Materials Properties Development and Standardization (MMPDS)*. Technical Report PB2003106632. U.S. Department of Transportation, Federal Aviation Administration, 2003. URL: `https://ntrl.ntis.gov/NTRL/dashboard/searchResults/titleDetail/PB2003106632.xhtml` (visited on 03/02/2026).

[81] Oscar Zambrano, John Jairo Coronado, and S. A. Rodríguez. “Failure analysis of a bridge crane shaft”. In: *Case Studies in Engineering Failure Analysis* 2 (2014), pp. 27–35. URL: `https://www.researchgate.net/publication/259997140_Failure_analysis_of_a_bridge_crane_shaft`.

[82] M. Ghasemian Malakshah et al. “Corrosion Fatigue of 17-4PH Stainless Steel in a Simulated Sea Water Solution”. In: *Journal of Advanced Materials in Engineering* 38.2 (2014), pp. 69–81. URL: `https://doaj.org/article/3c522c51d4b841518b6d2b8a5fae0070` (visited on 02/12/2026).

A

WP1 Supporting Material

A.1. WP1 Pipeline Demonstration and Pre-Towing Verification

Before the airfield campaign, a short bicycle run was recorded to verify the kinematics chain of the test setup, including logging, time alignment, event segmentation, and plotting of the measured channels. The resulting heading and velocity traces are shown in Figures A.1 and A.2, respectively. This dataset was included only to confirm that the acquisition and processing workflow functioned as intended, and was not used for any quantitative inference about aircraft towing loads.

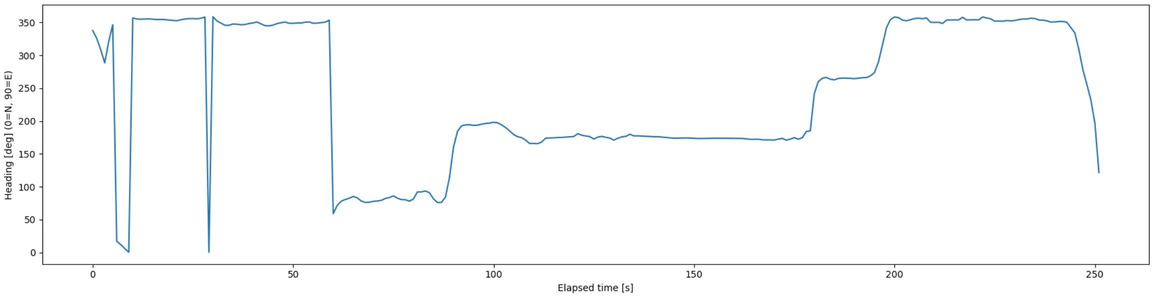

Figure A.1: Bike heading over a representative kinematics logging run

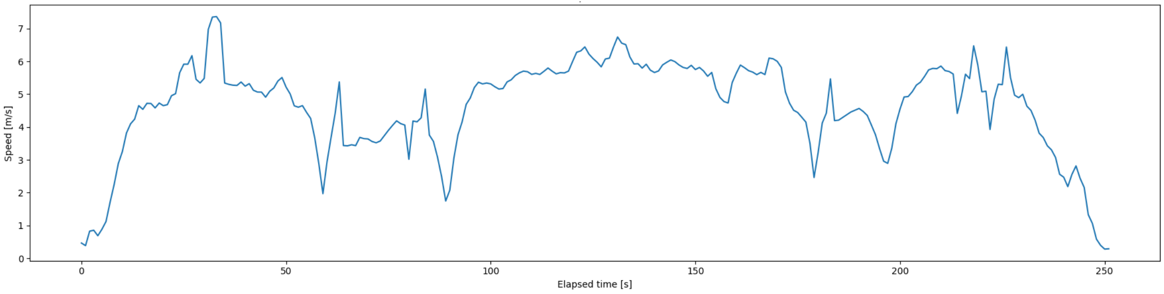

Figure A.2: Bike velocity profile over a representative kinematics logging run

In addition, GNSS tracks were overlaid on a map to visualise the driven paths and enable manoeuvre segmentation for full towing cycles. Moreover, this supported pre-towing instrumentation verification, as shown in Figure A.3.

Figure A.3: Map of the test area and paths used for pre-towing instrumentation verification

A.2. WP1 Instrumentation Wiring and Channel Mapping

This section documents the implementation-level instrumentation details used during WP1 field testing. It supports reproducibility of the Raspberry Pi-based acquisition chain by recording the pin assignments, bridge wiring, and ADC channel mapping used for the towbar strain-gauge measurements.

Raspberry Pi 40-pin layout and header usage

The Raspberry Pi 5 served as the central acquisition unit during WP1. Its 40-pin header interfaced with the IMU via I^{2}C, the GNSS via UART, and the ADS1263 24-bit ADC via SPI0 with manual control lines. The Raspberry Pi, ADC, and GNSS modules were stacked on the 2×20 header. Figure A.4 shows the Raspberry Pi 5 pin layout used as the reference for the WP1 header assignments listed in Table A.1. The corresponding acquisition code is provided in the repository linked on the title page.

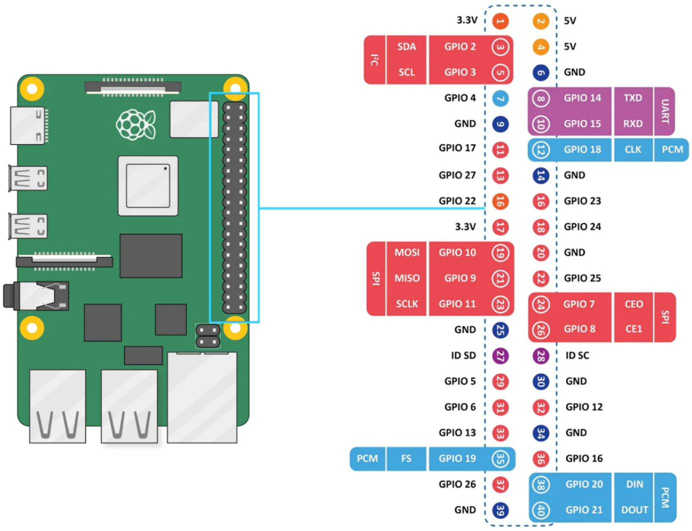

Figure A.4: Raspberry Pi 5 including pin layout[1]

Table A.1: Raspberry Pi 40-pin header usage

Pin #	BCM	Name	Dir.	Used by / Notes
1	—	3V3	—	Excitation for strain bridges; 3V3 logic for IMU/GNSS/ADC
3	GPIO2	SDA1 (I^{2}C)	I/O	IMU SDA
5	GPIO3	SCL1 (I^{2}C)	I/O	IMU SCL
6	—	GND	—	Common ground (ADC analogue GND, IMU, GNSS)
8	GPIO14	TXD0 (UART)	Out	GNSS RXD (Pi TX → GNSS IN)
10	GPIO15	RXD0 (UART)	In	GNSS TXD (GNSS OUT → Pi RX)
11	GPIO17	GPIO	In	ADC `DRDY` (data ready)
12	GPIO18	GPIO	Out	ADC `RESET`
15	GPIO22	GPIO	Out	ADC manual `CS` (chip-select)
19	GPIO10	MOSI (SPI0)	Out	ADC SPI MOSI
21	GPIO9	MISO (SPI0)	In	ADC SPI MISO
23	GPIO11	SCLK (SPI0)	Out	ADC SPI SCLK
14	—	GND	—	Extra ground near SPI block
17	—	3V3	—	Clean 3V3 feed to analog front-end

Strain bridges and ADC channel mapping

Axial and bending strains on the towbar were acquired via two diagonal half-bridges, read by two differential ADC channels (A and B) on the ADS1263. Both half-bridges share a common 3.3 V excitation from the Raspberry Pi / ADS1263 stack, and the ADC also samples the excitation (`VEX`) so that the signals can be processed ratiometrically. For small strains, the bridge response can be written as

$$\frac{V_{\text{out}}}{V_{\text{exc}}} \approx \text{GF}\,\varepsilon_{\text{axial}} \qquad \Longrightarrow \qquad \varepsilon_{\text{axial}} \approx \frac{1}{\text{GF}}\,\frac{V_{\text{out}}}{V_{\text{exc}}}, \tag{A.1}$$

---

[1] Source: `https://vilros.com/pages/raspberry-pi-5-pinout?srsltid=AfmBOopv_znS1NV7lyEIZfZkgiJXwFxIJai115ErkxmOHVDuVO59GXoo`

where,

- V_{out} bridge output (differential) voltage [V]
- V_{exc} bridge excitation voltage [V]
- GF strain-gauge factor [-]
- $\varepsilon_{\text{axial}}$ axial strain [-]

with GF the gauge factor from the datasheet, which in this case is set at $2.09 \pm 1.0\%$. In the acquisition script, the differential inputs are mapped as

$$\texttt{A\_POS} = 0,\ \texttt{A\_NEG} = 1; \quad \texttt{B\_POS} = 3,\ \texttt{B\_NEG} = 4; \quad \texttt{VEX\_POS} = 2,\ \texttt{VEX\_NEG} = 10\ (\text{AINCOM}),$$

which fixes how bridge and excitation voltages are reconstructed in post-processing. The corresponding wiring between the bridges and ADS1263 inputs is summarised in Table A.2.

Table A.2: Bridge and ADS1263 connections

Node	**Connects to**	**Notes**
Bridge excitation $+$ (A, B)	Pi 3V3 (Pin 1/17)	Common excitation node for both bridges + ADC reference
Bridge excitation $-$ (A, B)	GND (Pin 6/14)	Analogue ground return
Bridge A $+$ / $-$	ADS1263 AIN0 / AIN1	Differential input for half-bridge A
Bridge B $+$ / $-$	ADS1263 AIN3 / AIN4	Differential input for half-bridge B
Excitation sense $+$ / $-$	ADS1263 AIN2 / AIN10	VEX sense for ratiometric processing
ADC $V_{\text{REF}+}$ / $V_{\text{REF}-}$	3V3 / GND	Reference tied to excitation node

The complete field setup is shown in Figure 5.9 in Chapter 5. In that setup, the pin-insert connection board served as the interface between the towbar strain-gauge wiring and the ADC amplifier.

Connector reassembly convention The strain-gauge leads from the towbar were routed through a pin-insert connection board before entering the ADC readout chain. Because this board fixed the effective bridge-to-channel mapping, the wiring sequence had to remain unchanged between calibration and field use.

After any disconnection of the towbar strain-gauge wiring or electronics, the leads were reconnected in the same locations and in the same sequence as used during calibration. Reassembly was performed from bottom to top (from the end furthest from the Raspberry Pi towards the Raspberry Pi); for each channel, the coloured lead was inserted first, followed by the cream lead placed further along, and the channel order was maintained as orange, brown, red, and yellow.

B

WP2 Supporting Material

B.1. Parameter Data for the WP2 Finite-Element Model

This section summarises the principal geometric dimensions and joint-related parameters used to define the global NWLG finite element model. The parameters in Table B.1 define the simplified, representative NWLG geometry used in the comparative FE model; they should not be interpreted as certified dimensions for a Pilatus PC-24.

Table B.1: Key geometry and joint parameters used in the global NWLG model

Parameter	**Unit**	**Value**
Barrel outer diameter	mm	64.0
Piston outer diameter	mm	45.0
Strut axial offset (to crown/axle)	mm	110.0
Strut vertical placement (crown Z)	mm	340.0
Fork inner clear width (gap)	mm	180.0
Fork leg thickness (along Y)	mm	20.0
Fork height (along X)	mm	45.0
Axle diameter	mm	20.0
Axle overall length	mm	200.0
Crown thickness (along X)	mm	90.0
Crown height (along Z)	mm	20.0
Crown span (along Y)	mm	86.5
Standard pin diameter (crown / TL)	mm	10.0
Brace pin diameter	mm	20.0
Lug width (crown / TL)	mm	15.0
Lug height (crown / TL)	mm	5.0
Lug span (crown)	mm	56.5
Torque-link lug span (barrel)	mm	56.5
Torque-link rod diameter	mm	16.0
Mid torque-link pin length	mm	38.0
Oleo: min engagement	mm	50.0
Oleo: max engagement	mm	100.0
Oleo: travel	mm	50.0
Barrel hollow length	mm	100.0
Crown–fork connector angle	deg	30.0

C

WP3 Supporting Material

C.1. Material Properties of 17-4PH (H900)

This section provides the material-property source used for the 17-4PH (H900) specimen material adopted in the laboratory fatigue programme.

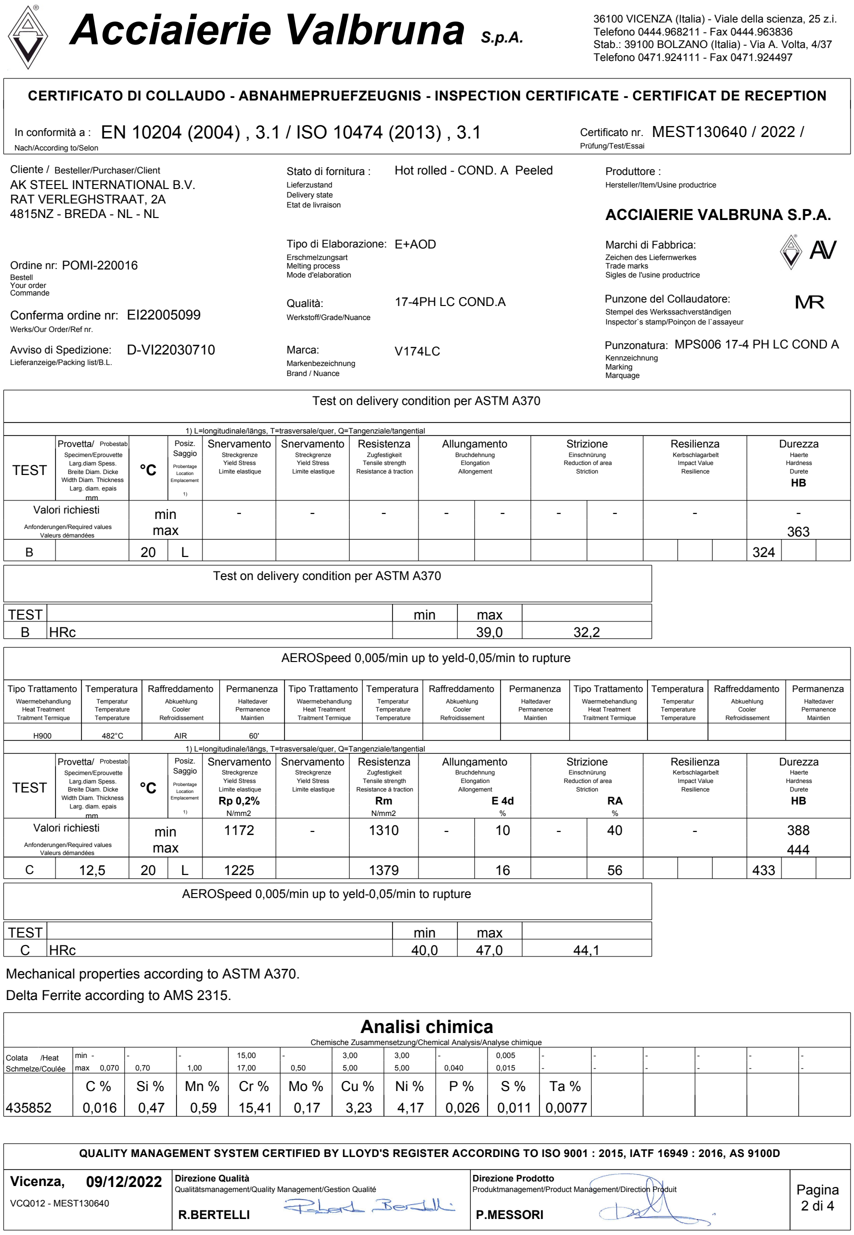

Acciaierie Valbruna S.p.A.

36100 VICENZA (Italia) - Viale della scienza, 25 z.i.
Telefono 0444.968211 - Fax 0444.963836
Stab.: 39100 BOLZANO (Italia) - Via A. Volta, 4/37
Telefono 0471.924111 - Fax 0471.924497

CERTIFICATO DI COLLAUDO - ABNAHMEPRUEFZEUGNIS - INSPECTION CERTIFICATE - CERTIFICAT DE RECEPTION

In conformità a : EN 10204 (2004) , 3.1 / ISO 10474 (2013) , 3.1
Nach/According to/Selon

Certificato nr. MEST130640 / 2022 /
Prüfung/Test/Essai

Cliente / Besteller/Purchaser/Client
AK STEEL INTERNATIONAL B.V.
RAT VERLEGHSTRAAT, 2A
4815NZ - BREDA - NL - NL

Ordine nr: POMI-220016
Bestell
Your order
Commande

Conferma ordine nr: EI22005099
Werks/Our Order/Ref nr.

Avviso di Spedizione: D-VI22030710
Lieferanzeige/Packing list/B.L.

Stato di fornitura : Hot rolled - COND. A Peeled
Lieferzustand
Delivery state
Etat de livraison

Tipo di Elaborazione: E+AOD
Erschmelzungsart
Melting process
Mode d'elaboration

Qualità: 17-4PH LC COND.A
Werkstoff/Grade/Nuance

Marca: V174LC
Markenbezeichnung
Brand / Nuance

Produttore :
Hersteller/Item/Usine productrice

ACCIAIERIE VALBRUNA S.P.A.

Marchi di Fabbrica: AV
Zeichen des Liefernwerkes
Trade marks
Sigles de l'usine productrice

Punzone del Collaudatore: MR
Stempel des Werkssachverständigen
Inspector`s stamp/Poinçon de l`assayeur

Punzonatura: MPS006 17-4 PH LC COND A
Kennzeichnung
Marking
Marquage

Test on delivery condition per ASTM A370

1) L=longitudinale/längs, T=trasversale/quer, Q=Tangenziale/tangential

TEST	Provetta/ Probestab Specimen/Eprouvette Larg.diam Spess. Breite Diam. Dicke Width Diam. Thickness Larg. diam. epais mm	°C	Posiz. Saggio Probentage Location Emplacement 1)	Snervamento Streckgrenze Yield Stress Limite elastique	Snervamento Streckgrenze Yield Stress Limite elastique	Resistenza Zugfestigkeit Tensile strength Resistance á traction	Allungamento Bruchdehnung Elongation Allongement		Strizione Einschnürung Reduction of area Striction		Resilienza Kerbschlagarbelt Impact Value Resilience			Durezza Haerte Hardness Durete **HB**		
Valori richiesti Anfonderungen/Required values Valeurs démandées		min max		-	-	-	-	-	-	-	-			- 363		
B		20	L											324		

Test on delivery condition per ASTM A370

TEST		min	max	
B	HRc		39,0	32,2

AEROSpeed 0,005/min up to yeld-0,05/min to rupture

Tipo Trattamento Waermebehandlung Heat Treatment Traitment Termique	Temperatura Temperatur Temperature Temperature	Raffreddamento Abkuehlung Cooler Refroidissement	Permanenza Haltedaver Permanence Maintien	Tipo Trattamento Waermebehandlung Heat Treatment Traitment Termique	Temperatura Temperatur Temperature Temperature	Raffreddamento Abkuehlung Cooler Refroidissement	Permanenza Haltedaver Permanence Maintien	Tipo Trattamento Waermebehandlung Heat Treatment Traitment Termique	Temperatura Temperatur Temperature Temperature	Raffreddamento Abkuehlung Cooler Refroidissement	Permanenza Haltedaver Permanence Maintien
H900	482°C	AIR	60'								

1) L=longitudinale/längs, T=trasversale/quer, Q=Tangenziale/tangential

TEST	Provetta/ Probestab Specimen/Eprouvette Larg.diam Spess. Breite Diam. Dicke Width Diam. Thickness Larg. diam. epais mm	°C	Posiz. Saggio Probentage Location Emplacement 1)	Snervamento Streckgrenze Yield Stress Limite elastique **Rp 0,2%** N/mm2	Snervamento Streckgrenze Yield Stress Limite elastique	Resistenza Zugfestigkeit Tensile strength Resistance á traction **Rm** N/mm2	Allungamento Bruchdehnung Elongation Allongement	**E 4d** %	Strizione Einschnürung Reduction of area Striction	**RA** %	Resilienza Kerbschlagarbelt Impact Value Resilience			Durezza Haerte Hardness Durete **HB**		
Valori richiesti Anfonderungen/Required values Valeurs démandées		min max		1172	-	1310	-	10	-	40	-			388 444		
C	12,5	20	L	1225		1379		16		56				433		

AEROSpeed 0,005/min up to yeld-0,05/min to rupture

TEST		min	max	
C	HRc	40,0	47,0	44,1

Mechanical properties according to ASTM A370.

Delta Ferrite according to AMS 2315.

Analisi chimica

Chemische Zusammensetzung/Chemical Analysis/Analyse chimique

Colata /Heat Schmelze/Coulée	min - max 0,070	- 0,70	- 1,00	15,00 17,00	- 0,50	3,00 5,00	3,00 5,00	- 0,040	0,005 0,015	- -	- -	- -	- -	- -	- -
	C %	Si %	Mn %	Cr %	Mo %	Cu %	Ni %	P %	S %	Ta %					
435852	0,016	0,47	0,59	15,41	0,17	3,23	4,17	0,026	0,011	0,0077					

QUALITY MANAGEMENT SYSTEM CERTIFIED BY LLOYD'S REGISTER ACCORDING TO ISO 9001 : 2015, IATF 16949 : 2016, AS 9100D

Vicenza, 09/12/2022 VCQ012 - MEST130640	**Direzione Qualità** Qualitätsmanagement/Quality Management/Gestion Qualité **R.BERTELLI** Robert Bertelli	**Direzione Prodotto** Produktmanagement/Product Management/Direction Produit **P.MESSORI**	Pagina 2 di 4

Figure C.1: Material datasheet for 17-4PH stainless steel, H900 condition

C.2. Specimen Allocation for Fatigue Tests

This table lists the WP3 fatigue specimens and the nominal loading spectrum assigned to each specimen in the TB, TBL, TB+RET, and TBL+RET test matrix.

Table C.1: Specimen identification and associated nominal loading spectra

TB		TBL	
Specimen ID	Applied nominal spectrum	Specimen ID	Applied nominal spectrum
LAB-TB1	$LAB\text{-}S_{\text{tb}}$	LAB-TBL1	$LAB\text{-}S_{\text{tbl}}$
LAB-TB2	$LAB\text{-}S_{\text{tb}}$	LAB-TBL2	$LAB\text{-}S_{\text{tbl}}$
LAB-TB3	$LAB\text{-}S_{\text{tb}}$	LAB-TBL3	$LAB\text{-}S_{\text{tbl}}$
LAB-TB+RET1	$LAB\text{-}S_{\text{tb+ret}}$	LAB-TBL+RET1	$LAB\text{-}S_{\text{tbl+ret}}$
LAB-TB+RET2	$LAB\text{-}S_{\text{tb+ret}}$	LAB-TBL+RET2	$LAB\text{-}S_{\text{tbl+ret}}$

C.3. Mission Schedule Definitions

This section reports the mission schedules used for WP3 spectrum assembly, including the light Mission A/B schedules and the paired TB/TBL schedules for Missions C and D. These tables present the complete set of prescribed manoeuvre sequences used for spectrum assembly in WP3.

Table C.2: Representative mission schedules for light ground-towing cycles (identical for TB and TBL)

(a) A. Light mission schedule (TB and TBL)

#	Manoeuvre m	Control	Value
1	Stationary baseline	time	1 s
2	Smooth pull acceleration	event	–
3	Straight pull (constant speed)	time	40 s
4	Wide-radius pull turn	event	–
5	Straight pull (constant speed)	time	10 s
6	Smooth pull braking	event	–
7	Smooth push acceleration	event	–
8	Straight push (constant speed)	time	10 s
9	Smooth push braking	event	–
10	Tight-radius push turn	event	–
11	Smooth push braking	event	–
12	Stationary baseline	time	1 s

(b) B. Light mission with rapid brake input (TB and TBL)

#	Manoeuvre m	Control	Value
1	Stationary baseline	time	1 s
2	Smooth pull acceleration	event	–
3	Straight pull (constant speed)	time	40 s
4	Wide-radius pull turn	event	–
5	Straight pull (constant speed)	time	10 s
6	**Rapid** pull braking	event	–
7	Smooth push acceleration	event	–
8	Straight push (constant speed)	time	10 s
9	Smooth push braking	event	–
10	Tight-radius push turn	event	–
11	Smooth push braking	event	–
12	Stationary baseline	time	1 s

Table C.3: Representative mission schedules for spectrum C (medium ground-towing cycle)

(a) C. Medium mission schedule (TB)

#	Manoeuvre m	Control	Value
1	Stationary baseline	time	1 s
2	Smooth pull acceleration	event	–
3	Straight pull (constant speed)	time	60 s
4	Wide-radius pull turn	event	–
5	Straight pull (constant speed)	time	35 s
6	Wide-radius pull turn	event	–
7	Smooth pull braking	event	–
8	Tight-radius pull turn	event	–
9	Smooth pull acceleration	event	–
10	Straight pull (constant speed)	time	20 s
11	Smooth pull braking	event	–
12	Tight-radius pull turn	event	–
13	Smooth pull acceleration	event	–
14	Straight pull (constant speed)	time	30 s
15	Smooth pull braking	event	–
16	Tight-radius pull turn	event	–
17	Smooth pull braking	event	–
18	Stationary baseline	time	1 s

(b) C. Medium mission schedule (TBL)

#	Manoeuvre m	Control	Value
1	Stationary baseline	time	1 s
2	Smooth pull acceleration	event	–
3	Straight pull (constant speed)	time	60 s
4	Wide-radius pull turn	event	–
5	Straight pull (constant speed)	time	35 s
6	Wide-radius pull turn	event	–
7	Smooth pull braking	event	–
8	Smooth push acceleration	event	–
9	Straight push (constant speed)	time	5 s
10	Smooth push braking	event	–
11	Tight-radius pull turn	event	–
12	Straight pull (constant speed)	time	30 s
13	Smooth pull braking	event	–
14	Tight-radius pull turn	event	–
15	Smooth pull braking	event	–
16	Stationary baseline	time	1 s

Table C.4: Representative mission schedules for spectrum D (heavy ground-towing cycle)

(a) D. Heavy mission schedule (TB)

#	Manoeuvre m	Control	Value
1	Stationary baseline	time	1 s
2	Smooth pull acceleration	event	–
3	Straight pull (constant speed)	time	85 s
4	Smooth pull braking	event	–
5	Tight-radius pull turn	event	–
6	Smooth pull acceleration	event	–
7	Straight pull (constant speed)	time	40 s
8	Wide-radius pull turn	event	–
9	Straight pull (constant speed)	time	30 s
10	Smooth pull braking	event	–
11	Tight-radius pull turn	event	–
12	Smooth pull acceleration	event	–
13	Straight pull (constant speed)	time	70 s
14	Smooth pull braking	event	–
15	Tight-radius pull turn	event	–
16	Smooth pull acceleration	event	–
17	Straight pull (constant speed)	time	85 s
18	Wide-radius pull turn	event	–
19	Straight pull (constant speed)	time	30 s
20	Smooth pull braking	event	–
21	Tight-radius pull turn	event	–
22	Smooth push acceleration	event	–
23	Smooth push braking	event	–
24	Stationary baseline	time	1 s

(b) D. Heavy mission schedule (TBL)

#	Manoeuvre m	Control	Value
1	Stationary baseline	time	1 s
2	Smooth pull acceleration	event	–
3	Straight pull (constant speed)	time	85 s
4	Smooth pull braking	event	–
5	Tight-radius pull turn	event	–
6	Smooth pull acceleration	event	–
7	Straight pull (constant speed)	time	40 s
8	Wide-radius pull turn	event	–
9	Straight pull (constant speed)	time	30 s
10	Smooth pull braking	event	–
11	Tight-radius pull turn	event	–
12	Smooth push acceleration	event	–
13	Straight push (constant speed)	time	35 s
14	Smooth push braking	event	–
15	Tight-radius push turn	event	–
16	Smooth pull acceleration	event	–
17	Straight pull (constant speed)	time	85 s
18	Wide-radius pull turn	event	–
19	Straight pull (constant speed)	time	30 s
20	Smooth pull braking	event	–
21	Tight-radius pull turn	event	–
22	Smooth push acceleration	event	–
23	Smooth push braking	event	–
24	Stationary baseline	time	1 s

D

Expert Opinion Source Text

D.1. NWLG Degradation Patterns Potentially Associated with Frequent TBL Towing

1. Background

Based on recurring maintenance findings across aircraft that may be subjected to frequent towbarless ("shovel-type") towing operations, a progressive pattern of component wear and reliability-related degradation has been observed.

The findings appear cumulative, aircraft cycle-dependent and during AOG's, rather than linked to isolated overload events.

2. Shock Strut Findings

2.1 Internal Hydraulic Leakage

Observed trends include:

- Increased internal bypass
- Reduced damping effectiveness
- No visible external leakage
- Inconsistent static extension despite correct (oleo/nitrogen) servicing

2.2 Suspected Isolation (Floating) Piston Seal Wear

There is suspicion of accelerated wear of the isolation piston seal separating nitrogen and hydraulic oil.

Possible contributing mechanisms:

- Elevated lateral loads during constrained towing
- Micro-misalignment under side-load
- Increased friction at internal sliding interfaces
- Circulation of fine wear particles

This correlates with internal leakage patterns without external seal failure.

3. Progressive Freeplay in Structural Interfaces

Observed in:

- Torque link bushings
- Steering actuator attachments
- Drag brace pivots
- Trunnion bearings
- Shimmy damper mounts

Typical characteristics:

- Bushing ovalization
- Bolt hole elongation
- Fretting at mating surfaces
- Increased steering compliance

Progressive freeplay may amplify vibration transmission and redistribute loads within the NLG assembly.

4. Nose Landing Gear Door Interconnection Wear

On aircraft where nose gear doors are mechanically interconnected with actuation linkages, observed wear includes:

- Bolt fretting
- Bushing wear
- Bearing clearance increase
- Hinge elongation
- Progressive door misalignment

Doors are not designed to absorb torsional load input; vibration and lateral load transfer may accelerate hardware degradation.

5. Tire and Wheel Effects

Even when tires are correctly balanced:

- High lateral scrubbing during tight static turns may cause internal carcass or cord damage
- Early structural degradation may not be externally visible
- Localized tread scuffing or stiffness variation may occur
- Balanced condition does not confirm internal tire integrity.

Operational Recommendation

Following towbarless towing, particularly after:

- Tight pivot turns
- Rough apron transitions
- Significant braking inputs

It is advisable to:

- Check nose tire pressure
- Inspect tread shoulders and sidewalls
- Monitor for abnormal taxi vibration

6. Corrosion and Surface Degradation

Increased corrosion has been observed on:

- Door hinge bolts
- Torque link hardware
- Steering actuator bolts
- Drag brace interfaces

Probable mechanism:

- Micro-movement removes protective coatings (fretting).
- Bare metal becomes exposed.
- Moisture and de-icing residue accelerate oxidation.
- Repeated vibration promotes coating breakdown.

Corrosion appears secondary to interface micro-movement rather than solely environmental exposure.

7. Fuel Load Consideration During Towbarless Towing

Aircraft gross weight directly influences:

- Nose gear static load
- Fork bending moment
- Shock strut side loading
- Bushing contact stress
- Tire deflection and scrubbing forces

When towed with full fuel:

- Static load on the NLG increases
- Dynamic inertia during braking or turning increases
- Bending moments proportionally increase

Operational Recommendation

When operationally feasible:

- Avoid towing with full fuel load using towbarless equipment
- Perform towing at minimum practical fuel load

Reducing aircraft mass reduces cumulative stress and fatigue exposure in NLG components.

8. Ground Surface and Slope Effects

Towbarless towing over:

- Uneven apron surfaces
- Expansion joints
- Sloped or inclined areas
- Hangar ramps
- Steep transitions

Introduces additional load vectors.

Mechanical Effects

On uneven or inclined surfaces:

- Vertical load distribution shifts rapidly
- Lateral forces increase due to tire constraint
- Additional torsional load is transmitted into torque links
- Shock strut experiences combined compression and bending
- Dynamic load spikes increase at surface transitions

On sloped surfaces:

- Braking forces increase longitudinal load
- Gravitational component increases nose gear reaction force
- Tire scrubbing force increases during turning

These combined load patterns may:

- Amplify bending moment at the fork
- Increase internal strut seal stress
- Accelerate bushing wear
- Increase fretting and corrosion initiation

Towbarless systems are less forgiving on uneven or inclined surfaces because load is applied at the tire contact patch without shear-limiting protection.

9. Engineering Load Hypothesis

Compared to shear-protected conventional towbar systems, towbarless towing may introduce:

- Increased lever arm (load at tire contact patch)
- Higher bending moments at fork and shock strut
- Elevated lateral and torsional load cycles
- Absence of mechanical load limiter
- Dynamic impulse loading from surface irregularities
- Increased loading on slopes and uneven terrain

These characteristics may accelerate wear in:

- Shock strut internal components
- Isolation piston seal
- Bushings and bearings
- Door interconnection hardware
- Steering and damping components
- Tire structure

The degradation appears cumulative and lifecycle-related.

10. Overall Conclusion

Aircraft exposed to frequent towbarless towing may demonstrate:

- Increased internal shock strut leakage
- Suspected accelerated isolation piston seal wear
- Progressive structural freeplay
- Accelerated NLG door hardware wear
- Increased corrosion at dynamic attachment points
- Potential unseen tire structural degradation
- Increased loading when towed at higher fuel weights
- Amplified load effects on uneven or sloped surfaces

The observed impact primarily affects component lifecycle and maintenance frequency rather than indicating immediate structural criticality.